Available online at www.sciencedirect.com
ScienceDirect
Physics reports April 8, 2017 (2017) 1–109
Physics reports

DRAFT

Stability and instability of hydromagnetic Taylor-Couette flows

Günther Rüdiger[a,*], Marcus Gellert[a], Rainer Hollerbach[b], Manfred Schultz[a], Frank Stefani[c*]

[a] *Leibniz-Institut für Astrophysik Potsdam, An der Sternwarte, 14482 Potsdam, Germany*
[b] *Department of Applied Mathematics, University of Leeds, Leeds, LS2 9JT, United Kingdom*
[c] *Helmholtz-Zentrum Dresden-Rossendorf, P.O. Box 510119, 01314 Dresden, Germany*

arXiv:1703.09919v1 [physics.plasm-ph] 29 Mar 2017

Abstract

Decades ago S. Lundquist, S. Chandrasekhar and R. J. Tayler first posed questions about the stability of incompressible Taylor-Couette flows of conducting material under the influence of large-scale background magnetic fields. These and many new questions can now be answered with numerical methods where the nonlinear simulations even provide the instability-induced turbulent values of several diffusivities. The cylindrical containers are here often assumed as axially unbounded and the background fields possess axial and/or azimuthal components. The influence of the magnetic Prandtl number Pm on the onset of the instabilities is demonstrated to be substantial. The potential flow subject to *axial fields* becomes unstable for a certain supercritical value of the Pm-dependent averaged Reynolds number $\overline{\mathrm{Rm}} = \sqrt{\mathrm{Re} \cdot \mathrm{Rm}}$, with Reynolds number Re and magnetic Reynolds number Rm. Rotation profiles as flat as the quasi-Keplerian rotation law scale similarly but only for $\mathrm{Pm} \gg 1$. For $\mathrm{Pm} \ll 1$ the instability instead sets in for supercritical Rm, which is the reason that to date the standard magnetorotational instability is hard to realize in a laboratory experiment. Among the instabilities of *azimuthal fields* due to axial electric currents inside and/or outside the fluid, those where the background field has the same radial profile as the background flow are particularly interesting. They are unstable against nonaxisymmetric perturbations if at least one of the diffusivities (viscosity or resistivity) is non-zero. For $\mathrm{Pm} \gg 1$ the onset of the instability again – with exception of the potential flow – scales with $\overline{\mathrm{Rm}}$, but the mode $m = 1$ scales with Reynolds number Re for $\mathrm{Pm} \ll 1$ (indicating the existence of solutions within the inductionless approximation, $\mathrm{Pm} = 0$). For the potential flow this critical ordinary Reynolds number is only 10^3, which allows experiments (Azimuthal MagnetoRotational Instability, AMRI) in Taylor-Couette containers filled with fluid metals. For flatter rotation profiles the higher modes ($m > 1$) scale with $\overline{\mathrm{Rm}}$, allowing even flows of high magnetic Mach numbers to become unstable. For positive shear magnetic instabilities also exist with and without axial electric currents, but they are of a double-diffusive character, hence $\mathrm{Pm} \neq 1$ is a necessary condition. The stability curves for superrotation plus current-free azimuthal field (Super-AMRI) also scale with Ha and Re for $\mathrm{Pm} \to 0$. Several new and successful experiments could thus be designed with liquid metals as the conducting fluid, starting with the experiment Promise which probed the interaction of twisted magnetic background fields with differential rotation resulting in unstable axially-traveling MHD waves. Several of these experiments together with the results of their nonlinear simulations are here reviewed together with relevant diversifications of the magnetic instability theory including numerical studies of the kinetic and magnetic energies, azimuthal spectra, mixing processes of a passive scalar, the Hall effect and axial density stratifications.

Keywords: Hydromagnetic instabilities; Taylor-Couette flows; Magnetorotational instability; Tayler instability; Fluid metals; Laboratory experiments,
PACS: 52.30.-g

*Corresponding author.
E-mail addresses: gruediger@aip.de, mgellert@aip.de, R.Hollerbach@leeds.ac.uk, mschultz@aip.de, f.stefani@hzdr.de

Contents

1 Historical introduction **4**

2 Stationary outer cylinder **7**
2.1 Axial field . . . 9
2.2 Azimuthal field . . . 12

3 Standard MagnetoRotational Instability (MRI) **16**
3.1 Potential flow . . . 17
3.2 Quasi-Keplerian flow . . . 19
3.3 Nonlinear simulations . . . 24
3.4 Angular momentum transport . . . 27

4 Azimuthal magnetorotational instability (AMRI) **29**
4.1 Potential flow . . . 29
4.2 Quasi-Keplerian rotation and beyond . . . 33
4.3 The AMRI experiment . . . 36
4.4 Eddy viscosity . . . 40
4.5 Super-AMRI . . . 41
4.5.1 Influence of boundary conditions . . . 42
4.5.2 Electric currents . . . 44

5 Chandrasekhar flows **44**
5.1 Inductionless approximation . . . 45
5.2 Potential flow . . . 45
5.3 Quasi-Keplerian flow . . . 46
5.4 Rigidly-rotating z-pinch . . . 50
5.5 Energies and cross-helicity . . . 51
5.6 Azimuthal spectra . . . 52

6 Helical MagnetoRotational Instability (HMRI) **53**
6.1 From AMRI to HMRI . . . 54
6.2 Potential flow and beyond . . . 56
6.3 Boundary conditions . . . 59
6.4 Quasi-Keplerian rotation . . . 59
6.5 Nonaxisymmetric modes . . . 60
6.6 Experiment PROMISE . . . 61

7 Tayler instability (TI) **64**
7.1 Wide gaps . . . 66
7.2 Kinetic and magnetic energy . . . 67
7.3 The GAllium-Tayler-Experiment (GATE) . . . 68

8 Tayler-Couette flow **69**
8.1 Rigid rotation . . . 69
8.2 Differential rotation . . . 71
8.3 Superrotation . . . 73
8.4 Influence of the boundary conditions . . . 75

9 Twisted fields **76**
9.1 Quasi-uniform azimuthal field . . . 77
9.2 Uniform axial current . . . 80

10 Transport coefficients **82**
10.1 Electromotive force . . . 83
10.1.1 Stationary pinch . . . 83
10.1.2 Quasi-Keplerian flow . . . 84
10.2 Angular momentum transport . . . 84
10.3 Mixing of a passive scalar . . . 85

11 Helicities, alpha effect **86**
11.1 Tayler instability . . . 87
11.2 Twisted background fields . . . 88
11.3 Axial shear . . . 90

12 Hall effect **92**
12.1 The Shear-Hall Instability (SHI) . . . 92
12.2 Hall-MRI . . . 94
12.3 Hall-TI . . . 94

13 Magnetized stratorotational instability **97**
13.1 Stratorotational instability . . . 97
13.2 Endplate effects . . . 99
13.3 Magnetized stratorotational instability . . . 100
13.4 Alpha effect . . . 102

14 References **104**

15 Acknowledgments **109**

1. Historical introduction

In 1923 G.I. Taylor considered the stability of a viscous flow between two axially unbounded cylinders rotating about the same axis with different frequencies but the same sign [1]. By use of the narrow-gap approximation he found that the flow can only be stable for rotation frequencies (normalized with the diffusion frequency) below a critical value that can be expressed by a critical Reynolds number whose theoretical value has been confirmed by experiments. This was the start of many theoretical developments towards an increasingly successful theory of hydrodynamic instabilities to understand the experimental findings.

The standard model for Taylor-Couette flow uses a stationary outer cylinder. If the outer cylinder does rotate, this tends to stabilize the flow, the more so the flatter the rotation profile is. Flows with

$$\mu_\Omega = r_{\rm in}^2 \tag{1}$$

with the definitions

$$\mu_\Omega = \frac{\Omega_{\rm out}}{\Omega_{\rm in}}, \qquad\qquad r_{\rm in} = \frac{R_{\rm in}}{R_{\rm out}} \tag{2}$$

are hydrodynamically stable as the Reynolds number

$$\mathrm{Re} = \frac{\Omega_{\rm in} R_0^2}{\nu} \tag{3}$$

for instability goes to infinity. Here $R_{\rm in}$ and $R_{\rm out}$ are the radii of the inner and outer cylinders, $\Omega_{\rm in}$ and $\Omega_{\rm out}$ are their rotation rates, ν the microscopic viscosity and $R_0 = \sqrt{R_{\rm in}(R_{\rm out} - R_{\rm in})}$. The condition (1) is also called the Rayleigh limit. It is easy to see that it represents the 'potential flow' $\Omega \propto 1/R^2$ (whose curl vanishes if Ω does not depend on z). The specific angular momentum $R^2\Omega$ of the potential flow does not depend on R.

For the often used standard model with stationary outer cylinder, with $R_{\rm out} = 2R_{\rm in}$ and for no-slip boundary conditions,

$$u_R = u_\phi = u_z = 0, \tag{4}$$

Chandrasekhar calculated $\mathrm{Re}_0 = 68.2$ [2]. For the nonaxisymmetric modes with the lowest azimuthal wave numbers $m = 1$ and $m = 2$ Roberts calculated $\mathrm{Re}_0 = 75$ and $\mathrm{Re}_0 = 127$ (see [3]). The Taylor vortices which are excited for the lowest rotation rate, therefore, are basically axisymmetric about the z-axis.

For inviscid fluids the condition (1) is replaced by the Rayleigh condition

$$\frac{1}{R^3}\frac{\mathrm{d}}{\mathrm{d}R}(R^2\Omega)^2 > 0, \tag{5}$$

which is sufficient and necessary for stability. Flows steeper than $1/R^2$ are unstable, but the potential flow is of neutral stability.

The present article reviews the results for modifications of the stability conditions (1) and (5) if the fluid is electrically conducting and in the presence of magnetic fields of relatively simple geometry. The fields may have only axial components or only azimuthal components or combinations of both. Michael formulated the question how *azimuthal* background magnetic fields modify the condition (5) for stability of ideal fluids (inviscid and perfect conducting) [4]. His criterion

$$\frac{1}{R^3}\frac{\mathrm{d}}{\mathrm{d}R}(R^2\Omega)^2 - \frac{R}{\mu_0\rho}\frac{\mathrm{d}}{\mathrm{d}R}\left(\frac{B_\phi}{R}\right)^2 > 0 \tag{6}$$

only ensures stability against axisymmetric perturbations. For $\Omega = 0$ the requirement for stability is [5, 6, 7]

$$\frac{\mathrm{d}}{\mathrm{d}R}\left(\frac{B_\phi}{R}\right)^2 < 0. \tag{7}$$

It shows that an azimuthal magnetic field in stationary cylinders is unstable against axisymmetric perturbations for positive n if it scales with radius R as R^{1+n}. In contrast, the field $B_\phi \propto 1/R$ due to an electric current along the central axis proves to be stable, while the field $B_\phi \propto R$ due to a uniform axial current has only marginal stability.

Michael's condition (6) shows that the combinations of stable flows with stable fields are always stable. Combinations of unstable flows with unstable fields are always unstable, while the combination of stable and unstable flows and fields leads to stability/instability depending on the relative amplitudes of the effects. Flows with high Mach numbers (ratio of the frequencies of global rotation and Alfvén rotation) are unstable if the rotation is unstable and stable if the rotation is stable. The full magnetohydrodynamic problem which led to (6) for real fluids (with finite values of viscosity and magnetic resistivity) has been formulated by Edmonds for a finite gap between two corotating cylinders of perfectly conducting material [8]. As Michael did, only axisymmetric perturbations were considered. The equation system was able to provide the critical Reynolds number of an instability as a function of the magnetic field (in form of its Hartmann number, see below) and the prescribed values of $r_{\rm in}$, μ_Ω and the magnetic Prandtl number

$$\mathrm{Pm} = \frac{\nu}{\eta} \tag{8}$$

as the ratio of the microscopic viscosity and the magnetic resistivity $\eta = 1/\mu_0\sigma$ (μ_0 the vacuum permeability, σ the electric conductivity). Characteristically, the liquid metals used in MHD experiments have very small magnetic Prandtl numbers, between 10^{-7} and 10^{-5}. The idea that it might be reasonable to put Pm = 0 in the equations (the so-called quasi-static or inductionless approximation) dominated the magnetohydrodynamic theory over several decades [9, 10, 11]. The equations have been solved numerically for finite values of $r_{\rm in}$ close to unity and μ_Ω. An instability only occurred for $\mu_\Omega < r_{\rm in}^2$ which means that the magnetic field suppressed the centrifugal instability as long as the Rayleigh limit is reached. The magnetic field did not generate a new axisymmetric instability.

Let us repeat that the stability criterion (6) only holds for axisymmetric perturbations. Indeed, the inclusion of nonaxisymmetric perturbations into the stability theory drastically changes the situation. Tayler considered the problem of stability against nonaxisymmetric perturbations of a uniform electric current within an axially unbounded cylinder [12]. The fluid itself may be a perfect conductor surrounded by vacuum while for the azimuthal field B_ϕ is proportional to R. A sufficient condition for stability in this case resulted as $m^2 \geq 2n + 4$, so that among the nonaxisymmetric modes only the azimuthal wave number $m = 1$ can be unstable, excluding the instability of the modes $m > 1$.

A particular version of Tayler's inequality for the azimuthal wave number $m = 1$ is

$$\frac{\mathrm{d}}{\mathrm{d}R}(RB_\phi^2) \leq 0 \tag{9}$$

as the sufficient and necessary condition for stability of a stationary ideal fluid against nonaxisymmetric perturbations [7]. All uniform and/or outwardly increasing fields are therefore not necessarily stable against perturbations with the mode number $m = 1$. This, in particular, is true for the field $B_\phi \propto R$ due to a uniform electric current.

Lundquist [13] argued that a uniform electric current can be stabilized by application of a uniform axial magnetic field if their energies are of the same order, i.e. $\langle B_z^2\rangle > \langle B_\phi^2\rangle$. The first experiments using mercury as a liquid conductor indeed seem to point in this direction [14]. Roberts [15] found instability against perturbations with high azimuthal mode numbers m for all ratios of azimuthal to axial field components. In his detailed paper Tayler [16] discussed the overall problem of current-driven instability under the influence of a *twisted* magnetic field without rotation. The innovation is that here the background field has its own nonvanishing current helicity $\boldsymbol{J}\cdot\boldsymbol{B}$. Valid only for inviscid fluids, his Fig. 7 demonstrates how positive growth rates of $m = 1$ perturbations without axial field are transformed to negative growth rates under the presence of an axial field of the same magnitude. Chandrasekhar showed that a sufficiently strong axial field will always suppress any axisymmetric instability of an azimuthal field by deriving the stability condition

$$\mathcal{I}B_z^2 > \int \frac{\xi_R^2}{R^2}\frac{\mathrm{d}}{\mathrm{d}R}(R^2B_\phi^2)\ \mathrm{d}R, \tag{10}$$

where $\mathcal{I} > 0$ and ξ_R is the (purely real) radial eigenfunction. Note how (10) reduces to

$$\frac{\mathrm{d}}{\mathrm{d}R}(R^2B_\phi^2) < 0 \tag{11}$$

as a sufficient condition for stability against axisymmetric perturbations [2]. Howard & Gupta [17] included differential rotation to extend this condition to

$$R\frac{\mathrm{d}\Omega^2}{\mathrm{d}R} - \frac{1}{\mu_0\rho R^3}\frac{\mathrm{d}}{\mathrm{d}R}\left(RB_\phi\right)^2 > 0. \tag{12}$$

Obviously, for the current-free field $B_\phi \propto 1/R$ only superrotating flows are stable. Below we shall demonstrate that dissipative super-potential flows which are hydrodynamically stable can easily be destabilized by helical magnetic fields with current-free azimuthal components. The resulting axisymmetric traveling wave instability has become known as the Helical MagnetoRotational Instability (HMRI) – see the Promise experiment. Note that the condition (10) only applies to axisymmetric perturbations and ideal fluids.

Tayler discussed the adiabatic stability of stars with mixed poloidal and toroidal fields [18]. For poloidal and toroidal field components of the same order he suggested stability of the system but the final answer to the question remained open.

The question how purely *axial* fields modify the rotating Taylor-Couette flow of conducting fluids has been addressed by Chandrasekhar in Ref. [19]. For axisymmetric perturbations in an axially unbounded cylinder he formulated the complete set of MHD equations, which leads to a 10^{th} order system of differential equations. After elimination of the pressure by means of the incompressibility condition $\mathrm{div}\,\boldsymbol{u} = 0$, six equations remain for the components of $\boldsymbol{u}$, and four equations for the two potentials of the field-perturbations $\boldsymbol{b}$. Applying the inductionless approximation $\mathrm{Pm} \to 0$ (which is not identical to taking $\nu = 0$, see [20]) the system is reduced to 8^{th} order.

The corresponding boundary conditions besides (4) follow from the general rule of electrodynamics that the normal component b_R of the magnetic field and the tangential component E_z of the electric field are continuous at the transition from the fluid to either cylinder walls. If it is assumed that the cylinders are made from a highly conducting material, then $E_z = b_R = 0$ at $R = R_{\text{in}}$ and $R = R_{\text{out}}$, resulting in the 'Fermi conditions'

$$b_R = \frac{\mathrm{d}b_\phi}{\mathrm{d}R} + \frac{b_\phi}{R} = 0. \tag{13}$$

For a given magnetic field amplitude, Chandrasekhar then computed the critical Reynolds number for the onset of instability, namely the smallest Reynolds number for all possible axial wave numbers. In all models the onset of the axisymmetric Taylor vortices is suppressed, where the suppression is weaker for the nonconducting cylinders. For these boundary conditions the results perfectly reflect the experimental results of Donnelly & Ozima [21, 3] obtained with mercury as the conducting fluid, with $\mathrm{Pm} \simeq 10^{-7}$. Both cylinders were made from stainless steel with $r_{\text{in}} = 0.95$, where the outer cylinder was stationary. Niblett stressed the importance of insulating boundary conditions in theory and experiments [22].

Within the narrow-gap approximation and imposing axisymmetry, Kurzweg solved the 10^{th} order system without any restriction on the magnetic Prandtl number [23]. For small Pm the magnetic field suppresses the Taylor instability but for large Pm and weak fields the instability is enhanced, leading to subcritical Reynolds numbers compared with the nonmagnetic case.

The magnetic boundary conditions in this work [23] are somewhat oversimplified, and do not completely match the formulation (13). Nevertheless, the new step to allow finite values of Pm was an important one for the following reason. Assume that some unknown instability exists which for small Pm scales with moderate values of the magnetic Reynolds number Rm = Pm Re. Then for small Pm the critical Reynolds numbers yield values that are too large for numerical methods to cope with, since $\mathrm{Pm} \to 0$ and finite Rm yields $\mathrm{Re} \to \infty$. The numerical codes for an 8^{th} order system could never find an instability which scales with Rm for $\mathrm{Pm} \to 0$. For small Pm the numerical calculations lead to $\mathrm{Re} \simeq 10.4\,\mathrm{Ha}$ with the Hartmann number

$$\mathrm{Ha} = \frac{B_0 R_0}{\sqrt{\mu_0\rho\nu\eta}}, \tag{14}$$

while quite another scaling appears for $\mathrm{Pm} \to \infty$, i.e. $\mathrm{Rm} \simeq 3.2\,\mathrm{S}$ with the Lundquist number $\mathrm{S} = \sqrt{\mathrm{Pm}}\mathrm{Ha}$. This scaling leads to a magnetic Mach number $\mathrm{Mm} \simeq 3.2$, so again the instability exists for large magnetic Mach numbers.

Our calculations below for axial fields and $\mu_\Omega = 0$ confirm the result of Kurzweg that for large Pm and weak fields the critical Reynolds numbers lie below the hydrodynamic value of 68 (for $r_{\rm in} = 0.5$). The latter value describes the wide-gap mode of the viscosimeter of Donnelly. In the narrow-gap mode it was $r_{\rm in} = 0.95$ with a Reynolds number of 185.

Both values $r_{\rm in} = 0.5$ and 0.95 are still in preferred use in MHD laboratories. Obviously, if the field is not too strong it can play a destabilizing role for a Taylor-Couette flow. For the ideal hydromagnetic Taylor-Couette flow this was first discovered by Velikhov [5, 24]. In the MHD regime the Rayleigh criterion for stability against axisymmetric perturbations, $\mu_\Omega > r_{\rm in}^2$, changes to

$$\frac{{\rm d}\Omega}{{\rm d}R} > 0 \tag{15}$$

i.e. only flows with superrotation are stable (see Fig. 1 in [5]). Velikhov found a growth rate along the Rayleigh line of $2\Omega_{\rm in} r_{\rm in}$. A dispersion relation has been derived for the Fourier frequency ω which only indicates instability if the Alfvén velocity $U_{\rm A} = B_0/\sqrt{\mu_0\rho}$ is smaller than the shear $-R^2{\rm d}\Omega/{\rm d}R$. His instability is thus an instability for large magnetic Mach numbers. We shall show that for dissipative fluids this new 'magnetorotational instability' (MRI) indeed scales for Pm $\to 0$ with the magnetic Reynolds number

$${\rm Rm} = \frac{\Omega_{\rm in} R_0^2}{\eta}, \tag{16}$$

which explains the absence of this mode in the early theories based on the inductionless approximation with Pm $\to 0$ [25]. For Pm $\gg 1$, on the other hand, the critical Rm does not remain constant but we shall find it growing with $\sqrt{\rm Pm}$.

The most complete theory of the subject at the time was formulated by Roberts [26]. The MHD equations were written for general magnetic Prandtl number, for a finite gap and with nonaxisymmetric modes included. The formulation of the boundary conditions avoided the Fermi conditions for perfectly conducting cylinders: fluid and walls have different but finite electric conductivities where the conductivity of the cylinders exceed the conductivity of the fluid by a factor of only 1.37. This problem proved much more difficult to solve than the problem with insulating walls. The critical Reynolds numbers (meaning minimal with respect to all wave numbers) have been computed for given magnetic Hartmann number, with the result that the Taylor instability is suppressed by the magnetic field and this happens more effectively for conducting boundaries than for insulating boundaries (his Fig. 2).

Following the experiments of Donelly & Ozima, the magnetic Prandtl number used by Roberts was that of mercury (10^{-7}), and the outer cylinder was stationary. This was the reason that the MRI did not appear in this study. As shown below for the rotation law satisfying Eq. (1), i.e. $\mu_\Omega = 0.25$ for $r_{\rm in} = 0.5$, the critical Reynolds number for standard MRI is Re $\simeq 66/\sqrt{\rm Pm}$ (see Section 3.1). This is a rather small numerical value for, e.g., Pm $\simeq 1$, indicating a new (magnetorotational) instability, as the Reynolds number for the nonmagnetic system at the Rayleigh limit is infinite. Roberts' code was certainly able to handle the magnetohydrodynamics near the Rayleigh limit for not too small Pm.

We shall revisit many of the mentioned questions (and preliminary answers) in the following where the stability of cylindric Taylor-Couette flows under the influence of large-scale magnetic background fields is considered when the fluid between the cylinders is electrically conducting. Present-day and future experiments will always form the focus of the calculations and simulations as has been already done in the first papers initiating this special branch of Taylor-Couette research at the beginning of this century [27, 28, 29, 25, 30].

As an introduction we start by considering the suppressing influence of axial and azimuthal magnetic fields on the classical Taylor-Couette flow with stationary outer cylinder. Then for much flatter rotation laws beyond the Rayleigh limit (1) the phenomena in connection with current-free fields between the cylinders are discussed as representatives of the magnetorotational instability. We shall see that by the detailed discussion of many combinations of flows and fields even the apparently very robust instability condition (15) can be overcome.

2. Stationary outer cylinder

The general MHD equations for the conducting fluid are

$$\rho\left(\frac{\partial \boldsymbol{U}}{\partial t} + (\boldsymbol{U}\cdot\boldsymbol{\nabla})\boldsymbol{U}\right) = -\nabla P + \rho\,\nu\,\Delta\boldsymbol{U} + \frac{1}{\mu_0}{\rm curl}\,\boldsymbol{B}\times\boldsymbol{B} \tag{17}$$

and

$$\frac{\partial \boldsymbol{B}}{\partial t} = \mathrm{curl}\,(\boldsymbol{U}\times\boldsymbol{B}) + \eta\,\Delta\boldsymbol{B}, \tag{18}$$

where $\boldsymbol{U}$ is the fluid flow, P the pressure, and $\boldsymbol{B}$ the magnetic field. The solutions must also fulfill the source-free conditions

$$\mathrm{div}\,\boldsymbol{U} = \mathrm{div}\,\boldsymbol{B} = 0. \tag{19}$$

The quantity $R_0 = \sqrt{R_{\rm in}(R_{\rm out}-R_{\rm in})}$ is used as the unit of length, η/R_0 as the unit of the perturbed velocity, ν/R_0^2 as the unit of frequency (inverse time). For both very wide and very narrow gaps it is often reasonable to replace R_0 by the gap width $D = R_{\rm out} - R_{\rm in}$. Note that $R_{\rm out} = 2R_{\rm in}$ is the only model with $R_0 = D$. We also define a characteristic magnetic field amplitude B_0 as the unit of the magnetic field fluctuations, R_0^{-1} as the unit of the wave number and $\Omega_{\rm in}$ as the unit of Ω. The dimensionless numbers of the problem are then the Reynolds number (3), the magnetic Prandtl number (8) and the Hartmann number (14) which is formed with the geometric average of the diffusivities, $\bar\eta = \sqrt{\nu\eta}$. We shall see that in most cases where no instability for $B_0 = 0$ exists, the magnetic Reynolds number $\mathrm{Rm} = \mathrm{Pm}\,\mathrm{Re}$ and the Lundquist number $\mathrm{S} = \sqrt{\mathrm{Pm}}\,\mathrm{Ha}$ are better representations of the characteristic eigenvalues. There are also exceptions to this rule when the stability/instability of rather steep rotation laws in the presence of toroidal fields is considered. Sometimes it also makes sense to use the averaged Reynolds number

$$\overline{\mathrm{Rm}} = \sqrt{\mathrm{ReRm}} = \frac{\Omega_{\rm in}R_0^2}{\bar\eta}, \tag{20}$$

formed with $\bar\eta$ instead of η hence $\mathrm{Mm} = \overline{\mathrm{Rm}}/\mathrm{Ha}$. The magnetic Mach number

$$\mathrm{Mm} = \frac{\mathrm{Rm}}{\mathrm{S}} = \frac{\overline{\mathrm{Rm}}}{\mathrm{Ha}}, \tag{21}$$

which does not involve any diffusivities, can be considered as a rotation rate normalized with the Alfvén frequency $B_0/\sqrt{\mu_0\rho R_0^2}$. The magnetic Mach numbers of astrophysical objects often exceed unity. Galaxies have Mm between 1 and 10, for the solar tachocline with a magnetic field of 1 kG one obtains $\mathrm{Mm} \simeq 30$, and for typical white dwarfs and neutron stars $\mathrm{Mm} \simeq 1000$. For magnetars with fields of $\sim 10^{14}$ G and a rotation period of ∼1 s, the magnetic Mach number is $\sim 0.1 - 1$.

In general, $\boldsymbol{U}$, $\boldsymbol{B}$ and P may be split into mean and fluctuating components $\boldsymbol{U} = \bar{\boldsymbol{U}} + \boldsymbol{u}$, $\boldsymbol{B} = \bar{\boldsymbol{B}} + \boldsymbol{b}$ and $P = \bar P + p$. In this work we immediately drop the bars from the variables again, so that the upper-case letters $\boldsymbol{U}$, $\boldsymbol{B}$ and P represent the large-scale or background quantities. By developing the disturbances $\boldsymbol{u}$, p and $\boldsymbol{b}$ into normal modes, the solutions of the linearized MHD equations are considered in the form

$$\boldsymbol{u} = \boldsymbol{u}(R)\mathrm{e}^{\mathrm{i}(\omega t+kz+m\phi)}, \qquad p = p(R)\mathrm{e}^{\mathrm{i}(\omega t+kz+m\phi)}, \qquad \boldsymbol{b} = \boldsymbol{b}(R)\mathrm{e}^{\mathrm{i}(\omega t+kz+m\phi)} \tag{22}$$

for axially unbounded cylinders. Here k is the axial wave number, m the azimuthal wave number and ω the complex frequency including growth rate and a possible drift (or oscillation) frequency.

For viscous flows in the absence of any longitudinal pressure gradient the basic form of the radial rotation law in the container is

$$\Omega(R) = a_\Omega + \frac{b_\Omega}{R^2}, \tag{23}$$

where a_Ω and b_Ω are two constants related to the angular velocities $\Omega_{\rm in}$ and $\Omega_{\rm out}$ with which the inner and outer cylinders rotate (we shall only be interested in positive $\Omega_{\rm in}$ and $\Omega_{\rm out}$). With $R_{\rm in}$ and $R_{\rm out}$ being the radii of the two cylinders, one obtains the coefficients

$$a_\Omega = \frac{\mu_\Omega - r_{\rm in}^2}{1-r_{\rm in}^2}\Omega_{\rm in}, \qquad\qquad b_\Omega = \frac{1-\mu_\Omega}{1-r_{\rm in}^2}\Omega_{\rm in}R_{\rm in}^2, \tag{24}$$

using the definitions (2).

According to the Rayleigh criterion the ideal flow is stable whenever the specific angular momentum increases outwards, i.e.

$$\mu_\Omega \geq r_{\rm in}^2. \tag{25}$$

It is not stable for high rotation rates, however, if the outer cylinder is stationary so that (23) becomes

$$\Omega(R) = \frac{\Omega_{\rm in}}{1-r_{\rm in}^2}\left(\frac{R_{\rm in}^2}{R^2} - r_{\rm in}^2\right). \tag{26}$$

This is the rotation law whose stability characteristics in the presence of either axial or azimuthal magnetic background fields are discussed in the following.

2.1. Axial field

Figure 1 displays the geometrical setup and repeats the main definitions of the input parameters. The relevant equations follow from Eqs. (17)–(19) and can be written as a system of ten first order equations. After eliminating p and b_z, the linearized equations become

$$\begin{aligned}
&\frac{{\rm d}^2u_\phi}{{\rm d}R^2} + \frac{1}{R}\frac{{\rm d}u_\phi}{{\rm d}R} - \frac{u_\phi}{R^2} - \left(\frac{m^2}{R^2}+k^2\right)u_\phi - {\rm i}\,(m{\rm Re}\,\Omega+\omega)\,u_\phi + \\
&\quad + \frac{2{\rm i}m}{R^2}u_R - {\rm Re}\frac{1}{R}\frac{\rm d}{{\rm d}R}\left(R^2\,\Omega\right)u_R - \frac{m}{k}\left[\frac{1}{R}\frac{{\rm d}^2u_z}{{\rm d}R^2} + \frac{1}{R^2}\frac{{\rm d}u_z}{{\rm d}R} - \right. \\
&\quad \left. - \left(\frac{m^2}{R^2}+k^2\right)\frac{u_z}{R} - {\rm i}\,(m{\rm Re}\,\Omega+\omega)\,\frac{u_z}{R}\right] + \frac{m}{k}{\rm Ha}^2\left[\frac{1}{R}\frac{{\rm d}b_R}{{\rm d}R} + \frac{b_R}{R^2}\right] + \frac{\rm i}{k}{\rm Ha}^2\left(\frac{m^2}{R^2}+k^2\right)b_\phi = 0,
\end{aligned} \tag{27}$$

$$\begin{aligned}
&\frac{{\rm d}^3u_z}{{\rm d}R^3} + \frac{1}{R}\frac{{\rm d}^2u_z}{{\rm d}R^2} - \frac{1}{R^2}\frac{{\rm d}u_z}{{\rm d}R} - \left(\frac{m^2}{R^2}+k^2\right)\frac{{\rm d}u_z}{{\rm d}R} + \frac{2m^2}{R^3}u_z - {\rm i}\,(m{\rm Re}\,\Omega+\omega)\,\frac{{\rm d}u_z}{{\rm d}R} - \\
&\quad - {\rm i}m{\rm Re}\frac{{\rm d}\Omega}{{\rm d}R}u_z - {\rm Ha}^2\left[\frac{{\rm d}^2b_R}{{\rm d}R^2} + \frac{1}{R}\frac{{\rm d}b_R}{{\rm d}R} - \frac{b_R}{R^2} - k^2b_R + \frac{{\rm i}m}{R}\frac{{\rm d}b_\phi}{{\rm d}R} - \frac{{\rm i}m}{R^2}b_\phi\right] \\
&\quad - {\rm i}k\left[\frac{{\rm d}^2u_R}{{\rm d}R^2} + \frac{1}{R}\frac{{\rm d}u_R}{{\rm d}R} - \frac{u_R}{R^2} - \left(k^2+\frac{m^2}{R^2}\right)u_R\right] - k\,(m{\rm Re}\,\Omega+\omega)\,u_R - 2\frac{km}{R^2}u_\phi - 2{\rm i}k{\rm Re}\,\Omega u_\phi = 0.
\end{aligned} \tag{28}$$

The field perturbations fulfill

$$\frac{{\rm d}^2b_R}{{\rm d}R^2} + \frac{1}{R}\frac{{\rm d}b_R}{{\rm d}R} - \frac{b_R}{R^2} - \left(\frac{m^2}{R^2}+k^2\right)b_R - \frac{2{\rm i}m}{R^2}b_\phi - {\rm iPm}\,(m{\rm Re}\,\Omega+\omega)\,b_R + {\rm i}ku_R = 0 \tag{29}$$

and

$$\frac{{\rm d}^2b_\phi}{{\rm d}R^2} + \frac{1}{R}\frac{{\rm d}b_\phi}{{\rm d}R} - \frac{b_\phi}{R^2} - \left(\frac{m^2}{R^2}+k^2\right)b_\phi + \frac{2{\rm i}m}{R^2}b_R - {\rm iPm}\,(m{\rm Re}\,\Omega+\omega)\,b_\phi + {\rm i}ku_\phi + {\rm Pm\ Re}\,R\frac{{\rm d}\Omega}{{\rm d}R}b_R = 0 \tag{30}$$

[31]. The last term in Eq. (30) describes the energy input by the induction of the global shear. It vanishes for Pm = 0 so that in the inductionless approximation differential rotation cannot be destabilized by uniform axial fields (no MRI, see next section). The hydrodynamic continuity equation

$$\frac{{\rm d}u_R}{{\rm d}R} + \frac{u_R}{R} + \frac{{\rm i}m}{R}u_\phi + {\rm i}ku_z = 0, \tag{31}$$

completes the system. The rotation law $\Omega = \Omega(R)$ in these relations is normalized with $\Omega_{\rm in} = \Omega(R_{\rm in})$. The vertical component b_z follows from the continuity condition

$$\frac{{\rm d}b_R}{{\rm d}R} + \frac{b_R}{R} + \frac{{\rm i}m}{R}b_\phi + {\rm i}kb_z = 0. \tag{32}$$

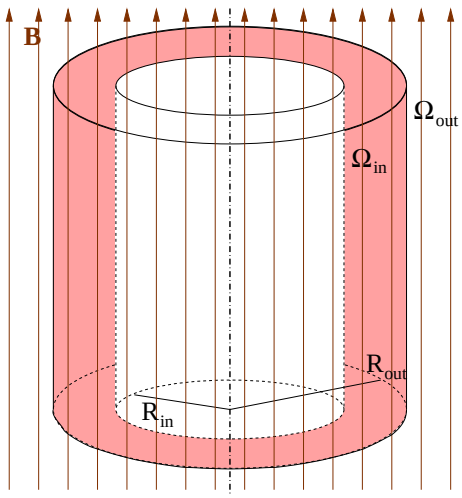

Figure 1. The geometry of hydromagnetic Taylor-Couette flows with uniform axial fields. The cylinders are made from perfectly conducting and/or insulating material. The rotation rates of both cylinders are fixed by boundary conditions. The majority of applications concerns axially unbounded containers while endplate effects are only discussed related to existing experiments. The standard container throughout the entire paper is defined by $R_{\rm out} = 2R_{\rm in}$.

An appropriate set of ten boundary conditions is needed to solve the system. For the hydrodynamic quantities we always use the no-slip conditions for the velocity $u_R = u_\phi = u_z = 0$. Generally, the normal component of the magnetic field and the tangential component of the electric field must be continuous. For perfectly conducting walls the conditions (13) apply at $R_{\rm in}$ and $R_{\rm out}$. For insulating walls the magnetic field at the boundaries must match the vacuum field with curl $\boldsymbol{b} = 0$, hence

$$b_R + \frac{{\rm i}b_z}{I_m(kR)}\left(\frac{m}{kR}I_m(kR) + I_{m+1}(kR)\right) = 0, \tag{33}$$

for $R = R_{\rm in}$, and

$$b_R + \frac{{\rm i}b_z}{K_m(kR)}\left(\frac{m}{kR}K_m(kR) - K_{m+1}(kR)\right) = 0, \tag{34}$$

for $R = R_{\rm out}$, where I_m and K_m are the modified Bessel functions. The conditions for the toroidal field are simply $kRb_\phi = m\,b_z$ at $R_{\rm in}$ and $R_{\rm out}$ (see [26]). In both cases five conditions exist at each boundary, so that the necessary ten conditions can be formulated. For both sorts of magnetic boundary conditions the resulting eigenvalues are often close together.

The homogeneous set of linear equations together with the choice of boundary conditions determines the eigenvalue problem for any given value of Pm. The real part $\Re(\omega)$ of ω describes a drift of the pattern depending on the rotational symmetry: the drift is along the z-axis for $m = 0$ and it is along the azimuth for $m \neq 0$. For a fixed Hartmann number, a fixed Prandtl number and a given axial wave number one finds the eigenvalues Re and $\Re(\omega)$. For a certain axial wave number a minimum of the Reynolds numbers exists, which is the desired critical Reynolds number.

Figure 2 shows the neutral stability for axisymmetric modes for containers with both conducting and insulating walls with stationary outer cylinder and for fluids of various magnetic Prandtl number. These results are merely a generalization of the early results in Ref. [26], where very similar methods were used to analyze the narrow-gap case $r_{\rm in} = 0.95$ for both types of magnetic boundary conditions. For the small magnetic Prandtl number of mercury the phenomenon of the magnetic stabilization of the centrifugal instability has already been found, which can be observed in Figs. 2 presenting the stability maps of the axisymmetric perturbations under the presence of axial fields. The magnetic suppression of the onset of the centrifugal instability is stronger for conducting walls than for insulating walls. $\mathrm{Re}_0 = 68$ is the classical hydrodynamic eigenvalue for $m = 0$, $\mu_\Omega = 0$ and $r_{\rm in} = 0.5$. Note the strong difference of the bifurcation lines for $\mathrm{Pm} \gtrsim 1$ and $\mathrm{Pm} < 1$. For small Pm the magnetic field always suppresses the instability so that all the given critical Reynolds numbers exceed the value 68. For $\mathrm{Pm} \to 0$ the stability lines no longer differ for

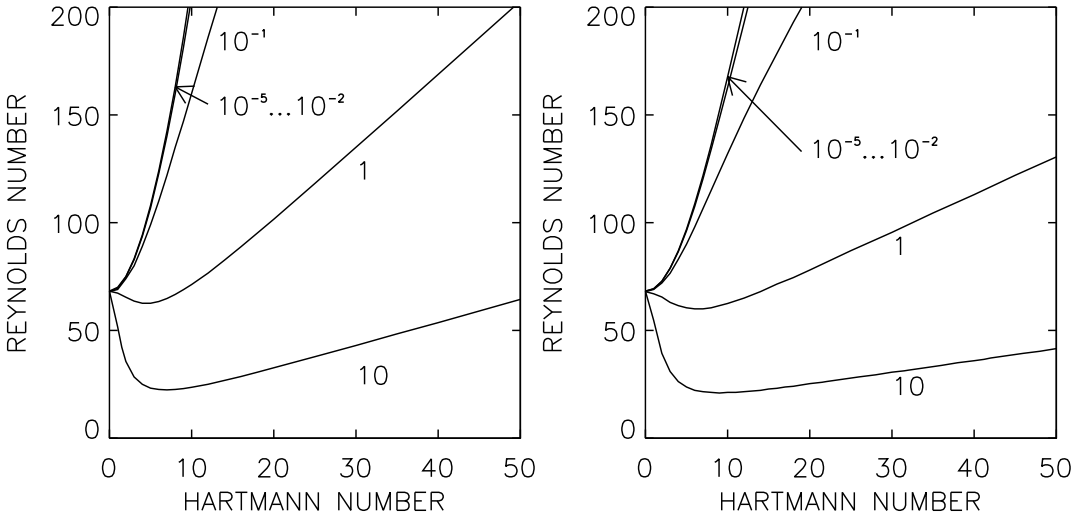

Figure 2. Stability maps for the axisymmetric modes of MHD Taylor-Couette flows with stationary outer cylinder for perfectly conducting (left) or insulating (right) boundary conditions. $\mathrm{Re}_0 = 68$ is the well-known eigenvalue for marginal instability of the hydrodynamic flow. The curves are marked with Pm. Note the existence of magnetically induced subcritical excitation of instability for large Pm [23]. The influence of the two differing boundary conditions is here only weak. $\mu_\Omega = 0$, $r_{\rm in} = 0.5$. From Ref. [32].

different Pm, which may be expressed as a statement that for small Pm the magnetically suppressed instability scales with Ha and Re. On the other hand, for $\mathrm{Pm} \gtrsim 1$ the resulting Reynolds numbers can be smaller than the nonmagnetic value $\mathrm{Re}_0 = 68$. For small Hartmann numbers the magnetic field, therefore, does *not* stabilize the flow. This high-Pm phenomenon – which we shall often meet in the following – becomes more effective for increasing Pm, but in all cases it vanishes for stronger magnetic fields. One can show that the minima which appear for high Pm scale like $\overline{\mathrm{Rm}} \simeq$const so that $\mathrm{Re} \propto \mathrm{Pm}^{-1/2}$ leading to $\Omega \propto \bar{\eta}$ for fixed gap width with $\bar{\eta} = \sqrt{\nu\eta}$. The critical rotation rate of the inner cylinder only depends on the product of ν and η.

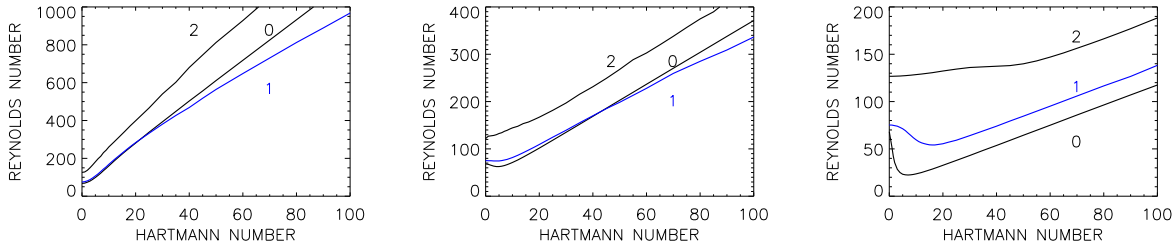

Figure 3. Stability maps of the modes $m = 0$, $m = 1$ (blue lines) and $m = 2$ for perfectly conducting cylinders and axial fields. From left to right: Pm = 0.1, Pm = 1, Pm = 10. Note the line crossing for $m = 0$ and $m = 1$ for small magnetic Prandtl number and large Hartmann numbers which lead to nonaxisymmetric modes as the preferred excitations. $\mu_\Omega = 0$, $r_{\rm in} = 0.5$.

While Fig. 2 only provides the bifurcation lines for the axisymmetric modes, Fig. 3 demonstrates the excitation conditions of the nonaxisymmetric modes $m = 1$ and $m = 2$ for various Pm. The nonmagnetic Rayleigh instability for $m = 0$ leads to $\mathrm{Re}_0 = 68, 75, 127$ for $m = 0, 1, 2$. Without magnetic fields the axisymmetric mode always has the lowest Reynolds number. However, the plots in Fig. 3 also show crossings of the instability lines for axisymmetric and nonaxisymmetric modes of the MHD flows with $\mathrm{Pm} \leq 1$. Below we shall demonstrate that this phenomenon also appears for containers with rotating outer cylinder.

So far however, the crossover phenomenon only appeared in calculations using perfectly conducting boundary conditions. In these cases the magnetic suppression of the instability against axisymmetric perturbations is much stronger

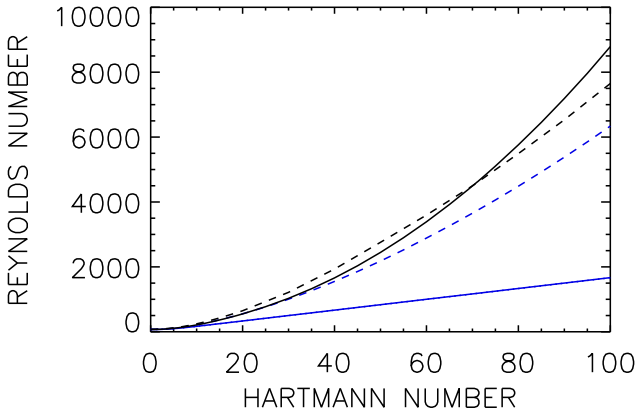

Figure 4. Axial background fields: stability maps for the modes $m = 0$ (solid lines) and $m = 1$ (dashed lines) for conducting cylinders (black) and insulating cylinders (blue). The prevalence of the nonaxisymmetric mode for strong fields only appears for conducting cylinders. For insulating cylinders the $m = 0$ mode is much less stabilized by the magnetic field than the $m = 1$ mode so that crossings cannot appear. $\mu_\Omega = 0$, $r_{\rm in} = 0.5$, $\mathrm{Pm} = 10^{-5}$.

than for insulating boundary conditions[1]. One finds from Fig. 4 that the differences of the critical Reynolds numbers of the nonaxisymmetric modes are much smaller than the differences for axisymmetric modes so that crossovers of the lines for insulating boundary conditions cannot happen. The most striking phenomenon is that for insulating cylinders the magnetic suppression of the axisymmetric mode is much weaker than the suppression of the nonaxisymmetric modes so that $m = 0$ is always the mode with the lowest Reynolds number [32].

2.2. Azimuthal field

We next consider Taylor-Couette flows with a stationary outer cylinder under the influence of an azimuthal magnetic field. Ref. [8] showed that current-free toroidal fields ($B_\phi \propto 1/R$) suppress the axisymmetric Taylor vortices, at least in the narrow-gap limit, with conducting boundaries, and dissipative fluids. This result holds true even if the narrow-gap approximation is not made. Allowing electric currents to flow within the fluid though can dramatically change the results, as we shall see below.

The radial profile of an azimuthal background field in a dissipative system is

$$B_\phi = a_B R + \frac{b_B}{R}, \tag{35}$$

where a_B and b_B are defined by the values of the azimuthal magnetic field at the inner ($B_{\rm in}$) and outer ($B_{\rm out}$) boundaries as

$$a_B = \frac{B_{\rm in}}{R_{\rm in}} \frac{r_{\rm in}(\mu_B - r_{\rm in})}{1 - r_{\rm in}^2}, \qquad b_B = B_{\rm in} R_{\rm in} \frac{1 - \mu_B r_{\rm in}}{1 - r_{\rm in}^2} \tag{36}$$

with

$$\mu_B = \frac{B_{\rm out}}{B_{\rm in}}. \tag{37}$$

The constants $B_{\rm in}$ and $B_{\rm out}$ are defined by the vertical electric currents inside the inner and outer cylinders. For $\mu_B = 1/r_{\rm in}$ we have $b_B = 0$ so that the magnetic field is of the form $B_\phi \propto R$, describing a uniform axial current within

[1] One can find this phenomenon also by comparison of the data in Fig. 2.

$R < R_{\rm out}$ ('z-pinch'). For $\mu_B = r_{\rm in}$ we have $a_B = 0$ and $B_\phi \propto 1/R$, which is current-free outside $R_{\rm in}$. A field of the form b_B/R is generated by running an axial current only through the inner region $R < R_{\rm in}$, whereas a field of the form $a_B R$ is generated by running a uniform axial current through the entire region $R < R_{\rm out}$ including the fluid. As the standard choice in this paper will be $r_{\rm in} = 0.5$ one finds $\mu_B = 0.5$ for the solution which is current-free between the cylinders and $\mu_B = 2$ for the solution with uniform axial electric current between the cylinders. Another important radial profile of the background field which we shall often consider is given by $\mu_B = 1$, describing a solution with almost uniform magnetic field between the cylinders. We have $b_B/a_B = R_{\rm in}^2/r_{\rm in}$ in this case. Expressing the electric currents in Ampere we obtain

$$I_{\rm axis} = 5R_{\rm in}B_{\rm in}, \qquad I_{\rm fluid} = 5(R_{\rm out}B_{\rm out} - R_{\rm in}B_{\rm in}) \tag{38}$$

with $I_{\rm axis}$ the axial current inside the inner cylinder and $I_{\rm fluid}$ the axial current through the fluid. Here R, B and I are measured in centimeter, Gauss and Ampere. Expressing $I_{\rm axis}$ and $I_{\rm fluid}$ in terms of the Hartmann number

$$\mathrm{Ha} = \frac{B_{\rm in}R_0}{\sqrt{\mu_0\rho\nu\eta}} \tag{39}$$

one finds

$$I_{\rm axis} = 5\mathrm{Ha}\,\sqrt{\frac{r_{\rm in}}{1-r_{\rm in}}}\,\sqrt{\mu_0\rho\nu\eta}, \qquad I_{\rm fluid} = \frac{\mu_B - r_{\rm in}}{r_{\rm in}} I_{\rm axis}. \tag{40}$$

For $\mu_B = r_{\rm in}$ we find $I_{\rm fluid} = 0$ for the solution with $a_B = 0$. On the other hand, for $\mu_B = 1/r_{\rm in}$ it is $(1-r_{\rm in}^2)I_{\rm axis} = r_{\rm in}^2 I_{\rm fluid}$ hence $I_{\rm axis} = 0$ for $r_{\rm in} = 0$ and $I_{\rm axis} = I_{\rm fluid}/3$ for $r_{\rm in} = 0.5$.

The dimensionless parameters of the instability problem are the same as defined above, but with $B_{\rm in}$ instead of B_0 as in (14). The necessary and sufficient condition for ideal flow stability is (6). Using (23) for the angular velocity and (35) for the magnetic field and normalizing with $r = R/R_0$, Eq. (6) takes the form

$$a_\Omega^2 + \frac{a_\Omega b_\Omega}{r^2} + \frac{b_B}{(\mathrm{Mm})^2 r^2}\left(a_B + \frac{b_B}{r^2}\right) > 0 \tag{41}$$

with $\mathrm{Mm} = \Omega_{\rm in}/(B_{\rm in}/\mu_0\rho R_0^2)^{1/2}$ as the magnetic Mach number representing a normalized rotation rate. The angular velocity part of (41) is positive for hydrodynamically stable flows beyond the Rayleigh limit. The magnetic part has a simple structure. It vanishes for $b_B = 0$. Hence, magnetic fields $B_\phi \propto R$ have no influence on the axisymmetric mode of the instability for any rotation profiles. On the other hand, the magnetic part in (41) is positive definite for $a_B = 0$ so that magnetic fields which are current-free in the fluid ($B_\phi \propto 1/R$) always stabilize any rotation profile.

Beyond these extremes it is always possible that the magnetic influence destabilizes rotation profiles beyond the Rayleigh limit against axisymmetric perturbations. It is also obvious that for negative magnetic parts in (41) (i.e. $\mu_B > 1/r_{\rm in}$) one always finds values of the magnetic Mach number which are small enough to provide negative values of (41) for any μ_Ω. Some sorts of magnetic fields with sufficiently strong currents can thus destabilize any rotation law even against axisymmetric perturbations. This is in particular true in the Rayleigh limit where $a_\Omega = 0$ so that the nonmagnetic part in (41) vanishes and all fields with $b_B < 0$ become unstable which according to (36) means $\mu_B > 1/r_{\rm in}$.

In the following we shall apply the two extreme azimuthal magnetic fields (with $a_B = 0$ and with $b_B = 0$) to the rotation profile having a stationary outer cylinder, and find completely different classes of solutions. The normalized equations with background toroidal fields are

$$\frac{\mathrm{d}^2u_R}{\mathrm{d}R^2} + \frac{1}{R}\frac{\mathrm{d}u_R}{\mathrm{d}R} - \frac{u_R}{R^2} - \left(k^2 + \frac{m^2}{R^2}\right)u_R - 2\mathrm{i}\frac{m}{R}u_\phi - \mathrm{i}\,\mathrm{Re}(\omega + m\Omega)u_R + 2\mathrm{Re}\Omega u_\phi - \frac{\mathrm{d}p}{\mathrm{d}R} + \mathrm{i}\frac{m}{R}\mathrm{Ha}^2 B_\phi b_R - 2\mathrm{Ha}^2\frac{B_\phi}{R}b_\phi = 0 \tag{42}$$

$$\frac{\mathrm{d}^2u_\phi}{\mathrm{d}R^2} + \frac{1}{R}\frac{\mathrm{d}u_\phi}{\mathrm{d}R} - \frac{u_\phi}{R^2} - \left(k^2 + \frac{m^2}{R^2}\right)u_\phi + 2\mathrm{i}\frac{m}{R}u_R - \mathrm{i}\,\mathrm{Re}(\omega + m\Omega)u_\phi - \mathrm{i}\frac{m}{R}p - \frac{\mathrm{Re}}{R}\frac{\mathrm{d}}{\mathrm{d}R}(R^2\Omega)u_R + \frac{\mathrm{Ha}^2}{R}\frac{\mathrm{d}}{\mathrm{d}R}\left(B_\phi R\right)b_R + \mathrm{i}\frac{m}{R}\mathrm{Ha}^2 B_\phi b_\phi = 0, \tag{43}$$

$$\frac{\mathrm{d}^2 u_z}{\mathrm{d}R^2} + \frac{1}{R}\frac{\mathrm{d}u_z}{\mathrm{d}R} - \left(k^2 + \frac{m^2}{R^2}\right)u_z - \mathrm{i}\,\mathrm{Re}(\omega + m\Omega)u_z - \mathrm{i}\,kp + \mathrm{i}\frac{m}{R}\mathrm{Ha}^2 B_\phi b_z = 0 \tag{44}$$

and

$$\frac{\mathrm{d}^2 b_R}{\mathrm{d}R^2} + \frac{1}{R}\frac{\mathrm{d}b_R}{\mathrm{d}R} - \frac{b_R}{R^2} - \left(k^2 + \frac{m^2}{R^2}\right)b_R - 2\mathrm{i}\frac{m}{R^2}b_\phi - \mathrm{i}\,\mathrm{Pm}\,\mathrm{Re}(\omega + m\Omega)b_R + \mathrm{i}\frac{m}{R}B_\phi u_R = 0, \tag{45}$$

$$\frac{\mathrm{d}^2 b_\phi}{\mathrm{d}R^2} + \frac{1}{R}\frac{\mathrm{d}b_\phi}{\mathrm{d}R} - \frac{b_\phi}{R^2} - \left(k^2 + \frac{m^2}{R^2}\right)b_\phi + 2\mathrm{i}\frac{m}{R^2}b_R - \mathrm{i}\,\mathrm{Pm}\,\mathrm{Re}(\omega + m\Omega)b_\phi + \mathrm{PmRe}R\frac{\mathrm{d}\Omega}{\mathrm{d}R}b_R - R\frac{\mathrm{d}}{\mathrm{d}R}\left(\frac{B_\phi}{R}\right)u_R + \mathrm{i}\frac{m}{R}B_\phi u_\phi = 0, \tag{46}$$

with the boundary conditions described above ([33]). The system is again supplemented by the incompressibility condition (31). The vertical component b_z follows from (32).

The wave number is again varied until the Reynolds number for a given Hartmann number reaches its minimum. The resulting wave number corresponds to the most unstable mode. Both the background flow and magnetic field are normalized with their values at $R = R_{\mathrm{in}}$, hence $\hat{\Omega} = \Omega/\Omega_{\mathrm{in}}$, $\hat{B}_\phi = B_\phi/B_{\mathrm{in}}$ (and the hats are then immediately dropped).

This system has the characteristic symmetry that if k is kept fixed, but m is replaced by $-m$, and simultaneously the eigenvalue $\mathrm{i}\omega$, the flow $\boldsymbol{u}$ and the field $\boldsymbol{b}$ are transformed to their complex conjugates, then the overall system remains unchanged. This means that $m = \pm 1$ constitute a single solution, with the same drift rate $\Re(\omega)/m$, Reynolds and Hartmann numbers.

In the *first case* B_ϕ may be assumed as current-free, i.e. $a_B = 0$ or $\mu_B = 0.5$ if $r_{\mathrm{in}} = 0.5$. Figure 5 (left) gives the resulting critical Reynolds numbers as functions of the Hartmann number for the modes with $m = 0$, $m = 1$ and $m = 2$. The three corresponding Reynolds numbers for the modes are (again) 68, 75 and 127 for $m = 0, 1, 2$. The above statement for ideal fluids is confirmed that current-free fields always suppress the axisymmetric modes as shown here for Pm = 1 and Pm = 10^{-5}. The suppression is stronger for smaller magnetic Prandtl numbers.

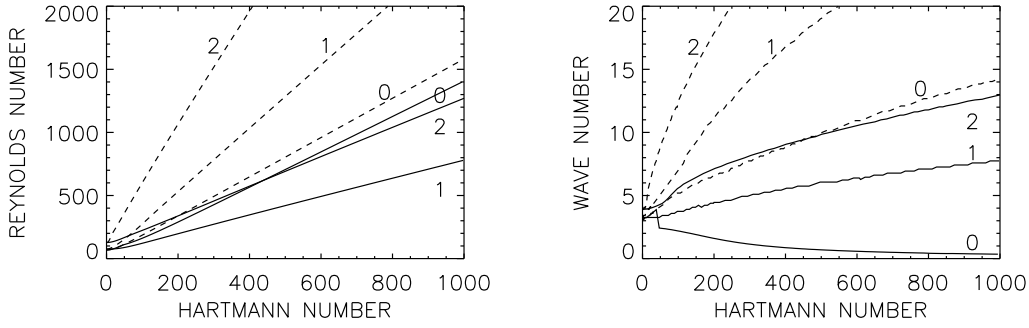

Figure 5. Azimuthal background fields: critical Reynolds numbers (left panel) and the corresponding wave numbers (right panel) for the modes with $m = 0$, $m = 1$ and $m = 2$ of the flow with stationary outer cylinder subject to current-free azimuthal fields for Pm = 1 (solid) and Pm = 10^{-5} (dashed). $r_{\mathrm{in}} = 0.5$, $\mu_\Omega = 0$, $\mu_B = 0.5$. Perfectly conducting cylinders.

There are, however, open questions about the nonaxisymmetric modes. It is obvious that strong differential rotation should lead to a suppression of the instability, as nonuniform rotation for sufficiently high electric conductivity always suppresses nonaxisymmetric modes. On the other hand, weak differential rotation may support the excitation of nonaxisymmetric modes in contrast to rigid rotation. A Taylor-Couette flow with stationary outer cylinder may easily serve as a model to answer this question.

From Fig. 5 one finds that even current-free azimuthal fields suppress nonaxisymmetric modes. The stabilizing action of the field is stronger on nonaxisymmetric rather than on axisymmetric modes. This finding complies with

the above mentioned idea that differential rotation strongly amplifies the dissipation of nonaxisymmetric modes. Note that the calculated lines of neutral stability of the mode $m = 0$ hardly differ for Pm = 1 and Pm = 10^{-5}. The eigenvalues along the line of neutral stability of the axisymmetric modes, therefore, appear to scale with Re and Ha for Pm $\to 0$. In both cases the magnetic field simply suppresses the axisymmetric mode as predicted by Eq. (41). The results, however, for the nonaxisymmetric modes and for Pm = 1 are surprising with respect to the line crossings in the left panel of Fig. 5. For Ha < 18 the lowest Reynolds number for instability is for $m = 0$ but for larger values $m = 1$ is preferred. For higher values of Ha even the $m = 2$ mode overcomes the axisymmetric solution. The same phenomenon might happen for small Pm but for much higher Hartmann numbers (not shown). We thus find again crossover effects for the instability of the rotation law with stationary outer cylinder, quite similar to the interaction with axial fields (see Fig. 3). Magnetically influenced Taylor-Couette flows – if the field is strong enough – appear to form nonaxisymmetric structures much easier than nonmagnetic flows. We shall see below that the nonaxisymmetry of the instability pattern shown by Fig. 5 (left) proves to be a characteristic property also of all Taylor-Couette flows subject to azimuthal fields formed by stable rotation with no electric current and/or no rotation with electric current. We call phenomena related to the first case the Azimuthal MagnetoRotational Instability (AMRI) and the second case the Tayler Instability (TI).

Another finding concerns the axial wavelengths of the unstable modes. Under the magnetic influence they become shorter and shorter except for $m = 0$, Pm = 1 and Ha ≥ 40. For this curve the axisymmetric Taylor vortex as the mode with the lowest Reynolds number (see [34]) develops from nearly spherical cells to cells strongly elongated in the axial direction under the influence of the current-free azimuthal magnetic field. The pattern becomes two-dimensional for Ha $\to \infty$. This surprising effect disappears for higher mode numbers m and for smaller magnetic Prandtl numbers. The real part of the eigenfrequency ω, which for axisymmetric modes often vanishes, has here finite values, indicating that the unstable patterns oscillate or migrate in the azimuthal or the axial direction.

For the *second case* the combination of differential rotation and a magnetic field due to a uniform axial electric current is considered ($b_B = 0$ or $\mu_B = 2$). We shall find a completely different situation with respect to the axisymmetry of the solutions. Figure 6 shows that the axisymmetric mode is not influenced by the magnetic field, in agreement with the consequences of Eq. (41). However, already for Hartmann numbers of order 10 the $m = 1$ mode crosses the line for $m = 0$. For stronger fields the most easily excited azimuthal mode is that with $m = 1$. For $\mathrm{Ha}_0 = 35.3$ the line for the neutral stability of the mode $m = 1$ even crosses the abscissa defined by Re = 0. The uniform axial electric current (the 'z-pinch') becomes unstable even without any rotation. We shall stress below that the characteristic Hartmann number Ha_0 for Re = 0 never depends on the magnetic Prandtl number Pm. However, as the dashed line for $\mu_\Omega = 1$ shows, the TI is eventually stabilized by rigid rotation. The red lines in this plot depend on the magnetic Prandtl number but the Hartmann number Ha_0 for stationary cylinders does not (see Section 7). We shall meet the value $\mathrm{Ha}_0 = 35.3$ for the stationary z-pinch inside perfectly conducting cylinders several times in this paper. The corresponding value for insulating cylinders is $\mathrm{Ha}_0 = 28.1$.

One can also show that the growth rates of the $m = 0$ modes of the flow field for various magnetic field strengths are identical. For $m = 1$ they become positive for Re ≥ 75 for weak fields but for sufficiently strong fields they are already positive for Re = 0. At the vertical axis (Re = 0) the growth rates increase with increasing Ha so that for large fields the growth rate scales with the Alfvén frequency Ω_A in perfect agreement with Fig. 6.

For information about the instability pattern and the energies which are stored in the various modes and in the flow and field components, one needs a nonlinear code solving the MHD equations. To this end a spectral element code has been developed from the hydrodynamic code of Fournier et al. [36]. It works with an expansion of the solution in azimuthal Fourier modes. A set of meridional problems results, each of which is solved with a Legendre spectral element method as in [37]. Between 8 and 16 Fourier modes are used. The polynomial order is varied between 10 and 16, with two elements in the radial direction. The number of elements in the axial direction corresponds to the aspect ratio Γ, the height of the numerical domain in units of the gap width, thus the spatial resolution is the same as for the radial direction. With a semi-implicit approach consisting of second-order backward differentiation and third-order Adams-Bashforth for the nonlinear forcing terms time-stepping is done with second-order accuracy. Periodic conditions in the axial direction are applied to minimize finite size effects. With the aspect ratio $\Gamma = 8$ all excitable modes in the analyzed parameter region fit into the system. Perfectly conducting boundary conditions are imposed here.

As a first application of this code, Fig. 7 shows the patterns of the radial flow component u_R for uniform axial

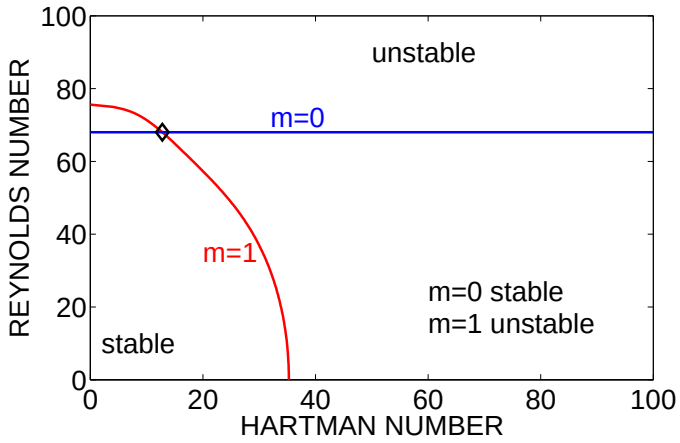

Figure 6. Azimuthal background fields: critical Reynolds numbers as function of the Hartmann number for the modes with $m = 0$ (blue) and $m = 1$ (red) for uniform axial electric current and resting outer cylinder. The diamond indicates the eigenvalues where the symmetry of the excited modes changes for $\mu_\Omega = 0$. $r_{\rm in} = 0.5$, $\mu_\Omega = 0$, $\mu_B = 2$. Pm = 1. Perfectly conducting cylinders. Adapted from [35].

electric current ($\mu_B = 2$), rapid rotation (Mm = 4.4) and stationary outer cylinder [38]. As expected, the instability is highly nonaxisymmetric. The axisymmetric mode also exists but does not dominate the structure which as a whole drifts in the positive azimuthal direction. Clearly, the pattern with differential rotation is of the mixed-mode type, but without rotation it is formed by a single nondrifting mode $m = 1$. There is no axisymmetry in the solution as Fig. 6 suggests, and the complete pattern is stationary.

For the flow with stationary outer cylinder and uniform axial electric current the kinetic and magnetic energy (normalized with the centrifugal energy $D^2\Omega_{\rm in}^2$) have also been computed. The question is how much centrifugal energy is stored in the nonaxisymmetric modes of flow and field and which sort of energy dominates. We write

$$\langle \boldsymbol{u}^2 \rangle = \hat{\rm q}_{\rm kin}\, \Omega_{\rm in}^2 D^2, \qquad \frac{\langle \boldsymbol{b}^2 \rangle}{\mu_0 \rho} = \hat{\rm q}_{\rm mag}\, \Omega_{\rm in}^2 D^2 \tag{47}$$

and find the numerical values $\hat{\rm q}_{\rm kin} \simeq 0.015$ and $\hat{\rm q}_{\rm mag} \simeq 0.012$ for very rapid rotation (Fig. 8, dashed lines). For Mm $\gg 1$ the coefficients $\hat{\rm q}_{\rm kin}$ and $\hat{\rm q}_{\rm mag}$ no longer depend on the Reynolds number. The faster the rotation of the inner cylinder, therefore, the more energy is stored in the nonaxisymmetric modes of the instability. Both energies can thus easily be expressed by the global energy $\Omega_{\rm in}^2 D^2$.

A very similar formulation can be used for the nonmagnetic Taylor-Couette flow. The pink curve in the left panel of Fig. 8 gives the kinetic energy in the nonaxisymmetric modes of the hydrodynamic Taylor-Couette flow. Clearly, it starts at Re = 75 and grows for faster rotation. Surprisingly, for very large Reynolds numbers the energy approaches (from below) the kinetic energy values of the MHD pattern for rapid rotation. Hence, for magnetized rapid rotators (with Pm = 1) the energies in the hydromagnetic modes are continuously reduced by increasing rotation until they both reach just the same value as the hydrodynamic Taylor-Couette flow produces. Figure 8 also demonstrates that for Pm = 1 the kinetic and magnetic energies are almost in equipartition. We shall later see that the magnetic energy in such simulations only exceeds the kinetic energy for large Pm.

3. Standard MagnetoRotational Instability (MRI)

So far we have discussed the stability of the Couette flows (23), which by themselves can be hydrodynamically unstable. If the fluid is electrically conducting and an axial magnetic field is applied then the critical Reynolds number increases with increasing magnetic field. Chandrasekhar explained the experimental data of Donnelly & Ozima for narrow gaps and with Pm = 0 by a magnetic suppression of the instability [2, 21].

The hydrodynamic Taylor-Couette flow is stable if its angular momentum increases with radius, but according to (15) the hydromagnetic Taylor-Couette flow is only stable if the angular velocity itself increases with radius.

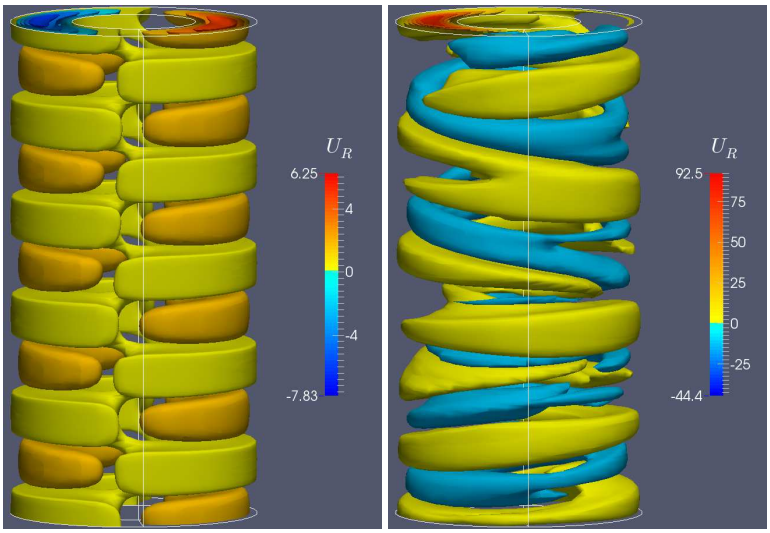

Figure 7. Isolines of the radial flow component measured as Reynolds numbers $u_R D/\nu$ for a Taylor-Couette flow with Re = 0 (left) for pure Tayler instability and with Re = 350 (right). The TI of the stationary flow produces a single nondrifting $m = 1$ mode. For Re = 350 also the axisymmetric mode is visible. $r_{\rm in} = 0.5$, Ha = 80, $\mu_\Omega = 0$, $\mu_B = 2$, Pm = 1. Perfect-conducting boundaries.

This remains true also for non-ideal fluids subject to axial magnetic fields. Weak magnetic fields reduce the critical Reynolds number for hydrodynamically unstable flows, and destabilize the otherwise hydrodynamically stable flow for $r_{\rm in}^2 < \mu_\Omega < 1$.

As we shall demonstrate, for small Pm and given Hartmann number the Reynolds numbers for neutral stability scale as 1/Pm for hydrodynamically stable flows, so that it is the magnetic Reynolds number Rm which controls the instability. Because of the high value of the molecular magnetic resistivity η for liquid metals (Table 1) it is not easy to reach magnetic Reynolds numbers of the required order of 10. This is the reason why the standard MRI has not yet been unambiguously observed experimentally in the laboratory [39, 40].

3.1. Potential flow

From all possible Couette flows only those with vanishing a_Ω form an irrotational vortex with curl $\boldsymbol{U} = 0$. For this flow the specific angular momentum $R^2\Omega$ is uniform in the radial direction. The rotation profile with $\mu_\Omega = r_{\rm in}^2$ (hence $\mu_\Omega = 0.25$ for $r_{\rm in} = 0.5$) is called the Rayleigh limit while the associated flow is called the 'potential flow'. It

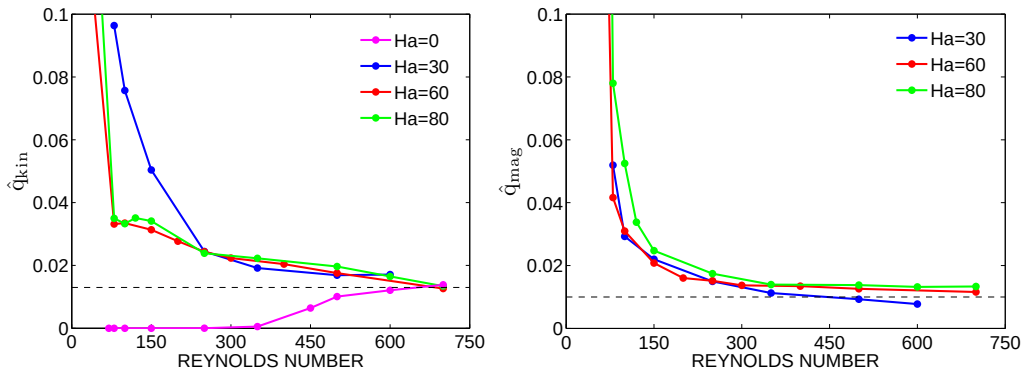

Figure 8. The kinetic (left) and magnetic (right) energy of the nonaxisymmetric modes normalized with the centrifugal energy $\Omega_{\rm in}^2 D^2$ for various Hartmann numbers. The pink line in the left plot gives the kinetic energy of the nonmagnetic flow. $r_{\rm in} = 0.5$, $\mu_\Omega = 0$, $\mu_B = 2$, Pm = 1. Perfectly conducting boundaries.

Table 1. Parameters of the liquid metals as conducting fluids, where $\bar{\eta} = \sqrt{\nu\eta}$. From [2, 41].

	ρ [g/cm^3]	ν [cm^2/s]	η [cm^2/s]	$\bar{\eta}$ [cm^2/s]	Pm
mercury	5.4	$1.1{\cdot}10^{-3}$	7600	2.9	$1.4{\cdot}10^{-7}$
gallium	6.0	$3.2{\cdot}10^{-3}$	2060	2.6	$1.5{\cdot}10^{-6}$
galinstan (GaInSn)	6.4	$3.4{\cdot}10^{-3}$	2428	2.9	$1.4{\cdot}10^{-6}$
sodium	0.92	$7.1{\cdot}10^{-3}$	810	2.4	$0.88{\cdot}10^{-5}$

plays an important role in the general theory of Taylor-Couette flows. In pure hydrodynamics, negative values of the radial gradient of $R^2\Omega$ are destabilizing and positive values are stabilizing. One might expect that instabilities subject to uniform $R^2\Omega$ should be easiest, i.e. the excitation needs minimal Reynolds numbers.

For the potential flow a particular scaling of the solutions to the MHD equations with axial background field, (27)–(32), exists with respect to the magnetic Prandtl number Pm. The quantities u_R, u_z, b_R and b_z scale as $\mathrm{Pm}^{-1/2}$ while u_ϕ, b_ϕ, k and Ha scale as Pm^0. Then for the axisymmetric modes the minimum Reynolds number scales as $\overline{\mathrm{Rm}}$=const, independent of the boundary conditions [42]. One has thus only to solve the equations for Pm = 1 and simultaneously knows the solutions for all other Pm. The minimum Reynolds number is 66 at a Hartmann number Ha $\simeq$ 7. Hence, the small minimum value of Re = 22, 248 for Pm = 10^{-5} (liquid sodium) is needed which seems to be promising for experiments (Fig. 9, left). Below we shall argue that significant problems with accuracy prevent its realization thus far.

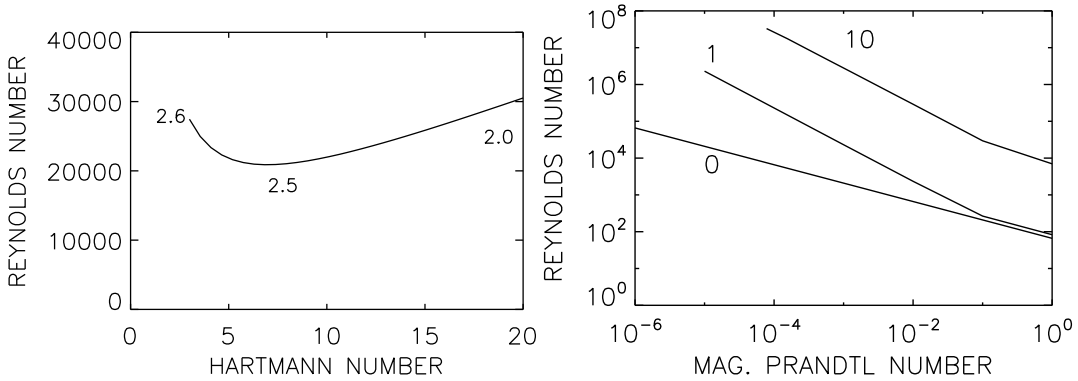

Figure 9. Potential flow: stability maps for standard MRI for $m = 0$ with Pm = 10^{-5} (left) and the minimum Reynolds numbers for $m = 0$, $m = 1$ and $m = 10$ as functions of Pm (right). The curve in the left panel carries the wave numbers normalized with the characteristic scale R_0. $r_{\rm in} = 0.5$, $\mu_\Omega = 0.25$. Perfectly conducting boundaries. Adapted from [43].

The wave numbers given in the left panel of Fig. 9 demonstrate the increase of the axial scales with increasing magnetic field in accordance with the magnetic counterpart of the Taylor-Proudman theorem. It is indeed known from early experiments ([44, 45]) and theoretical studies ([46, 47, 48, 49]) that the correlation lengths in MHD turbulences are the longer in field direction the stronger the applied background field is. On the other hand, if the wave number normalized with the gap width is smaller than π (for our standard container) then the axisymmetric vortices in the Taylor-Couette flow are axially aligned. The given numbers in the plot predict that the cells become longer and longer for growing Ha.

The right panel of Fig. 9 also demonstrates that the simple scaling with $\mathrm{Pm}^{1/2}$ of the potential flow only exists for the axisymmetric mode. For the modes with $m = 0$, $m = 1$ and $m = 10$ the dependencies of the characteristic Reynolds numbers on the magnetic Prandtl number are plotted. One finds that for Pm $\to$ 0 the nonaxisymmetric modes follow a much steeper scaling with Pm than the axisymmetric mode. For Pm of order unity, however, the various Reynolds numbers for excitation of $m = 0$ and $m = 1$ do not differ much, as is also true down to Pm $\simeq$ 0.1.

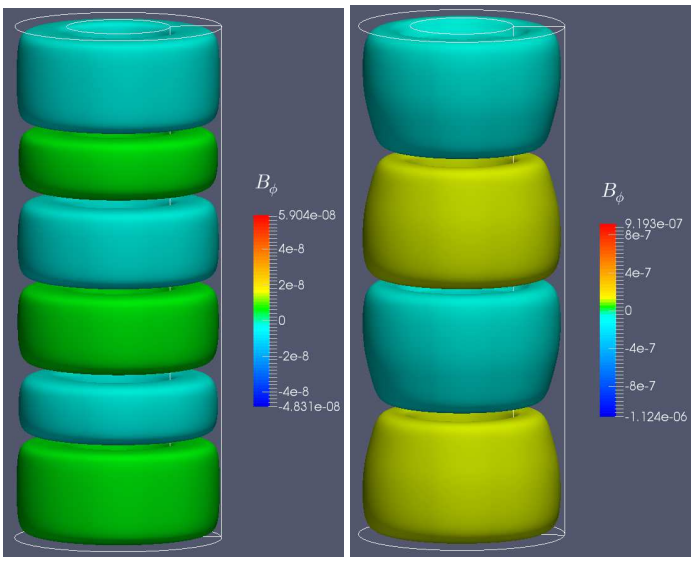

Figure 10. Standard MRI of the potential flow subject to axial background field. Isolines of the azimuthal field component (normalized with B_0) are shown for Ha = 7 (left) and Ha = 50 (right). Only the axisymmetric mode is excited despite of the high Reynolds number. $\Gamma = 10$, $r_{\rm in} = 0.5$, Re = 50,000, $\mu_\Omega = 0.25$, Pm = 10^{-5}. Insulating boundaries, see Section 3.3.

This is not true for Pm $\ll 1$. Figure 10 demonstrates for two different Hartmann numbers that for the supercritical Reynolds number Re = 50,000 only the axisymmetric mode is excited. All modes with $m > 0$ decay. The instability pattern even remains axisymmetric for similar examples with Re = 10^5 (not shown). But the models numerically prove the existence of standard MRI also for very small magnetic Prandtl numbers such as Pm = 10^{-5} for not too high Reynolds numbers. Note, however, that the resulting normalized magnetic perturbations are only weak compared with the background field. The two given models with different Hartmann numbers may also serve to probe the prediction that the axial wavelength increases with increasing magnetic field. This is indeed the case.

Only slightly beyond the Rayleigh limit (e.g. for $\mu_\Omega = 0.255$) and the other parameters unchanged the numerical simulations do no longer provide MRI. This is a direct consequence of different scalings of the MRI solutions for small Pm for different rotation laws (see Section 3.2).

3.2. *Quasi-Keplerian flow*

A quasi-Keplerian Couette flow may be defined by requiring that the cylinders rotate like planets following the Kepler law $\Omega \propto R^{-3/2}$. This becomes $\mu_\Omega = r_{\rm in}^{1.5} = 0.35$ for $r_{\rm in} = 0.5$.

Figure 11 shows the eigenvalues of the axisymmetric modes for this flow[2] for the two magnetic Prandtl numbers Pm = 1 (left) and Pm = 10^{-5} (right). Compared with Fig. 2 the eigenvalues for Ha = 0 along the vertical axis disappear to infinity, but the minima for both flows remain almost unchanged. For both magnetic Prandtl numbers the characteristic minima are at very different locations in the (Ha/Re) plane. Minimum Reynolds and Hartmann numbers increase for decreasing magnetic Prandtl number (Fig. 12). The characteristic Reynolds numbers scale as Re $\propto 1/\mathrm{Pm}$ – much steeper than the $1/\sqrt{\mathrm{Pm}}$ scaling for the potential flow. For the Hartmann number, Fig. 12 yields Ha $\propto 1/\sqrt{\mathrm{Pm}}$ – also steeper than Ha $\simeq$ const for the potential flow. For the quasi-Keplerian flow one finds the simple relations Rm $\simeq$ const and S $\simeq$ const for Pm $\to 0$. For small magnetic Prandtl numbers the minima thus have very similar coordinates in the (S/Rm) plane. We conclude that for Pm $\to 0$ the characteristic minima for MRI scale with the magnetic Reynolds number Rm and the Lundquist number S. Note that the microscopic viscosity does not play any role in that formulation. This is in contrast to the inductionless approximation for Pm = 0 where the remaining eigenvalues are Ha and Re including the microscopic viscosity (see Section 5.1). The solutions of the MHD equations for Pm = 0, therefore, also scale with the Hartmann number and the Tayler number. As the MRI for finite magnetic

[2]For historical reasons given for $\mu_\Omega = 0.33$ instead of $\mu_\Omega = 0.35$ (quasi-Keplerian rotation).

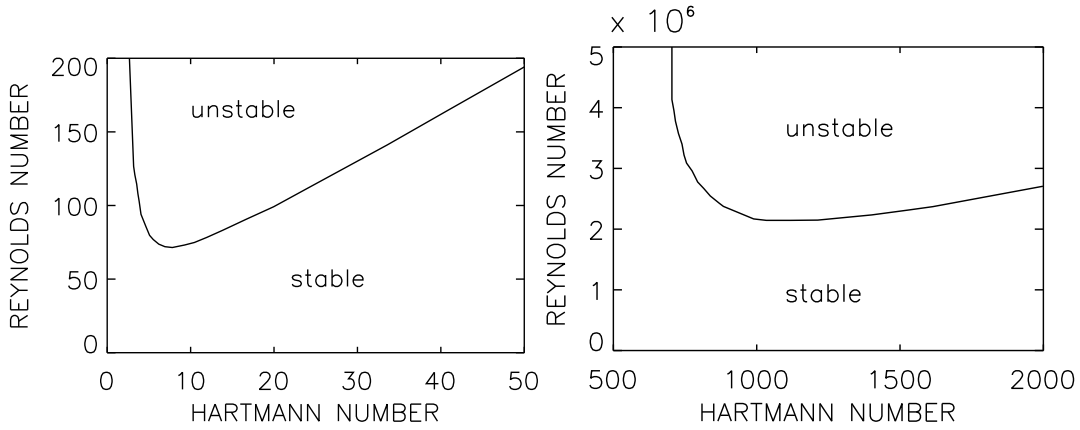

Figure 11. Stability maps of MRI for quasi-Keplerian MHD Taylor-Couette flows for Pm = 1 (left) and Pm = 10^{-5} (right). The combinations of Reynolds and Hartmann numbers below the curves are always stable. There are strong differences for small and large magnetic Prandtl numbers. $r_{\rm in} = 0.5$, perfectly conducting boundaries. From [32].

Prandtl numbers scales with S and Rm for small Pm the limit for Pm $\to$ 0 yields Ha $\to \infty$ and Re $\to \infty$ which, of course, can never form a solution of the equations of the inductionless approximation. These equations, therefore, cannot contain a solution for the magnetorotational instability with uniform axial fields (see [2]). The solutions exist for arbitrarily small Pm but not for Pm = 0.

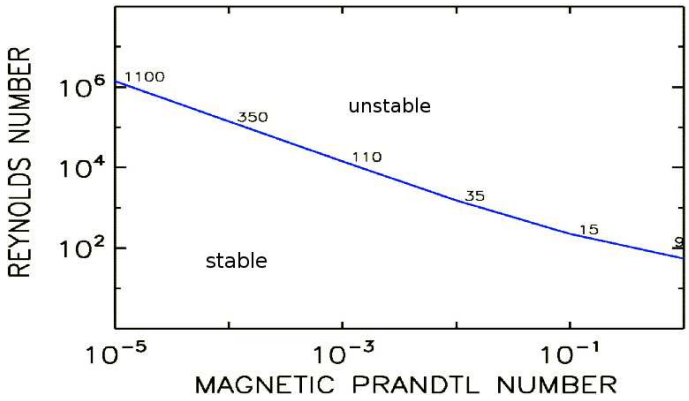

Figure 12. Minimum Reynolds numbers as function of the magnetic Prandtl number marked with the corresponding Hartmann numbers. The numbers lead to a common scaling with S and Rm for small magnetic Prandtl numbers. For Pm $\to$ 0 one finds Rm = 21 and S = 3.5. $r_{\rm in} = 0.5$, $\mu_\Omega = 0.33$. Perfectly conducting boundaries. Adapted from [30].

It follows that for small Pm the transition from the potential flow to the non-potential flow might be a dramatic one. For small Pm a vertical jump along the Rayleigh line from $1/\sqrt{\rm Pm}$ to 1/Pm, i.e. by a factor of 1/Pm must exist within a very small interval $\delta\mu_\Omega$. For Pm = 10^{-5} the vertical jump is by more than two orders of magnitudes. For Pm = 1, on the other hand, the transition from the potential flow to flatter radial flow profiles is much smoother.

Table 2 gives the numerical values for the excitation of the MRI in quasi-Keplerian flows, for perfectly conducting and insulating boundaries. The critical Reynolds numbers are lower for insulating cylinders, whereas the critical Hartmann numbers are lower for conducting cylinders. The magnetic Mach numbers of the two examples, therefore, differ by a factor of two. One also finds that for all Pm $\le$ 1 the strong-field branches of the lines of neutral stability can be described with Mm $\simeq$ 4. The standard magnetorotational instability, therefore, only works for large Lundquist numbers (S > 1) *and* large magnetic Mach numbers. However, we shall see below that for the nonaxisymmetric modes maximal Mm exist above which the fluid again becomes stable to these modes.

The MRI is so elementary that its main rules already follow from a simple analysis with a local short-wave

Table 2. Coordinates of the absolute minima in the (S/Rm) plane for rotating outer cylinder with $\mu_\Omega = 0.33$ and Pm = 10^{-5} .

	perfectly conducting walls	insulating walls
Reynolds number	$2.13 \cdot 10^6$	$1.42 \cdot 10^6$
mag. Reynolds number	21	14
Hartmann number	1100	1400
Lundquist number	3.47	4.42
magnetic Mach number	6.05	3.16

approximation of the MHD equations (27)–(32). For disturbances with $kR \gg 1$, the differential rotation can be approximated by a plane shear flow [50]. For the simplest case of plane-wave disturbances with only an axial wave number one finds the algebraic relation

$$\left(\omega + \eta k^2\right)^2 \left(\left(\omega + \nu k^2\right)^2 + 2\,(2-q)\,\Omega^2\right) + \Omega_{\rm A}^2 \left(\Omega_{\rm A}^2 - 2q\Omega^2 + 2\left(\omega + \nu k^2\right)\left(\omega + \eta k^2\right)\right) = 0 \tag{48}$$

for the growth rate ω, where $\Omega_{\rm A} = kV_{\rm A}$ (with the Alfvén velocity $V_{\rm A} = B_0/\sqrt{\mu_0\rho}$) is the Alfvén frequency and $q = -{\rm d}\log\Omega/{\rm d}\log R$ is the local shear. The neutral line between stability and instability defined by $\omega = 0$ yields

$$\tilde{\rm Rm} = \frac{{\rm Pm} + \tilde{\rm S}^2}{\sqrt{2\left(q\tilde{\rm S}^2 - 2 + q\right)}}. \tag{49}$$

Here, the dimensionless quantities $\tilde{\rm S}$ and $\tilde{\rm Rm}$ are redefined in terms of the wave number ($R_0 \to k^{-1}$). Equation (49) shows that the instability requires sufficiently large $\tilde{\rm Rm}$ exceeding

$$\tilde{\rm Rm}_{\rm min} = \sqrt{\frac{2}{q}\left({\rm Pm} + \frac{2-q}{q}\right)}. \tag{50}$$

The associated Lundquist number is $\tilde{\rm S}_{\rm min} = \sqrt{{\rm Pm} + 2(2-q)/q}$. For $\tilde{\rm Rm} > \tilde{\rm Rm}_{\rm min}$ the instability only exists for $\tilde{\rm S}$ between a lower and an upper limit, i.e. $\tilde{\rm S} \geq \sqrt{(2-q)/q}$ and ${\rm Mm} \geq 1/\sqrt{2q}$. For small Pm the expression (49) loses its dependence on Pm so that the viscosity disappears from the theory. The instability in this limit is controlled by $\tilde{\rm Rm}$ and $\tilde{\rm S}$, which are only formed with the magnetic resistivity η. For quasi-Keplerian flows ($q = 3/2$) one finds $\tilde{\rm S} \geq 1/\sqrt{3}$ and for the slope of the strong-field branch ${\rm Mm} \simeq 1/\sqrt{3}$. On the other hand, for large Pm the minima of the curves fulfill the conditions $\overline{\rm Rm} = 2/\sqrt{3}$ and Ha = 1.

Figures 13 indeed show that for small Pm the stability lines in the (S/Rm) plane do not depend on Pm, true both for conducting (left panel) and for insulating (right panel) boundary conditions. The right branch of the neutral stability lines at sufficiently high Rm can be characterized by ${\rm Mm} = 1/\sqrt{3}$. The left branch is controlled by the diffusivities. Its expression for large Rm can be obtained by setting the denominator in (49) to zero, hence ${\rm S} = 1/\sqrt{3}$ [51].

In Fig. 14 the lines of neutral stability are compared for Pm = 1 (dark lines) with those for Pm = 10 (red lines) in the (Ha/$\overline{\rm Rm}$) plane. The scaling for both axisymmetric and nonaxisymmetric solutions for large Pm is obvious. The numerical results for the global quasi-Keplerian flow with $r_{\rm in} = 0.5$ confirm these findings for the axisymmetric and nonaxisymmetric modes.

Figures 13 and 14 also demonstrate that nonaxisymmetric modes require stronger fields for their excitation than axisymmetric modes. There is, however, an even more interesting difference between the axisymmetric and nonaxisymmetric modes. For $m = 0$ and ${\rm S} \geq 1$ there is always a single critical Reynolds number, above which the MRI is excited for all larger Rm. The nonaxisymmetric modes behave differently. For ${\rm S} > S_{\rm min} \simeq 1$ ($\rm S_{min}$ the smallest possible Lundquist number) there are always two critical Reynolds numbers between which the nonaxisymmetric modes can exist. The nonaxisymmetric modes are thus stabilized by too slow and by too fast rotation. If it is too

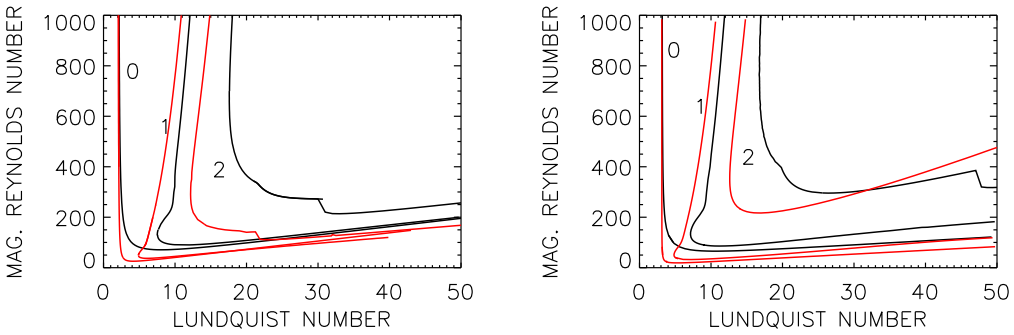

Figure 13. Stability lines for MRI with quasi-Keplerian flows, for the azimuthal modes $m = 0$, $m = 1$ and $m = 2$ (marked by m). Black lines: Pm = 1, Red lines: Pm = 0.01. Perfectly conducting boundaries (left), insulating boundaries (right). For small Pm the curves scale with Rm=const. The weak-field show opposite slopes for axisymmetric and nonaxisymmetric modes. The latter decay for too high Reynolds numbers. $r_{\rm in} = 0.5$, $\mu_B = 0.5$, $\mu_\Omega = 0.35$.

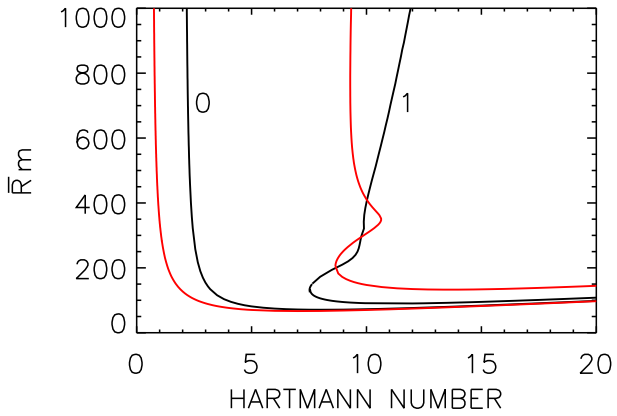

Figure 14. As in Fig. 13 with Pm = 1 (dark) and Pm = 10 (red). The minima scale with the averaged Reynolds number $\overline{\rm Rm}$ and the Hartmann number Ha for large Pm. Again the slopes of the weak-field branches differ for $m = 0$ and $m = 1$. Figures 13 and 14 demonstrate the strikingly different scalings of the eigenvalues for small and large Pm. $r_{\rm in} = 0.5$, $\mu_\Omega = 0.35$. Perfectly conducting boundaries.

strong, the differential rotation suppresses the nonaxisymmetric parts of the instability pattern. As an estimation one finds that Mm $\simeq$ 300 is the highest possible magnetic Mach number for the excitation of nonaxisymmetric modes. The dependence of this value on the magnetic Prandtl number is weak. For $m = 0$ such an upper limit does not exist.

For small magnetic Prandtl numbers (here Pm = 0.01) we again find a crossing phenomenon for strong fields in the neutral-stability curves for $m = 0$ and $m = 1$ [52]. In Fig. 13 (left) the lines for $m = 0$ and $m = 1$ cross for S $\simeq$ 20. For weaker fields the mode with the lowest Reynolds number is always axisymmetric, but for stronger fields the Reynolds numbers for $m = 1$ are smaller than those for $m = 0$. In these cases the MRI sets in as a nonaxisymmetric flow pattern. The nonaxisymmetric structure is lost, however, for too fast rotation when the magnetic Reynolds number reaches the upper value of the marginal stability of the $m = 1$ curve. We have found this sort of mode-crossing only for MHD flows with perfectly conducting boundary conditions.

One can show that a solution with a certain positive k is always accompanied by a solution with $-k$ with the same Reynolds number and drift frequency (for given Ha and m). As the pitch angle of the resulting spirals is given by $\partial z/\partial\phi = -m/k$, it is clear that the two solutions have opposite pitch angles, so that the solution is always a combination of a left screw and a right screw. In the ideal case the same number of left and right spirals will be

excited as there is no reason for a preference. Both the kinetic and magnetic helicities thus vanish on average. As a consequence, MRI does not produce any α effect (see Section 11).

The governing equation system is also invariant under the simultaneous transformations $m \to -m$, $k \to -k$ and $\Re(\omega) \to -\Re(\omega)$, with $\Re(\omega)$ as the real part of the mode frequency ω. Hence, the drift of both solutions and also the pitch angles, i.e.

$$\frac{\partial \phi}{\partial t} = -\frac{\Re(\omega)}{m} \qquad\qquad \frac{\partial z}{\partial \phi} = -\frac{m}{k}, \tag{51}$$

are equal so that the solutions are identical. It is thus enough to assume $k > 0$.

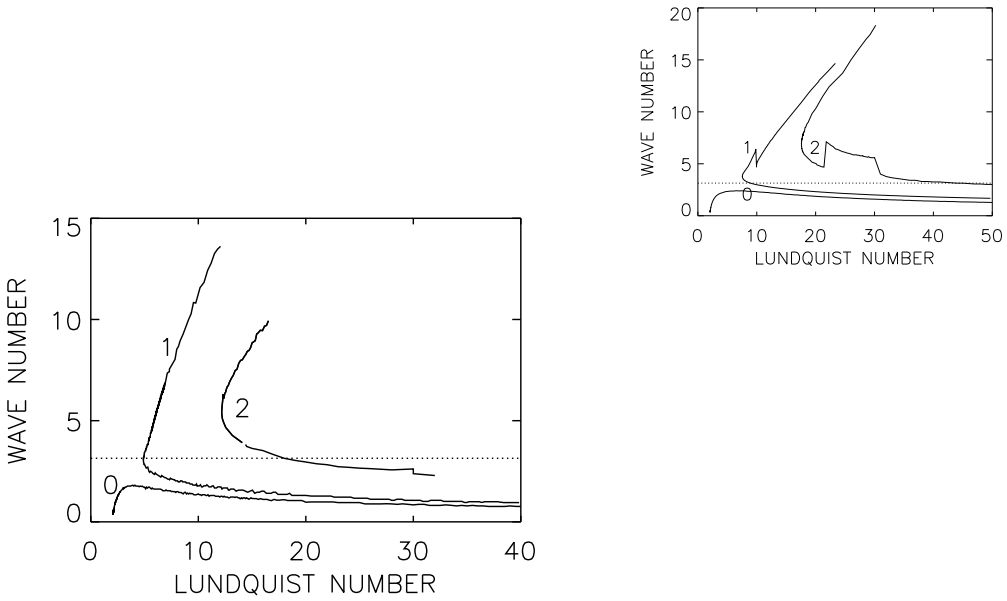

Figure 15. Wave numbers along the lines of marginal stability for the azimuthal modes $m = 0$, $m = 1$ and $m = 2$ (marked by m) for MRI with quasi-Keplerian flow. Left: Pm = 0.01, right: Pm = 1. Dotted lines mark the limit $k = \pi$ for circular cells in the (R/z) plane. The axisymmetric modes and the strong-field solutions of the nonaxisymmetric modes are always prolongated in axial direction. $r_{\rm in} = 0.5$, $\mu_\Omega = 0.35$.

The vertical extent δz of the cells of the instability pattern, normalized by the gap width $D = R_{\rm out} - R_{\rm in}$ between the cylinders, is

$$\frac{\delta z}{D} = \frac{\pi}{k}\sqrt{\frac{r_{\rm in}}{1 - r_{\rm in}}}. \tag{52}$$

For $r_{\rm in} = 0.5$ it is simply $\delta z/D = \pi/k$ so that for $k \simeq \pi$ the cells are almost circular in the (R/z) plane, and for $k \gg \pi$ the cells are very flat. Figure 15 shows that for both values of Pm the azimuthal rolls of the axisymmetric modes become more and more elongated in the vertical direction. Generally, only the cells of the weak-field branches of the nonaxisymmetric modes are very flat while the other modes possess circular or prolate cells.

The real part $\Re(\omega)$ of the frequency ω of the Fourier mode in units of the rotation rate of the inner cylinder

$$\omega_{\rm dr} = \frac{\Re(\omega)}{\Omega_{\rm in}}, \tag{53}$$

which for $m \neq 0$ describes an azimuthal drift

$$\frac{\dot\phi}{\Omega_{\rm in}} = -\frac{\omega_{\rm dr}}{m} \tag{54}$$

of the instability pattern, in units of the inner cylinder's rotation rate. For negative $\omega_{\rm dr}$ the pattern migrates in the direction of the global rotation (eastward). Because of these definitions a drift value of $-\mu_\Omega$ describes an exact corotation of the flow pattern with the *outer* cylinder as we are working in the fixed laboratory system.

3.3. Nonlinear simulations

Nonlinear numerical simulations reveal the axisymmetric character of the standard MRI for large magnetic Mach numbers. The nonlinear three-dimensional time-stepping problem is solved using the MPI-parallelized code [53], which itself is based on an earlier pipe flow solver by A.P. Willis[3]. The spatial structures in z and ϕ are described by the standard Fourier mode approximation, allowing energy spectra in these two directions to be easily constructed. The periodic domain length in the axial direction is chosen as 10 times the gap width, to allow sufficiently large structures in z. The resolution varies from $127 \times 64 \times 32$ and $511 \times 256 \times 128$, depending on the Reynolds number. In its present form the code only works without endplates in axial direction and only for insulating radial boundaries.

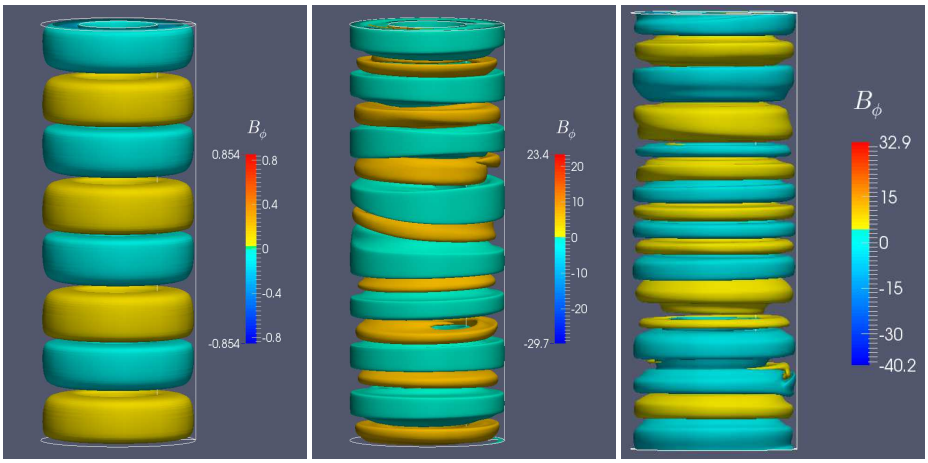

Figure 16. Instability patterns of MRI for quasi-Keplerian rotation, isolines of b_ϕ/B_0 for weak background field and increasing magnetic Mach numbers (Mm = 6.8, 96.2, 307.7, from left to right). The magnetic Reynolds numbers are 88, 1250 and 4000 (from left to right). The numbers on the colored scales at the right of each plot yield the amplitude of the local quantity $\sqrt{\rm q}$ (only one component, not averaged). $r_{\rm in} = 0.5$, $\mu_\Omega = 0.35$, S = 13, Pm = 1. Insulating boundaries hence $b_\phi = 0$ at the cylinders.

The equations for the quasi-Keplerian flow have been solved in axially unbounded containers with insulating boundary conditions. The right panel of Fig. 13 shows the neutral stability curves. For a weak field Fig. 16 shows the isolines of the azimuthal components of the magnetic field for models with increasing Reynolds numbers. At Rm = 88 the lowest Reynolds number lies below the instability curve of the nonaxisymmetric $m = 1$ mode, so that the exact ringlike geometry of the left plot in Fig. 16 is not a surprise. The cells are nearly circular in the (R/z) plane. For faster rotation (Rm = 1250, middle) nonaxisymmetric structures occur but remain weak. Nevertheless, the cell structure changes as the cells become more oblate, which cannot be understood by means of the Taylor-Proudman theorem. This trend is continued for even faster rotation (Rm = 4000) where again the axisymmetry of the solution prevails.

For stronger fields the nonaxisymmetric modes are obviously excited, but only for not too low and not too high Reynolds numbers. The right panel of Fig. 17 shows that very large Reynolds numbers indeed prevent the excitation of nonaxisymmetric modes. The instability map suggests that for S = 30 the Reynolds number 4000 lies outside the instability domain for $m = 1$ (see Fig. 13, right). For S = 100 only the model with Rm = 1000 (i.e. magnetic Mach number of order 10) shows a nonaxisymmetric pattern with low m while the models with faster rotation become more and more axisymmetric with increasing axial wave numbers (Fig. 18).

We also note that for all models with fixed Lundquist number the amplitude of the b_ϕ-component grows for growing Rm, i.e. for stronger shear. The magnetic energy averaged over the whole container should be increasingly

[3] See www.openpipeflow.org

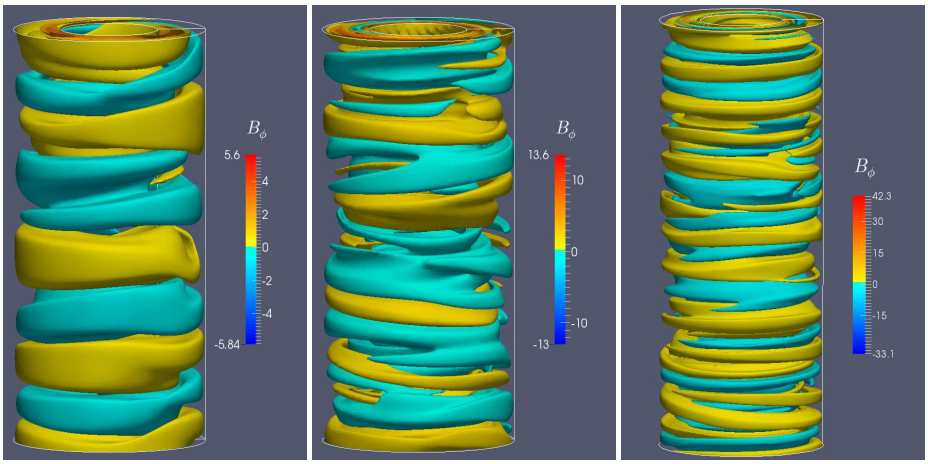

Figure 17. As in Fig. 16 but for S = 30. Magnetic Reynolds numbers are Rm = 500, 1500, 4000 and magnetic Mach numbers are Mm = 16.7, 50, 133.3 (from left to right).

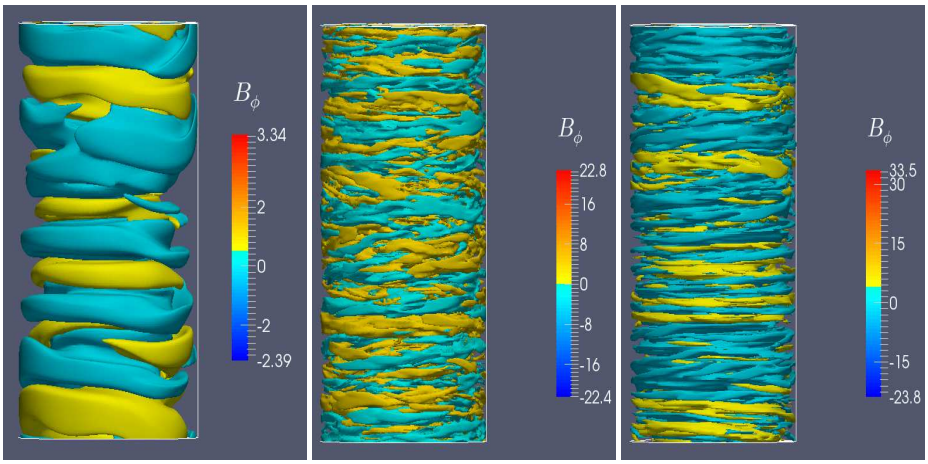

Figure 18. As in Fig. 16 but for S = 100. Magnetic Reynolds numbers are Rm = 1000, 10000, 20000 and magnetic Mach numbers are Mm = 10, 100, 200 (from left to right).

relevant. For several models with different magnetic Prandtl number Pm the normalized magnetic energy

$$\mathrm{q} = \frac{\langle \boldsymbol{b}^2 \rangle}{B_0^2} \tag{55}$$

is given in Fig. 19 in its dependencies on the magnetic Reynolds number and the Hartmann number. The blue (red) curves are for weak (medium) background fields; they only differ by Pm (the circles and triangles are for Pm = 1). One finds $\mathrm{q} \propto \mathrm{Rm}$, the Pm-dependence as rather weak, and an anticorrelation between q and Ha. There is, however, another clear relation to report. For the magnetic Elsasser number

$$\Lambda = \frac{\langle \boldsymbol{b}^2 \rangle}{\mu_0 \rho \eta \Omega} \tag{56}$$

one finds from the right panel of Fig. 19 the linear relation $\Lambda \simeq 0.007\,\mathrm{Rm}$ for large Rm and independent of Pm leading to the simple result $\langle \boldsymbol{b}^2 \rangle \simeq 0.007 \cdot \mu_0 \rho R_0^2 \Omega_{\rm in}^2$ which is identical to

$$\mathrm{q} \simeq 0.007\ \mathrm{Mm}^2. \tag{57}$$

Note that for Kepler disks Mm^2 equals the plasma-β as the ratio of kinetic pressure and magnetic pressure as in such disks the averaged pressure equals $\rho D^2\Omega^2$. The plasma-β value of 400 used in Ref. [54] corresponds to Mm = 20 close to the minimum values used in the simulations which lead to Figs. 16–21. According to Eq. (57) the resulting q will be expected as of order unity.

The normalized magnetic energy of the perturbations does not depend on the microscopic diffusivities. Not even 1% of the rotation energy of the Taylor-Couette flow exists in the form of stochastic perturbations of the magnetic field. Nevertheless, as the MRI occurs for large magnetic Mach numbers, Eq. (57) leads to the conclusion that the energy of the magnetic perturbations may easily exceed the energy of their magnetic background fields. It is unlikely that this finding is changed for much smaller or larger magnetic Prandtl numbers as the dependence of MRI on Pm is basically weak. If a magnetically induced viscosity is defined in a heuristic manner by $\nu_\mathrm{T} \simeq \langle \boldsymbol{b}^2\rangle/\mu_0\rho\Omega$ one finds $\nu_\mathrm{T} \simeq 0.007 R_\mathrm{in}^2\,\Omega_\mathrm{in}$, which might be relevant for the angular momentum transport in the unbounded differentially rotating container. One can also understand such expressions as a realization of the β viscosity concept [55, 56, 57].

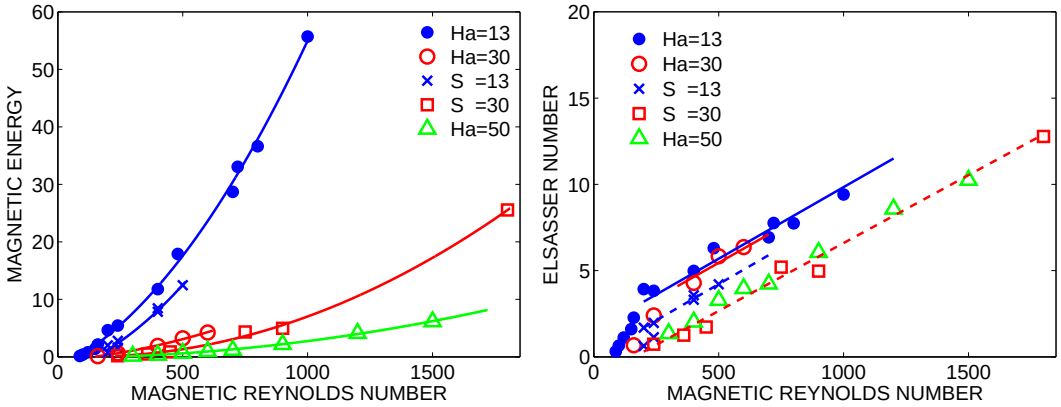

Figure 19. Left: Magnetic energy (55) of MRI averaged over the whole container as functions of the magnetic Reynolds number and for various magnetic field amplitudes. q and S are clearly anticorrelated. Right: The magnetic Elsasser number (56). The circles and the green triangles correspond to Pm = 1 while the other symbols belong to Pm = 0.1 or Pm = 0.2. The dependencies on S and Pm are rather weak. $r_\mathrm{in} = 0.5$, $\mu_\Omega = 0.35$.

Closing this section the calculations presented in Fig. 16 may be repeated with a basically smaller magnetic Prandtl number. The identical models represented in the (S/Rm) system are numerically repeated for Pm = 0.01 rather than Pm = 1 (Fig. 20). The magnetic Mach numbers are thus reduced by a factor of 100; they are now of order unity. The differences between the results in Figs. 16 and 20 are surprisingly small which demonstrates the basic role of the magnetic Reynolds number (for fixed Lundquist number) for geometry and energy of the MRI perturbations with axial fields. In this sense the role of the magnetic Prandtl number for excitation *and* formation of the MRI is only small.

MRI realizations for large magnetic Prandtl number (Pm = 100) are given by Fig. 21. The values of the averaged Reynolds number $\overline{\mathrm{Rm}}$ and Hartmann number Ha correspond to those used in Fig. 16. Figure 16 for Pm = 1 and Fig. 21 for Pm = 100 with Mm = 7, 100, 300 provide the same series of magnetic Mach numbers. In all cases the maximum values of b_ϕ/B_0 linearly grow with growing magnetic Mach numbers so that the relation (57) is indeed approached.

For the models with magnetic Prandtl numbers in the interval between 0.01 and 100 (Figs. 16, 20, 21) have been used to calculate the ratio ε of magnetic to kinetic energy averaged over the container

$$\varepsilon = \frac{\mathrm{Ha}^2}{\mathrm{Pm}}\,\frac{\langle \boldsymbol{b}^2\rangle}{\langle \boldsymbol{u}^2\rangle} \tag{58}$$

for various magnetic Reynolds numbers. The results show a slight dependence of the energy ratio on the magnetic Prandtl number $\varepsilon \propto \mathrm{Pm}^\kappa$ with $\kappa \sim 0.4$ (Fig. 22, left). The larger Pm the larger the magnetic energy related to the kinetic energy. For small Pm the fluid becomes less and less magnetized. On the other hand, the magnetic energy

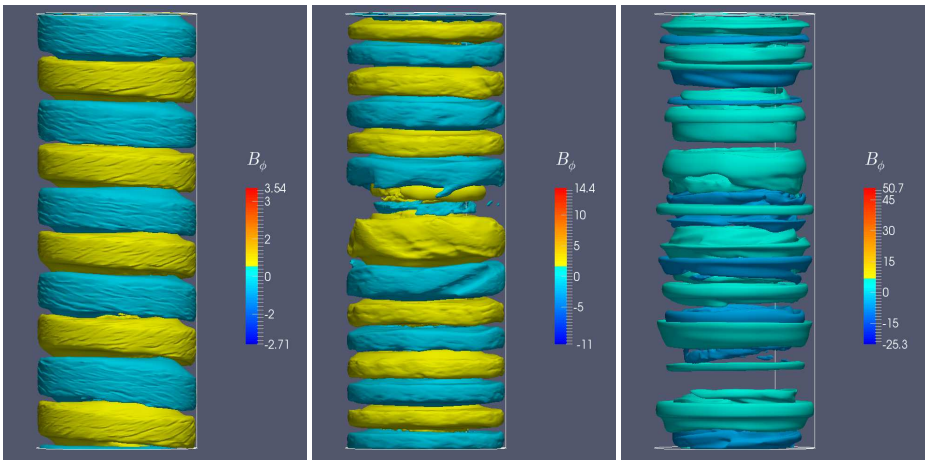

Figure 20. As in Fig. 16 but for Pm = 0.01 and S = 13. Magnetic Reynolds numbers are Rm = 400, 1250, 4000 and magnetic Mach numbers are Mm = 30.8, 96.2, 307.7 (from left to right).

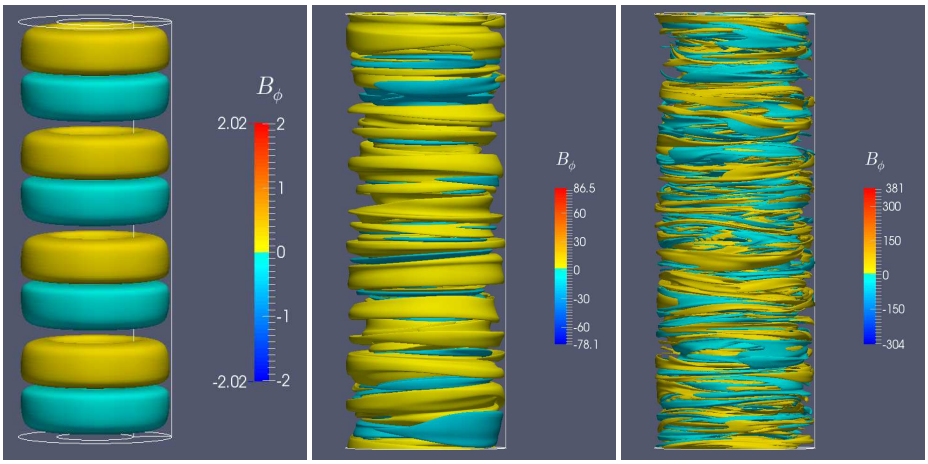

Figure 21. As in Fig. 16 but for Pm = 100. Ha = 13. It is $\overline{\mathrm{Rm}}$ = 88, 1250, 4000 for the averaged Reynolds number and the magnetic Mach numbers are Mm = 6.8, 96.2, 307.7 (from left to right).

dominates the kinetic energy only for large values of Pm. Written with a more appropriate normalization one finds for the kinetic energy $\langle \boldsymbol{u}^2\rangle/\Omega_{\rm in}^2 R_0^2 = \mathrm{q}/(\varepsilon \mathrm{Mm}^2)$ hence with (57)

$$\frac{\langle \boldsymbol{u}^2\rangle}{\Omega_{\rm in}^2 R_0^2} = \frac{0.007}{\varepsilon} \simeq 0.007\ \mathrm{Pm}^{-\kappa}. \tag{59}$$

with $\kappa \lesssim 0.4$. Again, for $\varepsilon \simeq 1$ the kinetic energy is also only about 1% of the rotational energy of the system but it is much higher for small Pm. The influence of the magnetic Prandtl number on this result is not very strong. It is weaker than the expected coefficient of order unity and it is slightly larger than the $\kappa \simeq 0.2$ which has been derived from numerical shearing-box simulations (Fig. 22, right). For the very small magnetic Prandtl numbers of liquid metals, however, one expects much smaller ε-values hence the MHD turbulence is only weakly magnetized. Nevertheless, the small exponents κ suggest the MRI as rather robust against variations of the magnetic Prandtl number.

3.4. Angular momentum transport

For Keplerian disks the rotation velocities are supersonic, with $R_{\rm in}\Omega_{\rm in} \gg c_{\rm ac}$, so that the magnetically induced viscosity should adopt high values. The angular momentum transport by MRI should thus be considered in detail.

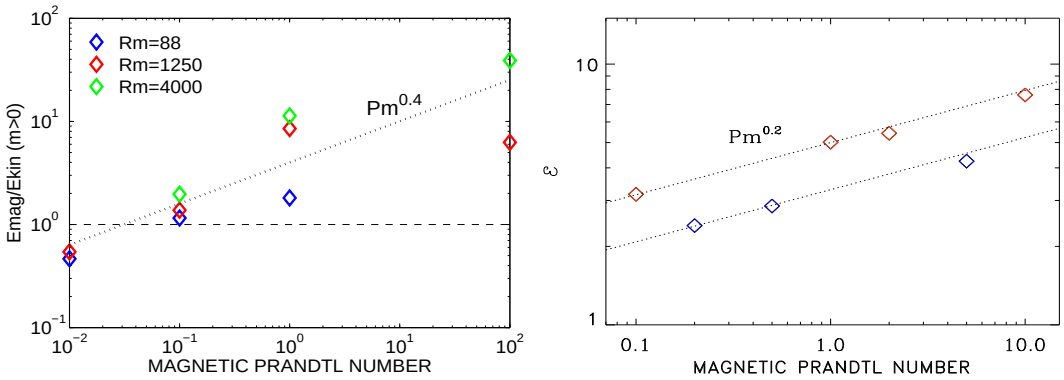

Figure 22. The ratio ε of the magnetic and the kinetic energy for the modes with $m > 0$ of MRI with Keplerian rotation law. Left: models with magnetic Prandtl numbers in the interval between 0.01 and 100 (taken from Figs. 16, 20, 21). $r_{\rm in} = 0.5$, $\mu_\Omega = 0.35$, S = 13. Right: results from a shearing-box simulation in Ref. [58]. The colors represent two different vertical wave numbers. The magnetic resistivity is fixed while the viscosity varies.

The radial angular momentum transport by MHD turbulence can be expressed by the component

$$T_{R\phi} = \langle u_R u_\phi - \frac{1}{\mu_0 \rho} b_R b_\phi \rangle \tag{60}$$

of the Reynolds and Maxwell stresses. The averaging procedure may be an integration over time and the whole container. Within the Boussinesq approximation one always has $T_{R\phi} \cdot {\rm d}\Omega/{\rm d}R < 0$, as the angular momentum transport is opposite to the gradient of Ω [59]. One can thus introduce an eddy viscosity $\nu_{\rm T}$ via

$$T_{R\phi} = -\nu_{\rm T} R \frac{{\rm d}\Omega}{{\rm d}R} \tag{61}$$

with positive $\nu_{\rm T}$. The sign of these correlations can even be computed with the linear theory. Here we shall use nonlinear simulations to also compute the amplitude of the eddy viscosity.

One may introduce dimensionless coefficients α via $T_{R\phi} = \alpha \Omega^2 R_0^2$ [60]. Hence, the MRI α can be computed with the definition $\alpha_{\rm mri} = T_{R\phi}/\Omega^2 R_0^2$. Note that this definition differs from the one used in astrophysics unless $R_0 \simeq H$, which is only fulfilled for thick accretion disks. From (60) it follows that

$$\frac{\nu_{\rm T}}{\nu} = \frac{\alpha_{\rm mri}}{q}\,{\rm Re}, \tag{62}$$

where the rotation profile $\Omega \propto R^{-q}$ has been used ($q = 1.5$ for Keplerian rotation).

As a first step we compute $\alpha_{\rm mri}$ with $\mu_\Omega = 0.35$ by averaging only over the azimuth. One finds that the angular momentum transport is positive everywhere, with a rather weak indication of a cell structure. The angular momentum transport shown in Fig. 23 is again only due to the nonaxisymmetric modes with $m > 0$. Only these modes have here been defined as the fluctuations in the definitions of $\boldsymbol{u}$ and $\boldsymbol{b}$. Let the averaging procedure concern the entire container. The results for $\alpha_{\rm mri}$ can then be represented by the linear relation

$$\alpha_{\rm mri} = 5 \cdot 10^{-5}\,{\rm S} \tag{63}$$

(Fig. 23). The numerical value of $\alpha_{\rm mri}$ depends linearly on the amplitude of the magnetic field, the size of the disk or torus and the electric conductivity. This relation proves to hold for all Reynolds numbers and magnetic Prandtl numbers. Note that $\alpha_{\rm mri}$ does not vary with the rotation rate and/or the microscopic viscosity. There is thus no dependence of the $\alpha_{\rm mri}$ on the magnetic Prandtl number. It does not, in particular, decrease for decreasing magnetic Prandtl number as suggested by a few shearing-box simulations [61, 62]. For the models used in Fig. 22 which all belong to one and the same Lundquist number S = 13, Eq. (63) leads to $\alpha_{\rm mri} = 0.65 \cdot 10^{-3}$, in accordance with results of the box simulations in Ref. [58] – also with respect to the nonexistence of a Pm dependence of $\alpha_{\rm mri}$.

For two examples for Pm = 1 (green diamonds in Fig. 23) even the outer boundary condition has been changed from perfectly conducting to insulating. The numbers do not show any influence of the boundary conditions on the resulting $\alpha_{\rm mri}$. Equation (63) also implies that the microscopic viscosity has no essential influence on the angular momentum transport parameter $\alpha_{\rm mri}$ and, moreover, does not influence the eddy viscosity values (see Eq. (62)).

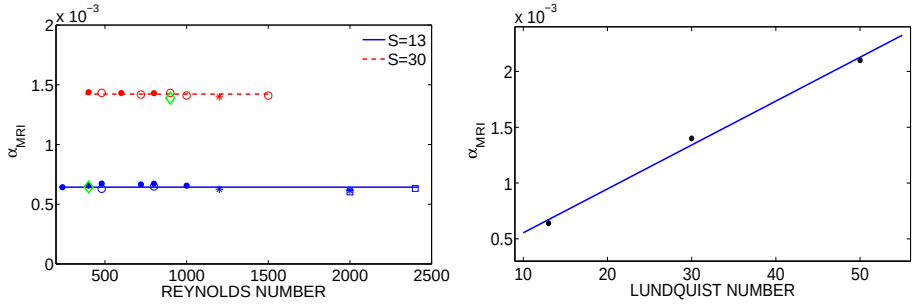

Figure 23. $\alpha_{\rm mri}$ versus Re (left) and S (right) for quasi-Keplerian rotation. Dots: Pm = 1, circles: Pm = 0.5, stars: Pm = 0.2, squares: Pm = 0.1. Green diamonds: Pm = 1 and pseudo-vacuum as outer boundary condition. Each dot represents many models with varying Re and Pm. $\alpha_{\rm mri}$ linearly grows with S. $r_{\rm in} = 0.5$, $\mu_\Omega = 0.35$. Perfectly conducting boundaries. From [52].

As an astrophysical application of the compact result (63), we ask how strong the axial magnetic field must be in order to produce $\alpha_{\rm mri} = 1$. For a protoplanetary disk $\eta = 10^{15}{\rm cm}^2/{\rm s}$ and $\rho = 10^{-10}{\rm g/cm}^3$ can be assumed [63]. Hence ${\rm S} \simeq 10^3(B_0/1{\rm G})(R_0/10{\rm AU})$, so that $B_0 = 1$ G is needed for $\alpha_{\rm mri} = 0.05$. It is obvious that the magnetic field amplitude must not be much smaller than about 1 G in order to get $\alpha_{\rm mri}$ values of the needed order. This estimate excludes dipolar large-scale stellar fields as the source of the background fields for MRI-induced eddy viscosities.

4. Azimuthal magnetorotational instability (AMRI)

According to Michael's criterion (6) hydrodynamically stable flows are also stable under the influence of curl-free azimuthal magnetic fields, i.e. $B_\phi \propto 1/R$. On the other hand, all rotation laws between two insulating cylinders in the presence of toroidal fields due to an axial current inside the inner cylinder are stable against axisymmetric perturbations [5, 64]. The reason is simple: the axisymmetric version of Eq. (45) fully decouples from the system so that this magnetic component decays because of missing energy sources. In particular, it cannot generate induction energy by the differential rotation term in Eq. (46). An axisymmetric MRI with purely azimuthal fields is thus not possible. These results, however, only hold for axisymmetric perturbations so that we have to ask for possible instability of nonaxisymmetric modes, which can indeed arise [65, 66]. Because of the absence of large-scale electric currents in the fluid between the cylinders we have called this phenomenon the Azimuthal MagnetoRotational Instability (AMRI). We shall derive in this section the theoretical background of this nonaxisymmetric instability, including its first experimental realization in a laboratory.

4.1. Potential flow

For the curl-free magnetic field with $B_\phi \propto 1/R$ (i.e. $\mu_B 0 r_{\rm in}$), Fig. 25 shows the lines of marginal stability for the potential flow with $\Omega \propto 1/R^2$ (i.e. $\mu_\Omega = r_{\rm in}^2$). Note that precisely this combination fulfills the condition $B_\phi \propto U_\phi$ which corresponds to a very special type of MHD flow (Chandrasekhar flows, see Section 5). One finds that the instability for $m = 1$ only exists between a minimum and a maximum Reynolds number. Too slow or too fast rotation enforces stability. The upper branch limits the instability domain by suppressing the nonaxisymmetric instability by too strong shear while the lower branch is defined by the minimum shear energy needed for the instability. The location of the maximum growth rate marked by dots in the left panel of Fig. 25 is closer to the lower branch than to the upper branch.

The curves in the (Ha/Re)-plane converge for small Pm and are no longer visible as distinct curves. For increasing magnetic Prandtl number the value of the minimum Reynolds number decreases, and the smallest critical Hartmann number is reached for Pm $\simeq$ 0.1. For very small Pm the minimum of the instability cone scales with Re, here with a value of about Re $\simeq$ 800, while the associated Hartmann number is ten times less. The coordinates of the characteristic

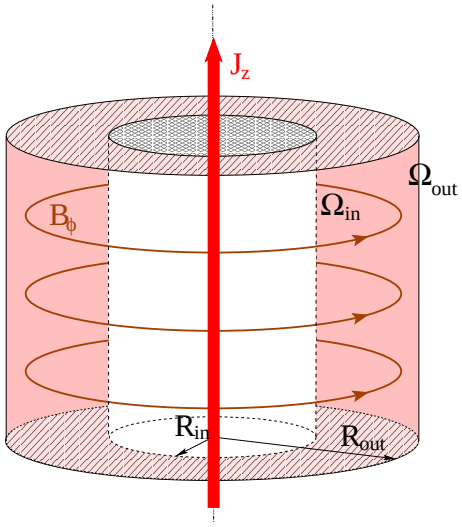

Figure 24. Setup for AMRI and TI calculations. The conducting fluid resides between two concentric and axially unbounded cylinders with radii $R_{\rm in}$ and $R_{\rm out}$ rotating with $\Omega_{\rm in}$ and $\Omega_{\rm out}$. $B_\phi = B_\phi(R)$ is the toroidal magnetic field due to axial currents inside the outer cylinder. From Eq. (36) one finds $\mu_B = r_{\rm in}$ as characteristic for azimuthal background fields which are current-free between the cylinders ($B_\phi \propto 1/R$) while $\mu_B = 1/r_{\rm in}$ leads to a pinch-type configuration with uniform axial electric current between the cylinders ($B_\phi \propto R$).

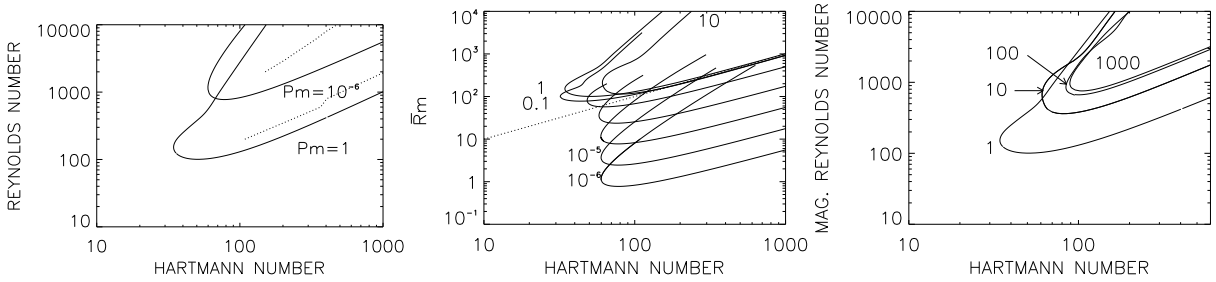

Figure 25. Potential flow: stability maps of the $m = 1$ modes influenced by current-free azimuthal magnetic fields for various Pm. Left: all curves for Pm $< 10^{-4}$ are basically identical (for small Pm the curves scale with Ha and Re). The dotted lines mark the location with maximal growth rates. Middle: same data with the averaged Reynolds number $\overline{\rm Rm}$ as the vertical coordinate. The dashed line marks Mm = 1. Right: for large Pm the potential flow scales with the magnetic Reynolds number Rm. $r_{\rm in} = 0.5$, $\mu_B = r_{\rm in}$, $\mu_\Omega = 0.25$, perfectly conducting boundaries. From [67].

minimum of the lines of neutral stability for all m and for small magnetic Prandtl numbers are given in Fig. 27. The curves in this plot demonstrate how for Pm $\to 0$ the lines in the (Ha/Re) plane no longer depend on the value of Pm, that is, the instability scales with Re and Ha for small Pm.

The right panel of Fig. 25 demonstrates the scaling of the instability curves for large Pm in the (Ha/Rm) plane. The curves converge for Pm $\to \infty$ for magnetic Reynolds number of about1000 and with minimal Hartmann number of about 100. The use of the average Reynolds number $\overline{\rm Rm} = \sqrt{\rm Re \cdot Rm}$ as the vertical axis leads to additional findings. The dotted line in Fig. 25 (right) represents the location of the limit Mm = 1. Note that the main part of the cones for Pm > 1 lies above the dotted line while it lies below this line for Pm < 1. For Pm $\to 0$ the entire instability domain no longer reaches values with Mm > 1. The relevance of AMRI for super-Alfvénic astrophysical applications might thus be rather restricted. On the other hand, for Pm $\to \infty$ the instability cone never reaches values with Mm < 1.

The eigenvalues for modes with $m > 1$ are given in Fig. 26 for Pm $= 1$ and Pm $= 10^{-4}$. These curves also have the characteristic form consisting of lower and upper branches with positive slopes, so again the rotation can be too slow or too fast for instability. For higher m the instability domains are smaller than for lower m. For all m the minima of the curves for Pm $\to 0$ move below the dashed line Mm = 1. The absolute minimum values of Re and Ha of all curves are plotted in Fig. 27. It shows the $m = 1$ mode as the most unstable mode with the lowest Reynolds and Hartmann

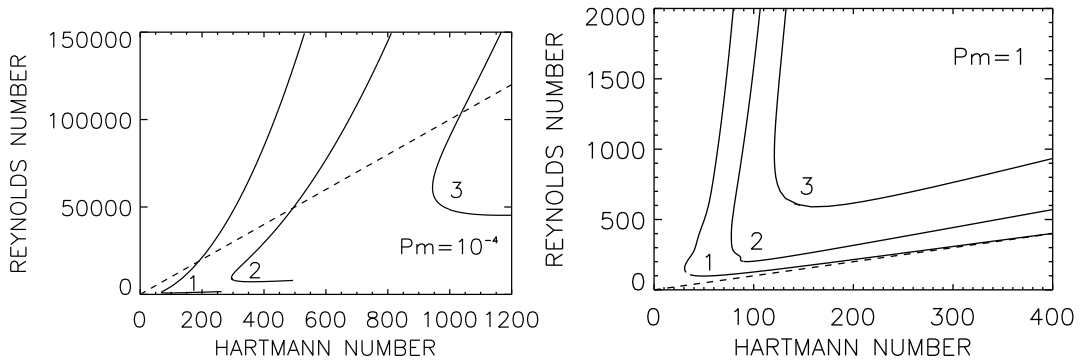

Figure 26. Stability maps for the $m = 1, 2, 3$ modes for potential flow with Pm $= 10^{-4}$ (left) and Pm $= 1$ (right). All curves for Pm $< 10^{-4}$ are identical. The dotted lines mark Mm $= 1$. For sufficiently small Pm all curves are located below Mm $= 1$. For fixed Ha the unstable modes decay for too slow and too fast rotation. $r_{\rm in} = 0.5$, $\mu_B = r_{\rm in}$, $\mu_\Omega = 0.25$. Insulating boundaries.

numbers. Decreasing Pm shifts the minimum values to higher values of Re and Ha, and this the more the greater m is. For small Pm the excitation of the higher modes requires much higher Reynolds and Hartmann numbers than for Pm $= 1$. The plots also show that for Pm $\to 0$ all the considered azimuthal modes scale with Re and Ha. Because of Mm $= \sqrt{\rm Pm}{\rm Re}/{\rm Ha}$ for small Pm all minima are thus subAlfvénic. We shall demonstrate below that these results are typical for the class of Chandrasekhar MHD flows.

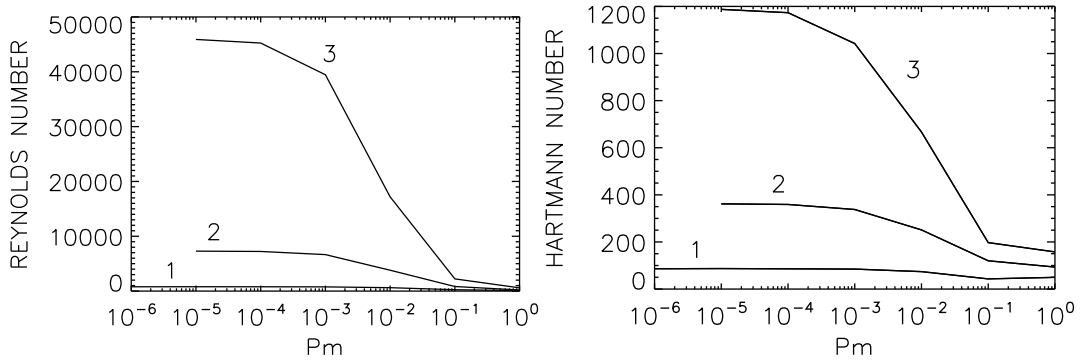

Figure 27. The minimum Re and Ha of the modes $m = 1, 2, 3$ taken from many models similar to Fig. 26 versus Pm. $\mu_B = r_{\rm in} = 0.5$, $\mu_\Omega = 0.25$. Insulating boundaries.

Figure 28 gives an example for the drift rate (53) along the lines of neutral stability. In this normalization the outer cylinder has a rotation rate of μ_Ω. The real part of the Fourier frequency ω has the opposite sign as the azimuthal migration of the pattern. Since Fig. 28 shows that $\omega_{\rm dr} < 0$ is always the case, the instability pattern drifts in the direction of the basic rotation. A typical value of the drift in units of $\Omega_{\rm in}$ for small Pm is -0.25 (marked in the plot), so that for $\mu_\Omega = 0.25$ the pattern basically corotates with the outer cylinder. For stronger fields the drift is slower.

We have still to ask how the growth rates behave between the two branches of neutral stability for a given Reynolds number. The growth rate is the negative imaginary part of the eigenfrequency ω. In relation to the experiment described in Section 4.3 we take Re $= 3000$ for the fixed Reynolds number. The left panel of Fig. 29 clearly shows the convergence of the growth rates

$$\omega_{\rm gr} = -\frac{\Im(\omega)}{\Omega_{\rm in}} \tag{64}$$

for small Pm so that it makes sense to probe their saturation between the two branches. It is obviously enough for the limit of small Pm to calculate the growth rates along the upper dotted line in Fig. 25. The results are plotted in Fig. 29 (right). The maximum growth rate for very rapid rotation is $0.050\ \Omega_{\rm in}$, so that the shortest growth time of AMRI for

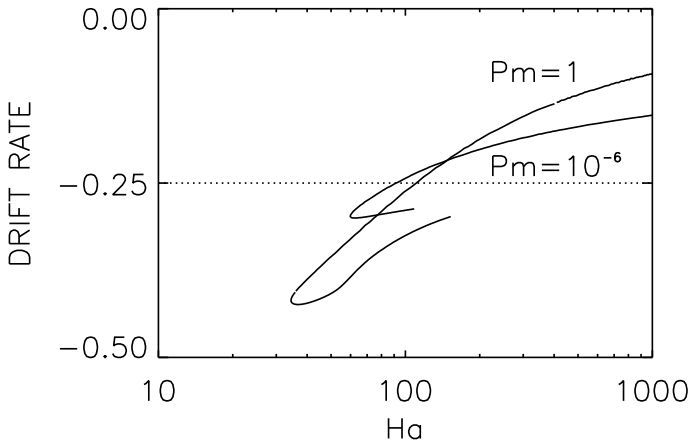

Figure 28. Drift frequency (53) along the lines of neutral stability. The dotted line marks the value −0.25 indicating exact corotation with the outer cylinder. All curves for Pm < 10^{-4} are identical. $m = 1$, $\mu_B = r_{\rm in} = 0.5$, $\mu_\Omega = 0.25$. Perfectly conducting boundaries.

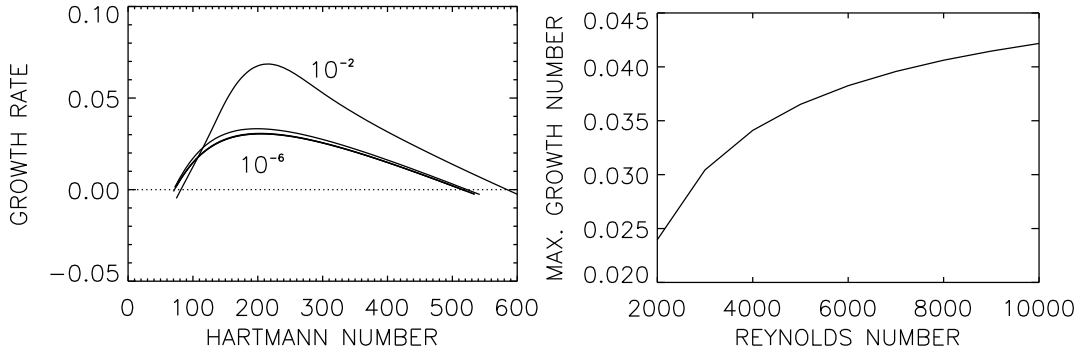

Figure 29. Left: growth rates along a line of constant Reynolds number (Re = 3000). The lines from top to bottom belong to Pm = 10^{-2}, Pm = 10^{-3} down to Pm = 10^{-6}. The curves for Pm < 10^{-4} are almost identical. Right: the maximal growth rates along the upper dotted line in Fig. 25 (left) for Pm = 10^{-6}. The Hartmann numbers grow from about 200 to about 500 (from left to right). $\mu_B = r_{\rm in} = 0.5$, $\mu_\Omega = 0.25$. Perfectly conducting boundaries.

the potential flow is about 0.9 rotation times of the *outer* cylinder, which is just of the order of the growth time for the standard MRI.

For the small magnetic Prandtl number Pm = 10^{-5} in Fig. 30 the isolines of the axial component of the flow and the radial component of the magnetic field for axially unbounded containers with nearly potential flow are given. The flow is measured in the form of Reynolds numbers $u_R D/\nu$, and the field is normalized with $B_{\rm in}$. The shear parameter $\mu_\Omega = 0.26$ (as also in Figs. 37 and 38) has been chosen here to correspond to the experiments described in Section 4.3. For small Reynolds numbers the pattern is nonaxisymmetric with $m = 1$. The maximal flow amplitude exceeds the maximal field amplitude by many orders of magnitudes, contrary to the common assumption that kinetic and magnetic energies of magnetohydrodynamic turbulence 'ought' to be equipartitioned. It is thus necessary to study the ratio of both energies in more detail, which leads to a surprising result. The left panel of Fig. 31 shows the ratio (58) for various Reynolds numbers as a function of the magnetic Prandtl number. The Hartmann number is fixed. The result is that for small magnetic Prandtl number (Pm $\lesssim 10^{-2}$) a relation $\varepsilon \propto$ Pm seems to hold, which implies that $\eta\langle \boldsymbol{b}^2\rangle/\mu_0\rho \simeq \nu\langle \boldsymbol{u}^2\rangle$, or equivalently $b_{\rm rms} = O(\sqrt{\rm Pm} u_{\rm rms})$. This dependence is weaker than that used earlier as $b_{\rm rms} = O({\rm Pm} u_{\rm rms})$ for small Pm [26]. For Reynolds numbers up to 50,000, and magnetic Prandtl numbers smaller than a value of (say) 0.01, the instability pattern is always dominated by the kinetic fluctuations. The critical Pm, however, depends on the applied Reynolds number; it becomes smaller for increasing Re. The plot also shows that the influence of the global Reynolds number on this relation is only weak. For faster rotation the ratio (58) is somewhat larger than for slower rotation. For forced MHD turbulence models a similar behavior for the viscous and Ohmic dissipation has

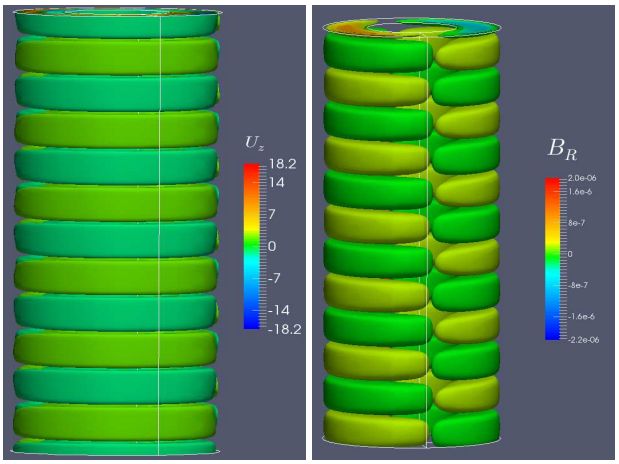

Figure 30. Snapshot of the isolines of axial flow (left) and radial magnetic field (right) patterns for axially unbounded containers. The flow is given in form of Reynolds numbers $u_z D/\nu$ and the field is normalized with $B_{\rm in}$. The modes with $m = \pm 1$ drift in the positive ϕ direction with the same rates. Also the axial flow pattern of the left panel is nonaxisymmetric but there is a remarkable phase shift to the radial field. The cells are slightly elongated in axial direction. The energy ratio (58) – taken for the maximal values of u_z and b_R – approximates 10^{-5}. Re = 1500, Ha = 100, $\mu_B = r_{\rm in} = 0.5$, $\mu_\Omega = 0.26$, Pm = 10^{-5}.

been found [68].

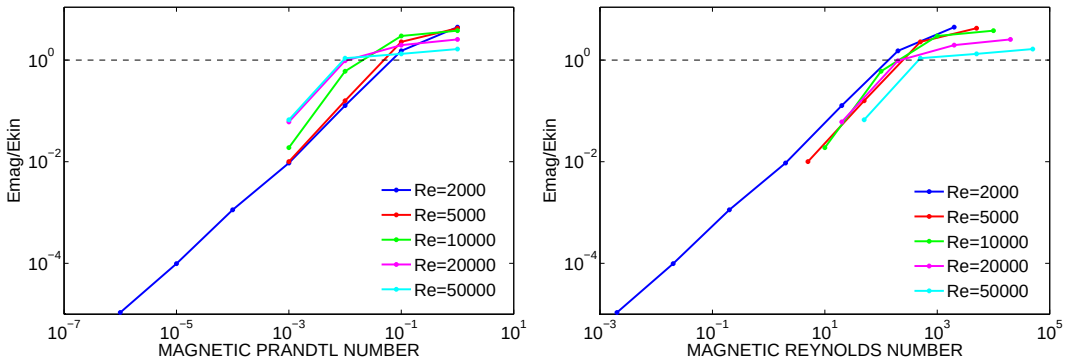

Figure 31. Ratio (58) of magnetic and kinetic energy as functions of Pm (left) or Rm (right). The latter scaling seems to be more clear. $\mu_B = r_{\rm in} = 0.5$, $\mu_\Omega = 0.25$. Ha = 600, insulating boundaries.

In Fig. 31 (right) the same ratio ε is plotted as it depends on the magnetic Reynolds number Rm, which yields a much clearer scaling of the data. The magnetic energy exceeds the kinetic energy only for Rm $\gtrsim$ 200. For larger Rm the energy ratio seems to remain constant. The models with Rm < 200 are only weakly magnetized, while for larger Rm the pattern is magnetically dominated. If this is true, experiments with liquid metals as the fluid between the cylinders will always lead to $\varepsilon \ll 1$ unless the Reynolds number exceeds 10^7. Working with the maximal values of field and flow given in Fig. 30, we have $\varepsilon = O(10^{-5})$ for Rm = 0.015, in agreement with the numbers given in Fig. 31 (right) and far away from equipartition. It thus makes sense in related experiments to observe the flow pattern rather than the magnetic pattern (see Section 4.3).

4.2. Quasi-Keplerian rotation and beyond

If a flatter rotation profile is considered the situation can be different. For quasi-Keplerian rotation ($\mu_\Omega = 0.35$) the neutral stability curves for the two possible boundary conditions are plotted in Fig. 32. They show a different scaling behavior for Pm $\to$ 0. For insulating boundaries (left panel) the curves with Pm $\ll$ 1 are almost identical in the (S/Rm) plane. They lie *above* the line Mm = 1. The instability, therefore, also exists for rapid rotation. In

contrast, the potential flow for small Pm always scales with Ha and Re (see Fig. 25) with severe consequences for the excitation conditions for rapid rotation (Mm > 1).

The consequences are reflected by the instability map for quasi-Keplerian flow with perfectly conducting boundaries (Fig. 32, right). The curves for large and medium Pm satisfy Mm > 1, while very small Pm yields Mm < 1, similar to the potential flow. It is also worth noting that for Pm = 1 the excitation of the $m = \pm 1$ modes is (slightly) easier for insulating than for perfectly conducting conditions. Nevertheless, substantial differences of the excitation conditions for small Pm for different boundary conditions are unexpected. The smooth transition from the scaling with Ha and Re for $\mu_\Omega = 0.25$ to the scaling with S and Rm for $\mu_\Omega = 0.35$ and Pm $\to 0$ for insulating boundary conditions [69] is not visible for fluids between conducting cylinders. It might happen that this transition needs much smaller Pm for different boundary conditions.

The next example with even flatter rotation profile with $\mu_\Omega = 0.5$ will demonstrate that the transition of the scaling properties happens simultaneously for both sorts of boundary conditions (Fig. 33).

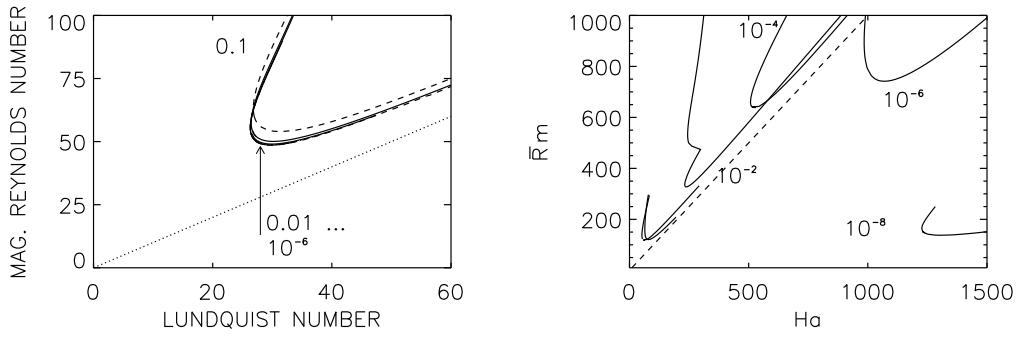

Figure 32. Stability maps for quasi-Keplerian flow. The curves are marked with Pm. For insulating boundaries (left) the curves scale with S and Rm for Pm $\to 0$, unlike for perfectly conducting boundaries (right). The straight lines represent Mm = 1. AMRI for quasi-Keplerian flow becomes super-Alfvénic (at least for insulating boundary conditions). $\mu_B = r_{\rm in} = 0.5$. $\mu_\Omega = 0.35$.

The figure demonstrates a much weaker influence of the boundary conditions than for the quasi-Keplerian flow (32). The differences between the neutral stability curves for both boundary conditions are very small. The scaling for Pm $\to 0$ with S and Rm no longer depends on the boundary conditions; the instability curves for Pm $\to 0$ always converge in the (S/Rm) plane. The important difference to the potential flow is that now all curves lie *above* the line Mm = 1 so that this instability also exists for rapid rotation. For all Pm the magnetic Mach number Mm lies between low and high rotation limits but it is always super-Alfvénic, e.g., for Pm = 1 AMRI exists for

$$1 \lesssim \mathrm{Mm} \lesssim 3. \tag{65}$$

Again, both the magnetic field and the rotation rate can be too weak or too strong for AMRI and again the excitation of the instability for Pm = 1 is slightly easier for insulating boundary conditions. Figure 33 also demonstrates that for Pm > 1 the scaling switches from S and Rm (valid for Pm < 1) to Ha and $\overline{\mathrm{Rm}}$. For both limits the influence of the boundary conditions is very weak. It seems to be clear, however, that the magnetic Mach numbers move from large values for small Pm to small values for large Pm. This is insofar surprising as the definition of the magnetic Mach number is entirely free of diffusivities.

For various Rm and Pm the growth rates (64) have been calculated between the two limiting values S where it vanishes; it is maximal somewhere between the two limits. In Figs. 34 the normalized growth rate is plotted for the parameters Rm and Pm. One finds quasilinear relations

$$\omega_{\rm gr} \simeq \epsilon_{\rm gr}\,\mathrm{Rm} \tag{66}$$

with $\epsilon_{\rm gr}$ varying slightly from $1.5 \cdot 10^{-4}$ for Pm = 1 to $2.1 \cdot 10^{-4}$ for Pm = 0.01 [70]. The growth rate slowly increases for smaller Pm but this effect is weak. The growth time in units of the rotation time is thus $\tau_{\rm gr}/\tau_{\rm rot} \simeq 10^3/\mathrm{Rm}$. Of

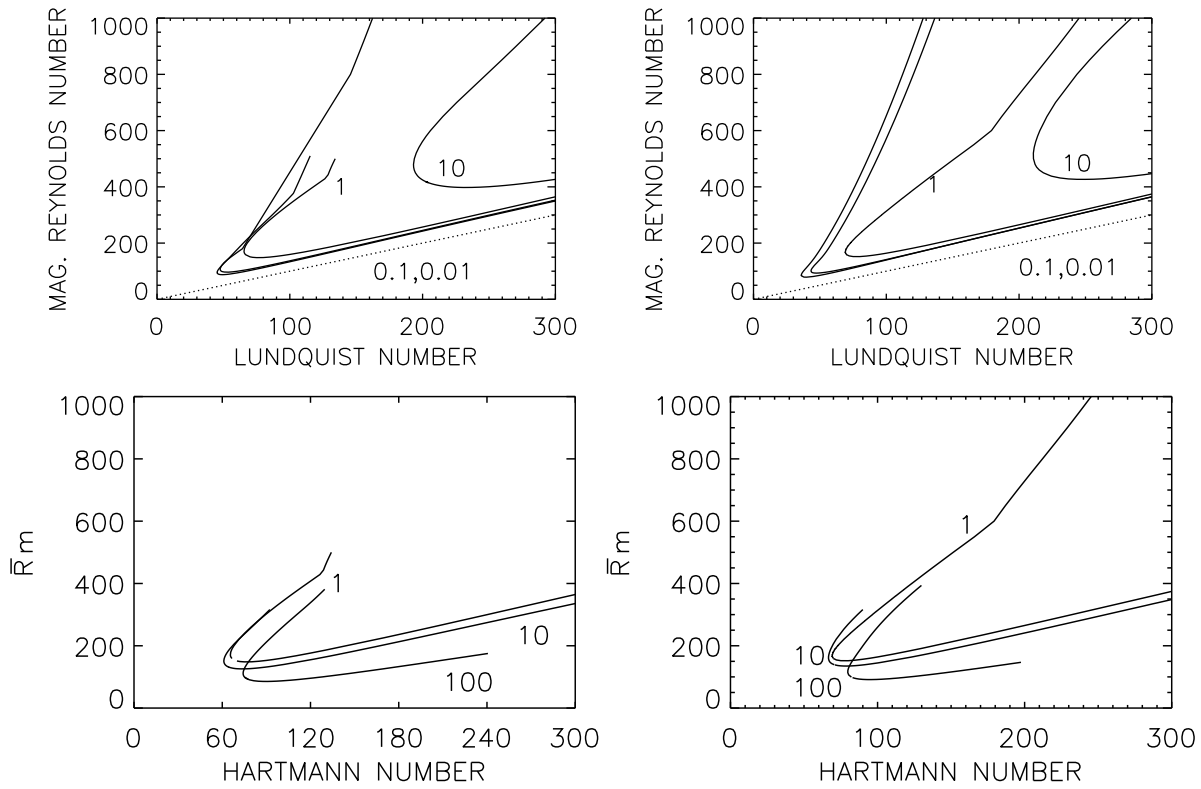

Figure 33. Quasi-uniform flow: stability maps of the modes $m = \pm 1$ for current-free azimuthal fields (AMRI) and small Pm (top) and large Pm (bottom). For both boundary conditions (left: insulating, right: conducting) the curves scale with S and Rm for Pm $\to 0$ and with Ha and $\overline{\mathrm{Rm}}$ for Pm $\to \infty$. The dotted lines define Mm = 1, the instability is super-Alfvénic for small Pm and sub-Alfvénic for large Pm. $\mu_B = r_{\rm in} = 0.5$, $\mu_\Omega = 0.5$.

course, the linear relation can only hold for small Rm. For Rm $\gg 1$ the growth rate no longer depends on Rm, so then $\omega_{\rm gr} \le 0.14$. The growth time of the instability for $\mu_\Omega = 0.5$ can therefore never be shorter than one rotation time.

The growth rates of the instability pattern and its axial wave number can be used to compute the characteristic Strouhal number

$$\mathrm{St} = \frac{u_{\rm rms}}{\ell \omega_{\rm gr}}, \tag{67}$$

with the axial cell size $\ell = \pi/k$. The growth rates have been calculated from linear models for various Hartmann numbers along the line of maximal instability in Fig. 25. The rotation profiles vary in the wide interval between $\mu_\Omega = 0.25$ and $\mu_\Omega = 0.5$. For the rms velocity only the axial intensity $\langle u_z^2 \rangle^{1/2}$ is used.

The numerical results in Fig. 35 underline the exceptional importance of the Strouhal number. The Strouhal number is almost unity for steep rotation profiles and large magnetic Prandtl number, in confirmation of an often-used assumption. This is certainly not a trivial result for consistent models of MHD flows. The self-consistent models of MHD instability (not driven) lead to Strouhal numbers of order unity. It becomes slightly smaller both for smaller Pm and for flatter rotation profiles. Hence, the nonlinear turbulence intensity $\langle u_z^2 \rangle$ can be estimated by means of the characteristic quantities k and $\omega_{\rm gr}$ of the linear theory alone. For dissipation coefficients such as the magnetic resistivity it should be allowed to move from the well-founded relation

$$\eta_{\rm T} \simeq \int_{-\infty}^{\infty} \langle u_i(t) u_i(t-\tau) \rangle \, \mathrm{d}\tau \tag{68}$$

to $\eta_{\rm T} \simeq u_{\rm rms} \ell$ as a good estimation [71]. This does not mean, however, that the effective viscosity can be estimated just with these quantities if the effect of the magnetic fluctuations cannot be neglected [72].

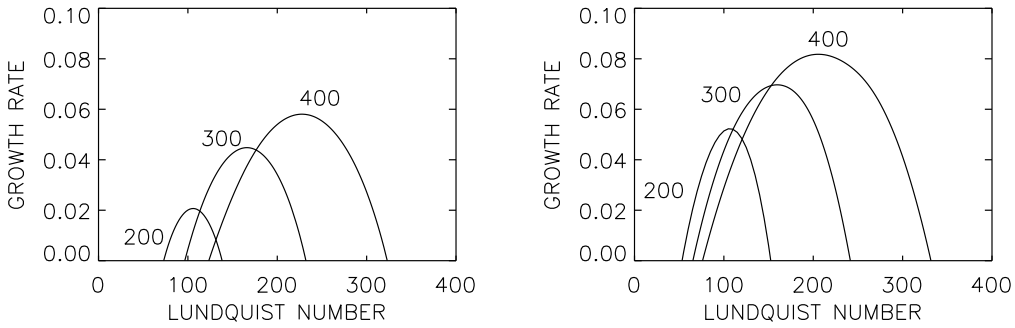

Figure 34. Growth rate (66) versus Lundquist number for various magnetic Reynolds numbers. The curves are marked with Rm. The normalized growth rates l grow linearly with Rm. $m = \pm 1$, Pm = 1 (left), Pm = 0.01 (right), $\mu_B = r_{\rm in} = 0.5$, $\mu_\Omega = 0.5$. Perfectly conducting cylinders.

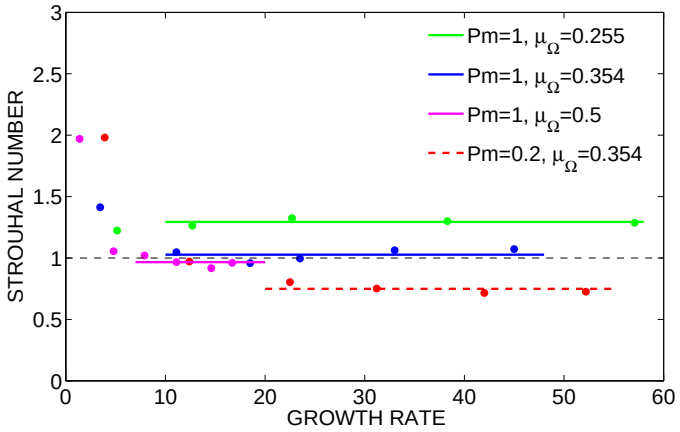

Figure 35. Strouhal numbers (67) versus growth rate for various Pm and shear parameters μ_Ω. The models possess the maximal growth rates as indicated in Fig. 25. The Strouhal numbers of AMRI are always of order unity (with a weak dependence on Pm). $\mu_B = r_{\rm in} = 0.5$.

4.3. The AMRI experiment

In this section, we will present results of a liquid metal experiment devoted to the investigation of AMRI and the helical version of the magnetorotational instability (to be discussed in Section 6). The switch of the scalings for fluids with low magnetic Prandtl number from Rm and S to Re and Ha allows experiments to work with slow rotation and weak fields, provided that the rotation profile is not too far from the potential flow. The most popular candidates for experiments with liquid metals are given in Table 1. Generally, they combine the viscosity of water with the electrical conductivity of the solar plasma. The low values of the magnetic Prandtl numbers of liquid metals in comparison to the solar plasma are due to their low viscosities. If liquid metal AMRI experiments are carried out close to the Rayleigh line, only the values of ν and $\bar{\eta} = \sqrt{\nu\eta}$ are relevant. The magnetic Prandtl numbers vary by two orders of magnitudes, but close to the Rayleigh limit this is not really important. The viscosity varies by a factor of only seven among the metals in Table 1, and the averaged diffusivity $\bar{\eta} = \sqrt{\nu\eta}$ is also very similar for all fluids.

While sodium, with its low magnetic diffusivity, is the liquid of choice for experiments that require high values of Rm (and S), such as dynamo experiments and experiments on standard MRI, GaInSn is more convenient for experiment governed by Re (and Ha). This has mainly to do with the much milder safety requirements compared to sodium, but also with the fact that GaInSn is liquid at room temperatures. While the latter advantage is shared by mercury, the health risks in dealing with that metal made it disappear from most liquid metal labs.

As a first guide to the experimentally relevant parameter space, Fig. 36 shows the growth rate and the drift rate (both normalized with the rotation rate of the inner cylinder) for a Reynolds number of Re = 3000 and low magnetic

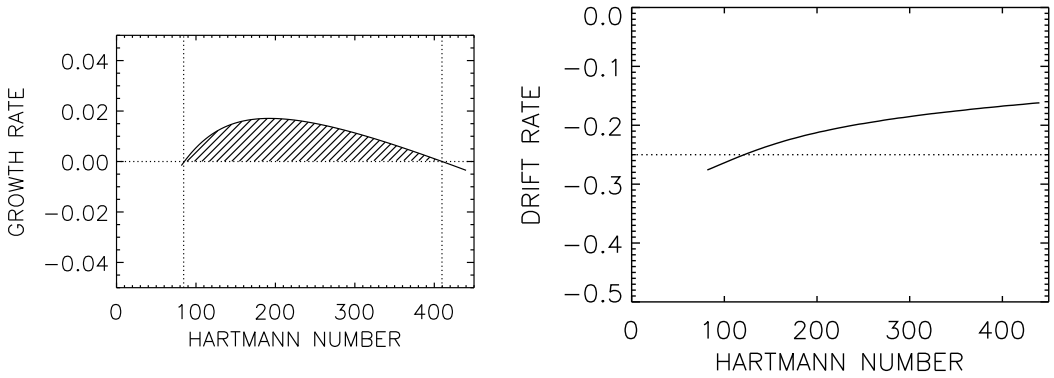

Figure 36. Towards a gallium experiment for AMRI with a rotation law very close to the Rayleigh line: growth rate $\omega_{\rm gr}$ (left) and drift rate $\omega_{\rm dr}$ (right) (both normalized with $\Omega_{\rm in}$) of the modes with $m = \pm 1$ as functions of Ha. The hatched area marks instability between the two limits of marginal stability, the dotted line in the right panel marks corotation with the outer cylinder. The maximal growth time of the instability is about 2 rotation times of the outer cylinder. Re = 3000, $\mu_B = r_{\rm in} = 0.5$,$\mu_\Omega = 0.26$, Pm = 10^{-6} [70].

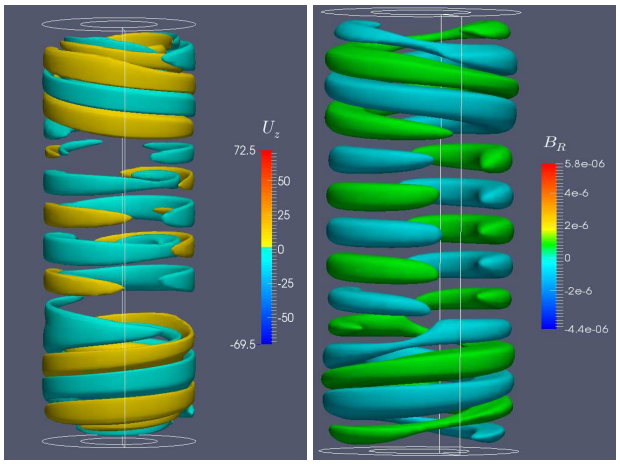

Figure 37. As in Fig. 30 but for an axially bounded container with $\Gamma = 10$ with perfectly conducting cylinders and insulating endplates which are split like the endplates of the Promise experiment. Because of the endplates a slight equatorial antisymmetry occurs and the flow amplitudes enhance near the two lids. The magnetic perturbations are hardly modified. The power supply is perfectly axisymmetric along the z-axis. Re = 1500, Ha = 100, $\mu_B = r_{\rm in} = 0.5$, $\mu_\Omega = 0.26$, Pm = 10^{-5}.

Prandtl number. The parameters strongly differ from the values used in Fig. 34. The main difference, however, is the different scalings of AMRI for steep ($\mu_\Omega = 0.26$) and flat ($\mu_\Omega = 0.5$) rotation laws [69] so that, as a consequence, (66) does not hold for the potential flow. The maximum growth rate lies between the two values of neutral stability and takes a value of 0.02 which corresponds to a growth time of about 8 rotation times of the inner cylinder. Compared with MRI, the AMRI also scales with the rotation time but is somewhat slower. The onset of the instability is at Ha $\simeq$ 85, corresponding to an axial electric current of 10.9 kA. It is very characteristic that for much higher Hartmann numbers (Ha $>$ 400 in Fig. 36, left) the instability disappears. The right panel of Fig. 36 gives the normalized azimuthal drift $\omega_{\rm dr}$ of the pattern of the $m = 1$ mode. The dotted line represents the relation $\dot{\phi} = \mu_\Omega \Omega_{\rm in} = \Omega_{\rm out}$ where the pattern corotates with the *outer* cylinder. Note that the instability pattern indeed corotates with the outer cylinder for Ha $\simeq$ 110, which is only slightly greater than the lower Hartmann number for neutral stability. The measurements will confirm this prediction.

A serious difficulty to realize AMRI (and all other versions of MRI) in the laboratory are the endplate effects of finite-length devices. Figure 37 shows simulations for a data set close to experimental realizations for a height-to-gap ratio $\Gamma = 10$ and with very small Pm. The corresponding version for $\Gamma \to \infty$ (i.e., with periodic boundary conditions),

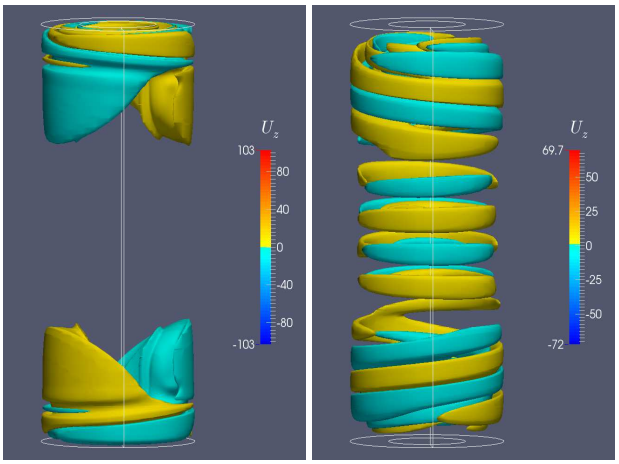

Figure 38. Vertical flow speeds as in Fig. 37 (left) but for a very nonaxisymmetric lead wire system with $m = 1$ symmetry (left) and a lead wire system with $m = 2$ symmetry (right).

as given by Fig. 30, leads to an energy ratio $\varepsilon \simeq 10^{-5}$ which for $\Gamma = 10$ is not basically changed. The endplates have two main effect: First, there is some concentration of the energy close to the endplate where the flow intensity is drastically enhanced. Second, we observe a symmetry breaking between left and right handed spirals which appear now preferentially in the lower/upper half of the cylinder (in contrast to the equal distribution as visible in Fig. 30).

The facility PROMISE (*P*otsdam *RO*ssendorf *M*agnetic *I*n*S*tability *E*xperiment) is shown in Fig. 39. Its heart is a cylindrical vessel made of copper. The inner wall extends in radius from 22 to 32 mm; the outer wall extends from 80 to 95 mm. This vessel is filled with the liquid alloy GaInSn whose material parameters are given in Table 1.

In the real experiment, however, the electric current is provided by a closed wire system which forms an external magnetic field which modulates the prescribed axisymmetric azimuthal field by a weak nonaxisymmetric component. One easily finds that this modulation corresponds to an additional $m = 1$ component which strongly influences the excitation of the $m = 1$ AMRI mode (see Fig. 38, left). This unfortunate situation can be overcome by a more complicated lead wire system providing an external magnetic modulation with $m \neq 1$. To produce the constellation given in Fig. 38 (right) two lead wires have been used in the same plane (at top and bottom of the container) separated by angles of 180°. The results are a good match to the vertical velocity component of the unbounded system (Fig. 30, left).

The copper vessel is fixed via a spacer on a precision turntable. The outer wall of the vessel thus serves as the outer cylinder of the Taylor-Couette device. The inner cylinder is fixed to an upper turntable, and is immersed into the GaInSn from above. It has a thickness of 4 mm, extending from 36 to 40 mm. The actual Taylor-Couette flow then extends between $R_{\rm in} = 40$ mm and $R_{\rm out} = 80$ mm. In the present configuration of the experiment the lower and upper lids are electrically insulating and split at a well defined intermediate radius of 56 mm which had been found in [73, 74, 75, 76] to minimize the Ekman pumping. The endplates are made of plexiglass which are split into two rings where the inner one is attached to the inner cylinder and the outer one to the outer cylinder.

This represents a major advantage compared to the initial version of PROMISE [78, 79, 75] in which the upper endplate was a plexiglass lid fixed to the frame while the bottom was simply part of the copper vessel, and hence rotated with the outer cylinder, producing strong Ekman pumping and a clear top/bottom asymmetry with respect to both rotation rates and electrical conductivity. This central module is embedded into a 2 x 39-winding coil for the production of a vertical field (which only becomes relevant when discussing the helical MRI in Section 6). The axial velocity perturbations are measured by two ultrasonic sensors from Signal Processing SA with a working frequency of 4 MHz which are fixed into the outer plastic ring, 12 mm away from the outer copper wall, flush mounted at the interface to the GaInSn (see Fig. 39). Since this outer ring is rotating, it is necessary to transfer the signals into the laboratory frame by the use of a slip ring contacts. The advantage of the ultrasound Doppler Velocimetry is that it provides full profiles of the axial velocity u_z along the beam-lines parallel to the axis of rotation.

The azimuthal magnetic field is produced by a water-cooled copper rod going through the center of the setup. In

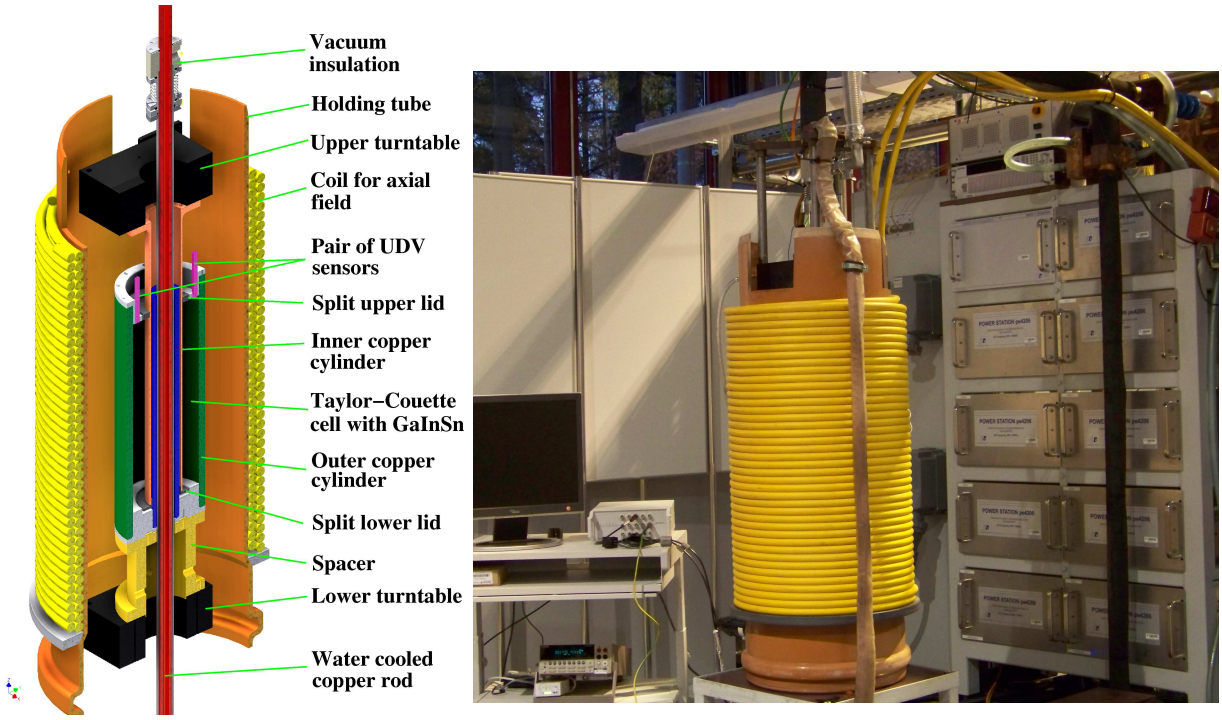

Figure 39. The facility of Promise: schematic sketch of the central Taylor-Couette setup and the coil for producing the axial field (left) and photograph of the installation, with the 20 kA power supply visible on the right.

the present configuration the current is supplied by a 20 kA switching mode power supply. Significant effort was spent on severe problems of electromagnetic interference [80], before the (initially extremely noisy) UDV data could be utilized for characterizing the AMRI. As mentioned above. the central copper rod is connected to the power supply in an asymmetric, one-sided manner.

With the container data the unit of velocity is $\nu/D \simeq 8.5{\cdot}10^{-3}$ mm/s. With the maximal $u_z \simeq 100$ taken from Fig. 38 (left) the maximal axial velocity which can be expected for the AMRI experiment as 0.85 mm/s. The experimental data have been analyzed in detail resulting in maximal values of 0.4 mm/s which can be considered as a rather good empirical confirmation of the simulations [77]. Note that the simulations of cylinders with $\Gamma \to \infty$ provide the lower value of about 20 and also the optimized container with $\Gamma = 10$ exhibits only 70 as the relevant quantity. The more perfect the experiment the lower amplitudes of the maximal u_z appear.

The relation $I_{\rm axis} = 5R_{\rm in}B_{\rm in}$ connects the toroidal field amplitude $B_{\rm in}$ at $R_{\rm in}$ with the axial current inside the inner cylinder. I, R and B must be measured in A, cm and G. Hence,

$$\mathrm{Ha} = \frac{1}{5}\frac{I_{\rm axis}}{\sqrt{\mu_0\rho\nu\eta}}. \tag{69}$$

The radial size of the container does not appear in this relation. For the gallium alloy GaInSn the value of the square root in (69) is 25.6. The resulting electric current for marginal instability is 10.9 kA, hence $B_{\rm in} = 545$ G. With the largest fluctuations of $b_\phi/B_{\rm in} \simeq 6 \cdot 10^{-6}$ taken from Fig. 37, one finds 3 mG as the maximum field fluctuation.

Analyzing more experimental runs we have compiled the dependence of quantities on the applied axial currents. Figure 36 (left) shows the theoretical growth rate for the infinite length system. The growth rates under the axisymmetric field condition give a consistent picture with a sharp onset of AMRI at $\mathrm{Ha} \simeq 80$ corresponding to current of 10.9 kA.

The left panel of Fig. 40 shows a typical experimental result for $\mathrm{Re} = 1480$, $\mu_\Omega = 0.26$, and $\mathrm{Ha} = 124$ which demonstrates how the upward and downward traveling waves interpenetrate each other in the upper and lower halves

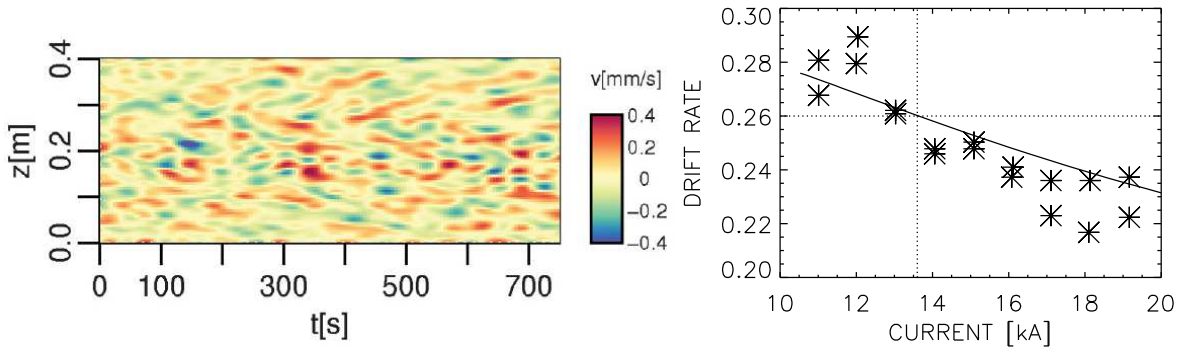

Figure 40. Results of the AMRI experiment for the original asymmetric lead wire system. Left: experimental results for the vertical flow in mm/s. The data also exhibit the (slight) equatorial antisymmetry predicted by the simulations (see Fig. 38, left). The magnetic symmetry breaking due to the one sided wiring of the central current makes the upward and downward traveling waves interpenetrate each other in the upper and lower halves of the cylinder. Re = 1480. Right: drift frequencies measured in positive azimuthal direction. The solid line corresponds to the line in Fig. 36 (right) but for $\mu_\Omega = 0.26$. One finds a nearly perfect agreement of the experiment with the simulations. $\mu_B = r_{\rm in} = 0.5$, Re = 2960. Experimental data from [77].

of the cylinder. Evidently, the selective occurrence of upward and downward traveling waves in the upper and lower halves which resulted from the first symmetry breaking in *axial direction* (due to the endcaps, see Fig. 38, left), is neutralized here by the second symmetry breaking in *azimuthal direction* (due to the one sided wiring).

Here we focus on the dependencies of the numerically and experimentally determined drift frequencies on the applied current, which proves to be a very robust property of the instability. From Fig. 36 (right),the pattern corotates with the outer cylinder for Ha $\simeq$ 120. In the right panel of Fig. 40 a nearly perfect agreement between theory and experiment can be seen. The theoretically expected enhanced frequency for lower Ha and a slightly reduced frequency for higher Ha can also easily be identified in the experimental data.

To summarize this section, the experiments revealed the existence of AMRI close to the Rayleigh line. While the observed and numerically confirmed effects of the double symmetry breaking on the AMRI are interesting in their own right, a new system of wiring of the central current, comprising a 'pentagon' of 5 back-wires situated around the experiment, is presently commissioned for further investigations.

4.4. Eddy viscosity

The instability-induced angular momentum transport which was calculated in Section 3.4 for MRI under the influence of an axial field will now similarly be computed for AMRI under the influence of a current-free azimuthal field.

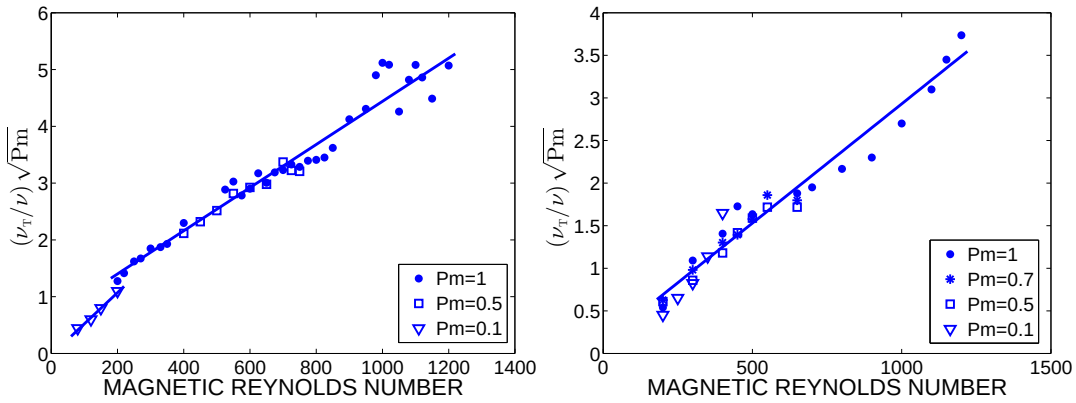

Figure 41. Normalized viscosity for $\mu_\Omega = 0.25$ (left) and $\mu_\Omega = 0.5$ (right). Given are the maximal values optimized with Ha for fixed Rm. Pm = 0.1 – 1 as indicated. For variation of the rotation law the numerical values seem to vary as $1/\sqrt{\mu_\Omega}$. $\mu_B = r_{\rm in} = 0.5$, perfectly conducting boundaries [81].

We shall simulate AMRI for two different rotation profiles, i.e. $\Omega \propto 1/R^2$ and $\Omega \propto 1/R$. The eddy viscosities are numerically computed in the instability cones for fixed Reynolds and Hartmann numbers, with the general result that ν_T peaks at the location of the maximum growth rates (dotted lines in Fig. 25, left). The effective viscosity is calculated by computing the right-hand side of the relation (60) within the instability domain in Fig. 25 (left). For a given Reynolds number, the Hartmann number is varied until the maximum value of ν_T is found, always close to the line of maximum growth rate. Finally, the maximum viscosity between the inner and outer cylinder is taken. The average procedure in (60) concerns only the azimuthal and axial directions.

For various magnetic Reynolds numbers, this procedure yields viscosities which grow linearly for increasing Rm. This is true for all rotation profiles between $1/R^2$ and $1/R$, including Keplerian (Fig. 41). For the magnetic Reynolds numbers of the order of 10^3 we do not find any indication of a saturation. For $\mathrm{Pm} < 1$ the resulting viscosity scales as $\nu_\mathrm{T}/\nu \propto \mathrm{Rm}/\sqrt{\mathrm{Pm}}$, which can also be written as

$$\frac{\nu_\mathrm{T}}{\nu} \simeq 5 \cdot 10^{-3}\overline{\mathrm{Rm}} \tag{70}$$

using the averaged Reynolds number (20). Unlike the MRI case, for AMRI we find a (weak) dependence of the viscosity on the magnetic Prandtl number, i.e. $\nu_\mathrm{T} \propto \sqrt{\mathrm{Pm}}\Omega_\mathrm{in}R_0^2$. The numerical factor is taken from Fig. 41. Note that we always only looked for the maximal values belonging to a given Re. We can thus assume that at least for $\mathrm{Re} \lesssim 10^3$ the effective viscosity does not exceed the given value.

With the results in Section 3.4 the eddy viscosities by MRI and AMRI can be compared. One finds

$$\frac{\nu_\mathrm{T,amri}}{\nu_\mathrm{T,mri}} \simeq \frac{100}{\mathrm{Ha_{mri}}}. \tag{71}$$

Obviously, the effective angular momentum transport for both instabilities also depends on the axial magnetic field strength B_0. As the AMRI values are maximal values and as $\mathrm{Ha_{mri}} \lesssim 100$ in our simulation in Section 3.4, we find both viscosities to be of the same order. If, however, the relation (71) is still valid for stronger fields (which we do not know) then ultimately the angular momentum transport by axial fields would be more effective than that by azimuthal fields.

4.5. Super-AMRI

In the following we will consider the stability of superrotation. i.e. rotation profiles with $\mathrm{d}\Omega/\mathrm{d}R > 0$, which are linearly stable in the hydrodynamic regime. Flows with stationary inner cylinder are the prototype of stable flows in hydrodynamics [82, 83]. The nonlinear behavior is less clear as some Taylor-Couette experiments have shown instability in this regime [84, 85, 86, 87]. There are several present-day experiments with Reynolds numbers of order 10^6 with various gaps between the cylinders and various aspect ratios $\Gamma = H/D$ (with H as the height of the container). The Princeton experiment has the smallest aspect ratio ($\Gamma \simeq 2$) with precisely controlled endplates split into several independently rotating rings [88, 89, 86, 57]. Other experiments have considerably greater aspect ratios, and also direct torque measurements, but no split-ring endplates, and hence potentially greater end-effects [90, 91, 92, 93, 94]. The measured torques are significantly greater than the results inferred in the Princeton experiment.

It is clear that superrotation cannot be destabilized by the standard magnetorotational instability MRI with axial background fields. A WKB method for inviscid fluids in current-free helical fields has been applied providing two limits of instability in terms of the shear in the rotation law [95, 96, 97]. In the same WKB framework, the existence of the upper threshold was also found for purely azimuthal fields [98]. Any upper threshold suggests a magnetic destabilization of superrotating flows for sufficiently strong positive shear. It has already been shown, however, that for *rapid* rotation the current-driven instability of toroidal fields may always be stabilized by positive shear [99]. It thus only remains to probe superrotating flows with slow rotation for instability.

The following models of Taylor-Couette flows in narrow gaps between perfectly conducting cylinders are considered, where the outer cylinder rotates faster than the inner one. It thus makes sense to here modify the definitions of the Hartmann and Reynolds numbers as

$$\mathrm{Ha} = \frac{B_\mathrm{in}D}{\sqrt{\mu_0\rho\nu\eta}}, \qquad \mathrm{Re_{out}} = \frac{\Omega_\mathrm{out}D^2}{\nu} \tag{72}$$

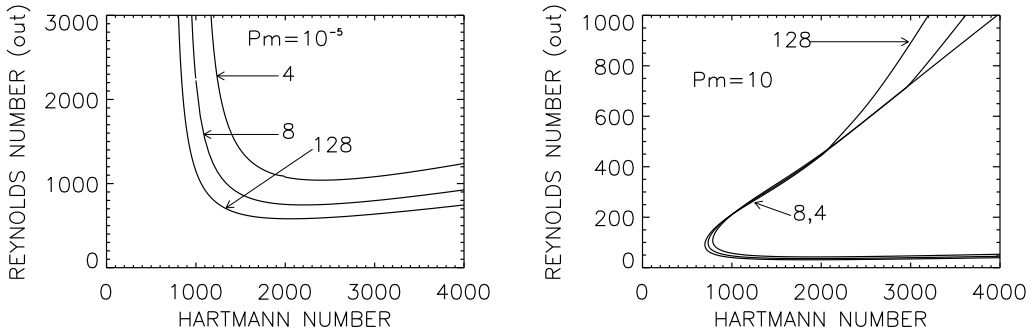

Figure 42. Superrotation: stability maps for small Pm (Pm = 10^{-5}, left) and large Pm (Pm = 10, right), the lines marked with their values of $\mu_\Omega > 1$. Reynolds numbers are formed with the outer rotation rate. A stationary inner cylinder can thus also be modeled with $\mu_\Omega \to \infty$. We find the curves converging for large μ_Ω. $\mu_B = r_{\rm in} = 0.95$, perfectly conducting cylinders.

with D as the gap width. The wave numbers k and the eigenfrequencies ω will also be normalized with D and the rotation rate $\Omega_{\rm out}$ of the outer cylinder. Wave numbers of π, therefore, describe a circular cell geometry in the meridional plane between the cylinders, and a drift value of $\omega_{\rm dr} = -1$ describes corotation with the outer cylinder. Cells with $k < \pi$ are prolate while cells with $k > \pi$ are oblate with respect to the rotation axis.

The lines in Fig. 42 represent the instability limit for the background field which is current-free in the very narrow gap ($r_{\rm in} = 0.95$) between the cylinders. The curves cannot cross the horizontal axis. The three hydrodynamically stable rotation laws have positive shear with $\mu_\Omega = 4, 8, 128$ and are magnetically destabilized in fluids with Pm = 10^{-5} (left panel) and Pm = 10 (right panel). The instability curves disappear for Pm = 1, demonstrating that the differential rotation is able to deliver the entire energy for the maintenance of the instability patterns only for Pm $\neq$ 1; the magnetic field only acts as a catalyst. Instabilities which only exist for $\nu \neq \eta$ belong to the class of double-diffusive instabilities [99]. They do not appear for Pm of order unity.

The numerical results given in Fig. 42 show that for small Pm the instability scales with the Reynolds number of the outer cylinder. The frequency of the inner cylinder does not play an important role. Note, however, that the rotation profile with the slowest inner cylinder becomes unstable most easily. The curves converge for $\Omega_{\rm in} \to 0$. It is also interesting to see how easily the flow can be destabilized for large Pm. While the Hartmann numbers for small and large Pm are very similar, the Reynolds numbers differ strongly. Obviously, for given molecular viscosity the excitation is easier the smaller the magnetic diffusivity.

Edmonds [8] argued that in narrow gaps the radial profiles of the azimuthal fields between the cylinders are almost uniform with only small influences on the excitation conditions. Test calculations indeed provided instability even for fields with uniform B_ϕ for very similar Reynolds numbers and Hartmann numbers. One may assume that for Pm $\neq$ 1 the superrotation becomes unstable under the mere presence of any toroidal field, but for Pm = 1 the dissipation processes prevent the excitation of this slow instability.

4.5.1. Influence of boundary conditions

To investigate the influence of the boundary conditions, Fig. 43 gives the instability map for one and the same rotation law ($\mu_\Omega = 5$) in models with slightly broader gaps ($r_{\rm in} = 0.9$) for the two cases of perfectly conducting and insulating boundary conditions. The magnetic Prandtl number is taken to be small (Pm = 10^{-5}, left) and large (Pm = 10, right). In the first case for insulating boundaries the superrotation laws are much more stable than for perfectly conducting boundaries. For conducting walls, both the Reynolds and Hartmann numbers are much smaller than they are for the insulating case. This is a striking difference to other magnetic instabilities. For the classical AMRI with negative shear the critical Hartmann numbers for both kinds of boundary conditions only differ slightly. Often, however, insulating boundary conditions lead to an easier excitation of the instability than conducting boundaries do. For large Pm, however, the differences for the two boundary conditions completely disappear as the two curves cannot be distinguished. One finds again positive slopes of both branches of the lines of neutral instability; only between

them the system is unstable. Note also, that all curves of marginal stability fulfill the condition Mm < 1 describing slow rotation.

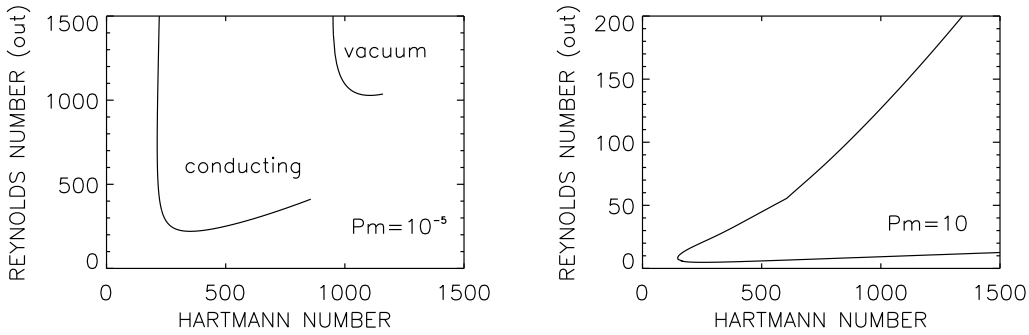

Figure 43. $\mathrm{Re}_{\mathrm{out}}$ versus Hartmann number for superrotation in a narrow gap with perfectly conducting and insulating cylinders. Left: Pm = 10^{-5}. Right: Pm = 10. All solutions are sub-Alfvénic and do not exist for Pm = 1. $m = \pm 1$, $\mu_B = r_{\mathrm{in}} = 0.9$. $\mu_\Omega = 5$.

The left panel of Fig. 44 gives the optimized wave numbers of the instability along the branches of instability for small and large Pm. The limit $k = \pi$ for nearly circular cells is marked by a horizontal dotted line. The cell geometry indeed depends on the magnetic Prandtl number. For small Pm the wave numbers are smaller than for large Pm hence the cells are prolate. Along the strong-field branch of the instability cone the wave numbers exceed those at the weak-field branch where the cells are almost circular in the meridional plane. For Pm $\gg 1$, however, the wave numbers at both branches are much larger so that the cells are always very flat. Note that the influence of the two boundary conditions is only weak, for Pm = 10 it vanishes completely.

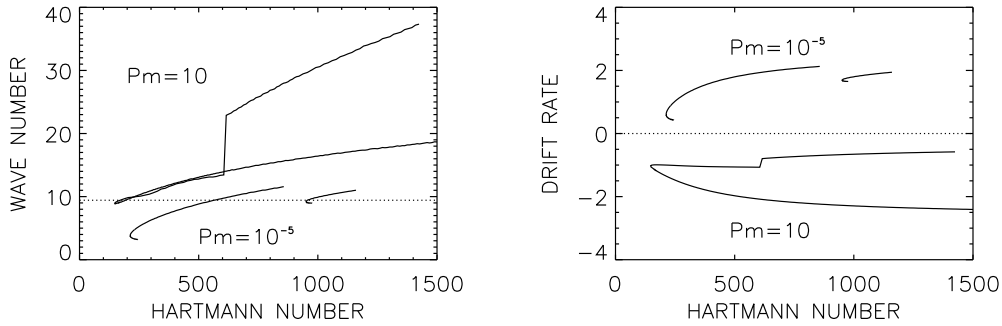

Figure 44. As in Fig. 43 but for wave numbers k (left) and drift frequencies ω_{dr} (right) for Pm = 10^{-5} and Pm = 10. The dotted line (3π) in the left panel gives the location of cells circular in the meridional (R/z) plane ($\ell = D$). The cells for small (large) magnetic Prandtl number are prolate (oblate) in this meridian. The drifts have opposite signs in both limits.

The drift rates even possess a very strong Pm-dependence. They are given in the right panel of Fig. 44 as the real parts ω_{dr} of the frequency ω of the Fourier mode of the instability normalized with the rotation rate of the *outer* cylinder. Because of (54) the azimuthal migration has the opposite sign of ω_{dr}. For small Pm we find positive ω_{dr} hence the instability pattern rotates *backwards*. Unlike for the AMRI with negative shear, large Pm yield negative drift values, and the pattern migrates with the rotation. For the lowest Hartmann number one even finds $\omega_{\mathrm{dr}} = -1$ so that in this particular case the pattern corotates with the outer cylinder. Again, for high values of Pm the influence of the boundary conditions even vanishes.

4.5.2. Electric currents

Figure 45 shows the Reynolds and Hartmann numbers from Eq. (72) for marginal instability for three narrow-gap models with slowly rotating inner cylinders as functions of the magnetic Prandtl number. The curves for different (but small) gaps between the cylinders are also representative for $\mu_\Omega \to \infty$ and for Pm $\to 0$. The results hardly change for faster inner rotation. For small Pm the resulting values of Ha and Re do not depend on Pm, hence the eigenvalues scale for small Pm with Ha and Re. For large enough positive shear these solutions thus also exist in the inductionless approximation. The question is still open whether an absolute minimum value of $\mu_{\Omega,0} > 1$ exists below which only stability occurs. The limit mentioned at the end of Section 6.4 for $r_{\rm in} = 0.9$ is only $\mu_{\Omega,0} = 2.7$ but it concerns the $m = 0$ solutions of the HMRI. – No solution exists for Pm ≤ 1 larger than the values shown in Fig. 45; fluids with Pm $= 1$ are always stable. Also solutions for Pm $\gg 1$ exist (Fig. 43, right) but the scaling of the eigenvalues for Pm $\to \infty$ is still unknown.

In order to transform the Hartmann numbers to the generating axial electric currents (i.e. within the inner cylinder) the relation $I_{\rm axis} = 5R_{\rm in}B_{\rm in}$ can be rewritten as

$$I_{\rm axis} = 5\frac{R_{\rm in}}{D}\ {\rm Ha}\ \sqrt{\mu_0\rho\nu\eta}, \tag{73}$$

where $R_{\rm in}{\rm Ha}/D$ represents a Hartmann number formed with $R_{\rm in}$ instead with D. For liquid sodium one has $\sqrt{\mu_0\rho\nu\eta} \simeq 8.2$ in cgs units. Equation (73) gives the minimum current for instability, since the numbers in Fig. 45 also hold for the Hartmann numbers which are the lowest for marginal instability.

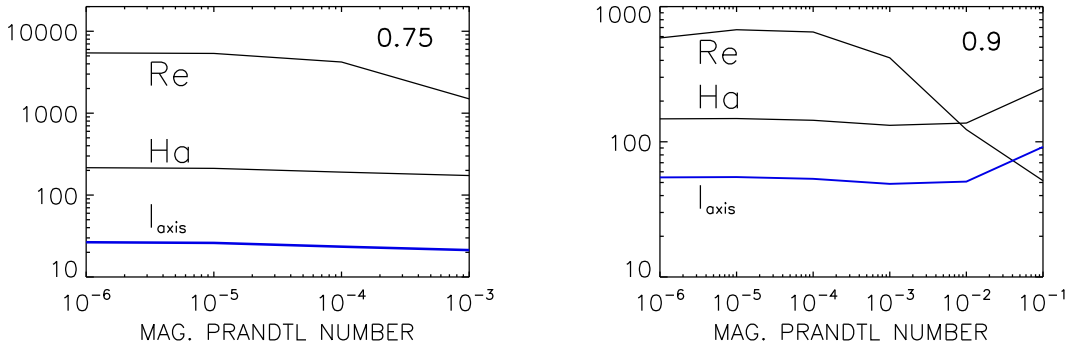

Figure 45. Minimal Hartmann numbers, the related outer Reynolds numbers and the necessary axial electric currents (in kA, along the inner rod) for two narrow-gap models with almost resting inner cylinders as functions of the magnetic Prandtl number. Solutions for Pm ≤ 1 larger than the given maximal values do not exist. Left: $\mu_B = r_{\rm in} = 0.75$, right: $\mu_B = r_{\rm in} = 0.9$. In all cases the instability appears to scale with Ha and Re for Pm $\to 0$. The necessary axial electric currents $I_{\rm axis}$ (blue lines) become smaller for wider gaps. They do not depend on the size of the container. $\mu_\Omega = 128$. Perfectly conducting boundaries.

Note how the marginal values are independent of Pm provided Pm $\ll 1$. One also finds the minimal Hartmann numbers almost independent of the gap width. The consequence is that the corresponding axial electric current decreases for wider gaps. The minimum current in the calculations is 28 kA for the gap with $r_{\rm in} = 0.8$. For wider gaps the necessary Hartmann number increases strongly, and also the necessary electric current. The linear size of the container does not influence the excitation of the instability. In all cases the critical Reynolds number of the outer cylinder (the inner-one is stationary) is of order 10^3, which should also be possible to be realized in the laboratory.

5. Chandrasekhar flows

The combination of a magnetic field $B_\phi \propto 1/R$ (current-free for $R \neq 0$) and a rotation profile $\Omega \propto 1/R^2$ (the potential flow) constitutes an example of a particular class of MHD flows defined by Chandrasekhar [100] as

$$\boldsymbol{U} = \boldsymbol{U}_{\rm A}, \tag{74}$$

or more generally,

$$\boldsymbol{U} = \mathrm{Mm}\, \boldsymbol{U}_\mathrm{A} \tag{75}$$

with the magnetic Mach number Mm taken as constant here. The radial profiles of $\boldsymbol{U}$ and $\boldsymbol{U}_\mathrm{A} = \boldsymbol{B}/\sqrt{\mu_0\rho}$ are required to be identical, but there may be a constant of proportionality between the two [101]. As shown by Chandrasekhar, all basic states satisfying (74) are stable in the absence of diffusive effects. In Section 4.1, however, we found that the potential flow can be destabilized by a toroidal magnetic field with $B_\phi \propto 1/R$ if at least one of the two molecular diffusivities ν and η is non-zero.

Taking $\Omega \propto R^{-q}$ and $B_\phi \propto R^{1-q}$ (thereby satisfying Eq. (75) with non-negative q) Michael's relation (6) yields $(2-q)\mathrm{Mm}^2 + q > 0$ as a sufficient condition for stability of the $m = 0$ mode. All Chandrasekhar states with $0 \le q \le 2$ are thus stable against axisymmetric perturbations, as any state satisfying (75) is stable. It becomes clear that the condition (6) is not a necessary condition for stability. The relations $\Omega \propto R^{-q}$ and $B_\phi \propto R^{1-q}$ defining the class of Chandrasekhar flows which we shall consider lead to

$$\mu_\Omega = r_\mathrm{in}\mu_B, \tag{76}$$

so that for $r_\mathrm{in} = 0.5$ simply $\mu_B = 2\mu_\Omega$. For the wide gap with $r_\mathrm{in} = 0.05$ and for rigid rotation the value is $\mu_B = 20$.

5.1. Inductionless approximation

Following [9, 2] we reconsider Eqs. (17) and (18) with respect to the inductionless approximation. A linearized and dimensionless version of these equations reads

$$\mathrm{Re}\left(\frac{\partial \boldsymbol{u}}{\partial t} + (\boldsymbol{U}\cdot\nabla)\boldsymbol{u} + (\boldsymbol{u}\cdot\nabla)\boldsymbol{U}\right) = -\nabla P + \Delta\boldsymbol{u} + \mathrm{Ha}^2(\mathrm{curl}\ \boldsymbol{b}\times\boldsymbol{B} + \mathrm{curl}\ \boldsymbol{B}\times\boldsymbol{b}) \tag{77}$$

and

$$\mathrm{Pm\,Re}\left(\frac{\partial \boldsymbol{b}}{\partial t} - \mathrm{curl}(\boldsymbol{U}\times\boldsymbol{b})\right) = \mathrm{curl}(\boldsymbol{u}\times\boldsymbol{B}) + \Delta\boldsymbol{b}. \tag{78}$$

The magnetic fields in these equations are normalized with characteristic B_0 of the background field. The mean flow $\boldsymbol{U}$ is normalized with a flow amplitude while the flow perturbations are normalized with η/D (with distance D). Reynolds number and Hartmann number are formed with these scales. Obviously, the limit $\mathrm{Pm} \to 0$ is only allowed for finite Re, hence the solutions within the inductionless approximation must possess finite Reynolds number. On the other hand, solutions of the linearized MHD equations which do not scale for small Pm with Re and Ha cannot possess a solution for $\mathrm{Pm} = 0$. We shall see in this section that the entire class of Chandrasekhar flows (74) possesses marginal instabilities scaling with Re and Ha for small Pm (at least for the fundamental mode $m = 1$) so that they also exist for $\mathrm{Pm} = 0$ – in great contrast to the eigensolutions of the standard MRI in Section 3 which do not exist for $\mathrm{Pm} = 0$ [25]. Also, the results of the inductionless approximation basically differ from those of the inviscid approximation. All eigensolutions which for small Pm scale with S and Rm should also fulfill the inviscid MHD equations with $\nu = 0$.

5.2. Potential flow

The potential flow with $q = 2$ under the influence of a current-free background field simultaneously belongs to the classes of Chandrasekhar flows and of AMRI. U_ϕ and B_ϕ are both proportional to $1/R$, hence $\mu_B = 2\mu_\Omega = 0.5$ for $r_\mathrm{in} = 0.5$. Stability maps (Figs. 25 and 26) show that just for this case and for $\mathrm{Pm} \to 0$ the Reynolds and Hartmann numbers for neutral stability do not depend on the magnetic Prandtl number. We show here that this particular scaling (which is the basis of the technical realization of several MHD experiments with fluid metals) is characteristic for *all* Chandrasekhar flows with (76). The potential flow with $\mu_\Omega = 0.25$ fulfills this condition and therefore scales with Re and Ha for small Pm, while quasi-Keplerian flows $\mu_\Omega = 0.35$ or quasi-uniform flows ($U_\phi \simeq$ const) with $\mu_\Omega = 0.5$ together with current-free fields ($\mu_B = 0.5$) do not fulfill this condition, resulting in a different scaling for $\mathrm{Pm} \to 0$ as known from Section 4.

Consider the dotted line in Fig. 25 (middle), which represents the location of $\underline{\mathrm{Mm}} = 1$. For different Pm it crosses the lines of neutral stability at different values of the averaged Reynolds number $\overline{\mathrm{Rm}}$. Following Chandrasekhar such solutions do not exist for ideal media with $\mathrm{Mm} = 1$. As they only exist for finite values of the diffusivities, the

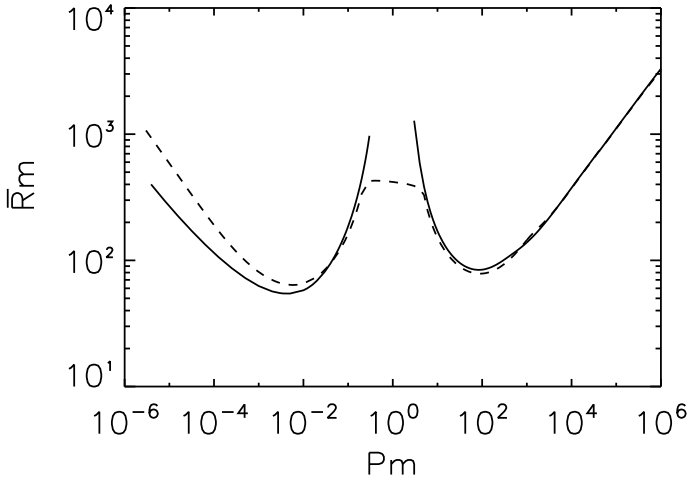

Figure 46. Potential flow: averaged Reynolds number $\overline{\mathrm{Rm}}$ of the crossing points as functions of Pm where the parameters for neutral stability fulfill the Chandrasekhar condition (75) with Mm = 1. Solid lines: perfectly conducting boundaries, dashed line: insulating boundaries. $r_{\mathrm{in}} = 0.5$, $\mu_B = 2\mu_\Omega = 0.5$, $m = 1$. From [67].

described instability is of *diffusive* nature. For small Pm the numerical values $\overline{\mathrm{Rm}}$ of the crossing points increase for decreasing Pm, which is true for the models with perfectly conducting and insulating cylinders. Both cases lead to very similar results. In the limit Pm $\to$ 0 the Hartmann numbers and $\overline{\mathrm{Rm}}$ of the crossing points scale with $\mathrm{Pm}^{-1/2}$, so that Rm and S remain finite (Fig. 46). One finds for Pm $\to$ 0 values of Rm $\simeq$ S $\simeq$ 0.8 (perfectly conducting cylinders) and Rm $\simeq$ S $\simeq$ 2 (insulating cylinders), for which solutions with Mm = 1 exist. The molecular viscosity no longer appears in the theoretical results.

In the limit Pm $\to \infty$ the opposite is true. Solutions with Mm = 1 only exist for finite values of $\mathrm{Re} = \mathrm{Ha}/\sqrt{\mathrm{Pm}}$. For Pm $\to \infty$ the averaged Reynolds number $\overline{\mathrm{Rm}}$ grows with $\mathrm{Pm}^{1/2}$, so that Re remains finite in this limit (Fig. 46). The magnetic resistivity completely drops out of the theory. Obviously, the Chandrasekhar theorem of the nonexistence of unstable solutions with Mm = 1 fails for potential flows if either of the two molecular diffusivities is non-zero.

In Section 4.1 it was also mentioned that for the potential flow the instability domain for very large Pm lies above the line Mm = 1, while for very small Pm it lies below this line. In the first case the crossing points belong to the lower branches of the instability cone while in the second case they belong to the upper branches (see Fig. 25). Figure 25 also contains the scaling laws of the lines of neutral instability for the two limits of Pm. For Pm $\to$ 0 the lines converge in the (Ha/Re) plane while for Pm $\to \infty$ they converge in the (Ha/Rm) plane. We shall demonstrate here that the Re-scaling for small Pm is a general feature of the Chandrasekhar flows but the scaling laws for Pm $\to \infty$ are more diverse. Systems with less but finite (negative) shear will scale with $\overline{\mathrm{Rm}}$ while the system with vanishing shear again changes the scaling law for large Pm (see Section 5.4).

5.3. Quasi-Keplerian flow

For the quasi-Keplerian flow within the Chandrasekhar class, Fig. 47 provides quite a similar behavior. The left panel demonstrates that for small Pm the $m = 1$ mode also scales with Ha and Re. The minimum critical Hartmann and Reynolds numbers exceed the corresponding values for the potential flow by almost one order of magnitude. The scaling with Ha and Re for small Pm differs strongly from that of the AMRI combination of quasi-Keplerian rotation ($\mu_\Omega = 0.35$) with the current-free magnetic field ($\mu_B = 0.5$), which is known to scale with Rm and S (see Section 4.2). Here the additional energy source connected with the axial electric current in the fluid determines the scaling rules for small Pm.

A serious consequence of this result that for Pm $\to$ 0 the scaling is with Re and Ha is that the instability of the $m = 1$ modes only exists for slow rotation, Mm $<$ 1 (see Fig. 47, right). Including higher m azimuthal modes, however, changes the situation. As seen in Figs. 48 and 49, the critical parameters are Re and Ha only for $m = 1$. For $m = 2$ and $m = 3$, the instabilities scale with Rm and S. As a consequence, these modes should also exist for vanishing viscosity. Figure 49 shows that for Pm $\to$ 0 the magnetic Mach number Mm = Rm/S easily exceeds unity.

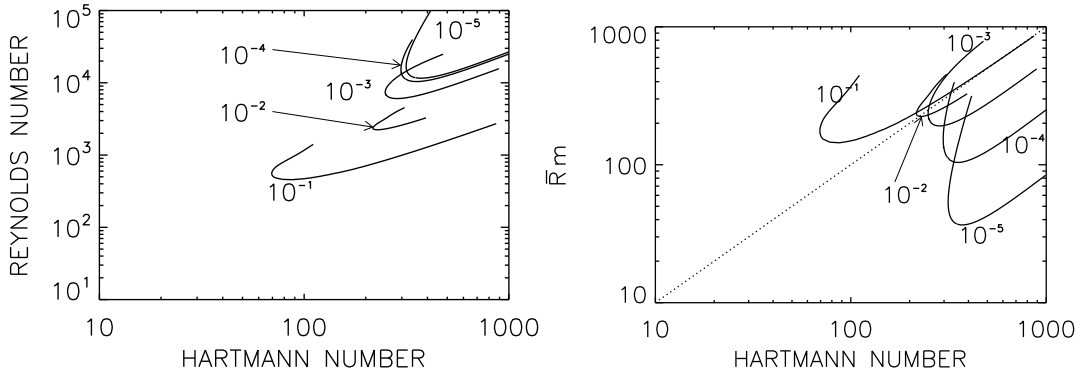

Figure 47. Quasi-Keplerian Chandrasekhar flow: lines of neutral stability in two different coordinate systems. In the (Ha/Re) plane (left) the convergence of the curves for Pm → 0 is visible. The solutions plotted in the (Ha/$\overline{\mathrm{Rm}}$) plane show that the curves for Pm → 0 lie below Mm = 1 (dotted line), they are sub-Alfvénic (right). $\mu_B = 2\mu_\Omega = 0.7$. Insulating boundaries. Adapted from [67].

The new scalings, therefore, generate astrophysical applications of these instabilities, where small Pm and large Mm are often associated.

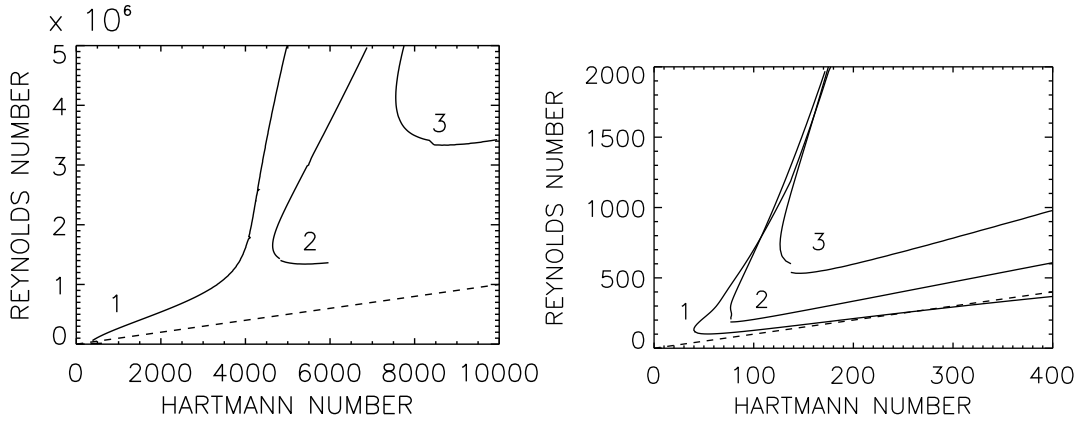

Figure 48. Neutral stability curves for quasi-Keplerian Chandrasekhar flow for Pm = 10^{-4} (left) and Pm = 1 (right). The curves are marked with their values of m. For small Pm only the $m = 1$ curve lies below the Mm = 1 line (dashed). $r_{\mathrm{in}} = 0.5$, $\mu_B = 2\mu_\Omega = 0.7$. Insulating boundaries.

The crossing points of the instability lines with Mm = 1 as a function of Pm for quasi-Keplerian flows are given for both sets of boundary conditions in Ref. [67]. In contrast to the situation for the potential flow there is no clear scaling with Rm or $\overline{\mathrm{Rm}}$ for small Pm. One finds $\mathrm{Rm} \propto \mathrm{Pm}^{1/3}$. For Pm → 0 the magnetic Reynolds number does not remain finite. There is thus no solution for $\nu = 0$ as exists for the potential flow.

Even the simplest model, with approximately uniform flow and field, belongs to the Chandrasekhar class of MHD flows which scale with Re and Ha for Pm → 0. If $\mu_B = 2\mu_\Omega = 1$, then U_ϕ and B_ϕ have the same values at both cylinders (for $r_{\mathrm{in}} = 0.5$). The magnetic profile is not current-free between the cylinders. Even without rotation the electric current thus becomes unstable against perturbations with $m > 0$ at Hartmann numbers $\mathrm{Ha}_0 = 109$ for insulating boundaries and $\mathrm{Ha}_0 = 151$ for perfectly conducting boundaries. These values do not depend on Pm [102]. This Tayler Instability will be discussed in more detail in Section 7. The left panel of Fig. 50 also shows an extra instability domain for rapid rotation which has no direct connection to Ha_0. It can thus not be due to the instability of electric current; indeed, the magnetic profile of $\mu_B = 1$ also contains the profile $1/R$ which is responsible for AMRI. This AMRI domain (with Mm > 1) is easily visible in Fig. 33, which also shows that for Pm ≪ 1 the necessary Reynolds numbers for AMRI are too high for Fig. 50. The two instabilities are separated by a stable branch with Mm ≃ 1, where the differential rotation has a stabilizing effect. The extension of the stable branch depends strongly on the boundary conditions. It is very long – possibly infinitely long – for perfectly conducting boundaries, but rather

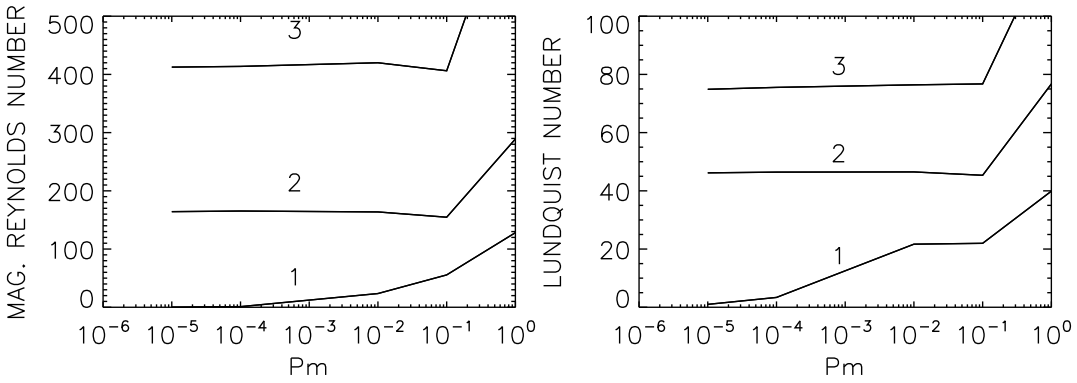

Figure 49. Minimal Rm (left) and S (right) of the neutral stability curves in Fig. 48. The main result is that for Pm → 0 the $m > 1$ lines scale with Rm and S, unlike the $m = 1$ lines which scale with Re and Ha. The solution with the lowest Reynolds and Hartmann numbers is always $m = 1$. The modes with positive and negative m are degenerate. For small Pm the instability is superAlfvénic only for the modes $m > 1$.

short for insulating ones (Fig. 50). Even for perfectly conducting cylinders the stable branch disappears for small Pm ≠ 1.

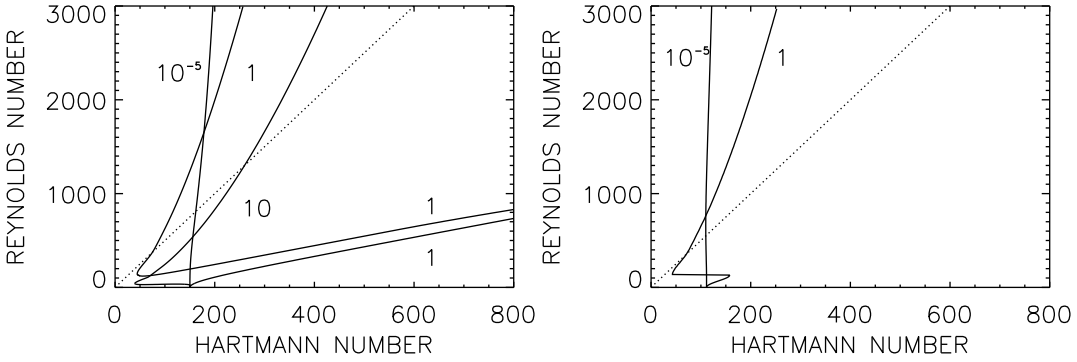

Figure 50. Quasi-uniform background flow for perfectly conducting boundaries (left) and insulating boundaries (right) for various Pm. The lines for Pm = 10^{-5} are valid for all Pm ≲ 0.01. Background flow U_ϕ and background field B_ϕ are approximately uniform. For Pm = 1 the dotted lines represent Mm = 5. $m = 1$, $r_{\rm in} = 0.5$, $\mu_B = 2\mu_\Omega = 1$.

Very slow rotation stabilizes the system slightly, but for faster rotation (Mm ≳ 1) and Pm ≳ 1 the instability becomes subcritical, i.e. it onsets for smaller Hartmann numbers than it does without rotation (Ha < Ha_0). The phenomenon of subcritical excitation for large Pm is very characteristic for Chandrasekhar-type flows. It only appears for slow rotation and Pm ≲ 1. The resulting stable branch around the line Mm = 1 is also characteristic for this sort of stability map. It separates the region of the TI (for slow rotation) from the region of the AMRI (due to differential rotation). This separation effect does not exist for rigid rotation. As expected for Mm ≫ 1 the strong differential rotation suppresses the nonaxisymmetric instability pattern, but again the effect is small for small Pm.

It remains to clarify the asymptotic behavior of the stability lines of the $m = 1$ mode for large Pm. We shall find a substantial discrepancy between the instability domains for small and large magnetic Prandtl numbers. While for small Pm the curves converge in the (Ha/Re) plane, for large Pm they converge in the (Ha/$\overline{\mathrm{Rm}}$) plane (Fig. 51, left). Since Mm = $\overline{\mathrm{Rm}}$/Ha, it is obvious that for large Pm the instability also exists for large magnetic Mach numbers. Rapid rotation does not suppress the instability in this case. For large Pm combinations of Reynolds and Hartmann numbers with Mm > 1 also become unstable, which is not the case for very small Pm. Another consequence is that for a fixed Hartmann number the critical Reynolds numbers behave like Re ∝ $\mathrm{Pm}^{-1/2}$ for Pm → ∞, so that the magnetic Reynolds number increases as Rm ∝ $\mathrm{Pm}^{1/2}$ for large Pm. The drift rates also depend on the magnetic Prandtl numbers. Figure 51 (left) shows these to be negative for Pm ≥ 1 and positive for Pm ≪ 1.

An exception from this rule, however, is given by the potential flow with $\mu_B = 2\mu_\Omega = 0.5$ which in Section 4.1

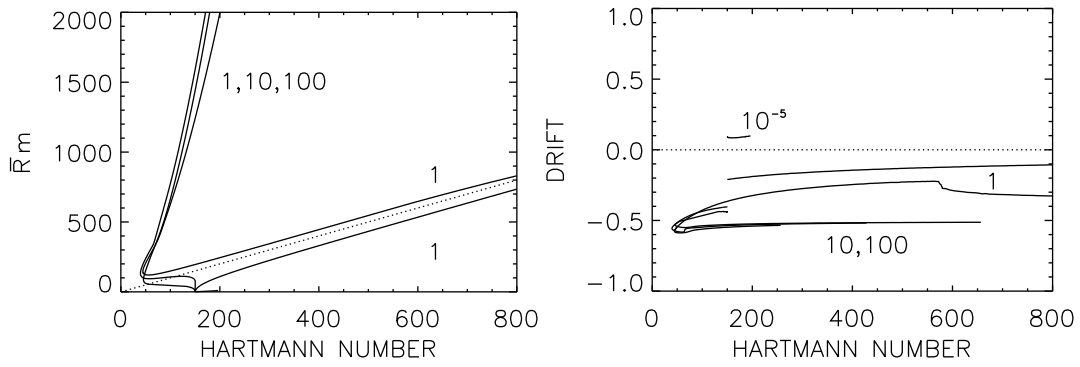

Figure 51. Neutral stability curves (left) and drift rates $\omega_{\rm dr}$ (right) for quasi-uniform field and for large Pm (marked). For Pm $>$ 1 the curves converge in the (Ha/$\overline{\rm Rm}$) plane. The sign of $\omega_{\rm dr}$ differs for small and large Pm, changing for Pm $\simeq$ 0.1. $m = 1$, $r_{\rm in} = 0.5$, $\mu_B = 2\mu_\Omega = 1$. Perfectly conducting boundaries.

has been discussed as a prominent application of AMRI. The result was that the stability lines of the potential flow converge for Pm $\to \infty$ in the (Ha/Rm) plane (Fig. 25) so that the stability curve scales for large Pm with the magnetic Reynolds number Rm rather than with the average Reynolds number $\overline{\rm Rm}$.

The profile $\Omega \propto 1/R$ characterizes the rotation of galaxies in their outer parts. If it is further assumed that their azimuthal fields are approximately uniform in this region, then Chandrasekhar states with $\mu_B = 2\mu_\Omega = 1$ may well apply to galaxies. The axial component of the magnetic field is maximally 10% of the azimuthal field. Also typical for galaxies is the relation Mm $\simeq$ 5, as given in Fig. 50 (right) by a dashed line. This line is located almost everywhere to the right of the instability lines for Pm $\lesssim$ 1, so that galactic fields together with the rotation according to $U_\phi \simeq$const should develop nonaxisymmetric magnetic perturbations[4].

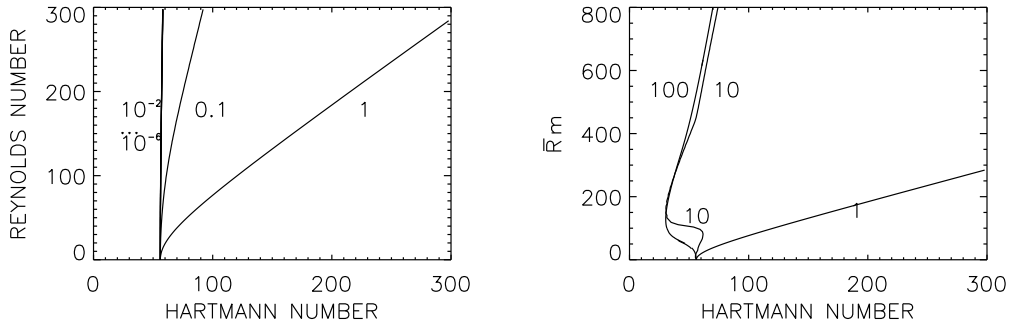

Figure 52. Stability curves for the Chandrasekhar flow system between the quasi-uniform field with $\mu_B = 1$ and the pinch-type system with $\mu_B = 2$. The different scaling rules are clearly demonstrated. For Pm $\to$ 0 the curves converge in the (Ha/Re) plane (left) while for Pm $\to \infty$ the curves converge in the (Ha/$\overline{\rm Rm}$) plane (right). $m = 1$, $r_{\rm in} = 0.5$, $\mu_B = 2\mu_\Omega = 1.5$. Perfectly conducting boundaries.

Figure 52 also demonstrates the general scaling laws for the Chandrasekhar flow between the combination with the potential flow and current-free fields ($\mu_B = 0.5$) and that of the rigidly rotating z-pinch with $\mu_B = 2$. The critical Hartmann number for TI without rotation is $\rm Ha_0 = 57$ for all Pm and for perfectly conducting boundaries. The plotted curves converge for small Pm in the (Ha/Re) plane (left panel) and they converge for large Pm in the (Ha/$\overline{\rm Rm}$) plane (right panel) – as is also true for $\mu_B = 2\mu_\Omega = 1$ (Figs. 50 and 51). It is thus clear that between the rotation laws $\Omega \propto 1/R^2$ and Ω = const the Chandrasekhar flows (75) indeed scale in the described sense for small and large Pm.

[4]Estimates for galaxies are Re $\simeq$ 1000, Ha $\simeq$ 200 and Pm $\simeq$ 1, the latter due to the interstellar turbulence.

5.4. Rigidly-rotating z-pinch

Even rigid-body rotation with $\mu_\Omega = 1$ can be a prominent example of the Chandrasekhar theorem, provided that the associated magnetic profile also satisfies the condition (76). This implies a uniform current throughout the entire region $R < R_{\rm out}$, known as a z-pinch configuration in plasma physics. Any resulting instability is purely current-driven. Such instabilities can occur for Re = 0 but not for Ha = 0. A nonrotating pinch is only unstable against nonaxisymmetric perturbations with $m = 1$ [12]. Acheson showed that the *necessary* condition for magnetic instability with $m > 1$ is not fulfilled for this flow [99]. This finding remains true for rigid rotation: we found no unstable modes with $m > 1$. For rigidly rotating Taylor-Couette flows in a wide gap with $B_\phi \propto R$ global calculations provided stability in the inviscid approximation [103].

The stability curves for $m = 1$ are shown in Fig. 53 for conducting and insulating boundary conditions. The curves basically differ from the former examples as the characteristic minima no longer exist. They also demonstrate the stabilizing effect of rigid rotation on the Tayler instability [104], which is strongest for Pm = 1. In this representation the rotational suppression becomes weaker for smaller and larger magnetic Prandtl numbers. In the (Ha/Re) plane the curves converge for Pm $\to$ 0, hence the eigenvalues also scale with Re and Ha. We find that for all models along the Chandrasekhar sequence in the (Ha/Re) plane the lines of marginal stability for $m = 1$ do not depend on Pm for sufficiently small Pm. The magnetic Mach number

$$\mathrm{Mm} = \sqrt{\mathrm{Pm}}\,\frac{\mathrm{Re}}{\mathrm{Ha}} \tag{79}$$

of the solutions for small Pm remains smaller than unity. A rotating pinch with small Pm and Mm > 1 is always stable.

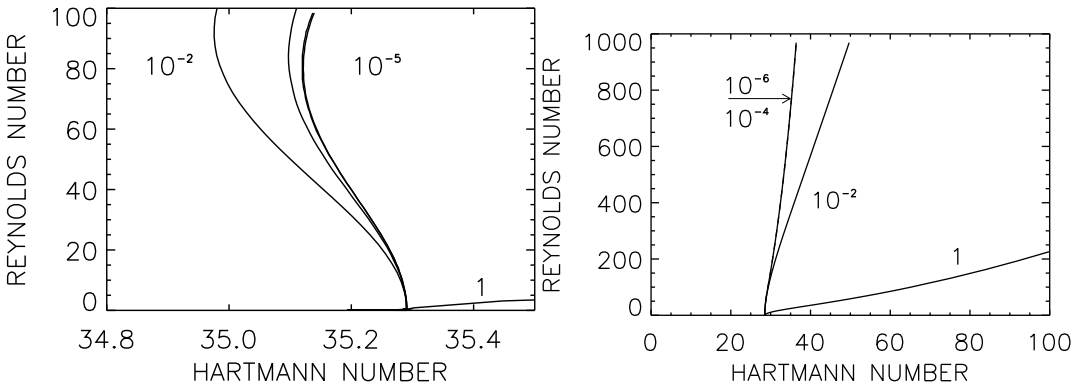

Figure 53. Stability maps of the only unstable mode $m = 1$ for the rigidly rotating z-pinch for perfectly conducting (left) and insulating (right) boundaries. The curves are marked with Pm; they converge for Pm $\to$ 0 and for Pm $\to \infty$ (see Fig. 87). The two (different)values of Ha_0 for Re = 0 do not depend on Pm. $r_{\rm in} = 0.5$, $\mu_B = 2\mu_\Omega = 1/r_{\rm in}$.

Figure 53 also illustrates the influence of the boundary conditions. Perfectly conducting cylinders yield $\mathrm{Ha}_0 = 35.3$, whereas insulating cylinders yield $\mathrm{Ha}_0 = 28.5$. For the conducting boundary conditions a supercritical excitation for slow rotation is clearly visible, $\mathrm{Ha} < \mathrm{Ha}_0$, but only if Pm $\neq$ 1. The solutions for Pm = 1 only show the phenomenon of rotational suppression for all Reynolds numbers, while for Pm $\neq$ 1 the suppression only exists for sufficiently rapid rotation. Without rotation $\omega_{\rm dr} = 0$ always holds, and the pattern is stationary in the laboratory system. For the rotating pinch the instabilities drift in the rotation direction for Pm $\geq$ 1, but in the opposite direction for Pm < 1. For Pm $\to \infty$ the lines in the right panel of Fig. 53 converge slightly below the line for Pm = 1 (see Fig. 85, below). We have thus the exceptional situation that both the limits for very small and very large Pm appear in one and the same coordinate system. The consequences of this phenomenon are described in Section 8.2.

One may ask whether the rotational stabilization can also be probed in the laboratory. A rigidly rotating wide pinch with $r_{\rm in} = 0.05$ and $\mu_B = 1/r_{\rm in}$ with insulating cylinders is thus considered for the small magnetic Prandtl numbers of liquid metals. The Chandrasekhar condition (76) is fulfilled with rigid rotation ($\mu_\Omega = 1$). Without rotation

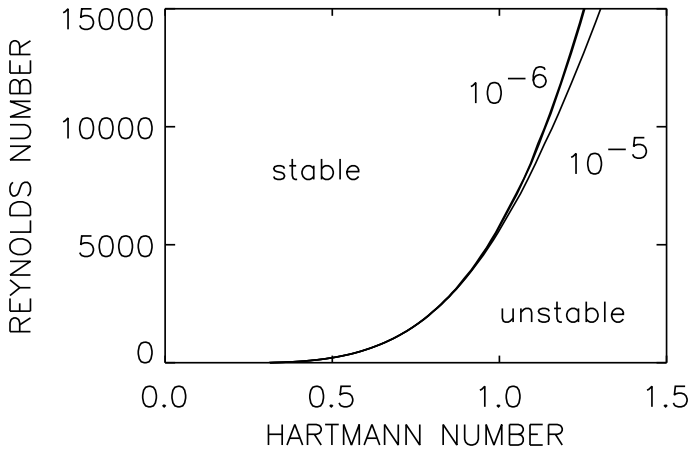

Figure 54. A rigidly rotating z-pinch in a wide gap for small Pm (marked). Note the convergence of the curves in the (Ha/Re) plane for small Pm. The Hartmann number (39) is formed with the inner magnetic field (see text). $m = 1$, $\mu_B = 1/r_{\rm in}$, $\mu_\Omega = 1$, $r_{\rm in} = 0.05$. Insulating boundary conditions.

the inner critical Hartmann number after (39) is $\mathrm{Ha}_0 = 0.31$ for this container[5], independent of Pm. We find the rotational stabilization is rather weak for not too fast rotation (Fig. 54). The figure also perfectly shows the scaling of the eigenvalues in the (Ha/Re) plane which is typical for the Chandrasekhar MHD flows. For a Reynolds number $\mathrm{Re} \simeq 10^3$ the supercritical magnetic field needed for instability is (only) two times larger than Ha_0. It should thus easily be possible to find the basic effect of the rotational suppression of the pinch-type instability in the laboratory. The constellation analyzed by Fig. 54 forms an ideal experimental setup for studies of the instability characteristics of a Chandrasekhar-type MHD flow.

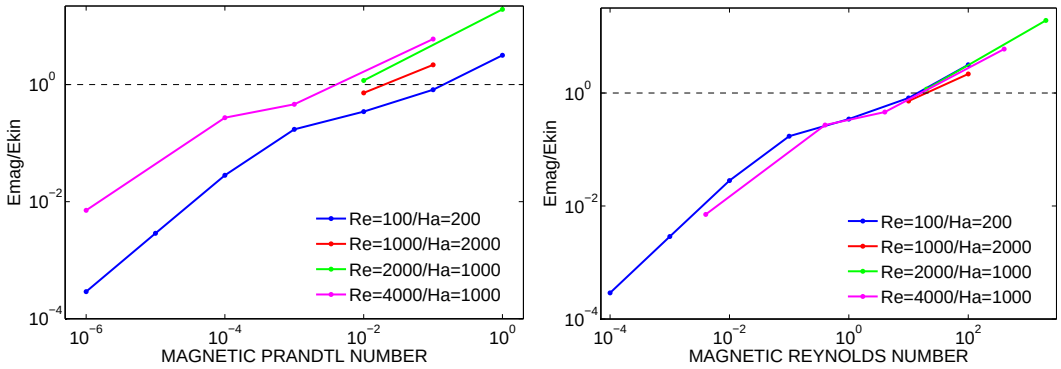

Figure 55. Energy ratio (58) for several models of the rigidly rotating z-pinch. Left: ε as a function of Pm. Right: ε as a function of Rm. The models show equipartition of the two energies only for $\mathrm{Rm} \simeq 20$. Dominating magnetic energy requires higher magnetic Reynolds numbers. $r_{\rm in} = 0.5$, $\mu_B = 2\mu_\Omega = 2$.

5.5. *Energies and cross-helicity*

For the energy ratio ε of magnetic to kinetic energy one finds similar properties as for the potential flow. For the latter it is known that the ratio of the energies is small for small Rm (Fig. 31). The same is true for the rigidly rotating z-pinch. Figure 55 demonstrates the numerical finding that ε of the pinch scales with Rm. Almost independent of Pm, ε exceeds unity only for $\mathrm{Rm} \gtrsim 20$, or in other words, if the numerical product of Re and Pm exceeds about 20. The same result also holds for the Chandrasekhar flow with quasi-Keplerian rotation [105].

[5] with outer values after definition (85) it is 28.4.

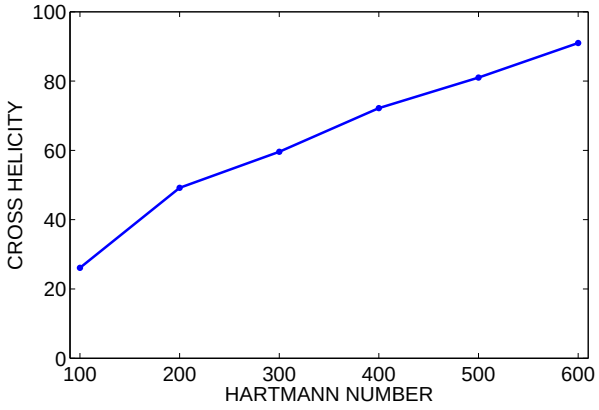

Figure 56. Cross-helicity in a rigidly rotating pinch, measured in units of $\nu B_{\rm in}/R_0$. Re = 200, $\mu_B = 2\mu_\Omega = 2$, $r_{\rm in} = 0.5$, Pm = 0.1.

For the rotating pinch the pseudo-scalar $\boldsymbol{\Omega}\cdot\boldsymbol{J}$ should exist, linear in the magnetic field. The question is whether the *cross-helicity* $\langle \boldsymbol{u}\cdot\boldsymbol{b}\rangle$ becomes non-zero in the fluid. For the stationary pinch the cross-helicity must vanish identically. Indeed, the numerical simulations for the rotating pinch provide the surprisingly simple result that for weak fields

$$\langle \boldsymbol{u}\cdot\boldsymbol{b}\rangle = h_{\rm cross}{\rm Ha}\; U_{\rm in}B_{\rm in}, \tag{80}$$

(with $U_{\rm in} = R_0\Omega_{\rm in}$). This result has been tested for several combinations of low values of Re and Ha. One finds from the linear part of the curve in Fig. 56 that $h_{\rm cross} \simeq 1.3\cdot 10^{-3}$, almost independent of the magnetic Prandtl number. The parallel components of the flow and field fluctuations are correlated due to the Coriolis force. Only the global rotation generates such a correlation averaged over the entire container. The expression (80) is symmetric in the dissipation coefficients ν and η via the Hartmann number. Being linear in Ha, the relation (80) is only valid for not too large Ha. For stronger fields the numerical coefficient $h_{\rm cross}$ is magnetically suppressed. The robustness of the result (80) also shows that the cross-helicity is not a consequence of the initial conditions, which could potentially have been the case as cross-helicity is conserved in ideal fluids [106].

5.6. Azimuthal spectra

For the rigidly rotating pinch only $m = 1$ is unstable, but the energy is nonlinearly transferred to modes with higher wave numbers. Figure 57 shows the resulting power spectra of this model for fixed Reynolds and Hartmann numbers but various magnetic Prandtl numbers. The Mach number varies between Mm = 0.2 for Pm = 0.01 and Mm = 2 for Pm = 1. Only the mode $m = 1$ provides the energy to initiate the nonlinear cascade so that the spectrum is rather steep. Neither the Iroshnikov-Kraichnan spectrum ($m^{-3/2}$, [106]) nor the Kolmogorov spectrum ($m^{-5/3}$, [107]) fit the resulting curves. A scaling m^{-2} that is found in forced turbulence [108] comes much closer.

It is typical for the magnetic instability that only the modes with the lowest $m \neq 0$ become unstable for finite Ha and Re. The rotating pinch gives an example where only a single linearly unstable mode ($m = 1$) injects the energy into the system. For the AMRI with $\mu_B = 2\mu_\Omega = 0.5$ modes with higher m also become unstable. For given Ha and Re the number of unstable modes decreases for decreasing magnetic Prandtl number. This is a consequence of the fact that for AMRI all azimuthal modes scale with Re and Ha for Pm $\to$ 0. Figure 57 (right) shows the kinetic and magnetic energies for all modes m for a fixed magnetic field with Ha = 600 and the high Reynolds number of Re = 10,000, but for several Pm. The magnetic and kinetic spectra have a similar shape, but they are only close together for large Pm. For small Pm the magnetic spectrum lies below the kinetic one. For Pm of order unity the spectrum is rather flat on the low m side, and rather steep for small Pm.

It is also obvious that the spectra for the kinetic and magnetic fluctuations have similar shapes. If a power law is fitted, both would slightly favor the Iroshnikov-Kraichnan spectrum compared with the Kolmogorov spectrum, but the differences are not significant. Although the Iroshnikov-Kraichnan profile is favored for MHD turbulence [109], Kolmogorov-like spectra are also known from the measurements of turbulence in the solar wind [110], as well as the result of 3D MHD simulations [111]. Often, however, the direct numerical simulations are done for Pm of order unity [68]. A clear preference between Iroshnikov-Kraichnan and Kolmogorov scaling cannot be made.

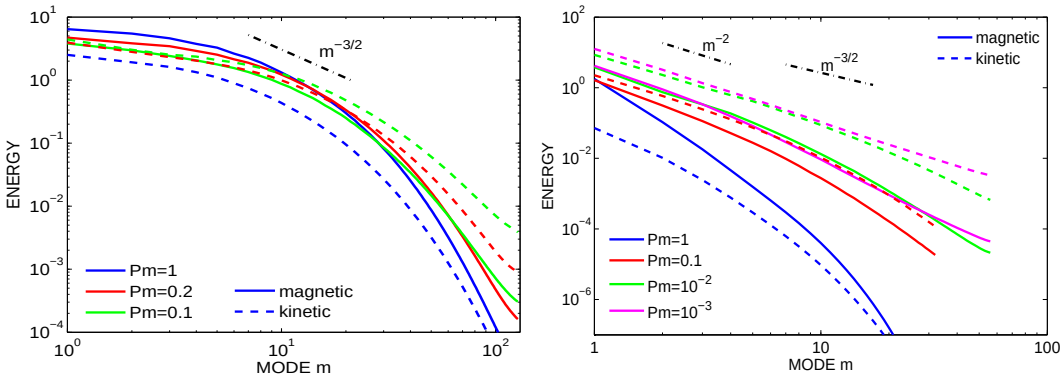

Figure 57. The azimuthal spectra of the magnetic fluctuations (solid lines) and kinetic fluctuations (dashed lines) for several Chandrasekhar flows. Left: potential flow ($\mu_B = 2\mu_\Omega = 0.5$) with Re = 10,000 and Ha = 600. Right: a rigidly rotating z-pinch ($\mu_B = 2\mu_\Omega = 2$) with Re = 1000 and Ha = 1000. The spectra are very similar. Insulating boundary conditions.

6. Helical MagnetoRotational Instability (HMRI)

To study the stability of fields which simultaneously possess axial and azimuthal components in the presence of differential rotation is insofar interesting as the fundamental modes with axial field are axisymmetric while those with azimuthal current-free fields are nonaxisymmetric. The first question concerns the symmetry type of the instability of such helical (or better: twisted) fields with a preferred handedness. It has been shown that possible instabilities of helical background fields can never be stationary so that a possible axisymmetric mode must travel along the rotation axis [112, 113]. For helical background fields the symmetry of the problem is changed so that z and $-z$ are no longer equivalent. One can speculate to utilize this axial drift to observe the instability in a laboratory experiment. To this end it would be important to know the oscillation frequency and its dependence on basic parameters such as the β describing the inner value $B_{\rm in}$ of the azimuthal field normalized with the uniform vertical field, i.e.

$$\beta = \frac{B_{\rm in}}{B_0}. \tag{81}$$

The numerical value of β gives the angle between the field line and the axial direction. Almost axial fields possess only small values of β. The following examples mainly concern the right-handed twisted magnetic field with $\beta = 2$ where the axial and the azimuthal field components are of the same order. The Hartmann numbers are now formed with the *axial field amplitude* B_0 (only for the exceptional case of $\beta = \infty$ is the toroidal field $B_{\rm in}$ used). The geometry of the mixed field instability modes can be described via the relations (51) and

$$\left.\frac{\partial z}{\partial t}\right|_\phi = -\frac{\omega_{\rm dr}}{k}, \tag{82}$$

which describes the phase velocity in the axial direction of the modes at a fixed azimuth. The wave is traveling upwards if the real part of the eigenfrequency, $\omega_{\rm dr}$, is negative.

The wave numbers k and m are both real values, and without loss of generality one of them, e.g. k, can be taken as positive. Then m must be allowed to have both signs. The sign of β fixes the spiral geometry of the background field with respect to the rotation axis. If the axisymmetric background field possesses positive B_z and B_ϕ (as mostly used for the calculations here) then it forms a right-hand spiral.

The introduction of the new parameter β makes the situation complex. In the present section we thus only consider azimuthal fields which are current-free in the fluid between the cylinders, i.e. $\mu_B = 0.5$ for $r_{\rm in} = 0.5$. The cylinders always form perfectly conducting boundaries. The only exception is Fig. 60, where for a demonstration of scaling laws for small Pm an almost uniform azimuthal magnetic field is considered.

We must also question the scaling of the results for small magnetic Prandtl number. From the foregoing sections we know that the MRI scales with Rm and S for Pm $\to$ 0. The consequence is that the ordinary Reynolds number

cannot remain finite for Pm → 0. The same is true for the AMRI with vanishing axial electric current within the non-potential flows. We should thus expect that the HMRI also scales with Rm and S for Pm → 0. However, all models of the Chandrasekhar-type with $\boldsymbol{U} = \boldsymbol{U}_\mathrm{A}$ scale with Re and Ha for Pm → 0. It is thus an open question how the eigenvalues for decreasing Pm behave for HMRI of the *potential flow*. Another prominent example is the Chandrasekhar-type flow with $\mu_B = 2\mu_\Omega = 1$ describing a rotation law with almost uniform azimuthal flow U_ϕ and azimuthal field B_ϕ.

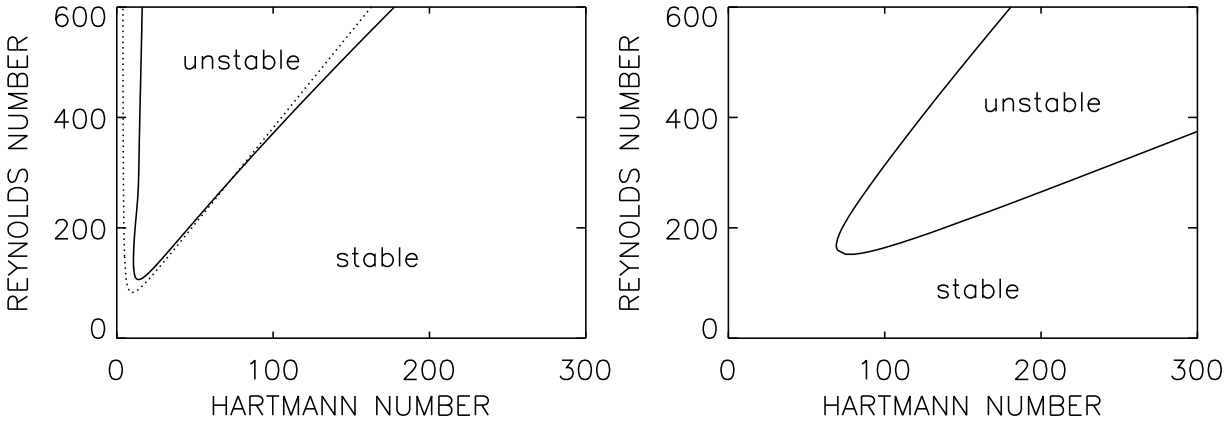

Figure 58. Stability maps for magnetorotational instabilities for quasi-uniform flow ($U_\phi \simeq$ const) with uniform axial fields (MRI, left) and with current-free azimuthal fields (AMRI, right), $\mu_B = r_\mathrm{in}$. Note the different definitions of the Hartmann numbers: Eq. (14) for the left panel and Eq. (39) for the right panel. Solid lines: $m = 1$, dotted line: $m = 0$. The slopes dRe/dHa of the solid lines ($m = 1$) are positive in both cases but they are not for the dotted line ($m = 0$). The modes with the lowest Reynolds numbers are axisymmetric for MRI and nonaxisymmetric for AMRI. $\mu_\Omega = r_\mathrm{in} = 0.5$, Pm = 1.

6.1. From AMRI to HMRI

We start with the stability of the flow $U_\phi \simeq$ const in the presence of a purely axial field. In this case both axisymmetric and nonaxisymmetric modes may be excited, with the axisymmetric $m = 0$ mode being the one with the lowest Reynolds number (Fig. 58, left). For Pm = 1 this overall minimum occurs for Ha ≃ 10 and Re ≃ 80. For larger Ha there is a switch to $m = 1$ being the mode with the lowest Reynolds number. The axisymmetric mode only dominates for weak fields, but including also the global minimum Re value. It also dominates the weak-field branch of the instability curve. This branch of the axisymmetric instability curve tilts to the left, whereas the strong-field branch tilts to the right. For the nonaxisymmetric mode both branches tilt to the right, forming a characteristic tilted cone. A purely azimuthal field without electric currents between the cylinders and subject to the same rotation law yields an instability for $m = 1$ for Ha ≳ 80 and Re ≳ 150 (Fig. 58, right). Both the upper and lower branches of the instability curve tilt to the right. For a given Hartmann number, the instability therefore only exists within a finite range of Reynolds numbers.

Figure 59 (left) shows the results for the combination of azimuthal and axial fields with $\beta = 2$. One finds the same general pattern as before: only the weak-field branch of the $m = 0$ mode tilts to the left; both branches of all nonaxisymmetric modes tilt to the right. Up to Ha ≈ 50 the axisymmetric mode is preferred, just as before for the standard MRI. For Ha > 50 the $m = 1$ spiral is preferred. Note also that the minimum Hartmann number for excitation is much smaller than for fields with $B_0 = 0$.

Obviously, the (axisymmetric) MRI and the (nonaxisymmetric) AMRI are basic elements both influencing the excitation conditions if the background field has a twisted geometry. More specifically, one finds that the weak-field branch of the instability in Fig. 59 is very similar to the weak-field branch of the MRI, while the strong-field branch resembles the strong-field branch of AMRI. The absolute minimum values of the Reynolds and Hartmann numbers always belong to the axisymmetric mode. The similarity of the instability maps in Fig. 59 for Pm = 1 and Pm = 0.01 also indicates that the HMRI scales with Rm and S for Pm → 0. This finding remains true if the background field satisfies the condition (76) for Chandrasekhar MHD flows. Figure 60 demonstrates that the instability lines of this *axisymmetric* mode for this magnetic configuration converge in the (S/Rm) plane for Pm → 0 and in the (Ha/Re)

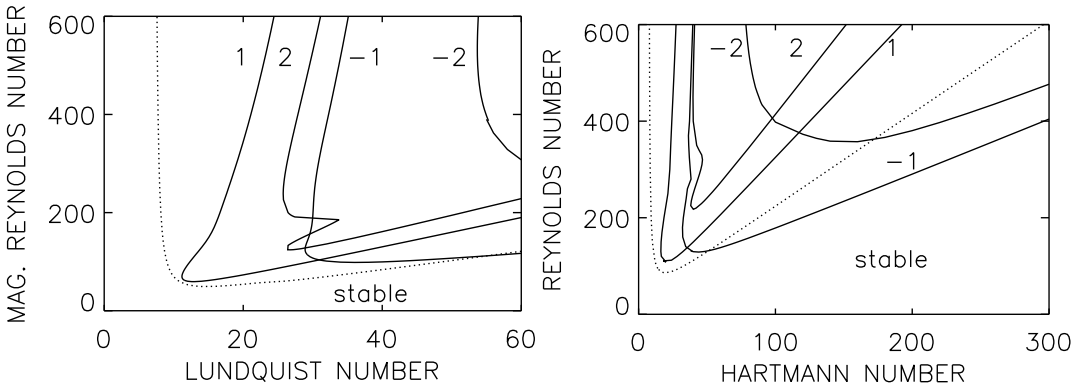

Figure 59. Critical magnetic Reynolds numbers for excitation of HMRI modes with $\beta = 2$ for various m. Pm = 0.01 (left) and Pm = 1 (right). The background field is current-free ($\mu_B = r_{\rm in}$) and the flow is quasi-uniform ($\mu_\Omega = r_{\rm in}$). Negative m describe right-hand spirals, positive m describe left-hand spirals and the dotted lines represent $m = 0$. Note that Lundquist and Hartmann numbers are formed with the axial field B_0 in (14). $r_{\rm in} = 0.5$. Perfectly conducting cylinders. From [114].

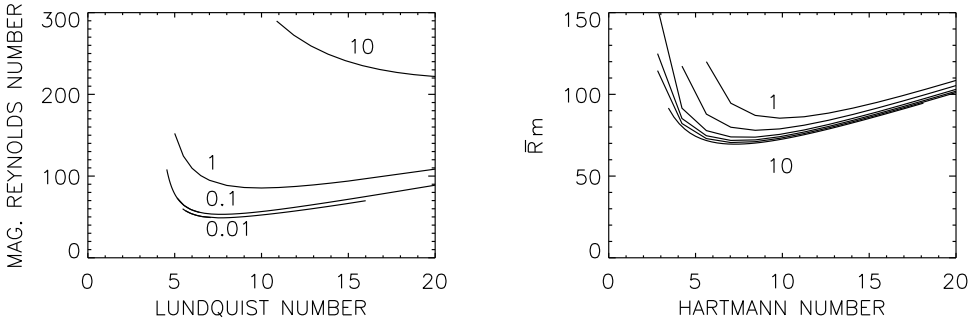

Figure 60. Stability maps of the axisymmetric perturbations for background fields with $\beta = 2$ for small Pm (left) and for large Pm (right). The curves are marked with the values of Pm. The result is that the HMRI models fulfill the same scaling laws as MRI (see Figs. 13 and 14). $r_{\rm in} = 0.5$, $m = 0$, $\mu_B = 2\mu_\Omega = 1$. Perfectly conducting boundary conditions.

plane for Pm $\to \infty$. This scaling rule of the eigenvalues for $m = 0$ in the presence of axial fields is *opposite* to the rules of Chandrasekhar-type flows for $m = 1$ without any axial field. Obviously, the helical structure of the total background field changes the scaling rules in the sense as they exist for MRI. The fields in Figs. 59 and 60 only differ by the parameter μ_B. In the second case the azimuthal field is of Chandrasekhar-type and in the first case it is not. In both cases, however, the scaling for small Pm is that of the MRI, which makes experiments with liquid metals so challenging. Consequently, the two branches of each curve in Fig. 60 have opposite slopes: the weak-field branch goes to the left while the strong-field branch goes to the right (which is also typical for the axisymmetric modes of MRI rather than for AMRI). Generally, for background fields forming a right-hand spiral ($\beta > 0$) the left-hand modes ($m > 0$) require a lower Hartmann numbers for their excitation.

Another key phenomenon is the different character of the eigenfrequencies: MRI is stationary, AMRI drifts in azimuthal direction, but the HMRI drifts in z as a necessary consequence of the $\pm z$ symmetry-breaking. The oscillatory nature of the axisymmetric HMRI is reflected by the finite values of the drift frequency $\omega_{\rm dr}$ for $m = 0$. They have the same sign as the parameter β (Fig. 61). Positive β generate positive $\omega_{\rm dr}$ (downwards traveling) and vice versa. Vanishing β leads to $\omega_{\rm dr} = 0$, i.e. to stationary axisymmetric instability patterns. The drift rates for $m = 0$ (axial migration) are very low while for the nonaxisymmetric modes (azimuthal migration) they are large and negative for $\beta = \pm 2$.

Note that for all m and all β the migration frequencies (54) of the nonaxisymmetric modes have very similar negative values, which means that all modes approximately corotate with the inner cylinder. They are much higher

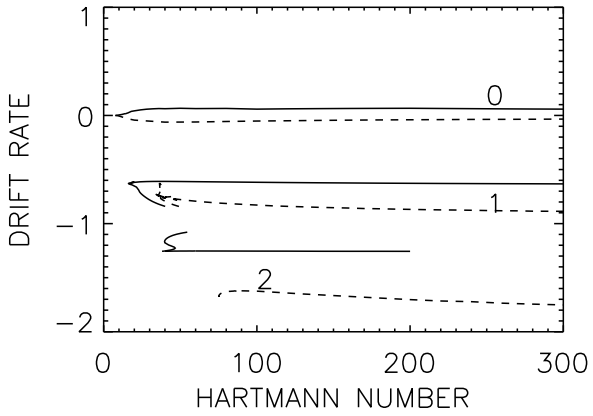

Figure 61. Drift rates $\omega_{\rm dr}$ for $\beta = 2$ (solid) and $\beta = -2$ (dashed) for the models of Fig. 59 (right). The curves are marked with the azimuthal wave numbers m. $m = 0, 1, 2$. The axisymmetric modes possess small $\omega_{\rm dr}$ of same sign as β leading to upward or downward axial pattern migration. The negative $\omega_{\rm dr}$ of the nonaxisymmetric modes leads to azimuthal migration in positive ϕ-direction.

than the frequency of the axial drift. The negative values demonstrate that all nonaxisymmetric instability patterns migrate in the positive ϕ direction. They exceed the value $\mu_\Omega = 0.5$ (the rotation rate of the outer cylinder in the laboratory system) so that they are always overtaking the outer cylinder. One may assume that the drift rates of the nonaxisymmetric modes are due to the rotation rates while the axial-traveling frequency scales with the viscosity frequency which is here only 1% of the global rotation.

A direct consequence of the $\pm z$ symmetry-breaking, and the associated axial drift of the axisymmetric HMRI modes, is that the distinction between convective and absolute instabilities becomes important, especially in axially unbounded cylinders. Convective instabilities are disturbances that grow only in a reference frame moving with the perturbation, whereas absolute instabilities grow even at a fixed point in space, as the perturbation drifts past. Absolute instability is thus a more restrictive condition than convective instability. Correspondingly, the analysis of [115, 116], in which the axial wavenumber k is allowed to be complex, shows that the absolute HMRI exists in a somewhat narrower parameter range than the convective HMRI. The basic scalings and transitions between scalings remain the same though. See also [117], who computed fully nonlinear solutions in background fields that varied periodically on very long axial wavelengths, and found absolute and convective instabilities to behave similarly even in the nonlinear regime. All nonlinear calculations in axially bounded cylinders are automatically also computing absolute rather than convective instabilities.

6.2. Potential flow and beyond

Figure 60 demonstrates that a helical field with $\mu_B = 2\mu_\Omega = 1$ (Chandrasekhar-type in the azimuthal plane) with a uniform axial magnetic component becomes unstable for eigenvalues Rm and S which are independent of Pm for small Pm. MRI and AMRI for this flow also scale with Rm and S for small Pm. As the potential flow in the presence of current-free fields also belongs to the class of Chandrasekhar flows with $\mu_B = 2\mu_\Omega = 0.5$, it is thus expected that the combination with a uniform axial field also scales with Rm and S for small Pm. The calculations do not confirm this expectation. The explanation of the low-Re and low-Ha phenomenon for the potential flow in the presence of axial fields is not based on the fact that the current-free azimuthal field together with the potential flow belongs to the class of Chandrasekhar MHD flows.The transition of HMRI with $\beta \neq 0$ from the potential flow to the quasi-Keplerian flow will now be discussed.

Figures 62 give a detailed insight into how the critical Reynolds number, Hartmann number and wave number behave for small Pm for the potential flow and beyond. Standard MRI is described by $\beta = 0$; immediately beyond the Rayleigh limit its critical Reynolds number jumps to values of 10^6 (not shown). This is no longer true for finite β. For β of order unity the Reynolds number takes much lower values at and close the Rayleigh line. For $\beta = 2$ and for (say)

$\mu_\Omega = 0.27$ (within the hydrodynamically stable area) low values for Re $\simeq$ $O(10^3)$ and Ha $\simeq O(10)$ are sufficient to excite the HMRI. Such values can easily be realized in the MHD laboratory by use of sodium or GaInSn as the fluid.

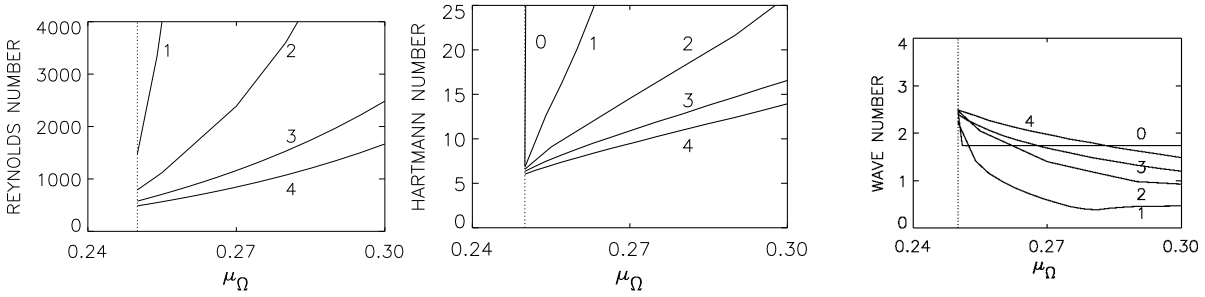

Figure 62. Critical Reynolds numbers (left), critical Hartmann numbers (middle) and the corresponding wave numbers (right) of the axisymmetric modes for various β and close to the Rayleigh line. The cells prove to be always elongated in axial direction. $r_{\rm in} = 0.5$, $\mu_B = r_{\rm in}$ (vacuum field), Pm $= 10^{-5}$, perfectly conducting cylinders. From [118].

Extensive numerical simulations for axially periodic boundary conditions and perfectly conducting cylinders have been done in the quasistationary approximation Pm = 0 for axisymmetric perturbations, based on the code developed and described by [11]. For infinite cylinders and for $\mu_\Omega = 0.27$ the flow is always hydrodynamically stable, but with external twisted magnetic field with $\beta = 4$ it loses its stability for the small Reynolds number $\mathrm{Re}_{\rm crit} = 842$. The result agrees with the value of the linear theory given in the left panel of Fig. 62. Figure 63 shows the downward drift of the

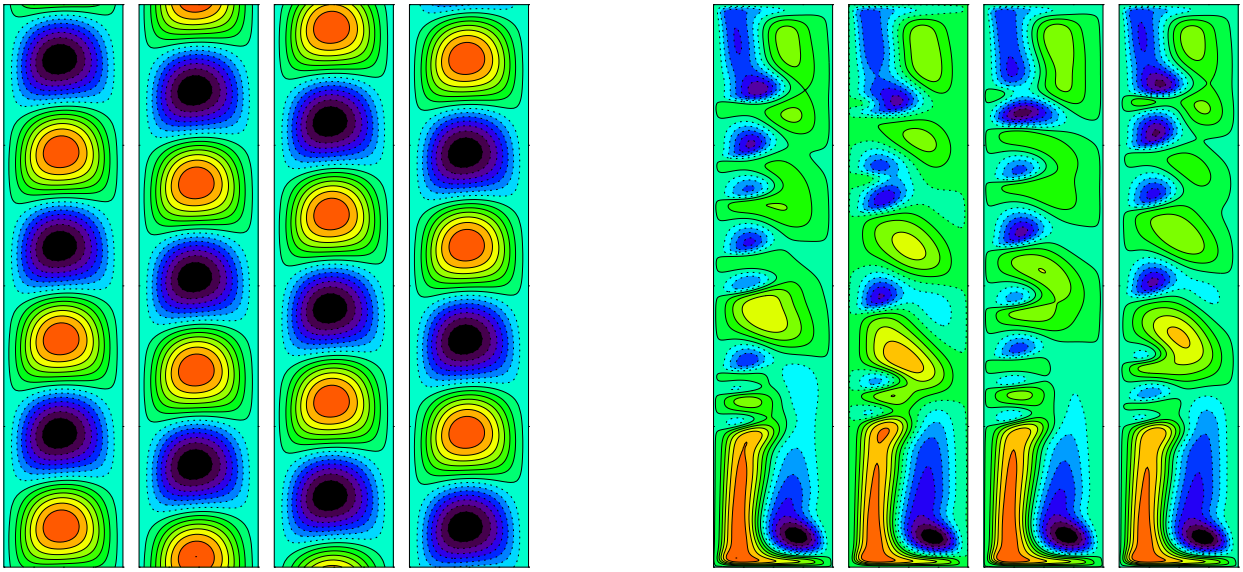

Figure 63. Snapshots (sequenced in time) of numerical simulations representing the downward-traveling wave without (left) and with endplates (right). The upper lid corotates with the outer cylinder while the lower lid is stationary in the laboratory. The contourlines of the streamfunctions of the flow are shown. Left: Re = 900, $\beta = 4$. Right: Re = 1480, $\beta = 6$. Ha = 9.5, $\mu_\Omega = 0.27$, Pm = 0, perfectly conducting cylinders, insulating endplates. From [119].

streamlines of the HMRI cells without and with (insulating) endplates. For μ_Ω between 0.25 and 0.27 the wave travels with $\omega_{\rm dr} \simeq 0.13$ in the axially periodic container, and with $\omega_{\rm dr} \simeq 0.12$ in the container with top and bottom endplates. In both cases there is a weak anticorrelation between the values of μ_Ω and $\omega_{\rm dr}$. These values agree with the results of the linear analysis (see the right panel of Fig. 64). The axial travel speed of the unbounded model with supercritical Re $\simeq$ 1600 is about 1 mm/s [119].

In the right panel of Fig. 63 the lower endplate is fixed, while the upper endplate corotates with the outer cylinder. The perturbing influence on the traveling instability pattern is much stronger for the stationary lower lid than it is for the rotating upper lid. These endplates do not prevent the traveling wave though; even the agreement between the linear and the nonlinear results proved to be satisfying. For the maximal axial velocity with $\beta = 4$ and Re = 1500 the simulations provided 1 mm/s, close to empirical data for the PROMISE container (see below).

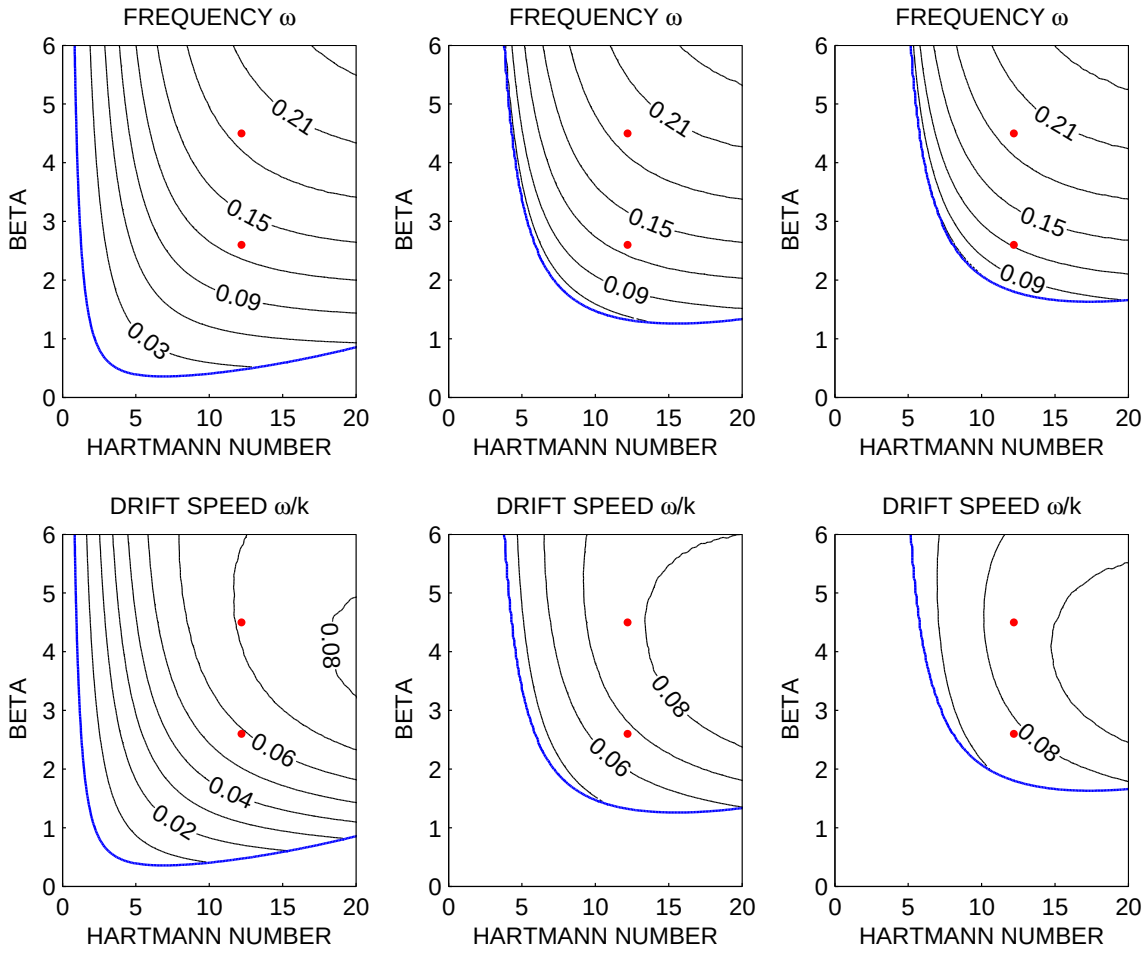

Figure 64. Drift frequency (top) and axial drift speed (bottom) versus Hartmann numbers for marginal stability of flows with $\mu_\Omega = 0.25$ (left), $\mu_\Omega = 0.26$ (middle) and $\mu_\Omega = 0.27$ (right). The maximum Reynolds number is Re = 4000 (blue lines). The red dots concern experiments discussed below. $\mu_B = r_{\rm in} = 0.5$, Pm $= 10^{-5}$. Perfectly conducting cylinders.

For marginal stability Fig. 64 provides the corresponding travel frequencies $\omega_{\rm dr}$ and the travel speeds $\omega_{\rm dr}/k$ as functions of Ha and β from the linear theory. The travel frequency is the lowest frequency in the system. A typical value for medium β is $\omega_{\rm dr} \lesssim 0.1$. A deeper inspection of the plots in the top row of Fig. 64 suggests that at least for $\mu_\Omega = 0.25$, only a very weak dependence of the frequencies on the values of β exist. Moreover, the travel frequencies normalized with the viscosity frequency $\omega_\nu = \nu/R_0^2$ written as functions of β and Ha show almost no dependence on the value of β. It has also been shown that only a slight dependence on the magnetic Prandtl number, i.e. $\omega_{\rm dr} \propto \omega_\nu {\rm Pm}^{-1/4}$, exists, without any influence of β [120]. For the phase velocity at the Rayleigh line the numerical value $\omega_{\rm dr}/k \simeq 0.01 - 0.02$ results, almost independent of β and scaling linearly with Ha. For the flows slightly beyond the Rayleigh limit the normalized travel velocity also hardly depends on the value of β if the Hartmann number is not too large. For the quasi-Keplerian flow the influence of β becomes much stronger and even depends on the boundary conditions.

6.3. Boundary conditions

It is also worth comparing the results for perfectly conducting cylinders with those obtained with insulating ones [121]. The numerical values explicitly mentioned in this paper are for $\mu_\Omega = 0.27$ and $\beta = 4$, which yield Re = 1521 and Ha = 16. For the model with perfectly conducting cylinders we find the smaller values Re = 842 and Ha = 9.5. Insulating boundaries thus increase both Re and Ha by almost a factor of two. Hence, an experiment with perfectly conducting boundaries would be the most promising design for exploring the magnetorotational instability in the laboratory. Note, however, that for MRI the situation is different: Reynolds numbers for insulating cylinders are lower than for conducting ones, but the Hartmann number behaves opposite.

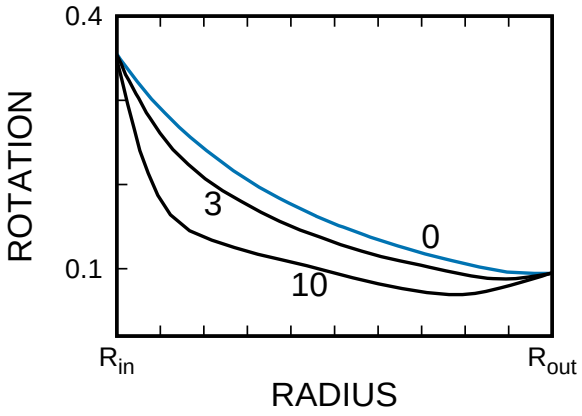

Figure 65. Influence of the Ekman-Hartmann layer on the rotation profile in the midplane between the endplates for various Hartmann numbers of the axial field. The blue line indicates the profile with no endplates. Re = 1775, $\beta = 0$, Pm = 0, $\mu_\Omega = 0.27$. Perfectly conducting endplates attached to the outer cylinder. From [73].

The material of the endplates for axially bounded containers also plays an important role. It is known that in the transition zone between differentially rotating fluid and rigid endplates an Ekman-Hartmann layer develops in the presence of an axial magnetic field [122]. This magnetized shear layer induces electric currents beneath the layer in the bulk of the container. Their radial component, together with the axial background field, provides azimuthal Lorentz forces accelerating or decelerating the global rotation. The rotation is suppressed in the range between the cylinders if the endplates corotate with the outer cylinder. For perfectly conducting endplates the Hartmann current reduces the rotation rate within the gap between the cylinders by almost 50% (for Ha $\simeq$ 10), but this effect is much weaker for insulating endplates. The material for the endplates, therefore, should ideally be a good insulator [123, 74]. The dramatic consequences of 'wrong' endplates for the rotation profile in the midplane (!) between the endplates are shown in Fig. 65 for various amplitudes of the axial magnetic field. This effect is not weak; the profile becomes very steep close to the inner cylinder and rather flat in the gap between the cylinders. Close to the outer cylinder the shear even changes its sign. The profile for Ha = 10 might be hydrodynamically stable.

6.4. Quasi-Keplerian rotation

Another question related to boundary conditions is whether the HMRI for quasi-Keplerian rotation and small Pm also scales with Re and Ha or with Rm and S. In a local and inviscid approximation it has been shown that solutions do not exist for rotation laws with $\mu_\Omega > 0.32$, which would suggest the quasi-Keplerian law with $\mu_\Omega \simeq 0.35$ to be stable [95, 20]. Calculations for containers with perfectly conducting cylinders and finite Pm do not confirm this strict result. Figure 66 shows for Kepler rotation that for small Pm the scaling with Re exists, but only for not too large β. A scaling with Re only exists for the narrow range of $\beta \simeq 2-4$ but no longer for $\beta \gtrsim 10$. Very small β (MRI) and very large β (AMRI) both lead to a scaling with Rm and S for Pm $\to 0$, yielding very high Reynolds and Hartmann numbers as eigenvalues for small Pm. For Pm $= 10^{-5}$ and $\beta = 4$, the critical Reynolds number at about 6000 is still rather low in comparison with values $O(10^6)$ which are characteristic for MRI. This finding is always true if at least one of the cylinders is perfectly conducting (see below).

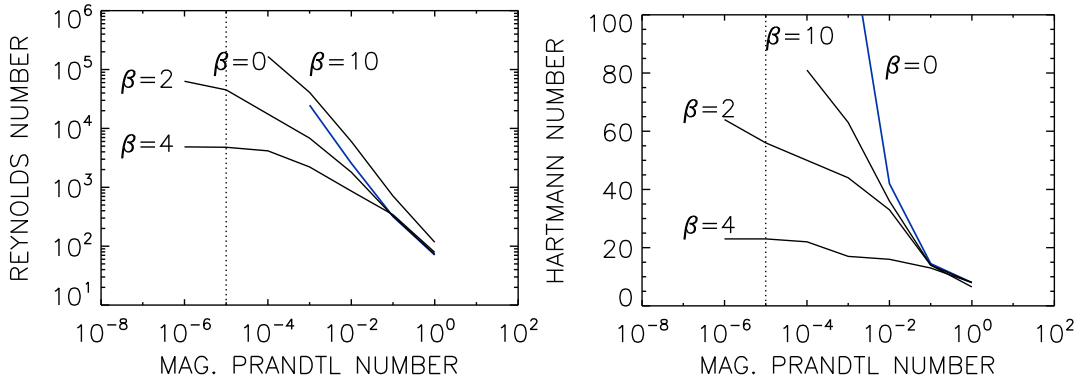

Figure 66. Quasi-Keplerian flow subject to twisted background field with current-free azimuthal component: critical Reynolds numbers (left) and Hartmann numbers (right) for the $m = 0$ modes as function of the magnetic Prandtl number for $\beta = 0$ (blue lines) and for $\beta = 2, 4, 10$ (dark lines). Hartmann number defined with B_0. The result is that $\beta = 0, 10$ scale with Rm and $\beta = 2, 4$ scale with Re. Vertical dotted lines mark the magnetic Prandtl number of liquid sodium. $r_{\rm in} = 0.5$, $\mu_B = r_{\rm in}$, perfectly conducting cylinders.

A similar statement holds for AMRI with quasi-Keplerian rotation as demonstrated in Section 4.2. As expected, for Pm $\to 0$ the eigenvalues for potential flow ($\mu_\Omega = 0.25$) converge in the (Ha/Re) plane, and for the quasi-uniform flow ($\mu_\Omega = 0.5$) they converge in the (S/Rm) plane. The quasi-Keplerian flow with its shear between the two examples scales with S and Rm, but only for insulating boundary conditions (Fig. 32, left panel). For conducting boundaries, the eigenvalues behave similarly to those of the potential flow. Obviously, this particular flow forms the transition between the scaling laws for Pm $\to 0$ of the models with steep and flat radial profiles of the angular velocity.

We know, however, that for HMRI the scaling for small Pm switches from Re $\simeq$ const close to the Rayleigh line to Rm $\simeq$ const for more flat rotation profiles (see Fig. 68). Solutions in the inductionless approximation, therefore, can only exist close to the Rayleigh line. For Pm $= 0$ they *must* disappear for a critical $\mu_{\Omega,0}$ somewhere beyond this line. The exact value of this limit depends on the construction of the model. Details are given in Fig. 67 where for Pm $= 0$ the isolines of Reynolds number and Hartmann number are plotted as functions of β and the shear parameter μ_Ω for two different inner boundary conditions. The outer boundary is always taken as insulating. As expected, one finds for both models maximal values $\mu_{\Omega,0}$ which, however, strongly differ for differing boundary conditions [124, 116]. There are only small differences for small Re and at the Rayleigh line but drastic differences occur beyond this line. For insulating inner boundary rotation profiles with $\mu_\Omega > 0.31$ require Reynolds numbers exceeding 10^4 to become unstable. With conducting inner boundary Reynolds numbers of 10^4 are sufficient to destabilize flatter profiles up to $\mu_\Omega \simeq 0.34$ (with $\beta \simeq 4$). The quasi-Keplerian rotation becomes unstable at Re $= 10^5$, but only if the inner cylinder is perfectly conducting. Insulating inner cylinders stabilize the quasi-Keplerian flow unless the Reynolds number exceeds a value of 10^6. The plots for the Hartmann numbers are very similar.

In Ref. [95] with $\mu_{\Omega,0} = r_{\rm in}^{-9.6}$ also an upper limit is given for HMRI stability, i.e. $\mu_{\Omega,0} \simeq 776$ for $r_{\rm in} = 0.5$. If existing, one would interprete this number as a suggestion that for strong superrotation (better, for stationary inner cylinder) there is another branch for HMRI scaling with Re and Ha, which exists in the inductionless approximation. In Section 4.5.2 we have shown that indeed for superrotation at least with $\beta = 0$ eigensolutions appear even for Pm $\to 0$.

6.5. Nonaxisymmetric modes

It is known that the nonaxisymmetric modes for twisted background fields behave similarly to the axisymmetric mode of MRI if the critical Reynolds and Hartmann numbers are considered as functions of Pm. In Fig. 66 for quasi-Keplerian flow the steep blue lines for $m = 0$ and $\beta = 0$ also represent the nonaxisymmetric mode $m = 1$ and $\beta \neq 0$. For Pm $\to 0$ they all scale with S and Rm (so that for small Pm very high Reynolds and Hartmann numbers are needed for excitation [43]). This is not only true for quasi-Keplerian rotation but also for *all* flows including the potential flow. The behavior of the Reynolds numbers is shown in Fig. 68 for $\mu_\Omega \geq 0.25$ and Pm $= 10^{-5}$. The solid lines represent the axisymmetric solutions whereas the dashed lines denote the nonaxisymmetric modes with $m = \pm 1$. The critical Reynolds numbers of the modes with $m > 0$ hardly change between $\mu_\Omega = 0.25$ and $\mu_\Omega = 0.4$; they always

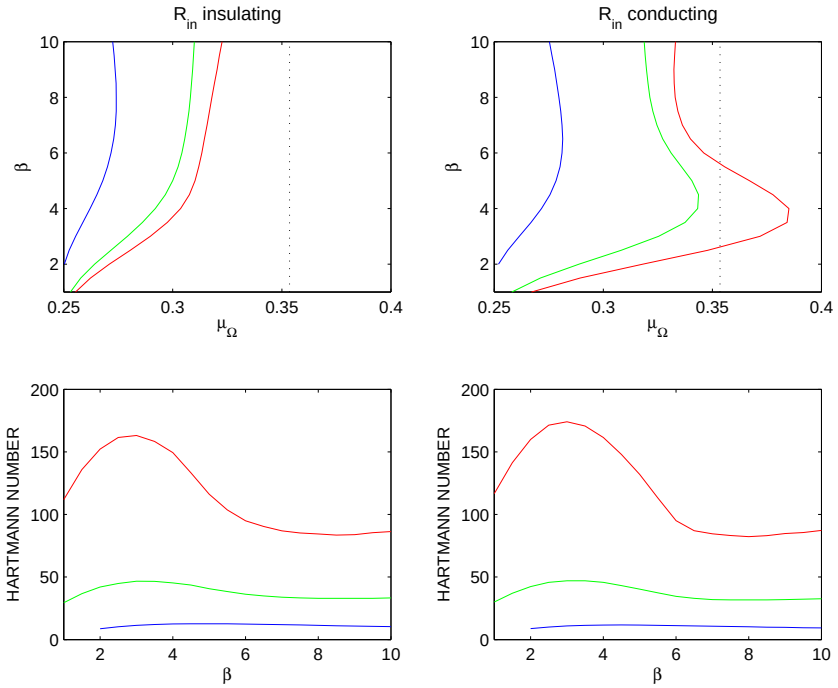

Figure 67. Isolines of Reynolds numbers (top) and Hartmann numbers (bottom) as functions of μ_Ω and β for insulating (left) and perfectly conducting (right) inner boundary condition. Re = 10^3 (blue), Re = 10^4 (green), Re = 10^5 (red). The dotted vertical line marks the quasi-Keplerian rotation law. $\mu_B = r_{\rm in} = 0.5$, Pm = 0.

exceed 10^6. There is no actual change of scalings for Pm $\to$ 0 for the nonaxisymmetric modes between the potential flow and beyond. The rather low Reynolds and Hartmann numbers shown for Pm $\to$ 0 in Fig. 66 for $\beta \neq 0$ close to the Rayleigh line are thus a basically axisymmetric phenomenon. Nonaxisymmetric modes can hardly be observed along this way.

Figure 68 also demonstrates how for nonvanishing β the Reynolds number for the axisymmetric mode is reduced by orders of magnitudes if the rotation law becomes steeper until the Rayleigh line is reached. The potential flow with axial fields and azimuthal fields of the same order thus becomes unstable against axisymmetric perturbations already for Reynolds numbers of $O(10^3)$. This is a consequence of the fact that for azimuthal fields which are current-free in the fluid the potential flow (i.e. $U_\phi \propto B_\phi \propto 1/R$) belongs to the Chandrasekhar-type of MHD flows and the quasi-uniform flow does not.

6.6. *Experiment* Promise

The simplest idea to realize the MRI in an experiment concerns a Rayleigh-stable flow between differentially rotating cylinders. Such a flow can be destabilized by an externally imposed magnetic field. If the imposed field is purely axial, however, the relevant parameter for the onset of the instability is the magnetic Reynolds number which must exceed about 10 [27, 29]. The kinetic Reynolds number for excitation of the MRI then becomes 10^6 or even 10^7 because of the small magnetic Prandtl numbers of liquid metals. Such large Reynolds numbers are not only difficult to realize in experiments but also end-effects become very important [125].

For a combined axial and azimuthal field the relevant parameter slightly beyond the Rayleigh limit is Re, which must only be $O(10^3)$ for instability (Fig. 68). For decreasing β the Reynolds number gradually rises until for $\beta = 0$ the necessary Reynolds number is $O(10^7)$, known for MRI with Pm $\simeq 10^{-6}$. The main difference of the solutions to those for purely axial imposed fields is that the HMRI pattern drifts along the rotation axis of the cylinders. In both cases the modes with the lowest Reynolds numbers are axisymmetric. Provided $B_0 > 60$ G and $\beta \simeq 3$, Reynolds numbers of only 10^3 are sufficient to excite the instability waves for conducting cylinders. The threshold numbers for insulating boundaries are higher.

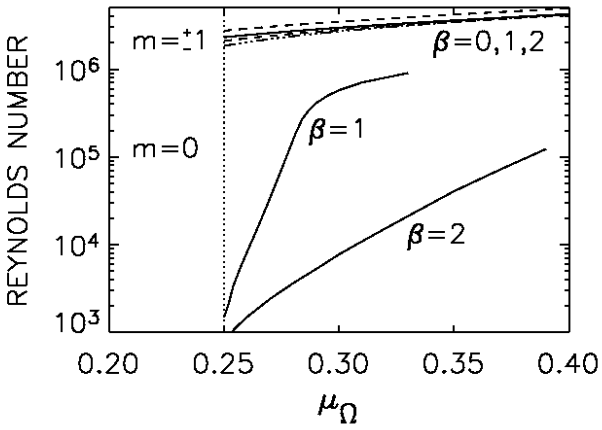

Figure 68. Critical Reynolds numbers for excitation of the nonaxisymmetric modes $m = 1$ (dashed lines) in comparison to the axisymmetric modes $m = 0$ (solid lines) for $\beta = 0, 1, 2$. The nonaxisymmetric modes always scale with Rm for Pm $\to 0$ (as for the standard MRI) while close to the Rayleigh line the axisymmetric modes with $\beta = 1, 2$ scale with Re. $\mu_B = r_{\rm in} = 0.5$. Pm $= 10^{-5}$, perfectly conducting cylinders.

However, the existence of the viscous endplates results in Ekman layers in which the velocity differs from the prescribed rotation law. A global meridional circulation with two Ekman vortices is the immediate consequence. As known for nonrotating endplates a radial inflow close to the boundaries appears and for solid-body rotation a radial outflow appears [74]. Figure 69 demonstrates the Ekman layer phenomenon for different sorts of endplates. While for the left panel the rigid endplates rotate with the angular velocity of the outer cylinder the endplates in the middle panel are split at $R_{\rm split} = R_{\rm in} + 0.4D$; the inner part is attached to the inner cylinder and the outer part is attached to the outer cylinder. Meridional planes are presented for the variables U_ϕ and the streamlines of the meridional flow. We notice for rigid endplates that the mean flow U_ϕ in this case significantly depends on z and that two strong Ekman vortices fill the whole container. If the plates are replaced by two rings then U_ϕ is almost independent of z in the bulk of the container and the Ekman circulation is strongly suppressed. If the axial magnetic field is applied (for the plots of the right panel with the two rings attached to the two cylinders) it looks even better as the Ekman vortices are further reduced. The rotation profiles are almost unchanged when compared to the hydrodynamic case. For this result insulating endplates must be used as for perfectly conducting lids the Ekman-Hartmann layer produces basically stronger modifications of the rotation law.

The experiments were done at the Promise facility as described in Section 4.3. This time, however, the coil for the production of an axial field was also used. Since this coil is not cooled, the current in the windings is restricted to values of around 150 A, which corresponds to a Hartmann number of 23.7. The endplates are made of plexiglass which are split into two rings where the inner one is attached to the inner cylinder and the outer one to the outer cylinder. Based on numerical simulations the splitting position is at $R_{\rm split} = 56$ mm, minimizing the Ekman pumping of rigid endplates [73, 75, 76].

The azimuthal magnetic field is imposed by a current up to 7 kA through a water-cooled rod along the central axis. The field within the fluid is current-free. The fluid within the vessel is the GaInSn alloy with the material parameters given in Table 1. For experiments with this apparatus as an improved version of Promise 1 (which worked with rigidly rotating endplates, see [78, 79]) detailed predictions are possible. The main target for the experiments are measurements of the vertical travel velocity $u_z = \omega/k$ by two ultrasonic high-focus transducers mounted on opposite sides of the top endplate.

For the marginal instability with the wave number k leading to the lowest Reynolds number for given Ha and β, the resulting normalized drift rates $\omega_{\rm dr}$ and axial phase speeds $\omega_{\rm dr}/k$ are given in Fig. 64 for the shear values $\mu_\Omega = 0.25 - 0.27$. They are normalized with $\Omega_{\rm in}$ and $R_0\Omega_{\rm in}$, respectively. The maximum Reynolds number for the calculations is 4000 (the blue lines in the plots). The minima of the lines define the necessary minimal β values with which an instability appears. This minimum β becomes smaller for greater Reynolds numbers. The limit $\beta \to 0$ would

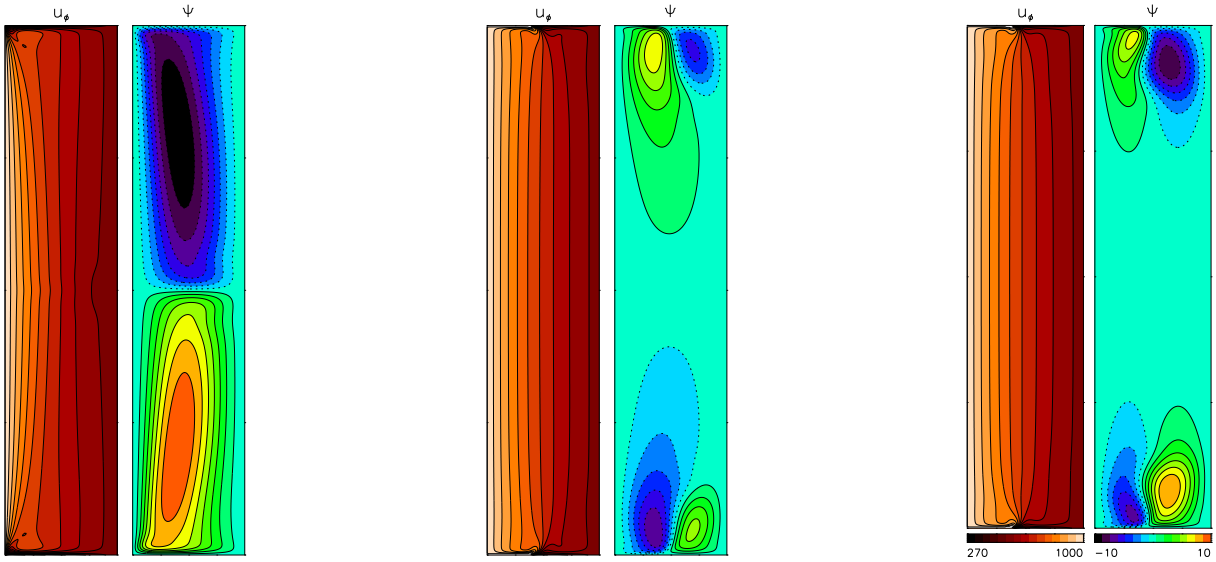

Figure 69. Simulated snapshots representing the flow pattern for rigidly rotating endplates (left) and for endplates formed by two rings attached to the cylinders (middle, right). The isolines of the azimuthal flow and the contourlines of the streamfunctions of the flow are shown. Axial magnetic fields (Ha = 10) are only applied in the simulations shown in the right panel (insulating endplates). Re = 1000, Pm = 0, $\beta = 0$, $\mu_\Omega = 0.27$. From [73].

require Re = 55,780 for $\mu_\Omega = 0.25$ (and for galinstan as the fluid conductor) together with $\omega_{\rm dr} = 0$. The corresponding critical Hartmann number is simply 7 independent of the magnetic Prandtl number (see Sect. 3.1). There is obviously a smooth transition from HMRI to standard MRI by this constellation.

The red symbols in Fig. 70 mark the parameters characterizing the main experiments with Promise 2. The supercritical Reynolds number Re = 2959 is fixed for all measurements. The axial magnetic field has been fixed to $B_0 = 77.2$ G (Ha = 12.2) and the azimuthal field was then varied by the application of an axial electric current with 4 kA ($\beta = 2.6$) or 7 kA ($\beta = 4.5$). The empirical results for the rotation ratios $\mu_\Omega = 0.23 - 0.27$ have been described in detail in Ref. [126]. For the Rayleigh limit $\mu_\Omega = 0.25$ the measured travel speed for the two β values varies between 1.5 mm/s and 1.8 mm/s, increasing slightly with β (Fig. 71). With the nonlinear code these measurements can be reproduced exactly (the diamonds in Fig. 71). The linear approximation with fixed Reynolds number, however, yields values that are too small (the red and blue crosses). Figure 70 shows the drift frequencies and the axial phase speed ω/k for the Rayleigh limit and Pm = 0. For Ha = 12.2 one finds $\omega/k = 0.03$ for both β values, hence $u_z \simeq 0.75$ mm/s. Along the low-field branches of the blue lines the travel frequency $\omega_{\rm dr}$ hardly varies (top row in Fig. 70). This is in particular true for $\mu_\Omega = 0.25$, and means that in this case $\mathrm{Re} \cdot \omega_{\rm dr} \simeq$ const so that it is shown that in this case the drift frequency is determined by the viscosity frequency independently of β and Re. Beyond the Rayleigh line the relations are more complicated. Interestingly enough, if the velocities are measured with the code during the linear onset of the instability (the squares in Fig. 71) then the results perfectly match the data of the linear theory taken from Fig. 70.

For $\mu_\Omega = 0.26$ the agreements are even better; now also the two linear results are close to the measurements. For $\mu_\Omega > 0.26$, however, all theoretical phase speeds increase for reduced shear while the experimental values decrease. Note that the given theoretical results were obtained for an unbounded container. The wave numbers given in the right panel of Fig. 62 (for the easiest excitation condition) represent wavelengths of about 15 cm, but the real container has a height of only 40 cm.

Figure 72 illustrates the variation of β in further detail. Fixing $\Omega_{\rm in} = 0.38\,{\rm s}^{-1}$, $\mu_\Omega = 0.26$, $I_{\rm coil} = 76$ A, the axial current is varied between 0 and 8.2 kA. We observe the HMRI wave only above 4 kA or equivalently, for $\beta \geq 1.9$. A comparison of the experimental results with numerical predictions is shown in Fig. 73. The 3D simulations have been done without endplate effects assuming an aspect ratio of $\Gamma = 10$. The values are averaged over the whole container including the near-wall domains where the vertical flow in the cells is larger than in the middle of the gap between the cylinders. The results obtained with an inductionless axisymmetric 2D code for Pm = 0 concern the

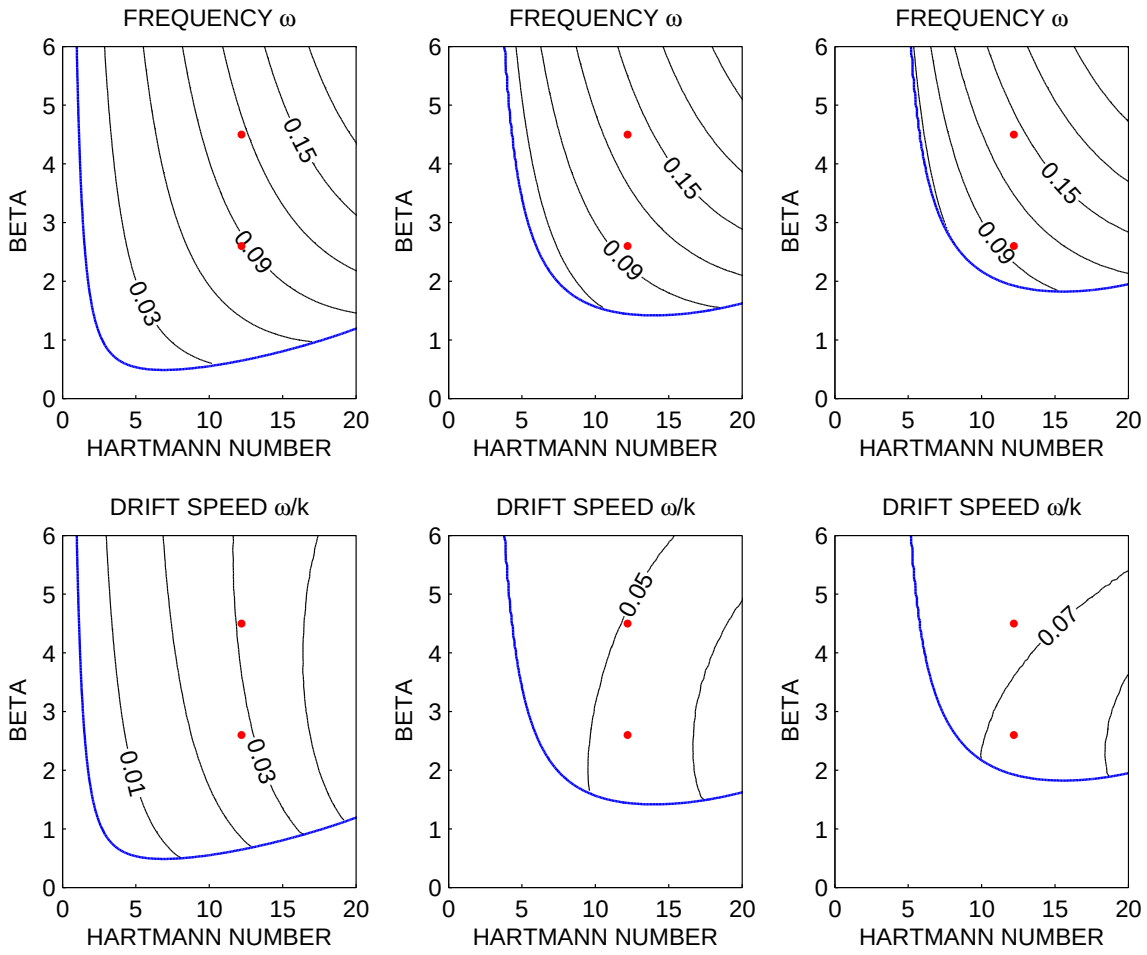

Figure 70. Drift frequency (top) and axial travel speed (bottom) for $\mu_\Omega = 0.25$ (left), $\mu_\Omega = 0.26$ (middle) and $\mu_\Omega = 0.27$ (right) with a supercritical fixed Reynolds number of Re = 2959. The solutions are of neutral stability only along the blue lines. The red symbols mark the locations of the values Ha and β used in experiments where the travel speeds have been measured (see Fig. 64). Perfectly conducting cylinders.

central part between the endplates [126]. The two very different codes provide very similar results for the maximum intensities also in agreement with the measurements. The critical β values, however, vary between the red symbols at the horizontal axis indicating the numerically determined threshold values for the convective and the absolute instability [115]. The experimental data well fit the numerical approaches. The 2D simulations for the bounded container reflect the onset of the *absolute* instability while for the unbounded container the onset of the *convective* instability is simulated.

By definition of the averaging procedure, the systematic phase velocity ($\omega_{\rm dr}/k$) of the waves is not reproduced in the plots. The instability starts with rather small intensities at the threshold value $\beta_0 = 1.9$ which is known from the linear theory (see Fig. 62, left). For slightly larger values the intensity grows like the difference $\beta - \beta_0$. Much stronger saturated intensities are reached for β values larger than the theoretical value for the absolute instability. The values are averaged over the axial coordinate z, explaining that they are smaller than the amplitude values given in Fig. 71. The typical value of the axial rms velocity for larger β is 0.2 mm/s.

7. Tayler instability (TI)

Almost all applications in the foregoing sections concern toroidal magnetic fields which are curl-free in the fluid between the cylinders. In these cases an instability cannot exist without global differential rotation. In Sections 5.3

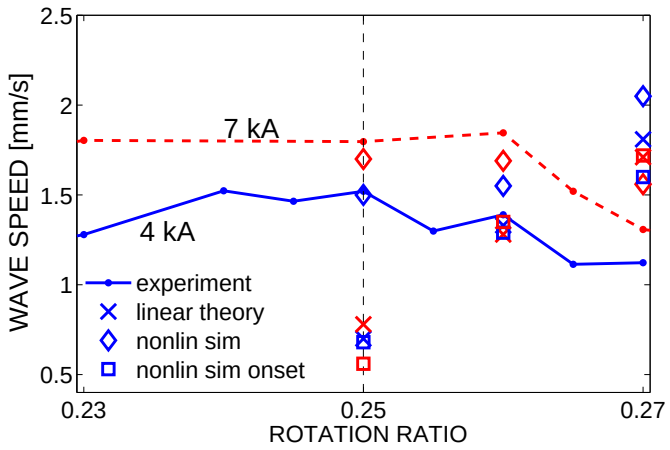

Figure 71. Axial travel speed measured with Promise for $\beta = 2.6$ (lower line) and $\beta = 4.5$ (upper line) as a function of the shear parameter μ_Ω. The values for the crosses are taken from the bottom row of Fig. 70 while the diamonds are results of nonlinear simulations which yield the values marked as squares during the onset phase of the instability. The vertical line mimics the Rayleigh limit. Ha = 12, Re = 2959. The linear speed of the inner cylinder is $u_{\rm in} = 2.51$ cm/s. Adapted from [126].

and 5.4, however, models with Re = 0 also proved to be unstable against nonaxisymmetric perturbations for azimuthal fields with $\mu_B > r_{\rm in}$. Hence, $a_B \neq 0$ in Eq. (36), so that axial electric currents exist in the fluid. It is also interesting to combine the stability criteria (7) for axisymmetric modes and (9) for nonaxisymmetric modes. As illustrated in Fig. 74 the solution $B_\phi \propto 1/R$ (i.e. $\mu_B = 0.5$) is always stable while the profiles $B_\phi \simeq$ const and $B_\phi \propto R$ (i.e. $\mu_B = 1$ and $\mu_B = 2$) are unstable against nonaxisymmetric perturbations. That the z-pinch with uniform electric current between the cylinders is always stable against $m = 0$ follows from the simplified Eq. (46), i.e.

$$\frac{{\rm d}^2 b_\phi}{{\rm d}R^2} + \frac{1}{R}\frac{{\rm d}b_\phi}{{\rm d}R} - \frac{b_\phi}{R^2} - k^2 b_\phi - {\rm i\,Pm\,Re}\,\omega b_\phi - R\frac{\rm d}{{\rm d}R}\left(\frac{B_\phi}{R}\right)u_R = 0, \tag{83}$$

which for $B_\phi \propto R$ fully decouples from the hydrodynamics as it also does b_ϕ in accordance with (45). All magnetic perturbations, therefore, decay because of missing energy sources. The last term in (83) is only able to destabilize fields with radial profiles *steeper* than $B_\phi \propto R$ against axisymmetric perturbations.

For real fluids in the presence of azimuthal fields the equation system is given in Section 2.2. Without rotation for any value of μ_B and for a given mode number m, the resulting eigenvalue for neutral stability is the Hartmann number ${\rm Ha}_0$. One can easily show that for Re = 0 the drift value $\omega_{\rm dr}$ vanishes, and ${\rm Ha}_0$ does not depend on the magnetic Prandtl number [127, 102]. In Fig. 74 the critical Hartmann numbers for the excitation of the axisymmetric mode ($m = 0$) and the nonaxisymmetric modes with $m = \pm 1$ for $-10 \le \mu_B \le 10$ are given for $r_{\rm in} = 0.5$. Of particular importance here are the values for $\mu_B = 1$ and $\mu_B = 2$, describing (approximately) uniform fields and uniform electric currents, respectively. For $\mu_B = 1$ the critical Hartmann numbers for excitation of the $m = 1$ mode are ${\rm Ha}_0 = 151$ and 109 for conducting and insulating cylinders, respectively; for $\mu_B = 2$ the values are ${\rm Ha}_0 = 35$ and 28. Uniform current and/or insulating boundary conditions lead to easier excitations.

For Hartmann numbers exceeding ${\rm Ha}_0$ the equation system yields finite growth rates. It is known that the growth rate of TI grows for growing magnetic fields. The open question is the influence of the magnetic Prandtl number. Figure 75 shows the growth rates for a purely toroidal field with $r_{\rm in} = 0.5$ and $\mu_B = 1$ (almost uniform magnetic field) and $\mu_B = 2$ (uniform electric current) for various Pm. In this representation they scale almost linearly[6] with the Hartmann number, with a weak dependence on Pm. Due to the normalization of the growth rates with the averaged frequency $\overline{\omega} = \overline{\eta}/R_0^2$, one obtains

$$\omega_{\rm gr} = F({\rm Pm})\,\Omega_{\rm A}, \tag{84}$$

[6]The discussion below of a wide gap flow reveals a quadratic behavior.

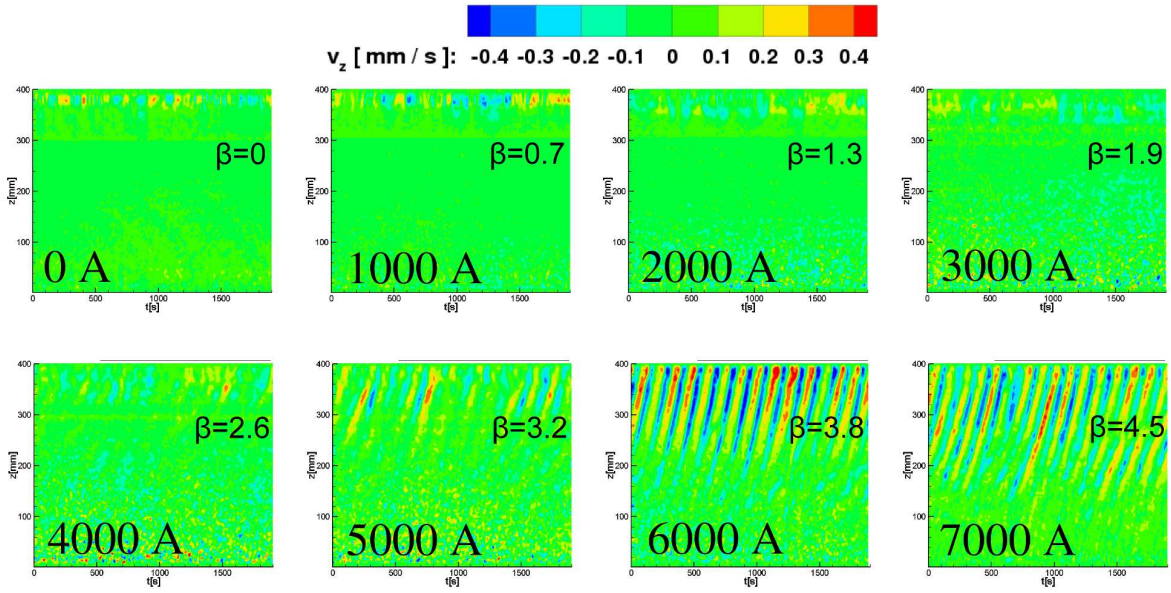

Figure 72. Results of Promise when varying the axial current. The fixed parameters are $I_{\rm coil} = 76$ A, giving Ha = 12. Measured UDV signals in dependence on time and vertical position, for 8 different axial current values. The phase velocity for the experiment with 7 kA is 0.9 mm/s. Re = 1775, $\mu_\Omega = 0.26$.

with the Alfvén frequency $\Omega_{\rm A} = \overline{\omega}$ Ha and F as a function of the magnetic Prandtl number. The amplitudes for $\mu_B = 1$ (uniform field) are $F(1) = 0.1$ and for $\mu_B = 2$ (uniform current) it is $F(1) = 1$. In this representation the fastest instability belongs to Pm = 1. Such fluids are thus more unstable than those with Pm $\neq 1$. The function F(Pm) becomes rather small for small and large Pm.

For a purely toroidal field the azimuthal wave numbers of the modes in Fig. 76 are $m = \pm 1$, where the left spiral has $m = 1$ and the right spiral $m = -1$. The left-handed and right-handed spirals are degenerate, having exactly the same growth rate. These modes do not drift in the azimuthal direction. Figure 76 shows that the nonlinear solutions do not consist of equal mixtures of both modes. Instead, either the left or the right mode suppresses the other. Which mode wins depends on the initial conditions. If the initial condition allows the excitation of both modes, it is the numerical noise that determines the winning mode. Both the kinetic and current helicities of the two possible solutions have the same magnitude but opposite signs. The solution consisting of an equal mixture of both modes proves to be unstable. Other examples of spontaneous parity-breaking bifurcations of this type also have been described in the Refs. [130, 131, 132].

7.1. Wide gaps

Containers with $r_{\rm in} = 0.05$ may be considered as approaching pipe flows within the outer cylinder. For such models the influence of the inner boundary condition should become negligible. It makes sense for all such cases to work with an *outer* Hartmann number after the rule

$$\mathrm{Ha}_{\rm out} = \frac{B_{\rm out} R_{\rm out}}{\sqrt{\mu_0 \rho \nu \eta}} = \frac{\mathrm{Ha}}{\sqrt{(1 - r_{\rm in}) r_{\rm in}^3}}. \tag{85}$$

Figure 77 demonstrates the behavior of the outer Hartmann number for $r_{\rm in} \to 0$ for both types of boundary conditions. For $r_{\rm in} \to 0$ the two nearly horizontal curves approach (as they should); the dependence on $r_{\rm in}$ is very weak for $r_{\rm in} \ll 1$. Note that insulating boundary conditions lead to (slightly) more unstable flows.

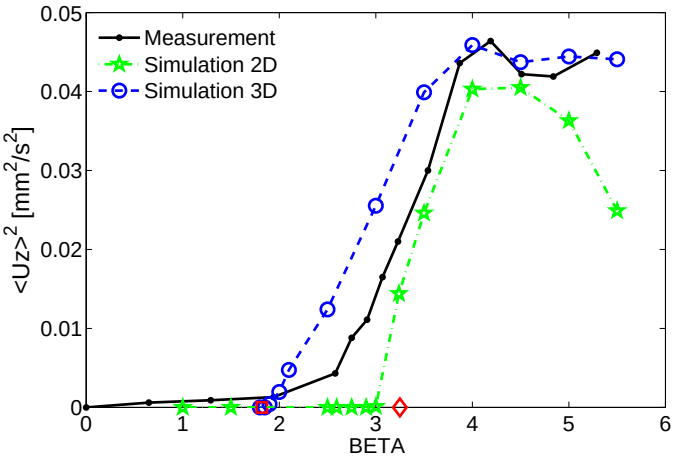

Figure 73. Rms of the axial velocity u_z at the UDV sensor position in dependence on $I_{\rm rod}$. Same parameters as in Fig. 72. Dashed lines show numerical results, the full line gives the experimental data. The 2D simulation for Pm = 0 (from [126]) concerned a container with split endcaps while the 3D simulation for Pm = 10^{-5} used axial periodicity with $\Gamma = 10$. The red marks at the horizontal axis indicate the predictions for the onset of the convective instability (circle) and the absolute instability (diamond). See the remark at the end of Section 6.1. $\mu_\Omega = 0.26$. Perfect-conducting cylinders.

The growth rates of the $m = 1$ instability of this pinch-type flow for Ha > Ha_0 are plotted in Fig. 78 (left) with the same normalization as used in Fig. 75. One finds that the (physical) growth rates in wide gaps behave like

$$\omega_{\rm gr} = \Gamma_{\rm gr} \frac{B_{\rm out}^2}{\mu_0 \rho \eta}, \tag{86}$$

where the coefficient $\Gamma_{\rm gr}$ varies only by a factor of four when the magnetic Prandtl number varies by four orders of magnitude [134]. The linear size of the container does not occur in Eq. (86). It is also surprising that the growth rate is inversely proportional to the diffusion frequency $\omega_\eta = \eta/R_{\rm out}^2$, what means that the growth time reduces for increasing electric conductivity (in opposition to the diffusion times). For small Pm, $\Gamma_{\rm gr}$ no longer depends on the magnetic Prandtl number (Fig. 78, right). Pm = 1 and $r_{\rm in} = 0.05$ yield $\Gamma_{\rm gr} = 0.0009$. Note also that the growth rates for the wide gap container (Fig. 78) are much smaller than those of the standard gap displayed by Figs. (75).

It remains to describe the experimental implication of the critical value $\mathrm{Ha}_0 \simeq 30$ for the neutral instability taken from Fig. 78 (left). The solution of the stationary induction equation inside the outer cylinder in the presence of a uniform electric current I is $B_\phi = I/(5R_{\rm out})$. With (85) it follows that

$$I = 5\mathrm{Ha}_{\rm out} \sqrt{\mu_0 \rho \nu \eta} \tag{87}$$

with $\sqrt{\mu_0 \rho \nu \eta} = 8.2$ in cgs units for liquid sodium[7]. Hence, the characteristic value of $\mathrm{Ha}_{\rm out} \simeq 30$ leads to (only) 1.2 kA and/or $B_{\rm out} \simeq 50$ G for (say) $R_{\rm out} = 5$ cm.

7.2. Kinetic and magnetic energy

For the very small magnetic Prandtl number Pm = 10^{-5} and for stationary cylinders the TI for increasing electrical currents have been numerically simulated. Figures (79) and (80) show the azimuthal components of flow and field for $\mathrm{Ha}_{\rm out} = 40$ to $\mathrm{Ha}_{\rm out} = 600$. While for the weak-field case the expected regular nonaxisymmetric pattern can be observed, stronger fields produce more and more elongated structures and intermittency. Strong currents simultaneously lead to much larger and much smaller axial scales. This effect can be observed at least for the spectrum of the kinetic fluctuations rather than in the spectrum of the magnetic fluctuations. This might be a consequence of the very small magnetic Prandtl number, which leads by the high value of η to an effective smoothing of small scales of the magnetic fluctuations.

[7] $\sqrt{\mu_0 \rho \nu \eta} = 25.8$ in cgs for liquid gallium.

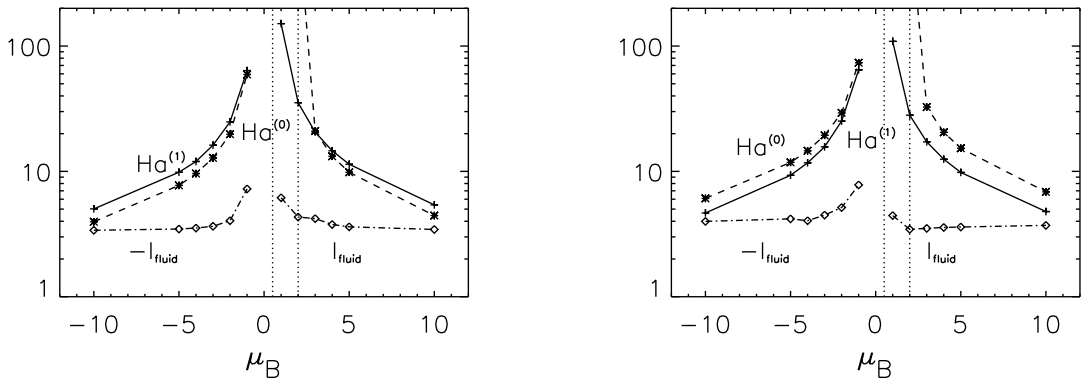

Figure 74. Critical Hartmann numbers $\mathrm{Ha}_0^{(m)}$ for $m = 0$ (dashed) and $m = 1$ (solid) for perfectly conducting (left) and insulating (right) boundary conditions for azimuthal fields with various μ_B. The profiles in the central area around $\mu_B = r_{\rm in} = 0.5$ (left dotted line) are stable against axisymmetric and nonaxisymmetric perturbations. The right dotted line at $\mu_B = 1/r_{\rm in} = 2$ represents the z-pinch solution for uniform axial current which is stable against axisymmetric perturbations but unstable against nonaxisymmetric perturbations ($m = 1$). The related electric currents (in kA) are calculated from (40) for liquid sodium. Hartmann numbers for all Pm. Exact data in [128], $r_{\rm in} = 0.5$.

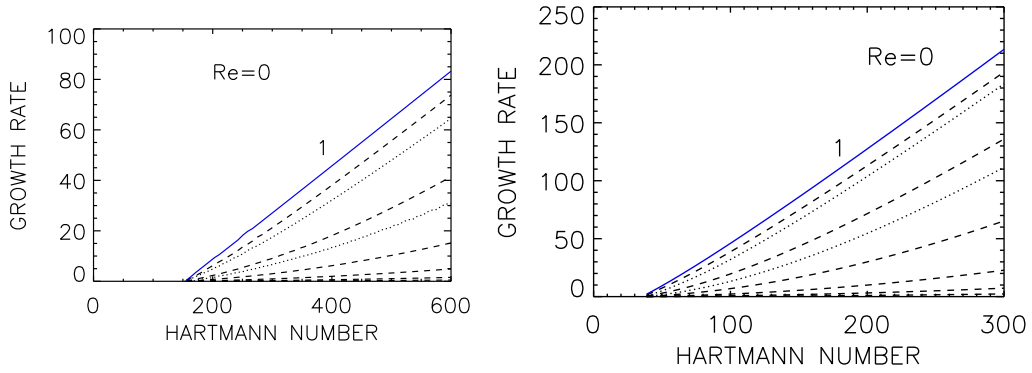

Figure 75. Azimuthal magnetic fields: growth rates of stationary flows normalized with $\overline{\omega} = \sqrt{\omega_\nu \omega_\eta}$ versus Hartmann number for $\mu_B = 1$ (left) and $\mu_B = 2$ (right), for Pm = 1 (blue lines), Pm = 0.1, 0.01, ... (dashed lines) and Pm = 10, 100, ... (dotted lines). The critical values H_0 do not depend on Pm but the growth rates do. The fastest growth belongs to Pm = 1. $r_{\rm in} = 0.5$, perfectly conducting boundaries.

The consequences of this situation for the resulting energies may also be discussed. The normalized magnetic energy (55) in its dependence on the inner Hartmann number is plotted in the left panel of Fig. 81. It is a steep function, $\mathrm{q} = Q\mathrm{Ha}^4$, with $Q \simeq 4 \cdot 10^{-8}$. On the other hand, the energy ratio (58) only grows linearly with Ha, i.e. $\varepsilon = E\mathrm{Ha}$ with $E \simeq 0.2$ (right panel). From these expressions it is easy to derive the relation between q and Rm′ in the form

$$\mathrm{q} \simeq 92\ \mathrm{Rm}'^{1.6}, \tag{88}$$

with $\mathrm{Rm}' = u_{\rm rms} R_0/\eta$. It also follows that

$$\mathrm{Rm}' \simeq 2.5\ \mathrm{S}^{2.5}, \tag{89}$$

if $\mathrm{S} = \sqrt{\mathrm{Pm}}\,\mathrm{Ha}$ has been used. The resulting exponent lies well between the values 1 and 2 for driven turbulence with high and low conductivity [135]. The stationary pinch with Pm ≪ 1 is not magnetically dominated.

*7.3. The GAllium-Tayler-Experiment (*Gate*)*

The stationary TI leads to a nondrifting nonaxisymmetric steady-state solution. Because of Re = 0 the eigenvalues Ha_0 do not depend on the magnetic Prandtl number, and can thus be computed for all $r_{\rm in}$ with a code for (say) Pm = 1

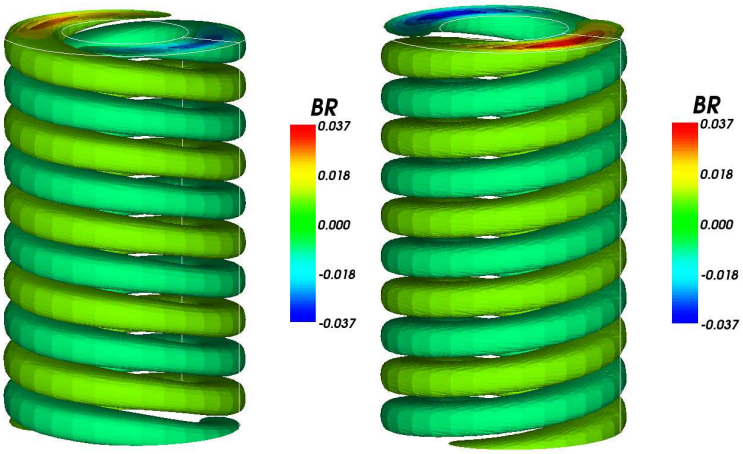

Figure 76. Instability patterns of a purely toroidal quasi-uniform background field without rotation. The two modes are equivalent: their kinetic helicities are $\pm 6.0 \cdot 10^{-4}$ and their current helicities are $\pm 3.5 \cdot 10^{-3}$ (both in units of $\Omega_A^2 R_0$). $r_{in} = 0.5$, $\mu_B = 1$, Ha = 200, Pm = 1. From [129].

(Fig. 77). On this basis and the calculation of the growth times an experiment can be designed to probe the theoretical predictions for Re = 0 as a first step. The experiment GATE consists of an insulating cylinder with a height of 75 cm and a radius $R_{out} = 5$ cm which is filled with GaInSn (Fig. 82). The liquid column is in contact with two massive copper electrodes which are connected by water cooled copper tubes to an electric power supply providing up to 8 kA. With 14 fluxgate sensors the modifications of the magnetic fields due to the TI are detected. Eleven of these sensors are positioned along the vertical axis, while the remaining three are positioned along the azimuth in the upper part. Such measurements give the geometry of the field, thus its shape in azimuthal and axial direction as well as the scaling of the growth rates with the applied electric current [136].

In all cases of instability the observed pattern of the magnetic perturbations is nonaxisymmetric with $m = 1$. Figure 83 shows the resulting growth rates and the calculations according to (86) for containers with very wide gaps ($r_{in} \le 0.25$). Note that for small Pm and for very small values of $r_{in} < 0.1$ the growth rates are almost independent of r_{in} (Fig. 78, right). The predicted threshold value for the electric current is 2.8 kA. For low growth rates the experimental data fit the theoretical curves well. One finds a relation $\omega_{gr} \simeq \gamma(I^2 - I_{crit}^2)$ with $\gamma = 2.7 \cdot 10^{-10}$, so that $\Gamma_{gr} \simeq 0.038$ results. The theory always provides maximal growth rates, optimized over the wave number. The theoretical values should thus always lie above the observed data, which is indeed the case.

8. Tayler-Couette flow

In this section the influence of rotation on the Tayler instability will be described. The rotation law $\Omega = \Omega(R)$ shall have the form (23) as a stationary solution of the angular momentum equation varying from $\Omega \propto 1/R^2$ (negative shear) via rigid-body rotation to superrotation with positive shear. Also the radial profile of the azimuthal magnetic field is a function of two free parameters in accordance to (35). Among many other possibilities the examples of quasi-uniform fields ($\mu_B = 1$) and the z-pinch due to a uniform electric field ($\mu_B = 2$) will be discussed in detail.

8.1. Rigid rotation

The most prominent example of this class is formed by a rigidly rotating z-pinch due to an uniform axial electric current. It belongs to the Chandrasekhar-type flows, and has $m = 1$ as the only unstable mode. The eigenvalues Re and Ha for small Pm do not depend on Pm. Figure 84 shows the influence of the magnetic Prandtl number on the suppression of the instability by rigid rotation for three values of the gap width. It makes sense to interpret the results by means of the averaged Reynolds number $\overline{\mathrm{Rm}}$, because of the convenient possibility to define the magnetic Mach number as the ratio of $\overline{\mathrm{Rm}}$ and Ha. The dashed lines in the plots correspond to Mm = 1. The rotational suppression of TI in this representation is strongest for Pm = 1. For very small and very large Pm there is almost no rotational suppression of TI. In this sense the magnetic Prandtl number Pm = 1 plays an exceptional role. Depending on the

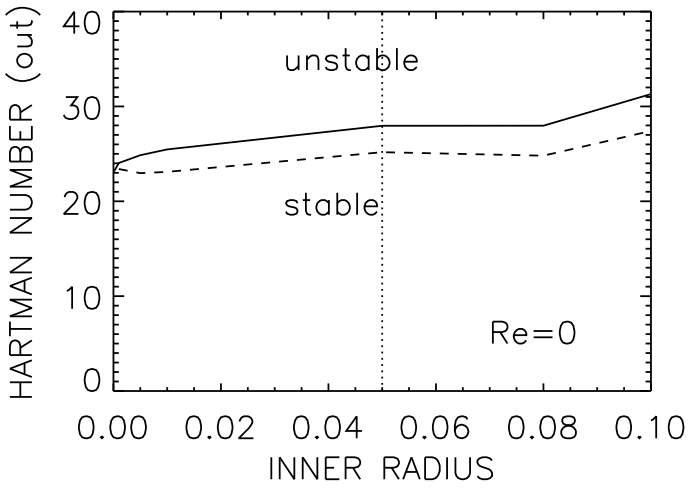

Figure 77. Outer Hartmann number (85) for z-pinches in wide gaps with $r_{\rm in} \le 0.1$. For $r_{\rm in} \to 0$ the values converge for perfectly conducting (solid line) and insulating (dashed line) cylinders. $\mathrm{Ha_{out}} = 28.4$ for $r_{\rm in} = 0.05$ (vertical dotted line) and conducting cylinders. All values independent of Pm. $\mu_B = 1/r_{\rm in}$. From [133].

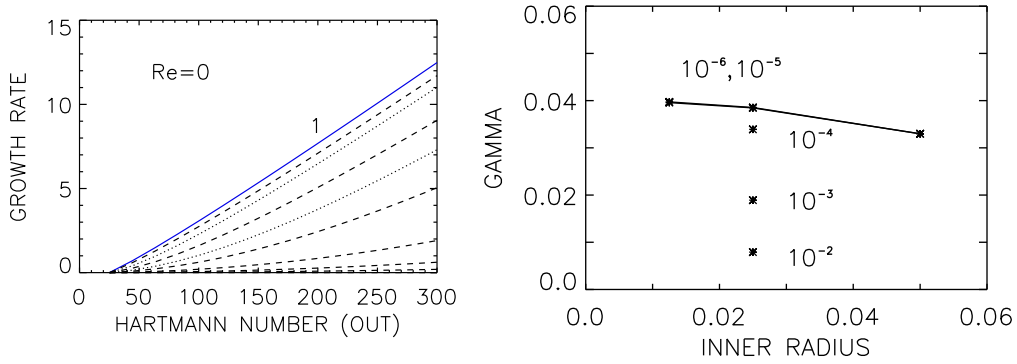

Figure 78. Left: as in Fig. 75 but for outer Hartmann numbers (85). $r_{\rm in} = 0.05$. Right: $\Gamma_{\rm gr}$ (marked with Pm) from Eq. (86) for various $r_{\rm in}$. $\Gamma_{\rm gr}$ for very small Pm results as almost independent of both parameters $r_{\rm in}$ and Pm. Pinch-type field with $\mu_B = 1/r_{\rm in}$, perfectly conducting cylinders. From [134].

magnetic Prandtl number a fluid with the same Reynolds numbers and Hartmann numbers can be stable or unstable. Clearly, for the magnetic Prandtl numbers used in Fig. 84 the Tayler instability for rigid rotation is a sub-Alfvénic phenomenon. For small Pm the lines of marginal stability move more and more below the dashed lines for Mm = 1, and for Pm $\to$ 0 the latter will never be crossed.

Figure 85 shows the influence of the magnetic Prandtl number on the strength of the rotational suppression for two different radial field profiles in the standard gap ($r_{\rm in} = 0.5$). The right panel shows the almost uniform field and the left panel the pinch-type field with uniform electric current. The magnetic Prandtl number varies over many orders of magnitude. The ordinary Reynolds number is used. The two standard values $\mathrm{Ha_0} = 35$ and $\mathrm{Ha_0} = 150$ for $r_{\rm in} = 0.5$ and for perfectly conducting cylinders appear. There are differences between the panels, but the common feature is that the rotational suppression becomes very weak for very small Pm. Note that in the left panel the stability curves for Pm $\to$ 0 converge, unlike the curves in the right panel. Only for this field profile does the magnetic Mach number $\mathrm{Mm} = \sqrt{\mathrm{Pm}}\mathrm{Re}/\mathrm{Ha}$ shift to zero for Pm $\to$ 0, as for $B_\phi \propto R$ and rigid rotation Re and Ha are independent of Pm for small Pm. Indeed, for $\mu_B = 2\mu_\Omega = 2$ the condition (76) of Chandrasekhar-type flows is satisfied, so that the convergence of the stability lines for small Pm in the (Ha/Re) plane is not surprising. It is not true for the alternative field profile with $\mu_B = 1$ (right panel of Fig. 85) which can thus easily reach super-Alfvénic values.

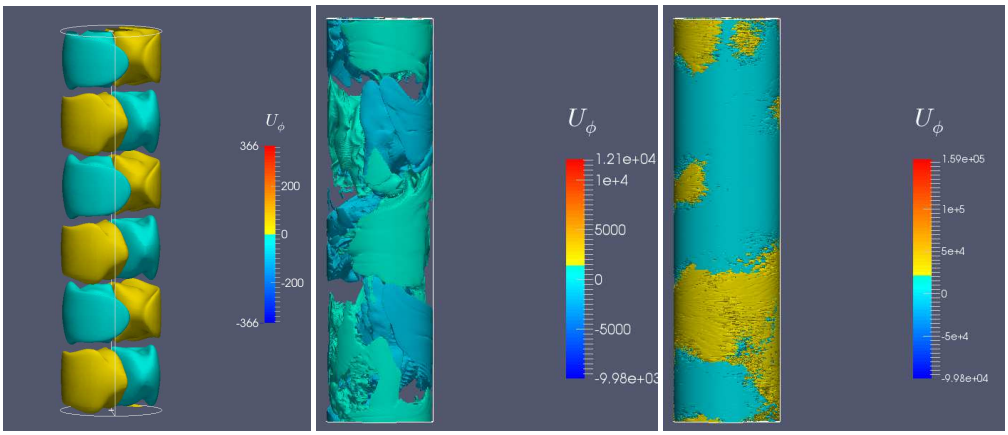

Figure 79. Azimuthal velocity component u_ϕ of the pinch-type instability for a wide gap. Left: $\mathrm{Ha_{out}} = 40$, middle: $\mathrm{Ha_{out}} = 200$, right: $\mathrm{Ha_{out}} = 600$. $r_{\mathrm{in}} = 0.05$, Re = 0, insulating cylinders, $\mathrm{Pm} = 10^{-5}$.

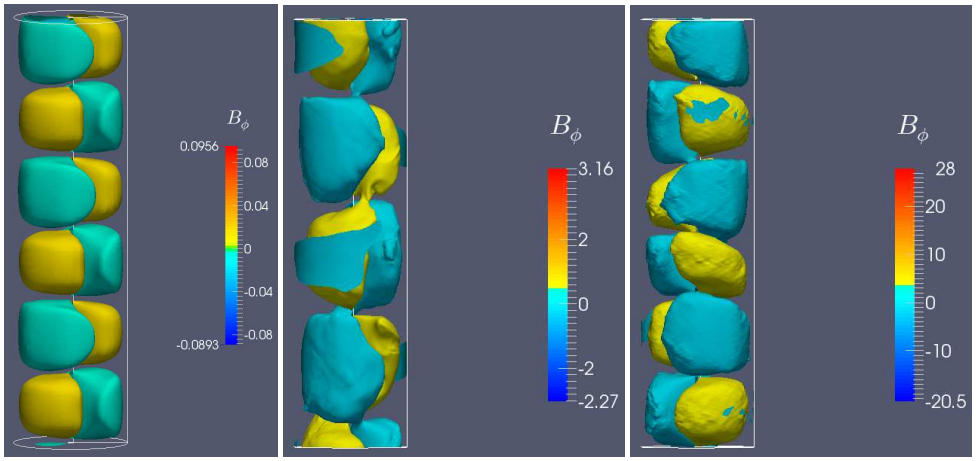

Figure 80. As in Fig. 79 but for the azimuthal magnetic component b_ϕ/B_{in}.

Figure 85 (left) provides another surprise. The plot demonstrates in the (Ha/Re) plane that the curves do not only converge for $\mathrm{Pm} \to 0$ but also for $\mathrm{Pm} \to \infty$. The rigidly rotating z-pinch with perfectly conducting cylinders, therefore, is stable for $\mathrm{Re} > \gamma\mathrm{Ha}$ where $\gamma = G$ is a large number for $\mathrm{Pm} \ll 1$ and a small number $\gamma = g$ (of order unity) for $\mathrm{Pm} \gg 1$. Hence, the pinch is stable if $\mathrm{Mm} > G\sqrt{\mathrm{Pm}}$ for $\mathrm{Pm} \ll 1$ and $\mathrm{Mm} > g\sqrt{\mathrm{Pm}}$ for $\mathrm{Pm} \gg 1$. The rigidly rotating z-pinch is thus more easy to keep stable for very small Pm while for very large Pm the stabilization needs very fast rotation.

Considered in the $(\mathrm{Ha}/\overline{\mathrm{Rm}})$ coordinate system the fluids with $\mathrm{Pm} \neq 1$ are less suppressed by rigid rotation than those with Pm = 1. Numerical simulations with Pm = 1 may thus be stable although the stability is lost for $\mathrm{Pm} \neq 1$. Instability for Pm = 1 requires fields with $\Omega_{\mathrm{A}} \geq \Omega_{\mathrm{in}}$ while much weaker fields become unstable for $\mathrm{Pm} \neq 1$.

8.2. *Differential rotation*

For the normalizations used in Fig. 75 the growth rates for the $m = 1$ instability of the stationary pinch are maximal for Pm = 1 but for the rigidly rotating pinch Pm = 1 leads to a maximal stabilization (Fig. 84). We shall find that also the combination of the almost uniform magnetic fields, $\mu_B = 1$, with differential rotation lead to a basic role of the magnetic Prandtl number. For perfectly conducting boundary conditions the critical Hartmann number for Re = 0 is $\mathrm{Ha}_0 = 150$ (see Fig. 50, left). The rotational stabilization of the toroidal fields depends on the form of the rotation profile. It is much weaker for subrotation, and stronger for rigid rotation (Fig. 86). For fixed Re the maximum

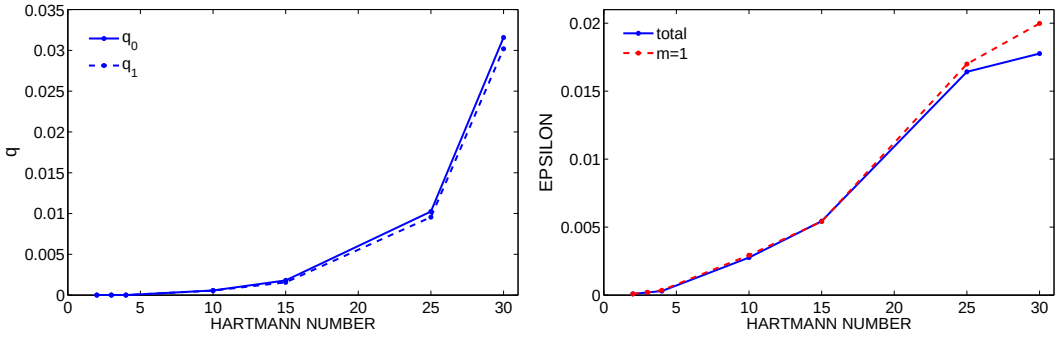

Figure 81. Stationary z-pinch with small Pm: dependence of q from (55) (left) and the ratio ε between magnetic and kinetic energies (right) on the Hartmann number. These results lead to the relation (88) between the magnetic energy and the microscopic magnetic Reynolds number Rm′. $\mu_B = 1/r_{\rm in}$, $r_{\rm in} = 0.05$, Re = 0, Pm = 10^{-5}, insulating cylinders.

field amplitudes which remain stable are much weaker for subrotation than for rigid rotation, hence rigid rotation stabilizes magnetic fields much more effectively. Note that the flow for $\mu_\Omega = 0.5$ in Fig. 86 belongs to the class of Chandrasekhar-type flows which for small Pm scale with Re and Ha, so that for Pm $\to$ 0 the instability is always sub-Alfvénic (see the nearly vertical dotted line in the plot for Mm = 1). Note also that the subcritical excitation with Ha < Ha_0 only occurs for rotation profiles steeper than $\mu_\Omega < r_{\rm in}$. The rotation law with $\mu_\Omega = r_{\rm in}$ is the rotation law with quasi-uniform linear velocity, $U_\phi \simeq$ const. The calculations show that for this particular rotation profile ($\Omega \propto 1/R$) the rotational support or suppression of TI is minimized for sufficiently slow rotation.

The existence of the phenomenon of missing rotational suppression is demonstrated in more detail by Figs. 87 for various magnetic fields and magnetic Prandtl numbers. Indeed, for small magnetic Prandtl number the lines of marginal stability become more and more perpendicular fulfilling the condition Ha $\simeq \mathrm{Ha}_0$. The entire domain with Ha > Ha_0 is unstable independent of the Reynolds number as long as the rotation is slow enough.

Figure 88 shows the results of varying rotation profiles on the z-pinch with uniform axial electric current ($\mu_B = 1/r_{\rm in}$) in a narrow gap. Rotation profiles with both negative and positive shear are considered. In this container the profile $\mu_\Omega = 0.5$ is centrifugally unstable even without magnetic fields, but note that the magnetic field destabilizes the flow. The other rotation laws are stable in the hydrodynamic regime. Rigid rotation and superrotation stabilize the field. For subrotation the behavior is opposite. While for rigid rotation and superrotation the critical Hartmann numbers grow for growing Reynolds number with Ha > Ha_0, for (slow) subrotation the associated Hartmann numbers represent subcritical excitation, i.e. Ha < Ha_0. Again, the characteristic rotation parameter $\mu_\Omega = r_{\rm in}$ separates the two regimes.

For Pm = 1 the influence of various rotation profiles is probed for pinches in a narrow gap with $r_{\rm in} = 0.95$. For slow rotation the quasi-Keplerian rotation with $\mu_\Omega = 0.92$ yields subcritical excitation (Ha < Ha_0) while flatter profiles and superrotation do not. It may be expected that strong rotational shear of any sign tends to suppress nonaxisymmetric patterns. We therefore expect that for sufficiently large Re the subrotation curves would eventually also turn over toward larger Hartmann numbers. As seen in Fig. 88 (right panel), this is indeed the case, for both rigid rotation *and* subrotation. Rigid rotation seems to be more effective in stabilizing the TI. The critical Hartmann numbers for instability are much higher for rigid rotation than for differential rotation. There is thus an extra destabilization effect of the differential rotation in the considered flows. The magnetic Mach number for strongest fields remain smaller than unity for rigid rotation, in opposition to subrotation where the given parameters yield Mm $\gg$ 1. However, the curves suggest that in all cases Mm < 1 for Ha $\to \infty$.

Figure 89 presents the instability map for the pinch-type field with quasi-Keplerian rotation in the standard gap with $r_{\rm in} = 0.5$, for various magnetic Prandtl numbers Pm $\leq$ 1. The critical Hartmann number for Re = 0 does not depend on the magnetic Prandtl number, but surprisingly the instability curves for all Pm < 1 also hardly differ if Re < 1000. As in Fig. 50 (left) the rotational suppression almost disappears for Pm < 1. For slow rotation and for Pm $\simeq$ 1 the instability even becomes subcritical (Ha < Ha_0), and the stabilization changes to a distinct destabilization. For faster rotation the subcritical excitation disappears, but the rotational suppression is weaker than for rigid rotation. For the phenomenon of subcritical excitation the influence of the magnetic Prandtl number is very strong. Note that

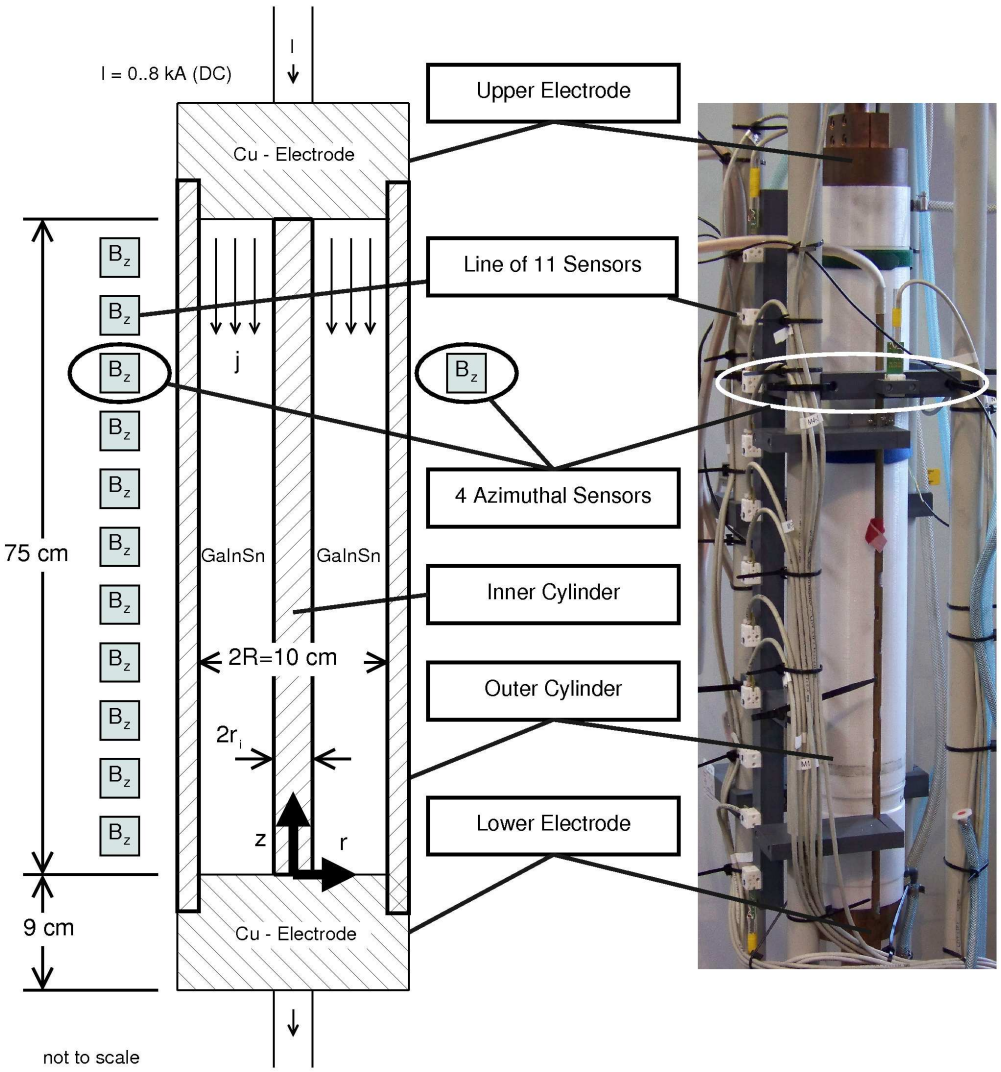

Figure 82. The construction of GATE as operated by the HZDR [136].

Pm = 0.1 already belongs to the small Pm regime where the subcritical excitations are very weak. Also here fluids with Pm = 1 behave exceptionally.

The flow pattern of the instability is shown in Fig. 90 for quasi-Keplerian rotation at three Reynolds numbers. The Hartmann number is fixed to Ha = 80. The magnetic Prandtl number Pm = 0.1 is already small, according to the classification in Fig. 89. The instability is nonaxisymmetric, the velocity amplitude increases linearly for rapid rotation, but the rms velocity decreases for faster rotation. This statement is supported by the behavior of the axial wavelength. Within the same interval the axial wavelength – which according to the Taylor-Proudman theorem should grow for faster rotation – also seems to jump by the same factor [137].

8.3. Superrotation

The stability of the almost uniform field $\mu_B = 1$ for rotation profiles with negative and positive shear is studied next, in dependence on the magnetic Prandtl number. For the narrow gap with $r_{\rm in} = 0.95$ Fig. 91 gives maps for Pm = 0.1, Pm = 1 and Pm = 10. The Hartmann number without rotation is $\mathrm{Ha}_0 \simeq 8945$. For Pm = 1 rigid-body rotation and superrotation are always stabilizing ($\mathrm{Ha} > \mathrm{Ha}_0$), opposite to subrotation with $\mu_\Omega < r_{\rm in}$. Sufficiently strong subrotation leads to subcritical excitation with $\mathrm{Ha} < \mathrm{Ha}_0$. Rotation laws with negative shear (here $\mu_\Omega = 0.93$)

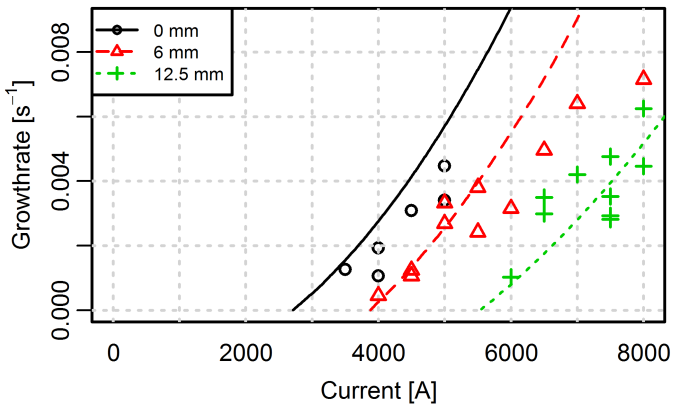

Figure 83. Observed and calculated growth rates for the stationary z-pinch for small $r_{\rm in}$ (black: $r_{\rm in} = 0$, red: $r_{\rm in} = 0.12$, green: $r_{\rm in} = 0.25$). The measured values do not exceed the calculated ones, indicating reasonable agreement between experiment and theory [133].

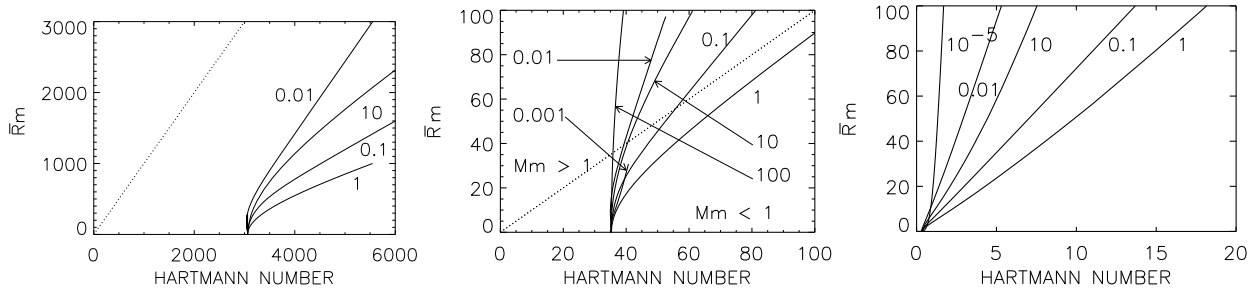

Figure 84. Suppression of TI by rigid rotation in z-pinches within a narrow gap (left, $r_{\rm in} = 0.95$), a medium gap (middle, $r_{\rm in} = 0.5$) and a wide gap (right, $r_{\rm in} = 0.05$) plotted in the (Ha/$\overline{\rm Rm}$) coordinates. The curves are marked with their magnetic Prandtl numbers. Pm = 1 always plays an exceptional role. For Pm $\neq$ 1 the supercritical Mach numbers are larger than for Pm = 1. $m = 1$, $\mu_B = 1/r_{\rm in}$, $\mu_\Omega = 1$. Perfectly conducting cylinders [102].

are strongly destabilizing. For small Pm the domain of stability in Fig. 91 is larger. For sufficiently rapid rotation, however, the lines for subrotation must also turn to the right, stabilizing the system, since strong shear of either sign always suppresses nonaxisymmetric patterns. The lines of marginal stability for rigid rotation and for superrotation lie below Mm = 1.

Note, however, that for both Pm > 1 (right panel) and Pm < 1 (left panel) and for slow rotation, the rotation profiles with positive shear lead to subcritical excitations, but not for Pm = 1. Superrotation can only provide subcritical excitation for $\nu \neq \eta$ (double-diffusive instability). The magnetic Mach number for the subcritical excitation and for both magnetic Prandtl numbers is only Mm $\simeq$ 0.05. The curves for rigid rotation and for superrotation are again always located below the line Mm = 1. To exist for Mm > 1 the TI needs the action of a differential rotation law with strong negative shear.

Superrotation at high Reynolds numbers is stabilizing for all Pm, with the effect greater for small Pm than for large Pm. For Pm = 10 the stabilization by superrotation is even weaker than that of rigid rotation. Here also large Pm destabilize nonuniform rotation, while small Pm stabilize them. The question arises about the possible existence of a minimum Hartmann number for steeper and steeper superrotation laws. The existence of such a limit is suggested by the suppression of nonaxisymmetric magnetic field perturbations by differential rotation whose effectiveness grows with increasing shear. The line of marginal stability can never cross the vertical axis, since nonmagnetically superrotation is always stable. Figure 92 for a z-pinch with uniform electric current shows converging lines up to $\mu_\Omega \to 128$, so that a minimum Hartmann number $\mathrm{Ha}_{\rm min}$ exists and can be estimated as smaller by a factor of three compared with $\mathrm{Ha}_0 = 3060$. For the small magnetic Prandtl number used for Fig. 92 (left) the ratio $\mathrm{Ha}_{\rm min}/\mathrm{Ha}_0$ is surprisingly small. For large Pm (right panel of Fig. 92, Pm = 10) the subcritical excitation also occurs with similar values. For larger Reynolds numbers almost all curves (except the curve for rigid rotation) are nearly identical; they only weakly depend

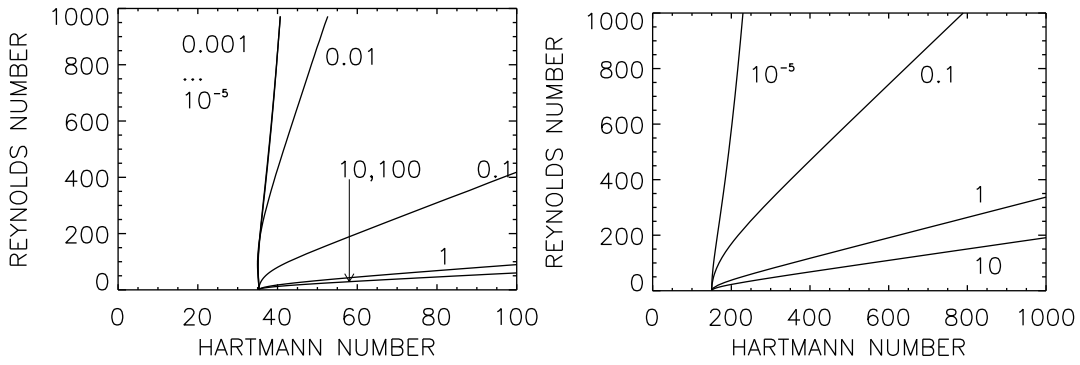

Figure 85. Stabilization by rigid rotation of fields due to uniform current ($\mu_B = 2$, left) and for quasi-uniform magnetic field ($\mu_B = 1$, right) for various Pm plotted in the (Ha/Re) plane. The parameters used for the left panel satisfy the Chandrasekhar condition (76). The curves converge in the (Ha/Re) plane for both limits Pm $\to 0$ and Pm $\to \infty$ (not true in the right panel). The maximum Mach number for unstable flows for Pm = 1 is Mm $\simeq 0.35$, they are larger for Pm $\neq 1$. $m = 1$, $r_{\rm in} = 0.5$, $\mu_\Omega = 1$, perfectly conducting boundaries.

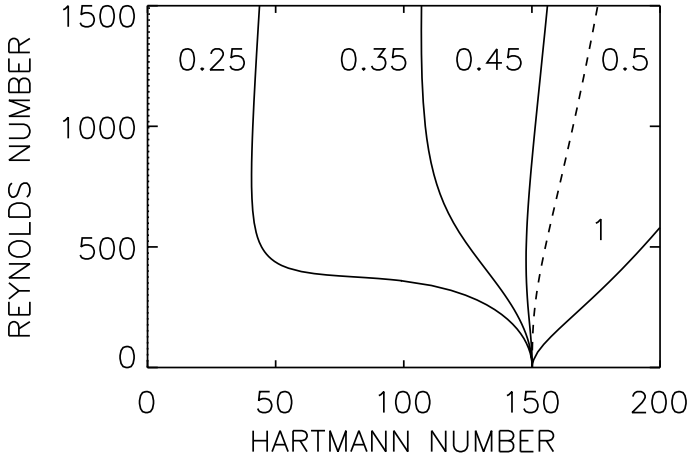

Figure 86. Stability map of the $m = 1$ mode for the quasi-uniform magnetic field subject to differential rotation for small Pm. The curves are marked with their values of μ_Ω. For slow rotation the rotation profile with $\mu_\Omega = r_{\rm in}$ yields a neutral line (dashed) between amplification and suppression of TI. As (only) this choice of μ_Ω fulfills the Chandrasekhar condition (76) the dashed line valids for all Pm $\ll 1$. For all eigenvalues we have Mm $\ll 1$. $m = 1$, $r_{\rm in} = 0.5$, $\mu_B = 1$, Pm $= 10^{-5}$. Perfectly conducting boundaries.

on the numerical values of shear and electric current. Compared with the curves for small Pm, however, the curves have a different form.

Another striking feature results from the comparison of Figs. 42 and Figs. 92, both for Pm $\neq 1$. For the rapid-rotation branches the dependence of the Reynolds number on the Hartmann number is extremely weak. These plots show that even the dependence of the eigenvalues on the radial profile of $B_\phi(R)$ is extremely weak. The lines of neutral stability of the flow with and without axial current for rapid rotation almost coincide. For positive shear and rapid rotation the presence of the electric current becomes irrelevant for the occurrence of an instability. One can show that all possible radial magnetic profiles between $B_\phi \propto 1/R$ and $B_\phi \propto R$ provide more or less the same instability curves, revealing that any differential rotation for Pm $\neq 1$ is able to deliver the entire energy for the maintenance of the instability patterns. The magnetic field only acts as a catalyst.

8.4. Influence of the boundary conditions

For wide gaps there is a surprisingly strong influence of the boundary conditions, similar to the combination of AMRI and superrotation (see Section 4.5.1). Figure 93 shows the stability maps for the standard container with $r_{\rm in} = 0.5$ for perfectly conducting and insulating cylinders. In both cases the superrotation laws are characterized by $1 \le \mu_\Omega \le 128$. For comparison also the rotation law with $\mu_\Omega = 0.25$ is used, which shows the instability-supporting

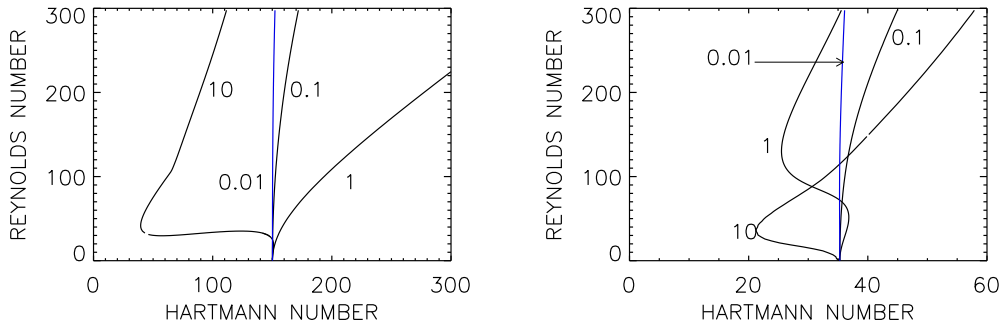

Figure 87. Stabilization by quasi-uniform flow with $\mu_\Omega = r_{\rm in}$ of the quasi-uniform magnetic field ($\mu_B = 1$, left) and of fields due to uniform current ($\mu_B = 2$, right) for various Pm (marked). The parameters used for the left panel satisfy the Chandrasekhar condition (76). For small magnetic Prandtl number the lines of marginal stability become perpendicular with Ha = Ha_0 (blue lines) hence the rotational suppression of TI disappears. The patterns of these modes are resting in the laboratory system. $m = 1$, $r_{\rm in} = 0.5$, perfectly conducting boundaries.

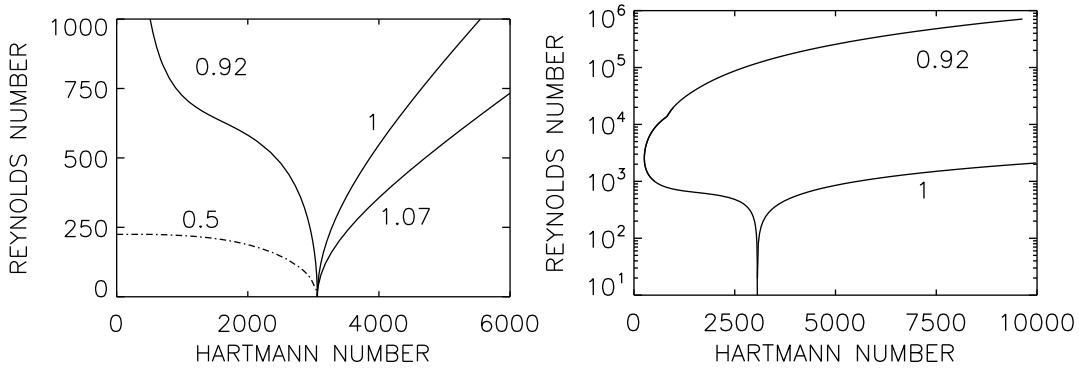

Figure 88. Stability maps for z-pinches in a narrow gap with differential rotation. Left: slow rotation, $\mu_\Omega = 0.5$ is hydrodynamically stable. $\mu_\Omega = 0.92$ represents quasi-Keplerian rotation. Right: rotational stabilization dominates for large Re in all cases. There are no line crossings. $m = 1$, $r_{\rm in} = 0.95$, $\mu_B = 1/r_{\rm in}$, Pm = 1. From [102].

behavior for both boundary conditions occurring for all rotation laws with negative shear. For positive shear, however, this behavior only exists for cylinders made from perfectly conducting material. With insulating boundary conditions the superrotation laws stabilize the pinch with the uniform electric-current (Ha > $\mathrm{Ha}_0 = 35$). Note the convergence of the eigensolutions for $\mu_\Omega \to \infty$. For large μ_Ω the Reynolds numbers taken for the outer cylinder also hold for the case of *stationary* inner cylinder.

9. Twisted fields

For combined axial and azimuthal background fields the nonaxisymmetric modes with m and $-m$ (corresponding to left and right spirals) differ in the excitation conditions. If the imposed field has both axial and azimuthal components, the system no longer exhibits $\pm z$ symmetry [113]. We shall see that for nonaxisymmetric modes, therefore, the $\pm z$ asymmetry of the background field breaks the $\pm m$ symmetry of the instabilities. Spiraling either in the same or the opposite sense of the twisted field geometry is possible. This azimuthal-symmetry breaking by helical background fields forms a characteristic difference between rapid rotation (AMRI) and slow rotation (TI). For rapid rotation the most unstable mode spirals opposite to the imposed field; for slow rotation it spirals in the same sense (see Fig. 96 below as an illustrative example).

We are interested in the linear stability of the background field $\boldsymbol{B} = (0, B_\phi(R), B_0)$ with $B_z = B_0$ =const. For the current helicity of the background field one finds $\mathrm{curl}\boldsymbol{B} \cdot \boldsymbol{B} = 2a_B B_0$, which may be either positive or negative. Both

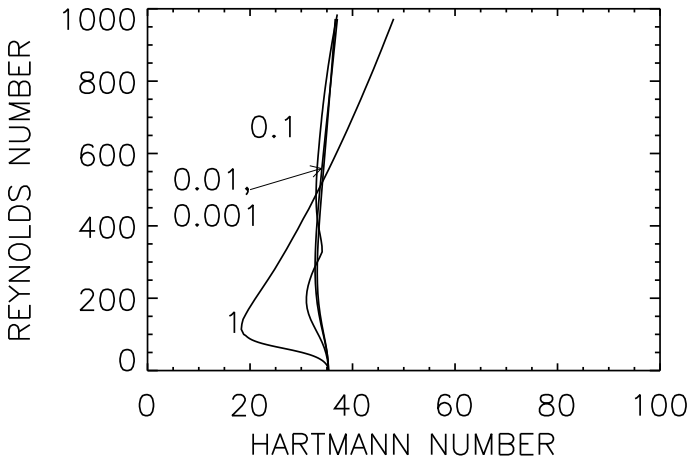

Figure 89. Stability map of the $m = 1$ mode of the z-pinch for quasi-Keplerian flow. The curves are marked with their values of Pm. The subcritical excitation with $\mathrm{Ha} < \mathrm{Ha}_0$ due to differential rotation disappears for $\mathrm{Pm} < 1$. $r_{\rm in} = 0.5$, $\mu_B = 1/r_{\rm in}$, $\mu_\Omega = 0.35$, perfectly conducting boundaries. From [137].

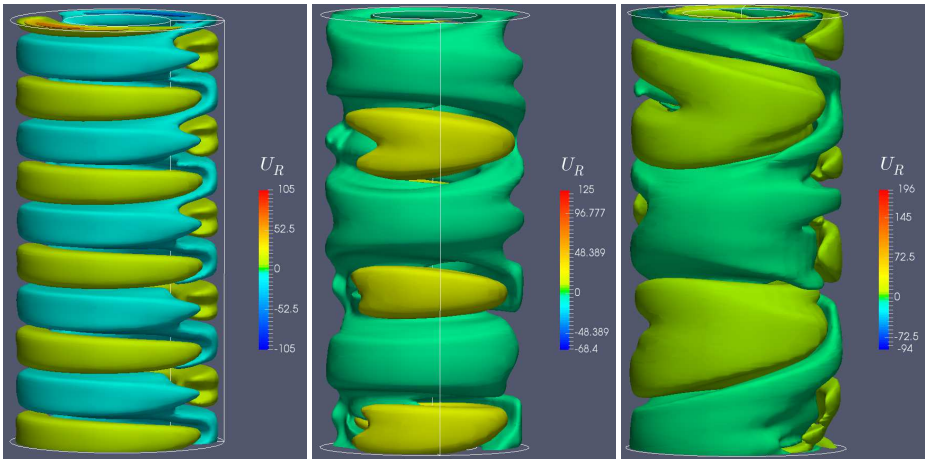

Figure 90. z-pinch and quasi-Keplerian rotation: isolines of u_R given as Reynolds numbers $\mathrm{Re}' = u_R R_0/\nu$ for Re = 500 (left), Re = 1000 (middle) and Re = 1500 (right). Ha = 80. $r_{\rm in} = 0.5$, $\mu_B = 1/r_{\rm in}$, $\mu_\Omega = 0.35$, Pm = 0.1. Perfectly conducting cylinders.

signs yield the same instability curves with left and right spirals interchanged. This current helicity vanishes for fields which are current-free between the cylinders ($a_B = 0$).

9.1. Quasi-uniform azimuthal field

Following Refs. [114, 139, 134] we start with the cases of nearly homogeneous azimuthal fields B_ϕ (i.e. $\mu_B = 1$) and later homogeneous electric currents (i.e. $\mu_B = 2$). As in (81) the inner field amplitude $B_{\rm in}$ will be normalized with the uniform axial field B_0. Then the current helicity of the background field is

$$\mathrm{curl}\boldsymbol{B} \cdot \boldsymbol{B} = \frac{2\beta}{3}\frac{B_0^2}{R_{\rm in}}. \tag{90}$$

The sign of β determines the sign of the helicity of the background field. Interchanging $\pm\beta$ simply interchanges left and right spirals. As an exception, for almost uniform azimuthal background fields with $\mu_B = 1$ both the Hartmann number and the ratio β can also be imagined to be formed with the outer field amplitudes. If the axisymmetric background field possesses positive B_ϕ and B_z then its current helicity is positive forming a right-hand spiral.

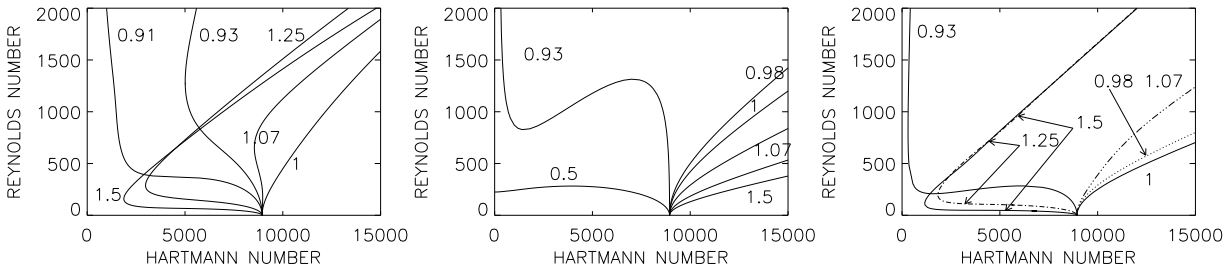

Figure 91. Quasi-uniform field and differential rotation of negative and positive shear in a narrow gap for Pm = 0.1 (left), Pm = 1 (middle) and Pm = 10 (right). The curves are marked with μ_Ω. $r_{\rm in} = 0.95$, $\mu_B = 1$, $m = \pm 1$, perfectly conducting boundaries. See the corresponding plots for the z-pinch with $\mu_B = 1/r_{\rm in}$ in Ref. [138].

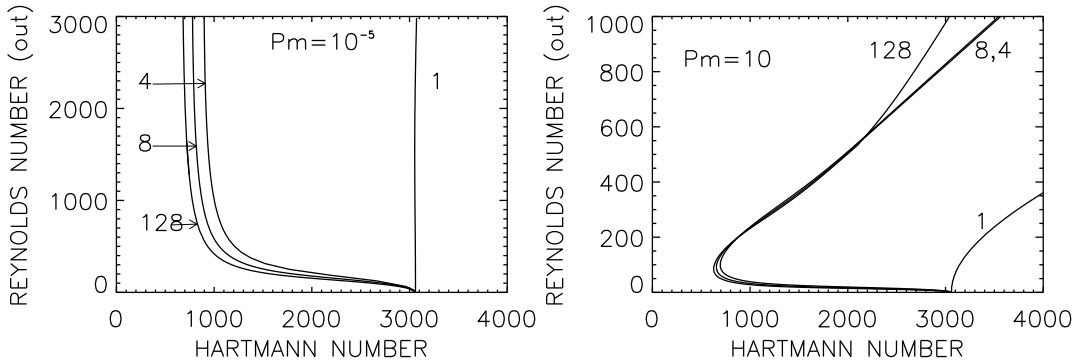

Figure 92. Stability curves of the z-pinch in a narrow gap subject to superrotation for small Pm (Pm = 10^{-5}, left) and large Pm (Pm = 10, right); the lines are marked with their values of μ_Ω. Note that the Reynolds numbers are defined with the *outer* rotation rate. $\mu_B = 1/r_{\rm in}$, $r_{\rm in} = 0.95$, perfectly conducting cylinders.

The phase relation (51) gives the angle between the components of the perturbation field patterns. If the axial wave number k is defined as a positive number (as we shall always do) then m must be allowed to have both signs. Negative m describe right-hand spirals, and positive m describe left-hand spirals.

The critical Hartmann numbers Ha_0 for nonrotating containers do not depend on Pm. Hence, the results for $\Omega = 0$ in Fig. 94 for the modes with $m = -1, \ldots, -5$ are valid for large magnetic Prandtl numbers and also for the small magnetic Prandtl numbers of liquid metals.

For $\mu_B = 1$, $m = 1$ and for perfectly conducting boundaries we have $\mathrm{Ha}_0 = 150$ for purely toroidal fields, i.e. $\beta \to \infty$. For decreasing β the critical Hartmann number is reduced to about 100. The most unstable mode is $m = -1$ for $\beta \gtrsim 8$. For β of order unity the mode with $m = -2$ yields the lowest Hartmann number. For $\beta \lesssim 0.4$ the mode with $m = -3$ starts to be preferred. Even higher m occur for smaller β but an increase of the axial field component ($\beta \ll 1$) is strongly stabilizing, more so as the normalized differences of the critical Hartmann numbers for various m become smaller and smaller. The energy needed to excite the nonaxisymmetric unstable modes grows strongly with decreasing β. If the axial field for $\beta < 2$ starts to dominate the azimuthal field then the system becomes more and more stable. In the limit $\beta \to 0$ there is no unstable mode remaining. These results do not change if formulated with the Hartmann number of the *axial* field rather than with the Hartmann number of the toroidal field. For positive β the twist of the background field is right-handed as is the twist of the most unstable modes. While without rotation for $B_z = 0$ no preferred helicity exists for the instability pattern, with axial field the resulting twist is the same as that of the background field.

If the nearly homogeneous field with $\mu_B = 1$ is subject to differential rotation with $\Omega \propto 1/R$, then the field and the flow belong to the Chandrasekhar-type considered in Section 5. For Pm $\to 0$ the corresponding eigenvalues Re and Ha no longer depend on Pm. For Pm = 1 the instability curves for $\mu_B = 2\mu_\Omega = 1$ are given in Fig. 95. For $\beta \lesssim 1$ the $m = 0$ mode yields the instability with the lowest Reynolds number. As in Fig. 50 for β of order unity a stability branch develops along the line for Mm = 1. We find for the AMRI domain (Mm > 1) that for large β the lowest

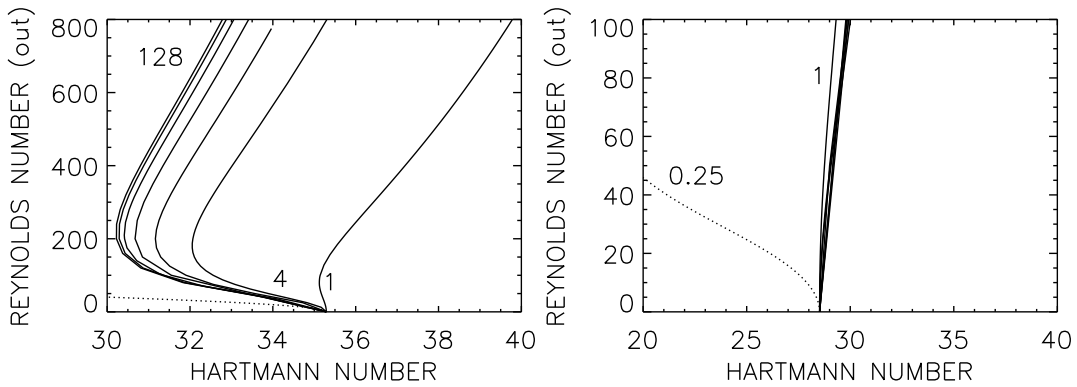

Figure 93. Stability maps of the z-pinch in a wide gap subject to superrotation for small Pm for perfectly conducting (left) and insulating (right) cylinders. The Reynolds numbers are defined with the outer rotation rate. The curves are marked with their values of μ_Ω. The solutions for rigid rotation ($\mu_\Omega = 1$) and for the potential flow ($\mu_\Omega = 0.25$) are given for comparison. Subcritical excitation ($\mathrm{Ha} < \mathrm{Ha}_0$) for superrotation does *not* exist for insulating boundary conditions. For subrotation ($\mu_\Omega = 0.25$) it exists independent of the boundary conditions. $r_{\rm in} = 0.5$, $\mu_B = 1/r_{\rm in}$, $\mathrm{Pm} = 10^{-5}$.

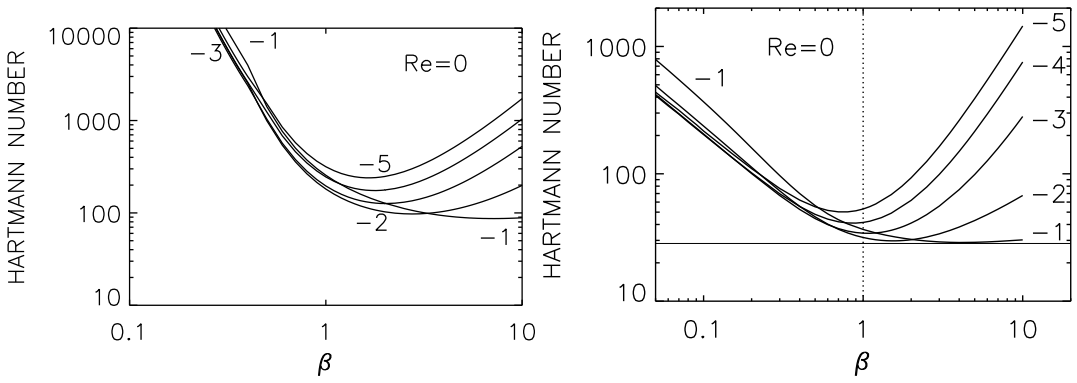

Figure 94. Twisted background fields: Hartmann numbers Ha_0 versus the ratio $\beta > 0$ for stationary cylinders. The curves are marked with m, they are invariant against the simultaneous transformation $m \to -m$, $\beta \to -\beta$. Twisted fields are more unstable than non-twisted fields. Strong axial magnetic field components have a stabilizing influence. $\mu_B = 1$ (left), $\mu_B = 2$ (right). All Pm, $r_{\rm in} = 0.5$, perfectly conducting cylinders. From [114].

Reynolds number belongs to nonaxisymmetric modes. The transition from nonaxisymmetry to axisymmetry can be accomplished simply by increasing the axial component of the background field. It is thus clear that there is a smooth transition from AMRI to the standard MRI.

The middle plot of Fig. 95 for β of order unity shows as Fig. 94 that the mode $m = -2$ indeed possesses lower Ha_0 than $m = -1$ (see [140]). Small shear and larger β, however, bring $m = -1$ back to the leading mode with the lowest critical Hartmann number.

Note also that the slopes of the lines in Fig. 95 change from positive for nonaxisymmetric modes to negative for axisymmetric modes. If the preferred modes with the lowest Reynolds numbers are nonaxisymmetric (for large β) then the spirals are always left-handed in the AMRI domain (Mm > 1) and right-handed in the TI domain (Mm < 1).

For nonlinear simulations we begin by noting that transforming $\beta \to -\beta$ has the expected result that positive/negative β do indeed yield right/left spirals. The helical structure of all solutions is clearly visible, dominated by low Fourier modes $m = 1$ and/or $m = 2$ in agreement with the linear analysis. The solutions are stationary, except for a drift in the azimuthal direction. Figure 96 (left) concerns the AMRI domain for fixed $\beta = 10$. One finds the expected $m = 1$ left-hand spirals in agreement with the linear results in Fig. 95. The nonaxisymmetric modes in the AMRI domain for large β have the signature $m = 1$. For the TI domain the most unstable mode is $m = -1$ for $\beta \gtrsim 10$ and $m = -2$ for $\beta \simeq 1$. Obviously, the unstable modes which characterize AMRI and TI according to the magnetic Mach number have different helicities. No mode mixture exists.

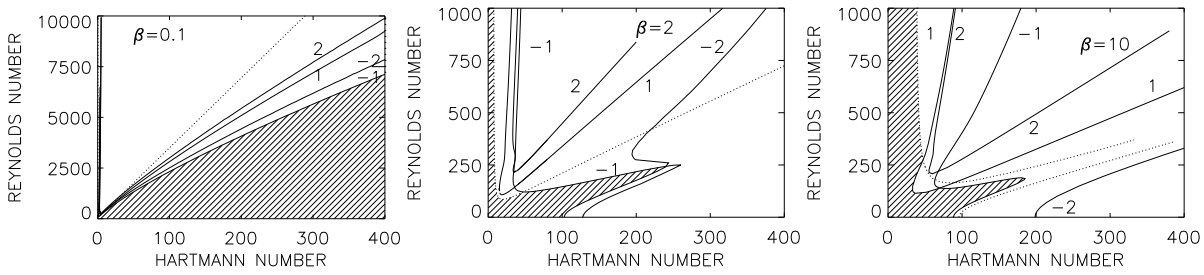

Figure 95. Stable (hatched) and unstable domains in the (Ha/Re) plane for quasi-uniform field and for various β. Left: $\beta = 0.1$, middle: $\beta = 2$, right: $\beta = 10$. The curves are marked with the azimuthal mode numbers m, for $m = 0$ the lines are dotted. Negative m stand for right-hand spirals and positive m stand for left-hand spirals. $r_{\rm in} = 0.5$, $\mu_B = 2\mu_\Omega = 1$, Pm = 1, perfectly conducting cylinders.

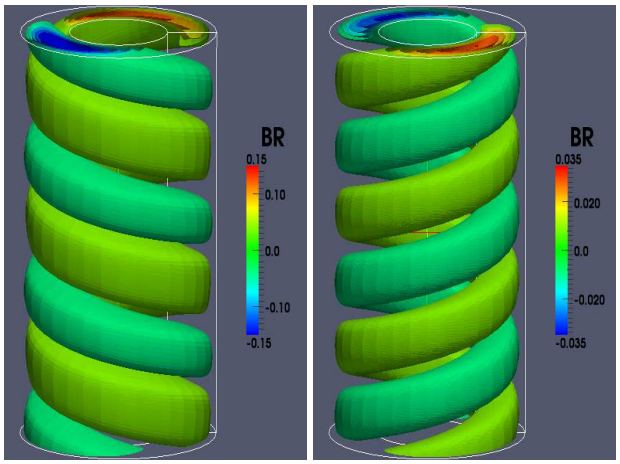

Figure 96. The radial component of the magnetic pattern for models taken from Fig. 95 (right, with $\beta = 10$). Left: AMRI with Re = 200 and Ha = 80 (Mm $\simeq$ 2.5). Right: TI with Re = 30 and Ha = 130 (Mm $\simeq$ 0.23). The fields are normalized with $B_{\rm in}$. $\mu_B = 2\mu_\Omega = 1$, Pm = 1, perfectly conducting cylinders. Adapted from [114].

The simulations also provide the amplitudes of the kinetic helicity $\langle \boldsymbol{u} \cdot \mathrm{curl}\, \boldsymbol{u} \rangle$ of the perturbations (averaged over ϕ). The two models of Fig. 96 with positive $\beta = 10$ provide negative values of order of $\langle \boldsymbol{u}^2 \rangle / R_0$. The signs of the kinetic helicity and the current helicity of the background field are opposite. According to Fig. 96 AMRI with Mm > 1 produces instability patterns with higher field strengths than TI with Mm < 1 does. This effect may be due to the action of the differential rotation. Indeed, the magnetic energy q (normalized with $B_{\rm in}^2$) calculated with the amplitudes of both examples differs by a factor of almost 20, which is just of the order of the ratio of the two magnetic Mach numbers.

9.2. *Uniform axial current*

We turn next to the pinch-type field due to a uniform electric current, Ref. [134]. Without rotation the critical Hartmann number Ha_0 does not depend on Pm and the azimuthal drift of the nonaxisymmetric instability pattern vanishes. We also know that for the nonaxisymmetric mode with $|m| = 1$ for very large β we have $\mathrm{Ha}_0 = 35$ for $\mu_B = 2$. This value is reduced if a small uniform axial field is added to the system. The axial field supports the pinch-type instability of the toroidal field. The critical Hartmann number reduces to $\mathrm{Ha}_0 \simeq 30$. However, for $|m| > 1$ the destabilization of the toroidal field by axial fields is much stronger, so that for β of order unity all modes with different mode numbers m possess the same critical Hartmann number. We thus find a destabilizing effect by axial fields components compared to fields of purely toroidal fields. If B_ϕ and B_z are of the same order then the field is more unstable than it is for $B_z = 0$ or $B_\phi = 0$.

For $\beta = 4$ we find $\mathrm{Ha}_0 = 29$ as the absolute minimum of the stability curve for $m = -1$. For stronger axial fields, the critical Hartmann number increases strongly to reach values of about 500 for $\beta \simeq 0.1$. Again, for strong axial

fields the modes with $m < -1$ possess *lower* critical Hartmann numbers than those with $m = -1$. For the smallest β in Fig. 94 (left) the $m = -4$ mode possesses the lowest critical Hartmann number. However, the pinch-type instability of toroidal fields in the presence of a uniform axial magnetic field without rotation is strongly suppressed by strong axial fields. The maximal stabilization happens for $m = -1$. With a sufficiently strong axial field rather strong toroidal fields can be stabilized.

The growth rates in units of the diffusion frequency $\omega_\eta = \eta/R_0^2$ for fixed $\beta = 1$ and Pm $= 1$ are plotted in the left panel of Fig. 98. The plot clearly demonstrates that the growth rates scale with the Hartmann number. For stronger fields, differences for the growth rates of various m appear. One finds the maximum growth rates belonging to azimuthal wave numbers $|m| > 1$.

These findings are confirmed by numerical simulations of the instability. They show the dependence of the handedness of the patterns on the sign of the helicity of the background field, i.e. the sign of β (Fig. 97). There is no clear dependence of the results on the magnetic Prandtl number. The main result concerns the azimuthal wave number m. The nonlinear simulations indeed show the prevalence of the higher modes $m = -3$ or $m = -4$ within the instability patterns. While the instability pattern of the nonrotating pinch with $B_z = 0$ is dominated by the mode with $|m| = 1$, the addition of a uniform axial field leads to the excitation of much more complex instability patterns.

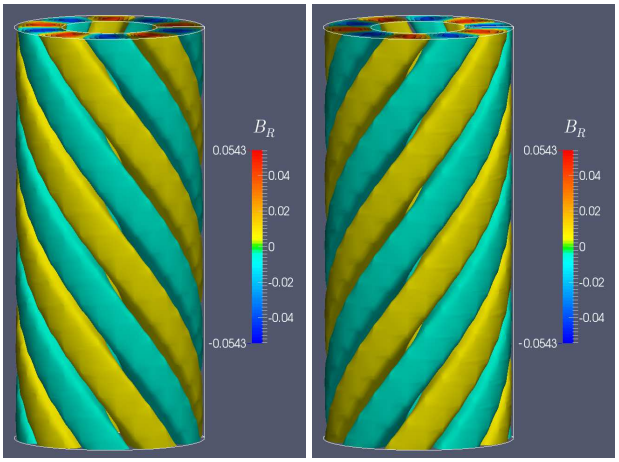

Figure 97. Numerical simulation of the instability patterns of a twisted background field of pinch-type without rotation with $\beta = -0.5$ (left) and $\beta = 0.5$ (right). The signs of the helicities of background field and instability always coincide. $r_{\rm in} = 0.5$, $\mu_B = 1/r_{\rm in}$, Re $= 0$, Ha $= 150$, Pm $= 0.1$.

Rigid rotation stabilizes the magnetic perturbations while differential rotation supports the instability. For the z-pinch with $\mu_B = 2$ the growth rates were calculated for supercritical Ha and for $\beta = 1$ (Fig. 98, left). The critical Ha_0 for $\beta = 1$ is ~ 35. For Ha $= 80$ one finds positive growth rates for slow rotation while for rapid rotation there is stability. For Re $= 0$ the mode with $m = -3$ grows fastest. The instability does not survive for Mm > 1. The mode with $m = -1$ withstands the rotational suppression best. The modes with the highest m are already suppressed by lower Reynolds numbers. The dominance of the modes with $|m| > 1$ disappears for rigid rotation. Note that the pinch with $\mu_B = 2\mu_\Omega = 2$ is a Chandrasekhar-type flow which for Pm $\to 0$ scale with Ha and Re. The only unstable mode is $|m| = 1$.

Another situation holds for nonuniform rotation. The growth rates for Ha $= 80$ and the rotation law with $\mu_B = 0.5$ are given in the right panel of Fig. 98. The slow rotation curve is almost identical to the rigid rotation curve. The modes are rotationally stabilized. Only $|m| = 1$ has positive growth rate for all rotation rates. Modes with $|m| > 1$ do not contribute to the instability for high Reynolds numbers because they are damped by strong differential rotation. For Mm $\gtrsim 1$, however, the magnetic instability is re-animated, but at most for the lower modes including the axisymmetric MRI mode with $m = 0$. Finally the $m = 0$ mode becomes dominant because its growth rate becomes higher and higher, finally scaling with the rotation frequency. For Mm > 1 the growth rate increases with increasing Ω rather than with $\Omega_{\rm A}$.

The dependence of the growth rates on the magnetic Prandtl number is a puzzling problem which can be demonstrated by use of new variables. Figure 99 (left) demonstrates for stationary flows that the mode with $|m| = 1$ grows

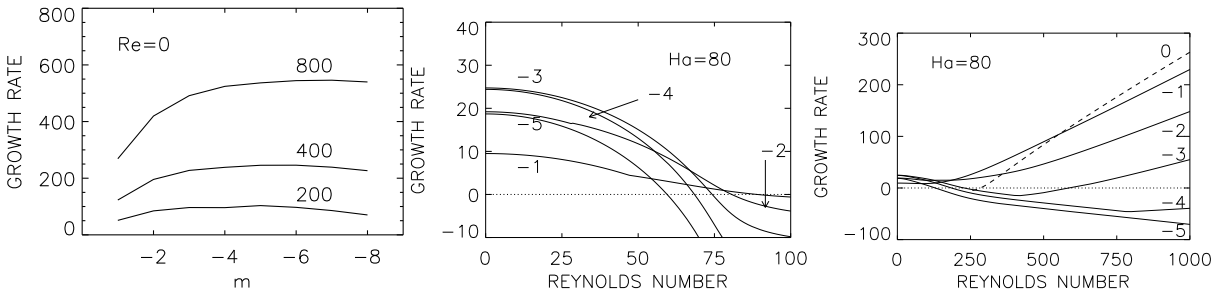

Figure 98. Growth rates normalized with the resistivity frequency ω_η without rotation (left) and under the influence of rigid rotation ($\mu_\Omega = 1$, middle) and differential rotation ($\mu_\Omega = 0.5$, right). The dashed line represents the growth rates for the axisymmetric MRI mode $m = 0$. The curves are invariant against the simultaneous transformation $m \to -m, \beta \to -\beta$. $r_{\rm in} = 0.5$, Ha = 80, $\mu_B = 1/r_{\rm in}$, $\beta = 1$, Pm = 1. See [134].

fastest for Pm = 1 if the growth rate is normalized with the geometrical average $\overline{\eta} = \sqrt{\nu\eta}$ of both diffusivities. A flow can thus be unstable for Pm = 1 whereas it is stable for Pm $\neq$ 1.

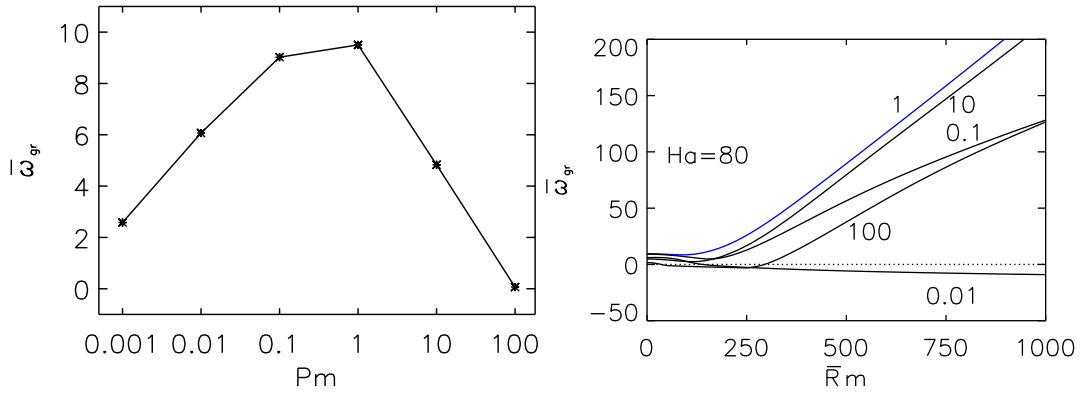

Figure 99. As in Fig. 98 but only for $m = -1$ and in unit of the dissipation frequency $\overline{\omega} = \sqrt{\omega_\nu \omega_\eta}$ (symmetric in ν and η) in dependence on the magnetic Prandtl number. Left: stationary cylinders, Re = 0, see Fig. 78 (left). Right: quasi-uniform flow, $\mu_\Omega = 0.5$. The curves are marked with Pm. In both cases the fastest growth of the perturbations belongs to Pm = 1. Ha = 80, $\beta = 1$. $r_{\rm in} = 0.5$, $\mu_B = 1/r_{\rm in}$, perfectly conducting cylinders.

For differential rotation with $\mu_\Omega = 0.5$ (almost uniform U_ϕ) the right panel of Fig. 99 gives the growth rates for a supercritical Hartmann number. The growth rates of the mode $m = -1$ and the global rotation rate are again normalized with $\overline{\eta}$. One again finds that with the special normalization models with Pm = 1 always have maximum growth rates for slow and fast rotation. Both small or large magnetic Prandtl numbers lead to slower growth of the instability. This effect is so strong that the considered field pattern can even be stabilized for too small or too high Pm. This is a remarkable restriction for numerical simulations with Pm = 1. Magnetic instability strongly depends on the magnetic Prandtl number of the fluid. For a fixed Hartmann number two regimes for the rotational influence on the growth rates exist. There is only a weak influence of small $\overline{\rm Rm}$ on the growth rate. For large averaged Reynolds numbers $\overline{\rm Rm}$ one finds linearly increasing growth rates. High values of $\overline{\rm Rm}$ strongly accelerate the instability in accordance with $\overline{\omega} \propto \overline{\rm Rm}$, which leads to $\omega_{\rm gr} \propto \Omega_{\rm in}$. In this case the physical growth rate results in $0.2\Omega_{\rm in}$, so that the growth time is shortened by the rotation to approximately only one rotation time.

10. Transport coefficients

First estimates of the perturbation velocity and the cell size for the unstable pinch can be taken from Fig. 90. The vertical cell size roughly equals the gap width, and for the Reynolds number of the fluctuation, ${\rm Re}' = u_{\rm rms} D/\nu$, the value 10 is provided. One obtains 10ν for the product of flow speed and cell size, which is often used as a first orientation for the viscosity or the resistivity of a turbulent fluid. Taking into account the standard correction factor of

order 0.1 then the value for the instability-generated diffusivities is only $\eta_T \sim \nu$ which is certainly a rather small value. We shall probe the relation of the eddy diffusivities to the pinch parameters in the following with more sophisticated methods.

10.1. Electromotive force

By definition, the eddy diffusivity connects the turbulence-induced electromotive force with the axial electric current in the pinch, i.e.

$$\langle \boldsymbol{u} \times \boldsymbol{b} \rangle = -\eta_T \,\mathrm{curl}\, \boldsymbol{B}, \tag{91}$$

where for simplicity all possible anisotropies due to rotation and magnetic field are ignored, see [141, 142, 143]. The axial component of the electromotive force is $\mathcal{E}_z = \langle u_R b_\phi - u_\phi b_R \rangle$, hence

$$\eta_T = R_{\rm in} \frac{\langle u_\phi b_R - u_R b_\phi \rangle}{2B_{\rm in}} \, \frac{1 - r_{\rm in}^2}{\mu_B r_{\rm in} - r_{\rm in}^2}. \tag{92}$$

As the angular momentum transport is also due to the Maxwell stress of the fluctuations, the turbulent viscosity should always exceed the molecular viscosity. The question is whether this is also the case for the instability-induced magnetic resistivity. First nonlinear simulations for not too small magnetic Prandtl numbers revealed the axial component of (91) as negative in the entire container, which ensures the expression (92) as positive definite [144]. The resulting eddy resistivity η_T did not depend strongly on the magnetic Prandtl number and the Reynolds number of rotation. The new simulations presented below in particular focus on the influence of the strength of the background field. Of course, the applied magnetic field must be due to an axial current; calculations for pure AMRI are thus not possible.

10.1.1. Stationary pinch

We start with the stationary pinch with $\mu_B = 1/r_{\rm in}$ (which strongly simplifies (92)) for various magnetic field amplitudes. Figure 100 presents snapshots of the non-averaged axial EMF for two models with one and the same Ha but different magnetic Prandtl numbers.

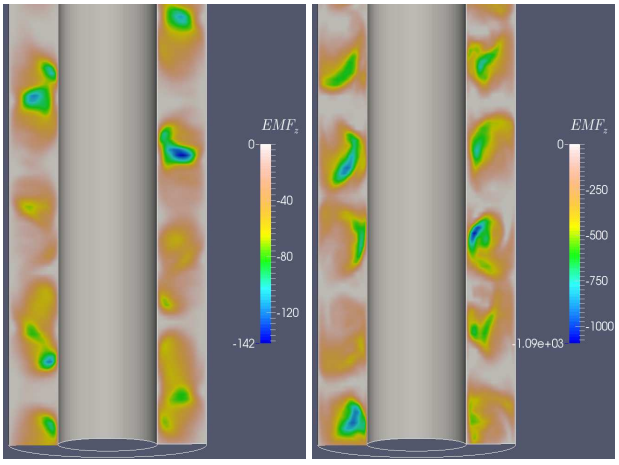

Figure 100. Axial component $u_R b_\phi - u_\phi b_R$ of the electromotive force for the stationary z-pinch with Pm = 0.1 (left) and Pm = 0.012 (right). The fluctuations are always negative. Ha = 100, $r_{\rm in} = 0.5$, $\mu_B = 1/r_{\rm in}$. Insulating boundary conditions.

The fluctuating axial EMF values are always negative. The dependence on the magnetic Prandtl number seems to be strong in the sense that the values scale with 1/Pm. This is also shown by the radial profiles of the axial EMF after averaging over all snapshots and the meridional planes.

Figure 101 gives the resulting eddy resistivity (92) for various magnetic Prandtl numbers as a function of the Lundquist number S for stationary and differentially rotating cylinders. In this representation the influence of the

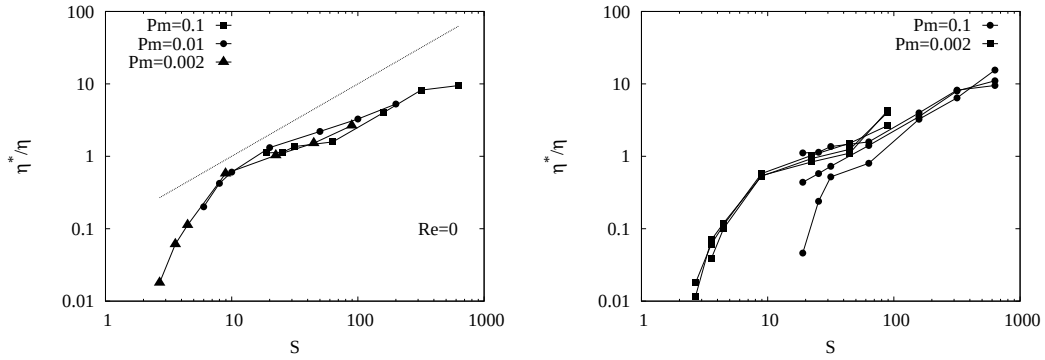

Figure 101. Instability-induced resistivity η_T/η for the z-pinch as a function of the Lundquist number for various Pm. Left: Re = 0, the dotted line gives S/10. Right: Influence of differential rotation for Re =0, 500 and 1000 for large and small Pm. The influence of slow rotation is only weak. $r_{in} = 0.5, \mu_\Omega = 0.35, \mu_B = 1/r_{in}$.

magnetic Prandtl number almost vanishes. This is because of the fact that the normalization used in Fig. 100 also scales with 1/Pm.

For small S the curve seems to scale with S^4, while a much flatter linear dependence on S appears for models with S > 10. The form of the curve even suggests a saturation of η_T/η for very large S. For those central parts of the curve where $\eta_T/\eta \propto S$, the eddy resistivity loses its dependence on the molecular diffusivity, so that simply $\eta_T \propto \Omega_A R_0^2$ with the Alfvén frequency $\Omega_A = B_{in}/\sqrt{\mu_0 \rho R_0^2}$. On the other hand, if by Eq. (89) $S \propto Rm'^{0.4}$, then for the medium parts of the plots one finds

$$\frac{\eta_T}{\eta} \simeq 0.7\, Rm'^{0.4}. \tag{93}$$

For the steep weak-field part of the profile with S^4 this yields $\eta_T/\eta \propto Rm'^{1.6}$. Very similar relations have also been found empirically with liquid-metal experiments [145].

The values of η_T/η for the stationary pinch are numerically small. For the smallest S the eddy resistivity is $\eta_T \ll \eta$, while even the much larger fields with $S \simeq 1000$ only yield $\eta_T/\eta \simeq 10$. The transition $\eta_T \simeq \eta$ happens at $S \simeq 30$, this value only depending on the value of r_{in}. As the typical Lundquist number for experiments with liquid metals does not exceed unity, one can hardly expect to find values of $\eta_T > \eta$ [146, 147, 145, 148, 149, 150].

10.1.2. Quasi-Keplerian flow

We find the influence of differential rotation on the resulting resistivities to be weak. The right panel of Fig. 101 shows results of simulations for the Reynolds numbers Re = 500 and 1000 for quasi-Keplerian rotation, in comparison with Re = 0. For small Pm these lines are almost identical. A rotational suppression is only visible for small S *and* large Pm. The latter finding means that the quenching certainly scales with Rm rather than with Re. The molecular viscosity, therefore, does not appear anywhere in the results for the instability-induced resistivity and its rotational quenching. A rough description of the results is given by $\eta_T/\eta \simeq 0.1S$, again leading to $\eta_T \simeq 0.1\Omega_A R_0^2$.

10.2. Angular momentum transport

To calculate the eddy viscosity the relation (61) can be used for the instability of toroidal background fields. It is sufficient to compute the angular momentum transport (60) for various μ_B. The angular momentum transport should change its sign for uniform rotation; it indeed is positive for negative shear profiles, and negative for positive shear profiles [151].

The model already discussed in Fig. 101 for the z-pinch in the presence of quasi-Keplerian rotation will now be applied to the calculation of the eddy viscosity. In dimensionless form it is

$$\frac{\nu_T}{\nu} = \frac{1}{q\mathrm{Re}}\langle u_R u_\phi - \frac{\mathrm{Ha}^2}{\mathrm{Pm}} b_R b_\phi \rangle \tag{94}$$

with the radial function q

$$q = -\frac{R}{\Omega_{\rm in}}\frac{{\rm d}\Omega}{{\rm d}R}. \tag{95}$$

The flow components are here measured as Reynolds numbers, and the field components are normalized with $B_{\rm in}$. For the quasi-Keplerian flow a simple approximation is $q = 1.5\Omega/\Omega_{\rm in}$ which for $r_{\rm in} = 0.5$ is of order unity. Figure 102 leads to the estimate $q\nu_{\rm T}/\eta \simeq 0.01$ S or simply to $\nu_{\rm T} \simeq 0.01\Omega_{\rm A}R_0^2$.

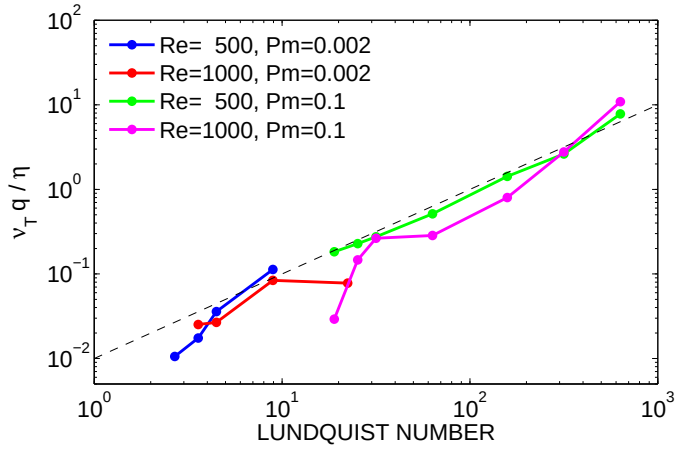

Figure 102. The quantity $q\nu_{\rm T}/\eta$ for quasi-Keplerian rotation as a function of S, similar to Fig. 101. The dotted line gives S/100. $r_{\rm in} = 0.5$, $\mu_B = 1/r_{\rm in}$, $\mu_\Omega = 0.35$.

For the instability-induced magnetic Prandtl number one immediately finds $\nu_{\rm T}/\eta_{\rm T} \simeq 0.1/q$, independent of Pm. The magnetic Prandtl number due to the pinch-type instability does not exceed unity. This is unexpected as for driven turbulence the eddy viscosity is formed by both the Reynolds stress and the Maxwell stress, while only the kinetic energy contributes to the eddy diffusivity [72]. Hence, one should expect the turbulent Prandtl number to be larger than unity, which is not the case though for these magnetically-induced instabilities.

10.3. Mixing of a passive scalar

The transport of a passive scalar is governed by the diffusion equation

$$\frac{\partial \rho C}{\partial t} + {\rm div}\,(\rho C\boldsymbol{u} - \rho D\boldsymbol{\nabla} C) = 0, \tag{96}$$

where C is the concentration, and D the microscopic diffusion coefficient. For $D \to \infty$ all possible fluctuations are immediately smoothed out and any mean-field transport decays. The adiabatic approximation requires $D = 0$. In the sense of the anelastic approximation we shall always apply the source-free condition of the mass flux, ${\rm div}\,\rho\boldsymbol{u} = 0$. The concentration is split into a mean and a fluctuating part, so that the diffusion equation in the presence of turbulence becomes

$$\frac{\partial \rho C}{\partial t} + {\rm div}\,(\rho\langle c\boldsymbol{u}\rangle - \rho D\boldsymbol{\nabla} C) = 0 \tag{97}$$

with c and $\boldsymbol{u}$ as the fluctuations of the concentration and the flow. The influence of a possible meridional circulation is neglected here. We have thus to compute the turbulent concentration flux vector $\langle c\boldsymbol{u}\rangle$, which is necessary to formulate the mean-field diffusion equation. In the sense of Boussinesq the concentration-flux vector may be written as an anisotropic diffusion in terms of the mean concentration gradient, i.e.

$$\langle cu_i\rangle = -D_{ij}\frac{\partial C}{\partial x_j}, \tag{98}$$

[59]. This is only reasonable, of course, if scales are considered which exceed the correlation scales (in space and time). The framework of magnetically-induced instabilities may well serve as a tool to study the various approximations of the diffusion theory in detail.

A basic anisotropy results if the turbulence is subject to a global rotation. Then the structure of the diffusion tensor is

$$D_{ij} = D_{\rm T}\,(d_1\delta_{ij} + d_2\Omega_i\Omega_j), \tag{99}$$

which describes an extra diffusion in the z-direction as a consequence of the Taylor-Proudman theorem. Terms linear in Ω do not exist.

Note that the material mixing results only by the action of the kinetic part of the momentum transport tensor rather than by its magnetic part, so that the diffusion tensor can be approximated by

$$D_{ij} \simeq \frac{1}{2}\tau_{\rm corr}\,\langle u_i(\boldsymbol{x},t)u_j(\boldsymbol{x},t)\rangle. \tag{100}$$

There is no magnetic influence on the diffusion coefficient except the magnetic suppression of the correlation tensor of the fluctuations. A nonlinear code must be used to compute the eddy diffusion of a passive scalar in the radial direction. The dimensionless transport equation

$$\frac{\partial C}{\partial t} + {\rm div}(C\boldsymbol{U}) = \frac{1}{\rm Sc}\Delta C \tag{101}$$

for the concentration C of the passive scalar is added to the equation system. The microscopic Schmidt number

$${\rm Sc} = \frac{\nu}{D} \tag{102}$$

is used in Eq. (101) with D as the molecular diffusivity of the fluid. Almost all of the existing simulations work with Sc = 1, e.g. [152]. The Schmidt number for gases is of order unity, while for fluids it is $O(100)$. In the present Section the molecular Schmidt number is varied from Sc = 0.1 to Sc = 2. The effective diffusivity can be modeled by the sum $D_{\rm eff} = D + D_{\rm T}$, where $D_{\rm T}$ is due only to the magnetically-induced instability.

To find $D_{\rm T}/D$ a numerical simulation is performed until the instability is fully developed. Then the transport equation (101) is switched on and several models with different Sc numbers are simulated for quasi-Keplerian rotation and with Pm = 0.1. The simulations indicate that $D_{\rm T}/D$ always scales linearly with Sc, so that the striking relation $D_{\rm T} \propto \nu$ results for Sc > 0.1. As it must, the effect vanishes for Sc $\to 0$. Schatzman suggested such a relation $D_{\rm T} = {\rm Re}^*\,\nu$ with ${\rm Re}^* = O(100)$ in order to explain diffusion processes in radiative zones of stars [153, 154, 155, 156]. Obviously, the factor Re*, which in a wider sense can be considered as a microscopic Reynolds number (of a pattern cell) can be computed as due to magnetic instability with the presented models. For slow rotation, Re* scales linearly with Mm, then reaches a maximum at Mm $\simeq 2$, and finally decreases rapidly for larger Mm, saturating around Re$^* = 1$ (Fig. 103, left). The magnetic Mach number Mm represents the global rotation in relation to the magnetic field strength.

In the right panel of Fig. 103 all models simulated in Ref. [137] are summarized, showing $D_{\rm T}/\eta$ as functions of S. Nonrotating models are marked in red, and are located among the other models. The dotted line represents the relation $D_{\rm T}/\eta = 0.01{\rm S}$ or $D_{\rm T} \simeq 0.01\Omega_A R_0^2$, similar to Fig. 102 for the instability-induced viscosity. The corresponding Schmitt number resulting from the simulations of differentially rotating z-pinches is thus also of order unity.

11. Helicities, alpha effect

Numerical simulations have shown that the MRI alone should be sufficient for the operation of the accretion disk dynamo [157, 158]. For low Pm it remained uncertain though whether the MRI dynamo has physical or numerical origin [159]. Another possibility was discussed by Spruit who suggested that differential rotation and TI can jointly drive a dynamo [160, 161]. Radial displacements converting toroidal into poloidal field are necessary for any dynamo. However, a dynamo effect is not guaranteed by the joint action of differential rotation and a magnetic instability converting toroidal field into poloidal. There are doubts especially concerning the TI which, in contrast to MRI,

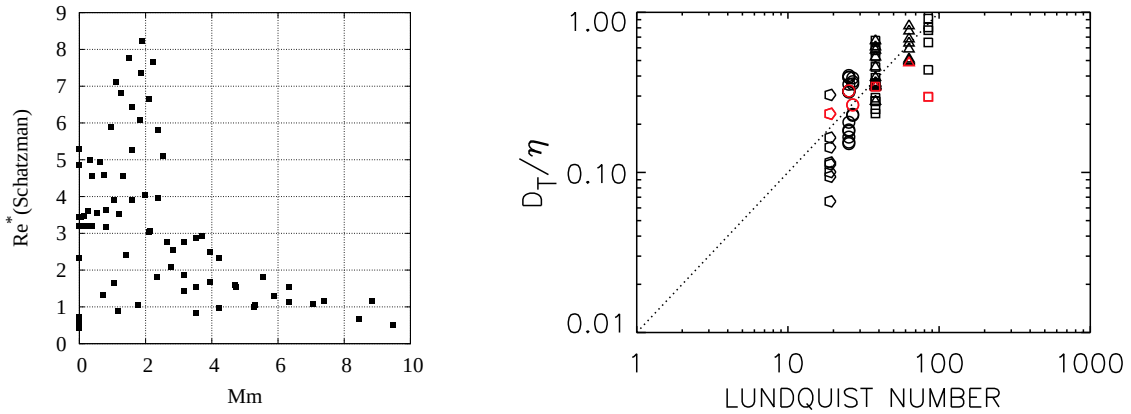

Figure 103. Diffusion of passive scalars. Left: The Schatzman number Re^* in its dependence on the magnetic Mach number. Right: D_T/η as a function of S of all computed diffusion models. Red symbols mark nonrotating models. The dotted line represents a linear dependence. $r_\mathrm{in} = 0.5$, $\mu_B = 1/r_\mathrm{in}$, $\mu_\Omega = 0.35$. From [137].

develops at the expense of magnetic energy. Estimations of dynamo parameters are necessary to probe the dynamo effectivity of a magnetic instability. The ability of turbulence to produce a mean electromotive force (EMF) along the background magnetic field plays a basic role in turbulent dynamos, i.e.

$$\langle \boldsymbol{u} \times \boldsymbol{b} \rangle = \alpha \boldsymbol{B} - \ldots, \tag{103}$$

where the term on the right side of this relation is called the α effect which, by definition, must be even in the magnetic field. The α value (or better, the α tensor) and also the kinetic helicity and/or current helicity represent pseudo-scalars (or better, pseudo-tensors). In rotating, radially stratified cosmic bodies the pseudo-scalar $\boldsymbol{g} \cdot \boldsymbol{\Omega}$ (with $\boldsymbol{g}$ as the vector of stratification) automatically exists. In Taylor-Couette flows unbounded in the axial direction no stratification vector parallel to the rotation axis exists. The only possible pseudo-scalar even in $\boldsymbol{B}$ is of magnetic nature: $\boldsymbol{B} \cdot \mathrm{curl}\, \boldsymbol{B}$ exists when the field geometry allows electric currents parallel to field components. For such fields the instabilities may produce finite values for the helicities and the α effect. Sign and amplitude of these quantities will now be discussed for twisted fields where axial currents are indeed parallel to an axial field component.

Helicity and α effect only exist in rotating turbulent and stratified media. In order to obtain finite values of these pseudo-scalars after the averaging procedure the density and/or the turbulence intensity must be nonuniform. The latter always happens close to the boundaries. A typical example of a helicity formation due to the boundary effect without density stratification showed that in a geodynamo model the helicity mainly appears along the tangential cylinder of the inner spherical core similar to a boundary layer effect [162]. Another situation exists in cases with any axial stratification. The stability of a system with axial magnetic fields and an *axial* gradient of the angular velocity has been considered in Ref. [163]. A pseudo-scalar $B_i B_j \Omega_{i,j}$ exists in this system yielding finite values of the helicities and the α effect (see Section 11.3 below).

11.1. Tayler instability

We proceed by evaluating the kinetic and current helicities and the α effect for the TI. Solving the linear stability problem may serve to estimate the sign and latitudinal profile of the kinetic and current helicities

$$\mathcal{H}^\mathrm{kin} = \langle \boldsymbol{u} \cdot \mathrm{curl}\, \boldsymbol{u} \rangle, \qquad \mathcal{H}^\mathrm{curr} = \langle \boldsymbol{b} \cdot \mathrm{curl}\, \boldsymbol{b} \rangle, \tag{104}$$

which for driven turbulence both contribute to the α effect [164, 63]. The averaging in Eqs. (103) and (104) is over the azimuth. If only the toroidal background field is present it follows that the helicity has opposite signs for positive and negative azimuthal wave number m, i.e. $\mathcal{H}^\mathrm{kin}(m = 1) = -\mathcal{H}^\mathrm{kin}(m = -1)$ [33]. For any unstable mode with finite helicity, there is thus another unstable mode with the same growth and drift rates but opposite helicity (see Fig. 76). If all modes are excited, and there is no symmetry-breaking bifurcation in the nonlinear regime, the instability of purely

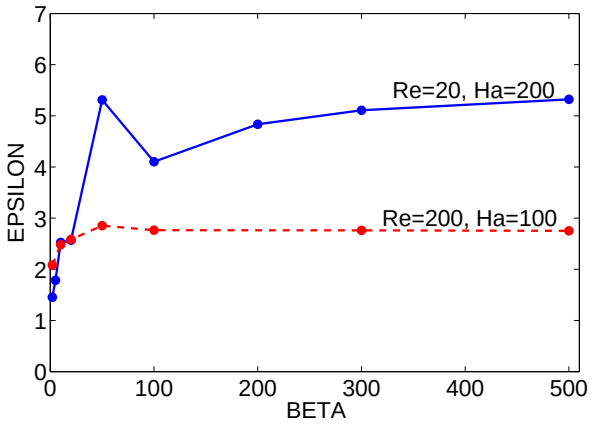

Figure 104. Ratio ε of the magnetic and kinetic energy for models with Mm < 1 (blue line) and Mm > 1 (red line). $\varepsilon > 1$ because of the large magnetic Reynolds numbers. See Fig. 96 for the special case $\beta = 10$. Ha is defined with the azimuthal field $B_{\rm in}$. $r_{\rm in} = 0.5$, $\mu_B = 2\mu_\Omega = 1$, Pm = 1. Perfectly conducting cylinders.

toroidal field cannot produce finite kinetic helicity, as the resulting net helicity vanishes [129]. The same argument leads to the same conclusion for the current helicity $\mathcal{H}^{\rm curr}$. The EMF also reverses when the sign of m is changed hence the α effect also vanishes. The same is true for a possible $\boldsymbol{\Omega} \times \boldsymbol{J}$-term which may appear in the expression (103) for the EMF as a consequence of a rotationally-induced anisotropy of the diffusivity tensor. The $\boldsymbol{\Omega} \times \boldsymbol{J}$ effect due to the Tayler instability of toroidal fields also does not exist.

11.2. Twisted background fields

For twisted background fields where the background field possesses finite azimuthal (B_ϕ) and axial (B_0) components, we present two series of solutions with helical fields. The definition (81) is used for the ratio β of the azimuthal and axial field components. The profiles of the azimuthal flow and field components form a system of the Chandrasekhar-type with $\mu_B = 2\mu_\Omega = 1$. We present Ha = 100, Re = 200 for the first series, and Ha = 200, Re = 20 for the second, with Pm = 1 for both. The first series is rotationally dominated (Mm > 1) in contrast to the second one (Mm < 1).

For the two parameter sets Fig. 104 shows the ratio ε of the magnetic and kinetic energies. For sufficiently large β the axial magnetic component is too weak to have any significant influence. Generally, $\varepsilon > 1$ for all parameters, which for large β is consistent with the results plotted in Figs. 30 and 55. This is not true for small β, where the axial field starts to dominate. For $\beta < 1$ the instability is so strongly stabilized that the resulting energies of the perturbations are reduced.

The helicities for the two runs are presented in Fig. 105. For both series, both helicities have the same sign but opposite to the sign of β. For β of order unity the background field has a strong twist that forces the instabilities to have a parity of opposite sign. If one then gradually increases β, each time using the previous solution as the new initial condition, this parity of the instabilities is preserved all the way to $\beta \to \infty$, where the basic state no longer has a twist, and both left and right instabilities could exist equally well as in Fig. 76.

For large β the basic state makes sufficiently little distinction between left and right modes that both could exist, but because of the way we have reached the model with $\beta = 500$, we consistently obtain the right mode although a left mode would also be possible. This feature that both left and right modes are allowed for sufficiently large β but not for smaller β is analogous to an imperfect pitchfork bifurcation. It is thus important to specify carefully the nature of the initial conditions used in each run.

We are also interested in the signs and amplitudes of the α effect, in both azimuthal and axial directions. According to the general rule that the azimuthal α effect is anticorrelated with the (kinetic) helicity, we expect the azimuthal α effect to be positive for $\beta > 0$. The expected sign of the axial α effect is not clear. There are theories and simulations leading to $\alpha_{\phi\phi}$ and α_{zz} with opposite signs ([165] for an overview).

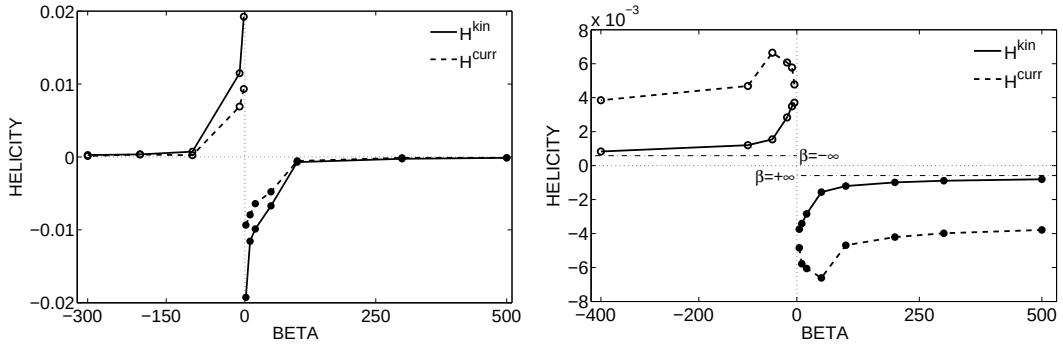

Figure 105. Kinetic helicity (solid lines) and current helicity (dashed lines) of the perturbations as functions of β for the models presented in Fig. 104 Mm > 1 (left) and Mm < 1 (right). The dashed lines indicate the limits $\pm 6 \cdot 10^{-4}$ of the kinetic helicity of the modes in Fig. 76. The helicities and β are anticorrelated.

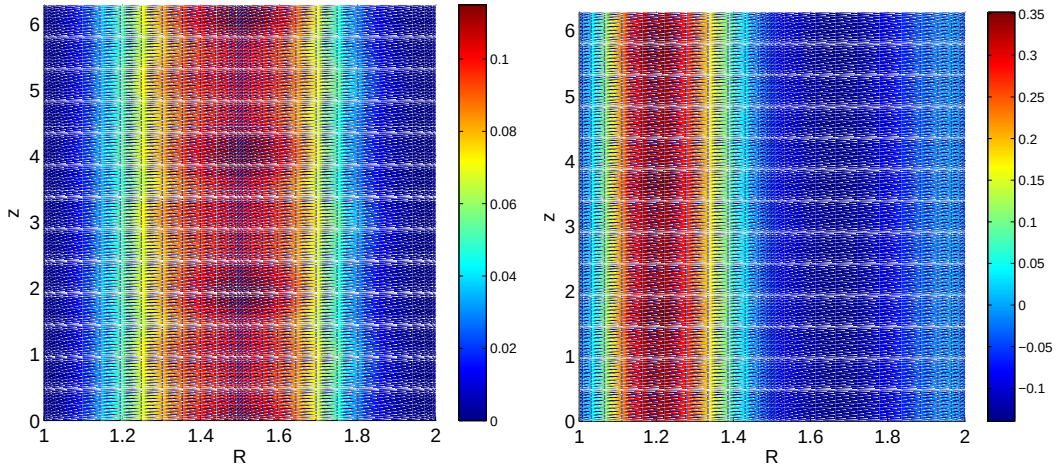

Figure 106. (R/z) maps of $\alpha_{\phi\phi}$ after averaging over azimuth and time for Mm < 1 (left, Re = 20, Ha = 200) and for Mm > 1 (right, Re = 200, Ha = 100) for positive helicity of the background field. $\beta = 3$, $r_{\rm in} = 0.5$, $\mu_B = 2\mu_\Omega = 1$, Pm = 1. Perfectly conducting cylinders.

Figure 106 gives the numerical results for slow and rapid rotation. On the basis of Eq. (103) the dimensionless α effect in the form

$$C_\alpha = \frac{\alpha R_0}{\eta} \tag{105}$$

is plotted for $\alpha_{\phi\phi}$. It yields $C_\alpha > 0$ almost everywhere in the meridional plane. The influence of rotation on α is not strong, but C_α is smaller for rapid rotation than for slow rotation (Fig. 107). This surprising result is opposite to the well-known behavior of the α effect for rotating and stratified convection. The signs of $\alpha_{\phi\phi}$ and β coincide. The plot mainly shows how the amplitudes of $\alpha_{\phi\phi}$ vary with β, being roughly inversely proportional in both cases. For large values of β the α effect scales as C/β with $C \simeq 0.05$, so that for $B_{\rm in} \gg B_0$ we have $C_\alpha \ll 1$.

Obviously, C_α is much too small for the operation of an α^2 dynamo. On the other hand, an $\alpha\Omega$ dynamo always leads to large β, which leads to small C_α. Too small C_α requires stronger differential rotation to maintain the dynamo action. Stronger differential rotation, however, leads to higher β, and so on. The formal argument is as follows: Dynamo waves of $\alpha\Omega$ type require for self-excitation that $C_\alpha C_\Omega \geq 1$, with the magnetic Reynolds number of the

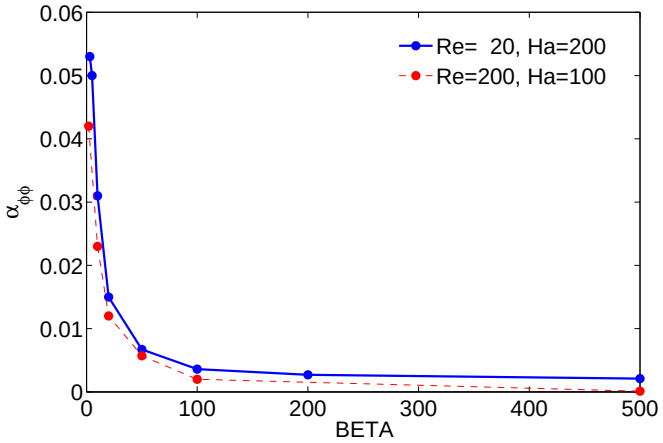

Figure 107. Dimensionless C_α according to (105) of the azimuthal α effect as a function of β for slow and rapid rotation. One finds $\alpha_{\phi\phi}\beta > 0$, i.e. α effect and background helicity are positively correlated. Note that for Mm > 1 (red line) $\alpha_{\phi\phi} \to 0$ for $\beta \to \infty$, as it must. The blue line for Mm < 1 reflects for very large $|\beta|$ the effect of spontaneous parity breaking in accordance to Fig. 105 (right). $r_{\rm in} = 0.5$, $\mu_B = 2\mu_\Omega = 1$, Pm = 1. Perfectly conducting cylinders.

differential rotation $C_\Omega = -R_0^3/\eta\, {\rm d}\Omega/{\rm d}R$. The amplitudes of the field components B_ϕ and B_R can be estimated by

$$\frac{|B_\phi|}{|B_R|} \simeq \sqrt{\frac{C_\Omega}{C_\alpha}} \tag{106}$$

so that dynamo excitation requires

$$\frac{|B_\phi|}{|B_R|} C_\alpha \geq 1. \tag{107}$$

We know from Fig. 107 that $C_\alpha \simeq C/\beta$ (with $C_\alpha < 0.05$), so that (107) yields the condition

$$C > \frac{|B_R|}{|B_z|} \tag{108}$$

for dynamo action by differential rotation and current-driven α effect. For disk dynamos B_R dominates B_z, and for spherical dynamos B_R is comparable to B_z. The condition for self-excitation becomes $C > 1$, which according to Fig. 107 cannot be fulfilled. On the basis of the numerical results given in Fig. 107 an $\alpha\Omega$ dynamo cannot operate for this particular choice of the magnetic Prandtl number [166, 129].

11.3. Axial shear

In the majority of the models the radial profile of the toroidal field was prescribed. The simplest way to obtain a natural radial profile is to consider the result of an axial shear ${\rm d}\Omega/{\rm d}z$ acting on a given uniform axial field B_0 [163]. If the induced toroidal field B_ϕ becomes strong enough a Tayler instability can be observed, leading to a growing nonaxisymmetric field. Not only must the magnitude of B_ϕ be strong enough, but also a certain limit B_ϕ/B_0 must be exceeded, as an additional poloidal field component suppresses the instability. As an illustration we mention that for Pm = 15 the instability sets in at a Lundquist number of the axial field of order 20. The excitation condition for lower magnetic Prandtl numbers are given in Fig. 108 (left). The curves for small Pm seem to converge. The minimum values of Rm are about 20, while the corresponding S values are of order 10. These numbers correspond to the values for MRI given in Table 2 which for small Pm indeed lead to Reynolds numbers exceeding 10^6 (Fig. 108, right).

A new and nonlinear relation between the α effect and the external field and differential rotation is

$$\alpha \propto B_i\, B_j\, \Omega_{i,j}, \tag{109}$$

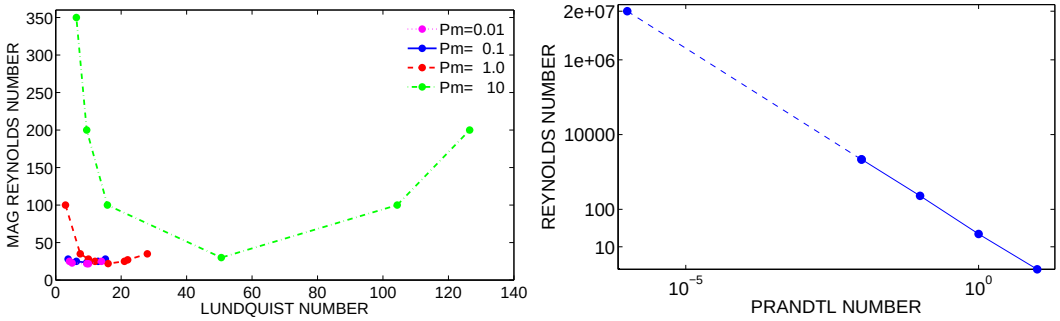

Figure 108. Axial shear $\Omega \propto z$ and uniform axial field B_0. Pm = 0.01 – 10. Left: the lines of neutral stability for small Pm; the curves scale with S and Rm for small Pm. Right: The corresponding minimum Reynolds numbers for instability. Reynolds and Hartmann numbers are defined with $R_{\rm out}$.The dashed line suggests an extrapolation to smaller Pm. $r_{\rm in} = 0$. For numerical details see [167].

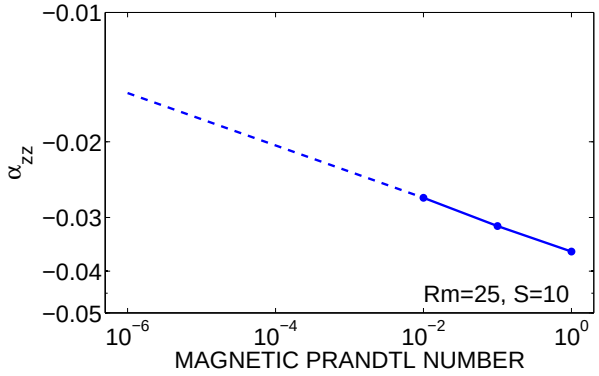

Figure 109. Pm-dependence of the α_{zz} for the interaction of axial field and negative axial shear in units of the maximal velocity of the driving endplate. The dashed line suggests a possible extrapolation to smaller Pm (not yet confirmed). Rm = 25, S = 10.

where B_i means the axial external field and $\Omega_{i,j}$ the axial shear of the basic rotation [167]. The sign of this pseudo-scalar does not depend on the sign of the magnetic field, but does depend on the sign of the shear. The relation (109) requires a quadratic law, $\alpha \propto B_0^2$, which is indeed confirmed by the simulations.

For Fig. 109 the axial component α_{zz} is directly computed for positive and negative shear via the z-component of the electromotive force (103). One finds the same signs for α_{zz} and $\mathrm{d}\Omega/\mathrm{d}z$. In the sense of an order-of-magnitude estimate the normalized α becomes

$$C_\alpha = \frac{|\alpha_{zz}|R_{\rm out}}{\eta} \simeq 0.01\ {\rm Rm}_{\rm out} \tag{110}$$

with ${\rm Rm}_{\rm out} = R_{\rm out}^2 \Omega_{\rm out}/\eta$. The Pm-dependence is very weak. With ${\rm Rm}_{\rm out} \simeq 10$ the C_α is maximally of order 0.1.

The potential difference for axial shear between the endplates is

$$\Delta\Phi = 10^{-8} \alpha_{zz} B_0 H \tag{111}$$

(measured in Volt, Gauss and cm/s) with H the height of the container. With (110) follows

$$\Delta\Phi = 10^{-8} C_\alpha \eta B_0 \Gamma. \tag{112}$$

Hence, with $\eta \simeq 10^3$ cm^2/s for sodium or gallium, 1 kG for the axial field and $\Gamma = 10$ a potential difference of $\Delta\Phi \simeq 0.1 C_\alpha$ (in V) is generated, which according to (110) leads to about 10 mV. For longer containers the potential difference grows linearly. The container filled with a liquid metal acts as a generator of an observable potential difference between its endplates – if the above mentioned instability conditions can be fulfilled. The data of Fig. 109

have been obtained for a model with piecewise constant Ω and a jump between the two cylinder parts. Only one of the endplates must be forced to rotate so that $\mathrm{Rm}_{\mathrm{out}} = O(10)$ should be possible.

The α experiment in Riga worked with $B \simeq 1$ kG and velocities of the order of m/s, so that $\Delta\Phi$ exceeded 10 mV [168]. However, this experiment used a prescribed helical geometry to mimic the symmetry-breaking between left and right helicities. It has not been demonstrated so far that a rotating fluid with a non-prescribed helicity leads to an observable α effect. However, by nonlinear numerical simulations the mean electromotive force in plane Couette flows of a nonrotating conducting fluid under the influence of a large-scale magnetic field on driven turbulence has been calculated. A vertical stratification of the turbulence intensity results in an observable α effect owing to the presence of horizontal shear [169].

12. Hall effect

Fluids with Hall effect can be described as conductors with conductivity tensors with off-diagonal elements. Under these conditions a feedback of toroidal to poloidal field exists which in combination with differential rotation – inducing toroidal fields from poloidal ones – makes the magnetic field unstable even for an axisymmetric geometry. The instability, however, can only exist if the timescale of the Hall effect is shorter than the diffusion time and longer than the shear time. Otherwise the diffusion or the Hall effect would dominate, destroying any instability. We shall first show that the growth time of such an instability is determined by the rotation time, so that the instability is basically fast.

12.1. The Shear-Hall Instability (SHI)

It is known that a stable rotational shear in a fluid with Hall effect can destabilize a magnetic background field [170, 171, 172]. This 'shear-Hall instability' is a basic property of only the induction equation without any contribution by the momentum equation. The mechanism remembers global dynamo models where the differential rotation transforms poloidal field components to toroidal field components and the meridional flow generates the poloidal fields from the toroidal fields [173]. After the Cowling theorem such a mechanism can only maintain nonaxisymmetric fields against the magnetic resistivity losses. It is indeed possible to imagine a replacement of the meridional flow by the Hall term which itself is also able to produce poloidal fields from toroidal ones. As even axisymmetric field configurations can be destabilized by this process it is immediately clear that SHI is by no means a dynamo mechanism. One needs nondecaying background fields to feed the entire system.

The induction equation with Hall effect included is

$$\frac{\partial \boldsymbol{B}}{\partial t} = \mathrm{curl}\,(\boldsymbol{U} \times \boldsymbol{B}) + \eta \Delta \boldsymbol{B} - \beta_{\mathrm{Hall}}\,\mathrm{curl}\,(\mathrm{curl}\,\boldsymbol{B} \times \boldsymbol{B}) \tag{113}$$

where the Hall parameter β_{Hall} does not depend on the magnetic field. One can show that the Hall effect exactly conserves the magnetic energy. The only source of energy is due to the shear, so that the Hall term alone is unable to feed an instability [174, 175]. The sign of the Hall parameter β_{Hall} depends on the definition of the elementary charge; we shall only use it as a positive number.

The linearized version of Eq. (113) for a current-free background field becomes

$$\frac{\partial \boldsymbol{b}}{\partial t} = \mathrm{curl}\,(\boldsymbol{u} \times \boldsymbol{B}) + \mathrm{curl}\,(\boldsymbol{U} \times \boldsymbol{b}) + \eta \Delta \boldsymbol{b} - \beta_{\mathrm{Hall}}\,\mathrm{curl}\,(\mathrm{curl}\,\boldsymbol{b} \times \boldsymbol{B}). \tag{114}$$

If the Hall term exceeds the first term on the right side of this equation then the induction equation decouples from the Navier-Stokes equation, and one may ask whether the remaining equation can have an own solution. This is indeed the case. For plane short waves subject to a global rotation with $\Omega \propto R^{-q}$ a dispersion relation

$$(\tilde{\omega}_{\mathrm{gr}} + 1)^2 + \mathrm{Rb}(\mathrm{Rb} - q\tilde{\mathrm{Rm}}) = 0 \tag{115}$$

results where $\tilde{\omega}_{\mathrm{gr}}$ is the growth rate normalized with the resistivity frequency $\omega_\eta = \eta k^2$ (with $\boldsymbol{k}$ as the wave number). $\tilde{\mathrm{Rm}}$ is also formed with ηk^2. Note that for neutron stars the ratio

$$\mathrm{Rb} = \frac{\tau_{\mathrm{diff}}}{\tau_{\mathrm{Hall}}} = \frac{\beta_{\mathrm{Hall}} B_0}{\eta} \tag{116}$$

lies between 1 and 100 for magnetic fields of order 10^{12} G. In dependence on the orientation of the field this parameter can have both signs. An instability can indeed exist if for positive or negative Rb we have $|\mathrm{Rb}| < |q|\tilde{\mathrm{Rm}}$ and q and Rb are of the same sign. There must also be a lower bound of Rb, as the Hall effect can also be too weak for an instability. It can also be too strong as only the shear produces the needed energy rather than the Hall effect. For a rotation profile depending only on R the necessary condition for shear-Hall instability is [176]

$$(\boldsymbol{k}\cdot\boldsymbol{B})\,k_z\frac{\partial\Omega}{\partial R}<0. \tag{117}$$

For axial $\boldsymbol{B}$ this condition simplifies to $qB_z > 0$, hence there is instability if the signs of the two factors are equal. SHI is thus even able to destabilize flows with positive shear $\mathrm{d}\Omega/\mathrm{d}R$ if the magnetic field is antiparallel with the rotation axis. That the sign of the magnetic field here plays an important role is a direct consequence of the nonlinear form of Eq. (114).

Introducing another dimensionless quantity which only includes material parameters we write

$$\beta_0=\frac{\mathrm{Rb}}{\mathrm{S}}. \tag{118}$$

The parameter β_0 may also have both signs, depending on the orientation of the magnetic field relative to the rotation axis. The amplitude of β_0 can be imagined as smaller than unity.

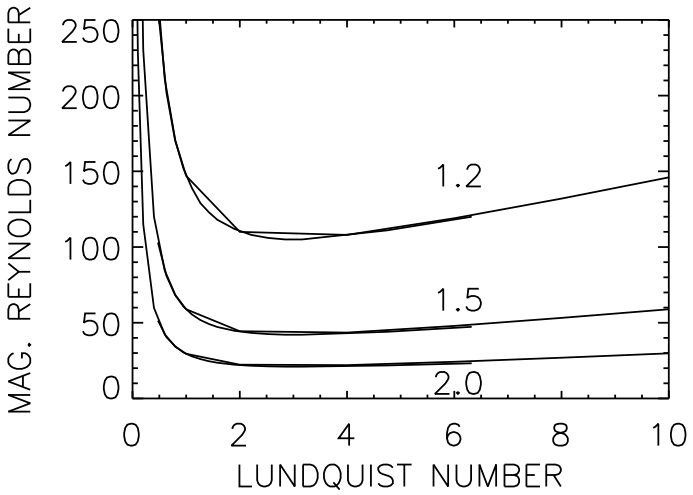

Figure 110. Shear-Hall instability (SHI) with axial magnetic fields for positive shear (i.e. $q < 0$) for $\mathrm{Pm} = 10^{-5}$ and $\mathrm{Pm} = 1$ does not provide visible differences. The curves have been calculated for $\mu_\Omega = 1.2, 1.5, 2$. Their minima possess large magnetic Mach numbers. Hall parameter $\beta_0 = -1$. $m = 0$, $r_{\mathrm{in}} = 0.5$, insulating boundary conditions.

Figure 110 illustrates SHI of superrotating fluids for insulating boundary conditions. The boundary conditions for the hydromagnetic Taylor-Couette flow are not influenced by the Hall effect. The calculation of the Hartmann number uses the axial field strength as prescribed by the definition (14). The flow is unstable only for $\beta_0 < 0$ when rotation axis and magnetic field are antiparallel. Equation (114) has been solved for three rotation profiles with positive shear. The rather strong differences of the resulting characteristic Reynolds numbers for fixed Hartmann number demonstrate how important the differential rotation for the instability mechanism is. For weaker shear one needs faster rotation to excite the instability. In Fig. 110 for Prandtl numbers differing by five orders of magnitude the differences of the curves number are very small. Hence, the eigenvalues scale for $\mathrm{Pm} \to 0$ with the Lundquist number S and the magnetic Reynolds number Rm. It is then easy to calculate the magnetic Mach number as $\mathrm{Mm} = \mathrm{Rm}/\mathrm{S}$. In all cases with $\mathrm{Pm} \lesssim 1$ the instability exists for rapid rotation with $\mathrm{Mm} > 1$.

With spherical models it has been shown that the growth rates of SHI scale with the rotation rate and not with the rather long Hall time [177, 178]. The dispersion relation (115) leads to the same conclusion. The maximum of the first bracket as a function of Rb is taken for $\mathrm{Rb} = q\tilde{\mathrm{Rm}}/2$ so that $\tilde{\omega}_{\mathrm{gr,max}} + 1 = q\tilde{\mathrm{Rm}}/2$. Dropping the tildes indeed leads to $\omega_{\mathrm{gr,max}} \propto \Omega$ for the growth rates of SHI.

12.2. Hall-MRI

Flows with negative shear (positive q) are much more complicated, as they can even be unstable in the presence of magnetic fields without Hall effect. We expect, however, that for positive Rb the shear-Hall instability supports the MRI but the strength of the support must be calculated. The dark lines in Fig. 111 indicate marginal stability without Hall effect for axisymmetric and nonaxisymmetric MRI modes. As usual the instability domain for the nonaxisymmetric mode is much smaller than for the axisymmetric mode. It is increased, however, for fluids with Hall effect if the magnetic axis and the rotation axis have the same orientation so that $B_z \mathrm{d}\Omega/\mathrm{d}R < 0$. This case is realized in the left panel of Fig. 111 for strong Hall effect with $\beta_0 = 1$. The minimum Lundquist number for instability is now smaller than for MRI, but for large magnetic fields the critical Reynolds number with Hall effect becomes greater than without Hall effect. Hence, for positive β_0 the Hall effect destabilizes for weak fields and stabilizes for strong fields. The red dashed lines representing the $m = 1$ mode with Hall effect are also shifted so that nonaxisymmetric modes become more (less) unstable for weak (strong) fields. Note also that the dashed red line for the mode $m = 1$ in the left panel of Fig. 111 no longer has the positive slope of both branches as it appears for nonaxisymmetric MRI modes without Hall effect. In the Hall regime the nonaxisymmetric mode has the same open geometry as the axisymmetric mode of MRI, so that it is not suppressed for rapid rotation. The different geometry of the neutral stability curves of the nonaxisymmetric modes with and without Hall effect seems to be the most striking consequence of the Hall-MRI. The Hall-MRI thus produces much more complex patterns than the axisymmetric rings which are mainly excited by standard MRI without Hall effect. The minimum magnetic Reynolds number is also reduced by the Hall effect, but this reduction remains small. One only finds a reduction by a factor of $\lesssim 2$, as realized in Fig. 111 (left) for strong positive Hall effect.

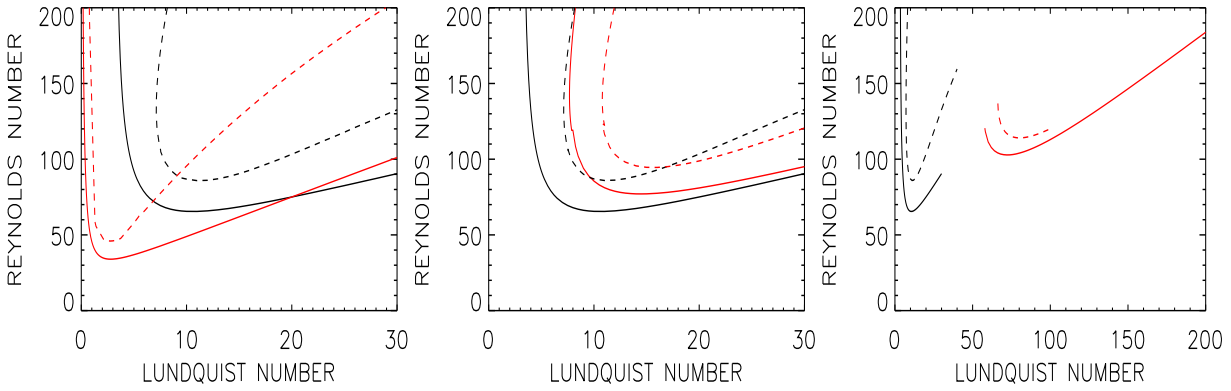

Figure 111. Hall-MRI: instability maps for quasi-Keplerian flow subject to axial fields with (red) and without Hall effect. Black lines: $\beta_0 = 0$ (MRI, no Hall effect). Red lines: $\beta_0 = 1$ (left), $\beta_0 = -0.1$ (middle) and $\beta_0 = -1$ (right). Kepler rotation is maximally destabilized by positive Hall effect (field parallel to rotation axis). Solid lines: $m = 0$, dashed lines: $m = 1$. $r_{\rm in} = 0.5$, $\mu_\Omega = 0.35$, Pm = 1. Insulating boundary conditions.

For the opposite case of negative Hall effect, for fields antiparallel to the rotation axis, the MRI is suppressed for weak fields and enhanced for strong fields. In Fig. 111 the plots for negative β_0 (middle and right panels) show the red lines for Hall-MRI as shifted towards large S. Even the small value $\beta_0 = -0.1$ gives a drastic stabilization of the axisymmetric and nonaxisymmetric modes. Moreover, both branches of the $m = 1$ mode have the typical positive slopes, so that there is also a maximum Reynolds number beyond which the nonaxisymmetric modes are suppressed. The characteristic Lundquist numbers for instability at the global minimum Reynolds number also strongly increase for $\beta_0 = -1$. It seems that the stabilization by negative β_0 appears to be much more effective than the destabilization by positive β_0.

12.3. Hall-TI

Another situation holds if the magnetic background field contains electric currents. The influence of the electric current is twofold. It enters the expression of the Hall effect in Eq. (113) and produces an own pinch-type instability, so that strong modifications of the TI must be expected [179]. We start with the Chandrasekhar-type flow with almost uniform toroidal field, i.e. $\mu_B = 2\mu_\Omega = 1$, for which we know that for Pm $\to 0$ it scales with Reynolds number and

Hartmann number. For azimuthal fields the Hartmann number is defined by Eq. (39). The numerical results are given in Fig. 112 for Hall parameters β_0 between −0.5 and 0.5. The value β_0 and the magnetic Prandtl number Pm are the free parameters of the system for a prescribed hydromagnetic Taylor-Couette flow. We again define Ha as positive and use both signs of β_0 corresponding to opposite magnetic field orientations.

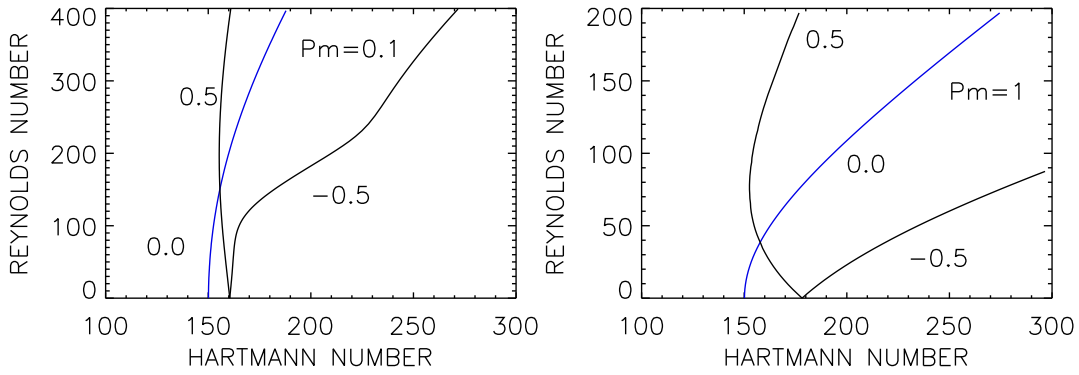

Figure 112. Hall-TI of quasi-uniform azimuthal fields and quasi-uniform flows with two magnetic Prandtl numbers. The curves are labeled by the Hall parameter β_0. Pm = 0.1 (left), Pm = 1 (right). $m = 1$. Note the increase of Ha_0 for both signs of β_0. The plots for $\beta_0 \to -\beta_0$ and simultaneously $m \to -m$ are identical. Blue lines for $\beta = 0$. $r_{\rm in} = 0.5$, $\mu_B = 2\mu_\Omega = 1$, $m = 1$. Conducting boundaries.

The Hall-free curves start at $\mathrm{Ha}_0 = 150$ for Re = 0. For $\beta_0 \neq 0$, $\mathrm{Ha}_0 > 150$. The increase does not depend on the sign of the Hall term. For either sign, in stationary containers the Hall effect stabilizes the azimuthal field. For $\beta_0 < 0$ the rotation together with the Hall effect has a strongly stabilizing influence. To become unstable the magnetic field must be much stronger under the influence of rotation than without rotation. On the other hand, for $\beta_0 > 0$ the Hall effect has a destabilizing influence ($\mathrm{Ha} < \mathrm{Ha}_0$) if the rotation is not too rapid. The destabilization is thus similar to that of the shear-Hall instability with axial fields (Section 12.2). For axial fields positive β_0 also destabilize flows with negative shear.

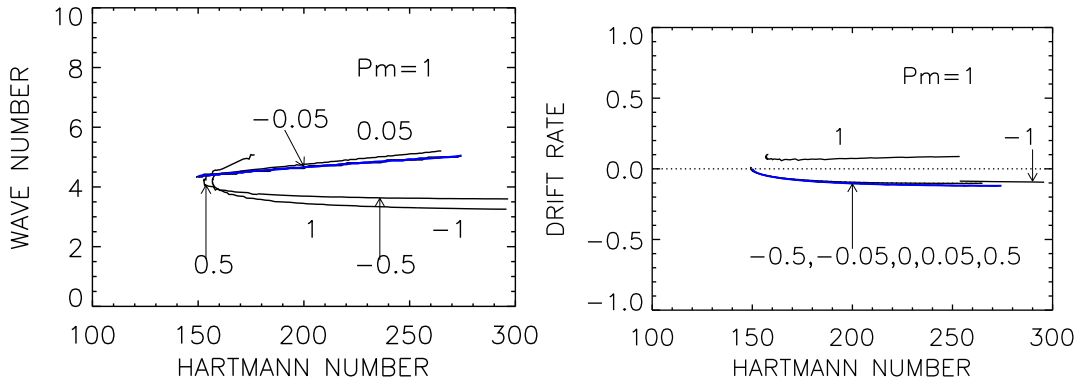

Figure 113. Same as in Fig. 112 (right) but for wave numbers (left) and drift rates (right) along the neutral lines of the Hall-TI. The lines are marked with β_0; the blue line denotes $\beta_0 = 0$. The influence of the Hall effect is only weak. $m = 1$, $r_{\rm in} = 0.5$, $\mu_B = 2\mu_\Omega = 1$, Pm = 1. Conducting boundaries.

In accordance with the relation (117), for azimuthal fields the positive Hall effect also destabilizes flows with negative shear. For positive β_0 the stability domain is reduced, and for negative β_0 it is increased. The stabilization (destabilization) of negative (positive) Hall β_0 is a common phenomenon of all models. In other words, for positive q, positive B_ϕ (i.e. $\beta_0 > 0$) lead to smaller critical field amplitudes than negative B_ϕ (i.e. $\beta_0 < 0$). If the nonaxisymmetric Tayler instability would limit the strength of the toroidal fields B_ϕ, then the resulting amplitudes are different for different signs of B_ϕ due to the action of the Hall effect. The effects, however, are not substantial. Wave number and drift rates are influenced even less by the Hall effect (Fig. 113). Generally, positive (negative) Hall effect decreases

(increases) the axial size of the instability cells. If the Hall effect destabilizes then it acts against the Taylor-Proudman theorem. On the other hand, a stabilizing Hall term elongates the cells in the axial direction.

The question still remains how the Hall effect modifies the growth times of the TI. Figure 114 shows the growth rates of the Hall-TI for various parameters. They are computed for Ha = 300 and for increasing rotation rates. The growth rates – normalized here with the viscosity frequency $\omega_\nu = \nu/R_0^2$ – vanish at the stability lines. One finds that for the considered parameters the Hall effect strongly influences the growth rates of TI. For negative β_0 the rotational stabilization of TI is amplified. For positive β_0, however, the rotational suppression without Hall effect *is compensated* by the Hall effect. Hence, the *maximal* growth rate is always given by the value for $\Omega = 0$, and this quantity in the normalization used scales with $\mathrm{Ha}/\sqrt{\mathrm{Pm}}$, so that the physical growth rate for $\Omega = 0$ scales with the Alfvén frequency Ω_A. The positive Hall effect (almost) reproduces this value at a certain magnetic Reynolds number where the Hall-influenced growth rate has its maximum. This surprising phenomenon only occurs for positive Hall effect and under the presence of differential rotation. For positive Hall effect the TI grows much faster than for negative Hall effect. These findings strongly resemble the consequences of the SHI effect for axial fields described in Section 12.1. Indeed, the relation (117) does not exclude the existence of an azimuthal SHI. Contrary to the solutions with positive m, however, for $m < 0$ (if k_z is assumed as positive definite) the destabilization occurs for negative β_0 rather than for positive values. For destabilization the product of $m\beta_0$ must be positive, while for stabilization it must be negative.

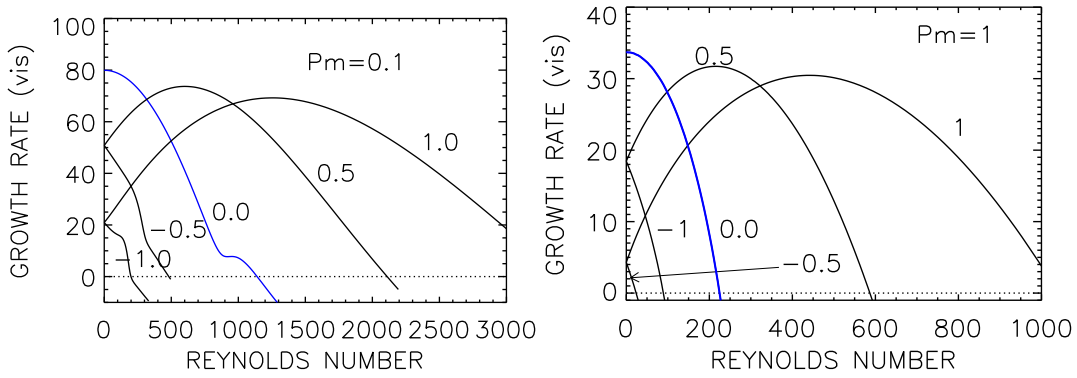

Figure 114. Growth rates for Hall-TI normalized with ω_ν for $m = 1$ with and without Hall effect for Ha = 300. The curves are marked by their Hall parameter β_0; the blue lines give the TI without Hall effect. Pm = 0.1 (left) and Pm = 1 (right). $r_\mathrm{in} = 0.5$, $\mu_B = 2\mu_\Omega = 1$. Perfectly conducting boundaries.

The situation at the vertical axis, Re = 0, is also of interest. The Hall effect considerably reduces the growth rates of TI without rotation, and this reduction is the same for both signs of β_0. On the other hand, the growth rates vanish for characteristic upper Reynolds numbers beyond which the TI with $m = 1$ decays. These Reynolds numbers Re_max also reflect the suppressing action of negative β_0, and the enhancing action of positive β_0. These actions, however, are asymmetric: the increase of Re_max for positive β_0 compared with Re_max for $\beta_0 = 0$ (blue lines) is much larger than the same difference for negative β_0.

One also finds that even a weak Hall effect – resulting in a long Hall time of order of the diffusion time – does not generally prolong the growth time of the Tayler instability, which also in this case scales with the Alfvén time. In this sense the Hall effect is only a modification of another instability and does not impose its own timescale on the instability.

The results for large Pm are also interesting. Without Hall effect the differential rotation strongly supports the TI as long as the rotation is slow and the magnetic Prandtl number is large. The blue line in the left panel of Fig. 115 reflects a distinct subcritical excitation with $\mathrm{Ha} < \mathrm{Ha}_0$ for the lower Reynolds numbers. Because of the action of the differential rotation on nonaxisymmetric modes this phenomenon is finally compensated, leading to $\mathrm{Ha} > \mathrm{Ha}_0$ for sufficiently large Reynolds numbers. We take from Fig. 115 that the negative Hall effect destroys the subcritical excitation for slow rotation. The positive Hall effect produces a stable branch in the $(\mathrm{Ha}/\overline{\mathrm{Rm}})$ plane which separates two unstable branches. The large-field branch shows no subcritical excitation behavior but the weak-field branch introduces extremely weak fields for which the system becomes unstable. This instability domain has no relation to the TI but it is due to the SHI for negative shear. According to the condition (117) it will disappear for $m = -1$.

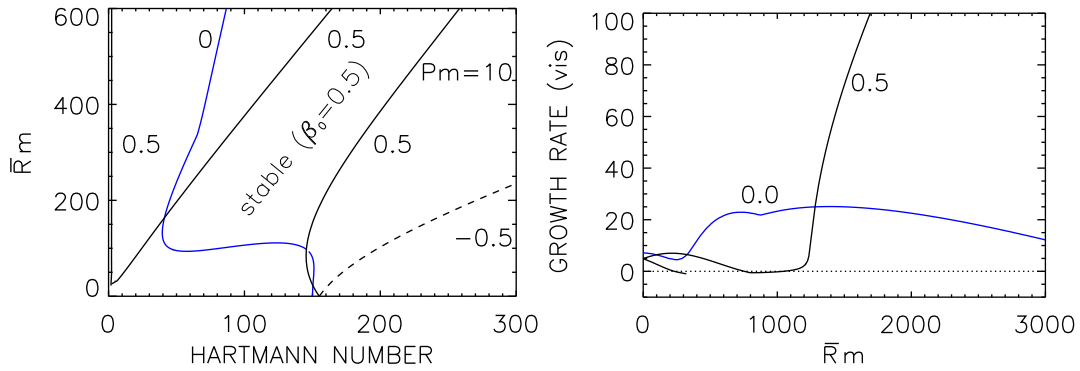

Figure 115. Stability map (left) and growth rate in units of ω_ν (right, Ha = 300) for Hall-TI with large Pm. The curves are marked by their Hall parameter β_0; the blue lines give the TI without Hall effect. Pm = 10, $r_{\rm in} = 0.5$, $\mu_B = 2\mu_\Omega = 1$. Perfectly conducting boundaries.

13. Magnetized stratorotational instability

We know that a combination of a stable differential rotation and a stable axial density stratification in the Taylor-Couette flow leads to a new instability, which has been called the StratoRotational Instability (SRI) [180, 181, 182, 183, 184]. Under the presence of a stable axial density gradient nonaxisymmetric disturbances are unstable even beyond the Rayleigh line. The existence of this stratorotational instability has been verified in laboratory experiments [185, 186, 187, 188]. The new question is whether the combination of density stratification, differential rotation and toroidal fields is stabilizing or destabilizing, or whether new instabilities arise.

The MHD equations for incompressible stratified fluids are

$$\frac{\partial \boldsymbol{U}}{\partial t} + (\boldsymbol{U}\cdot\nabla)\boldsymbol{U} = -\frac{1}{\rho}\nabla P + \boldsymbol{g} + \nu\Delta\boldsymbol{U} + \frac{1}{\mu_0\rho}\mathrm{curl}\boldsymbol{B}\times\boldsymbol{B}, \qquad \frac{\partial \rho}{\partial t} + (\boldsymbol{U}\cdot\nabla)\rho = 0, \tag{119}$$

and div $\boldsymbol{U}$ = div $\boldsymbol{B}$ = 0, where $\boldsymbol{U}$, P, ρ and $\boldsymbol{B}$ are the total quantities as the sums of the mean and fluctuating parts, and $\boldsymbol{g}$ is the uniform vertical gravitational acceleration. The induction equation is identical with Eq. (18). A new dimensionless number in the problem is the Reynolds number formed with the buoyancy frequency N instead of Ω, i.e.

$$\mathrm{Rn} = \frac{NR_0^2}{\nu}, \tag{120}$$

with the buoyancy frequency from $N^2 = -g\mathrm{d}\log\rho/\mathrm{d}z$, derived from the stable density gradient, $\mathrm{d}\rho/\mathrm{d}z < 0$. Sometimes it is also convenient to describe the influences of the density stratification by the Froude number

$$\mathrm{Fr} = \frac{\mathrm{Re}}{\mathrm{Rn}}. \tag{121}$$

The Froude number is thus simply the ratio between the rotation rate $\Omega_{\rm in}$ of the inner cylinder and the buoyancy frequency N, and represents a normalized rotation rate. Equations (119) also describe a system under the presence of a stable temperature gradient in the adiabatic approximation, i.e. Pr $\to \infty$.

13.1. Stratorotational instability

The Rayleigh criterion (5) for Taylor-Couette flows which are stable against axisymmetric perturbations has been extended to stratified flows [189]. A stable vertical density stratification, however, destabilizes the Taylor-Couette flow against nonaxisymmetric perturbations even beyond the Rayleigh line as long as $r_{\rm in}^2 < \mu_\Omega < \mu_{\rm max}$. The most unstable mode is $m = 1$. The limit $\mu_{\rm max}$ depends on the gap width between the cylinders, the maximum μ_Ω represents rotation laws which are slightly flatter than the quasi-uniform flow $U_\phi \simeq$ const.

The combination of stable rotation law and stable density stratification only allows unstable nonaxisymmetric modes if the Froude number does not deviate too much from unity. Figure 116 (left) shows the lines of neutral

stability for the rotation laws with $\mu_\Omega \geq 0.2$. The curves are labeled with μ_Ω. The quasi-Keplerian flow is represented by $\mu_\Omega = 0.35$, and the quasi-uniform flow $U_\phi = \text{const}$ by $\mu_\Omega = 0.5$. In this figure all rotation profiles for $\mu_\Omega \leq \mu_{\max}$ prove to be unstable. For any rotation law always two Reynolds numbers exist between which the flow is unstable. Hence, not only too slow rotation but also too fast rotation suppresses the instability. This finding explains why sofar the SRI did not appear in hydrodynamic simulations of axially-stratified Kepler disks. That a lower limit exists of the Reynolds number for the onset of SRI is quite natural. It is a non-trivial result, however, that also too strong differential rotation is able to suppress the excitation of the *hydrodynamic* nonaxisymmetric instability patterns.

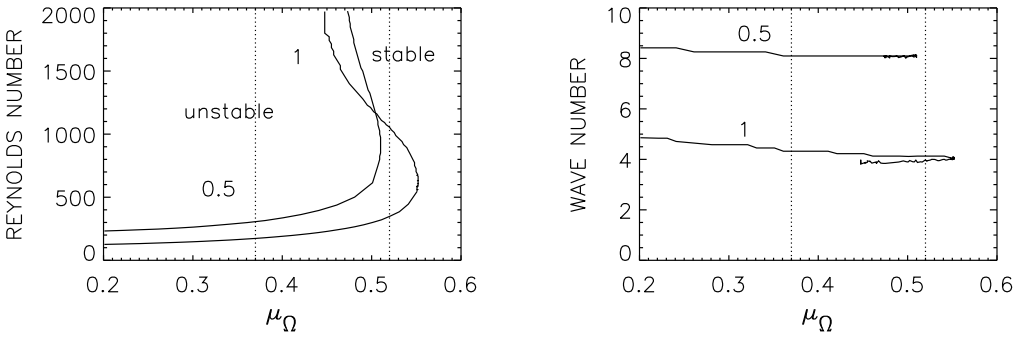

Figure 116. Stratorotational instability for various rotation laws between the cylinders. Left: neutral stability lines for Fr = 0.5 and Fr = 1 as function of μ_Ω. Note the existence of lower and upper Reynolds numbers for large μ_Ω. For too fast rotation the SRI decays. Right: the corresponding axial wave numbers normalized with the gap width. Vertical dotted lines represent quasi-Keplerian and quasi-uniform flow. Axially unbounded flow, $m = 1$, $r_{\rm in} = 0.52$, Pr = ∞.

While for steep rotation laws the stability maps in the (Rn/Re) plane form open cones with lines of neutral stability of positive slope (with lower and upper Reynolds numbers for fixed Rn) a particular evolution starts for more flat rotation profiles. For $\mu_\Omega \gtrsim 0.52$ the lines of neutral stability encircle closed domains in the (Rn/Re) plane which always contain the line Fr = 1 (Fig. 117). Now even lower and upper stratification numbers Rn exist limiting the instability. The isolines, therefore, possess two different forms. They are closed if the rotation profile is sufficiently flat, and they are open for steeper profiles [188].

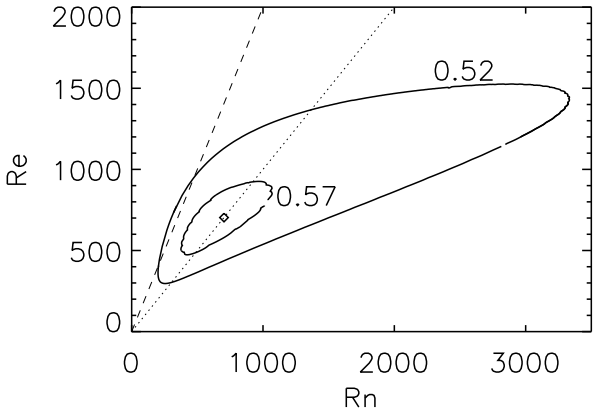

Figure 117. Stability map in the (Rn/Re) plane for flat rotation laws with $\mu_\Omega \geq 0.52$. Fr = 1 (dotted line) and Fr = 2 (dashed line). SRI disappears for $\mu_\Omega \simeq 0.57$ with Re = Rn $\simeq$ 700. Axially unbounded flow, $m = 1$, $r_{\rm in} = 0.52$.

At $\mu_\Omega \gtrsim \mu_{\max}$ the closed instability domain disappears and SRI can only be excited for very large Reynolds num-

bers, e.g. with Re $\simeq 60,000$ for $\mu_\Omega = 0.6$. Simple laws concerning the axial wave numbers k are suggested by Fig. 116 (right). One finds k as almost independent of μ_Ω but inversely scaling with Fr, hence $kD \simeq 4/\mathrm{Fr}$ with D as the gap-width between the cylinders. The axial wavelength, therefore, becomes $\ell \simeq \mathrm{Fr}\, D$ [180].

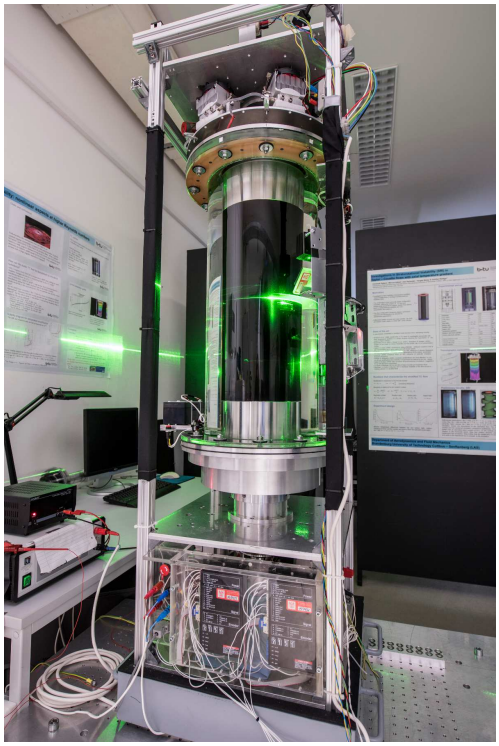

Figure 118. The BTU Cottbus University SRI experiment. The tank with a gap width of 7.5 cm is filled with silicone oil ($\nu = 0.05$ cm^2/s). The axial density stratification is produced by heating and cooling of the endplates. Courtesy U. Harlander.

Developing earlier experiments further, it has been shown that the necessary stratification can also be produced by a temperature gradient due to heating (cooling) the upper (lower) endplate of the container [190], with the normalized temperature difference $\delta = \Delta T/T$. The result is a stably-stratified fluid which becomes unstable under the influence of a differential rotation if the Froude number is of order unity. The required temperature difference is only 5 K, so that $\delta \ll 1$. Such a new experiment was designed at BTU Cottbus with $r_{\rm in} = 0.52$, height $H = 70$ cm and a gap width of $D = 7.5$ cm. The tank is filled with silicone oil M5 with Pr = 58 (Fig. 118).

The resulting drift of the nonaxisymmetric pattern makes it rotate faster than the outer cylinder. Figure 119 shows the normalized drift rates $\dot\phi/\Omega_{\rm in}$ – taken in the laboratory system – as they depend on the rotation ratio μ_Ω. The simulations always lead to $\dot\phi/\Omega_{\rm in} > \mu_\Omega$, i.e. $\dot\phi/\Omega_{\rm out} > 1$, which describes the pattern rotating faster than the outer cylinder. The experimental drift rates grow linearly with μ_Ω. The drift measurements from the SRI experiment confirm the results of the linear theory. The agreement between the drift measurements and the numerical simulations of the experiment with the heated containers demonstrated in Fig. 119 is almost perfect.

13.2. Endplate effects

Even the potential flows with $\delta T = 0$ are strongly influenced by the endplates if the latter are rotating rigidly and if they are fixed at the outer cylinder (as in the majority of the experiments). Such endplates induce a shear instability which strongly influences the onset of the stratified fluids. Figure 120 demonstrates the $m = 2$ character of the radial flow component whose maximum relative to the linear speed of the inner cylinder is 20/Re, i.e. about 5%. Faster rotation may further reduce this value. More important is that this shear instability penetrates the whole container, but this is true only close to the Rayleigh line while for flatter rotation profiles the effect rapidly disappears.

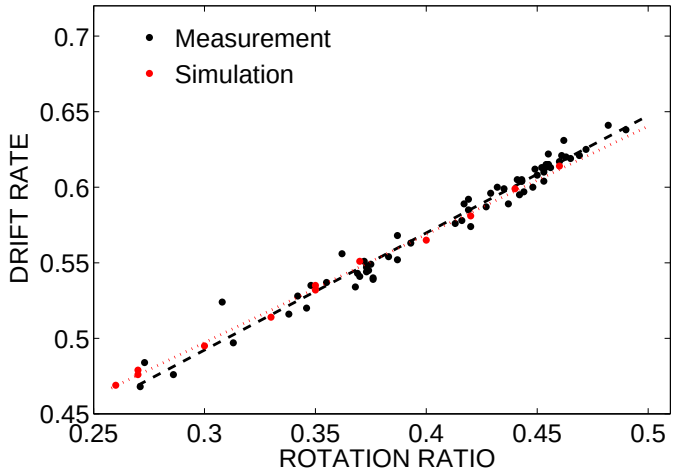

Figure 119. Simulated drift rates compared with experimental data from the SRI experiment with temperature stratification (Fig. 118) as functions of the rotation ratio μ_Ω. The drift rates always exceed μ_Ω so that the pattern rotates (slightly) faster than the outer cylinder.

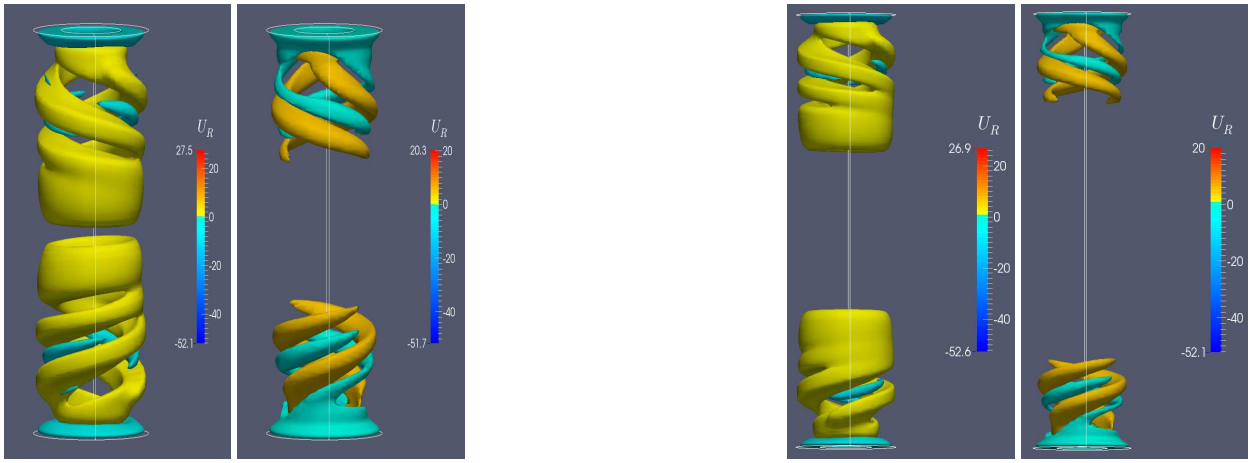

Figure 120. Endplate effects for homogeneous fluids with $\Gamma = 10$ (a,b) and $\Gamma = 16$ (c,d) rotating with $\mu_\Omega = 0.267$ (a,c) and $\mu_\Omega = 0.275$ (b,d). The velocities are measured as Reynolds numbers, $\mathrm{Re}' = u_R D/\nu$. The rigid endplates rotate with the outer cylinder. $\mathrm{Re} = 400$, $r_{\mathrm{in}} = 0.52$, $\delta T = 0$.

The plots c and d of Fig. 120 show that larger aspect ratios with $\Gamma > 10$ help to concentrate the endplate instability at the caps so that the SRI can be better observed in the central region between the two cylinders. One finds that greater Reynolds numbers also help to prevent the instability of homogeneous but axially bounded Taylor-Couette flows.

13.3. Magnetized stratorotational instability

Let us consider the influences of azimuthal fields which are current-free between the cylinders on SRI. Figure 121 shows the critical Reynolds numbers for all ratios μ_Ω, but only for $\mathrm{Pm} = 1$. Three vertical lines are additionally plotted: the Rayleigh limit $\Omega \propto 1/R^2$, the Keplerian profile $\Omega \propto 1/R^{3/2}$, and the $U_\phi = \text{const.}$ profile $\Omega \propto 1/R$. With respect to the minimum Reynolds number, the AMRI with stratification lies above the line for AMRI without stratification, i.e. the density stratification stabilizes AMRI. If SRI exists then it needs even higher Reynolds numbers and Hartmann numbers for excitation. The curve for the combination of SRI and AMRI, therefore, lies between the two extremal curves. In relation to the hydrodynamical SRI the current-free azimuthal field simply destabilizes the differential rotation. Related to the non-stratified AMRI the density stratification always stabilizes the flow.

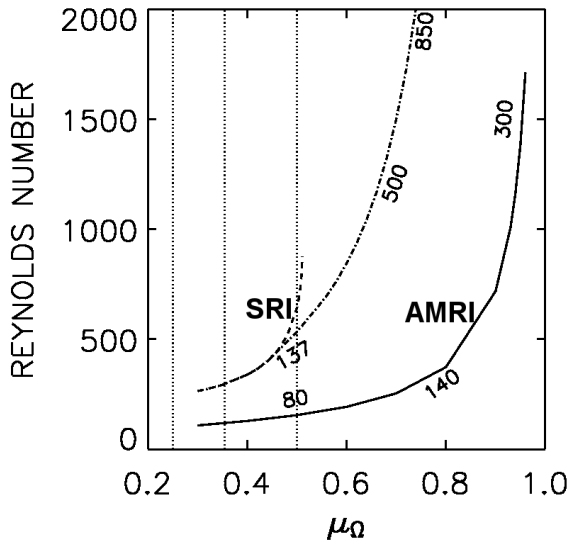

Figure 121. SRI under the presence of azimuthal fields (current-free between the cylinders): minimum Reynolds numbers versus the shear parameter μ_Ω, labeled by the corresponding Ha (defined with $B_{\rm in}$). Dashed line: SRI (hydrodynamic), solid line: AMRI (without density-stratification), dot-dashed line: AMRI with stratification. Vertical dotted lines: potential flow, quasi-Keplerian rotation, quasi-uniform flow (from left to right). AMRI with density stratification is more stable than AMRI without stratification but it is less stable than SRI. $m = 1$, $r_{\rm in} = 0.5$, $\mu_B = r_{\rm in}$, Fr = 0.5, Pm = 1. Insulating boundary conditions. Adapted from [191].

A rotation profile with $\mu_\Omega = 0.6$, which is too flat for SRI, is next combined with an azimuthal magnetic field which is current-free between the cylinders. The density stratification is in accordance with the fixed value Fr = 0.5 which leads to perturbations with maximum growth rates. The resulting lines of marginal stability in the (S/Rm) plane possess the typical AMRI structure with only a weak dependence on the magnetic Prandtl number, which in Fig. 122 (left) varies over three orders of magnitude. The hydrodynamic flow is stable but the magnetohydrodynamic flow is not. As characteristic for AMRI the curves converge for Pm $\to$ 0, which is also the case for the AMRI without stratification in the same coordinate system. The comparison between AMRI without stratification and with stratification also reveals the significant suppression of the instability by the density stratification (Fig. 33).

Calculations for small and large values of Pm and for the quasi-Keplerian flow are collected in Fig. 122 (right) in the (Ha/Re) plane. SRI now exists for a certain finite value of the Reynolds number $\mathrm{Re}_0 \simeq 265$ for Ha = 0. There is, however, a strong dependence of the influence of the magnetic field on the magnetic Prandtl number. As usual the magnetic field stabilizes the flow for Pm ≤ 1 and destabilizes for Pm $\gg 1$. For comparison the (dashed) line of marginal stability of AMRI without stratification for Pm = 1 is given, which exists for much lower Reynolds numbers. The strong stabilization of AMRI by the stable density stratification is again visible.

The azimuthal field can also be due to axial electric currents between the cylinders. In this case the influence of the vertical density stratification on TI is considered for rotation laws with stationary outer cylinder. An almost homogeneous toroidal field with $\mu_B = 1$ may be applied so that without rotation the mode $m = 1$ is unstable while $m = 0$ is stable (Fig. 123, left). For $m = 1$ and Re = 0 the critical Hartmann number is $\mathrm{Ha}_0 = 150$ which does not depend on Pm and on the density stratification. Of course, a critical Reynolds number $\mathrm{Re}_0^{(0)}$ also exists for $m = 0$; the magnetic field stabilizes this mode for vanishing and nonvanishing density stratifications. For nonstratified fluids the marginal-stability line for $m = 0$ does not depend on the value of Pm, and the value Re_0 is smaller than the $\mathrm{Re}_0^{(1)}$ for $m = 1$. Without magnetic field and without axial stratification the Reynolds numbers $\mathrm{Re}_0^{(0)} = 68$ and $\mathrm{Re}_0^{(1)} = 75$. The stability line for $m = 0$ linearly grows with growing magnetic field[8].

For not too large Pm the density-stratification basically *stabilizes* the flow. For Fr = 0.5 we have $\mathrm{Re}_0^{(0)} = 294$ and $\mathrm{Re}_0^{(1)} = 226$, much larger than the above values for nonstratified flows. The most unstable mode without magnetic

[8]For the z-pinch this line is horizontal (Fig. 6.

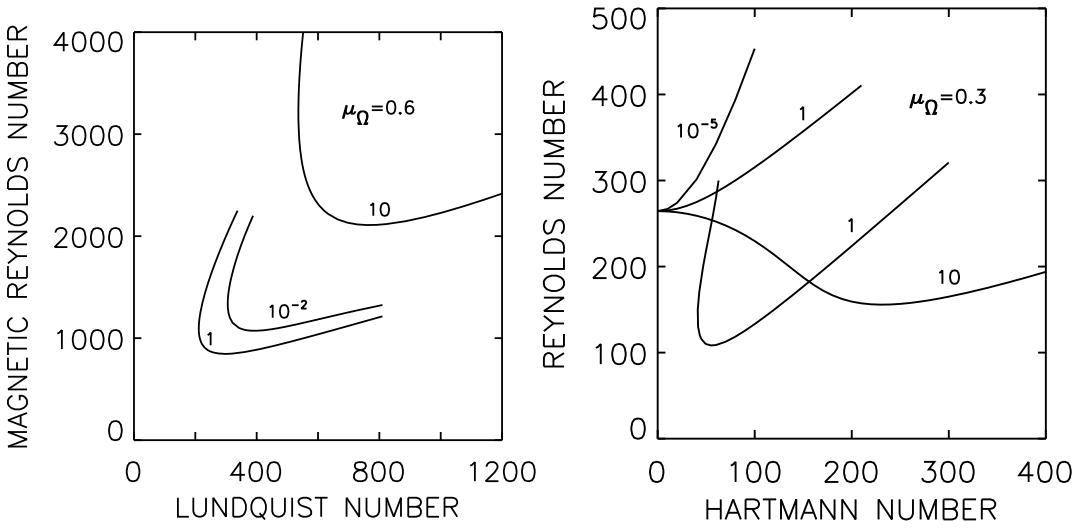

Figure 122. SRI with current-free azimuthal fields for two different rotation laws. Left: $\mu_\Omega = 0.6$ (centrifugally stable). Right: $\mu_\Omega = 0.3$ (centrifugally unstable). The curves are labeled by Pm. The minimum Rm for Pm = 1 corresponds to the dot-dashed line in Fig. 121. Solid lines: $m = 1$, dashed line: non-stratified fluid (Fr = 0, AMRI) with Pm = 1. $m = 1$, $r_{\rm in} = 0.5$, $\mu_B = r_{\rm in}$, Fr = 0.5. Insulating cylinders.

field is $m = 0$, but $m = 1$ is the most unstable mode with magnetic field. It is also the most unstable mode for all finite Ha. For small Pm this mode is stabilized by weak magnetic fields, before a dramatic destabilization happens for larger magnetic fields. On the other hand, for Pm $\gg 1$ the flows are strongly destabilized for all Hartmann numbers.

The transition from the coordinate points $(0, \mathrm{Re}_0)$ to $(\mathrm{Ha}_0, 0)$ representing the centrifugal instability and the TI is not straightforward. A 'ballooning' of the stability region with respect to both parameters (Re > Re_0 plus Ha > Ha_0) is produced by the density stratification. Under the influence of differential rotation and density stratification stronger magnetic field amplitudes prove to be stable than they were without rotation. The effect already exists for rather slow rotation rates. Obviously, both the centrifugal and the Tayler instability are stabilized by the density stratification. Without rotation the density influence on Ha_0 remain negligibly small. For faster rotation the maximal stable magnetic field is smaller than this critical value. The effect exists for all magnetic Prandtl numbers but the maximal Hartmann number becomes smaller for decreasing Pm.

Finally, the stability of the density stratified quasi-Keplerian flow under the influence of a homogeneous axial magnetic field is considered. In the absence of a magnetic field the SRI leads to $\mathrm{Re}_0^{(1)} \simeq 265$. The field stabilizes the flow for small Pm, and destabilizes it for large Pm. The curves in Fig. 123 (left) recall the stability lines of Fig. 2 for $m = 0$. Again for Pm = 10^{-5} the critical Reynolds number strongly increases with increasing field. For Ha = 10 the critical Reynolds number is of order 10^3. It should thus be possible to realize a magnetized SRI experiment with liquid metals in the laboratory.

The solid line in the plot gives the $m = 1$ MRI mode for nonstratified flow and Pm = 1 (see Fig. 13). Comparing with the dotted line for Pm = 1 and Fr = 0.5, one has to conclude that the density stratification *strongly* suppresses the nonaxisymmetric modes of the standard MRI.

13.4. Alpha effect

The experiments [186] produced the necessary vertical stratification with salt injections in water, which is not possible if the fluid is a liquid metal. The question is whether the temperature-driven SRI experiment can be operated with liquid metals. Preliminary estimates show that this concept should also work with gallium or sodium (Pr $\simeq 0.02$). The thermal expansion coefficient of gallium is similar to that of water. In the following the possibilities are discussed to measure the α effect with SRI experiments under the influence of axial or azimuthal fields. In the latter case only current-free fields are considered, so that in all cases the relation (103) holds, excluding complications by the occurrence of eddy diffusivity terms. Finite values of the α effect require the existence of a finite pseudo-scalar $\boldsymbol{g} \cdot \boldsymbol{\Omega}$ in the fluid, where $\boldsymbol{g}$ denotes a stratification direction which here is parallel with the rotation axis. Models with axial fields

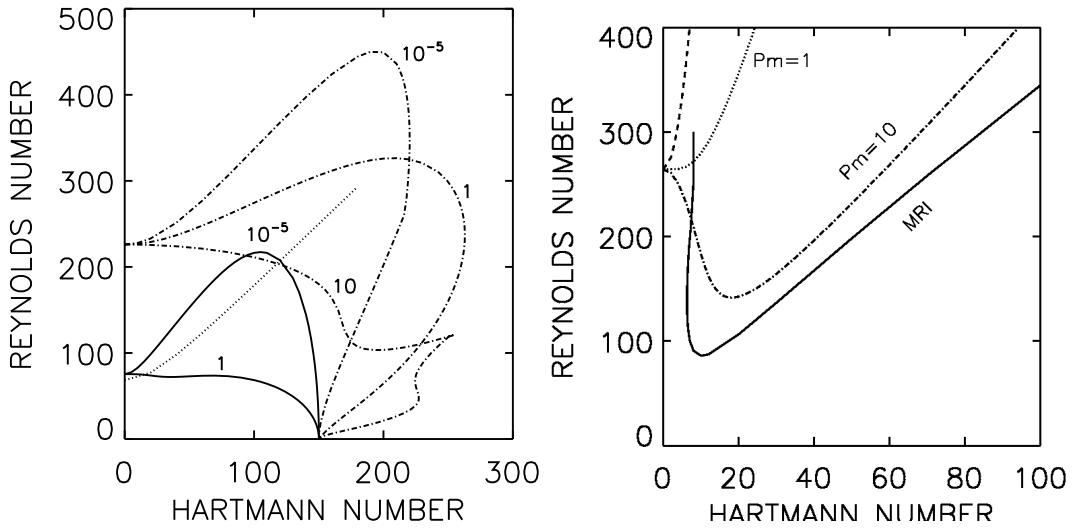

Figure 123. Stratorotational instability influenced by uniform magnetic fields. The curves are labeled by magnetic Prandtl numbers. Left: quasi-uniform azimuthal field ($\mu_B = 1$) and stationary outer cylinder ($\mu_\Omega = 0$). $m = 0$ (dot-dot-dot-dashed line) and $m = 1$ (dot-dashed line). Stability lines for $\delta = 0$ are also given: $m = 0$ (dotted line), $m = 1$ (solid line). Right: uniform axial field. Pm = 10^{-5} (dashed line), Pm = 1 (dotted line) and Pm = 10 (dash-dotted line). Solid line: standard MRI with $\delta = 0$ and Pm = 1. $\mu_\Omega = 0.35$. Fr = 0.5, $r_{\rm in} = 0.5$. Perfectly conducting cylinders [191].

are known to be interesting for experimental realizations. If it would be possible to measure electromotive forces in azimuthal direction then even models with azimuthal fields could be interesting, see [192]. The question is thus whether experiments are imaginable for SRI flows of conducting materials subject to azimuthal magnetic background fields. As we shall see by means of Fig. 124 (left) the tensor component $\alpha_{\phi\phi}$ proves to be much larger than the α_{zz} even for toroidal fields which are current-free between the cylinders ($\mu_B = 0.5$).

The correlation function

$$\boldsymbol{f}^\alpha = \frac{\langle \boldsymbol{u} \times \boldsymbol{b} \rangle}{u_{\rm rms} b_{\rm rms}}, \tag{122}$$

(averaged over ϕ and z) reflects the sign of the α effect. By definition it is smaller than unity, and it does not contain the arbitrary numerical factor which all eigenfunctions can be multiplied by in the linear theory. For the normalized α component C_α according to (105) one obtains

$$C_\alpha = f^\alpha \, {\rm PmRe}' \sqrt{\rm q} \tag{123}$$

with ${\rm q} = b_{\rm rms}^2/B^2$ (B axial or azimuthal component). This relation, of course, only exists for current-free background fields. For axial fields in the presence of the quasi-Keplerian rotation law the numerical simulations yield ${\rm q} < {\rm Rm}'^2$ as a good approximation for Pm < 1. Hence,

$$C_\alpha \simeq f^\alpha \, {\rm Rm}'^2. \tag{124}$$

The simulations for magnetized SRI lead to ${\rm Re}' = O(100)$ for the flow perturbations, almost independent of Pm. From Fig. 124 the correlation functions also hardly depend on Pm. As a consequence, the relation (124) reflects a rather strong dependence on the magnetic Prandtl number. As by definition f^α does not exceed unity, the resulting C_α are thus rather small if applied to liquid metals with their small Pm. As an exception the α experiment in Riga worked with velocities of about 1 m/s and characteristic scale of 10 cm, so that for liquid sodium ${\rm Re}' = O(10^5)$, or equivalently ${\rm Rm}' = O(1)$. This experiment used a prescribed forcing helical geometry in order to mimic the symmetry-breaking between left and right helicity so that f^α might be close to one, hence $C_\alpha \lesssim 1$. The C_α from MSRI experiments would be many orders smaller than this value.

One can easily estimate the potential difference between the endplates of the container for α effect experiments with axial background fields. From Eq. (103) the potential in the direction of $B_z = B_0$ is given by Eq. (111), where

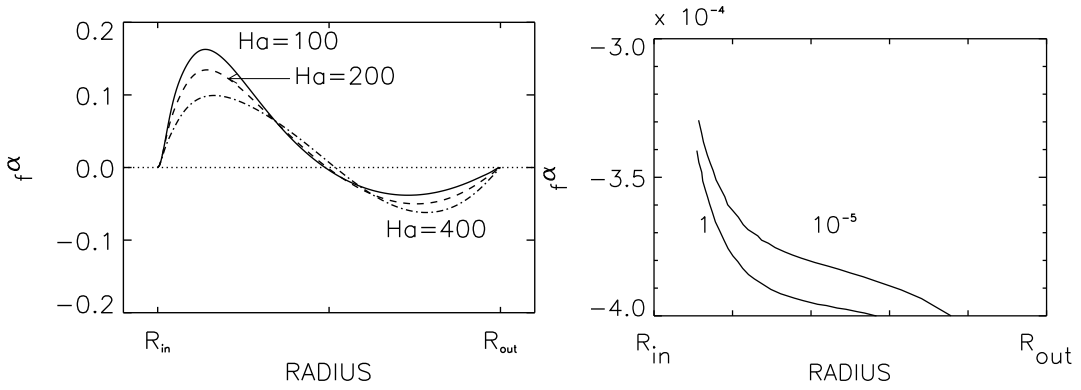

Figure 124. Correlation function (122) for azimuthal (left) and axial field (right) for quasi-Keplerian rotation. Left: $\mu_B = 0.5$, Pm = 0.01; the Reynolds numbers are taken from Fig. 122. Right: Ha = 6 and Re = 360 taken from Fig. 123. $r_{\rm in} = 0.5$, $\mu_\Omega = 0.35$, Fr = 0.5. Perfectly conducting cylinders.

H is the distance between the endplates. For (say) $H \simeq 1$ m and $B_0 \simeq 1$ kG the potential difference is $\Delta\Phi \simeq 0.1|\alpha|$ in mV. Equation (111) can also be written as

$$\Delta\Phi = 10^{-8} C_\alpha \mathrm{Ha} \frac{\eta\sqrt{\mu_0\rho\nu\eta}}{R_{\rm out}/1\mathrm{cm}}\,\Gamma \tag{125}$$

which for liquid sodium leads to $\Delta\Phi = 0.1\ C_\alpha \mathrm{Ha}\ \Gamma/R_{\rm out}$ in mV with $R_{\rm out}$ in cm hence $\Delta\Phi \approx C_\alpha$ in mV is a rough estimate.

The next question concerns the signs of the EMF correlations (122) for prescribed orientation of the density stratification. Figure 124 gives the results for strong axial density gradients (Fr = 0.5) subject to quasi-Keplerian rotation for an azimuthal curl-free field (left panel) and a uniform axial field (right panel). In the first case the correlation function is positive in the inner part of the container and negative in the outer parts. It is positive, however, if finally averaged over the radius, hence $\alpha_{\phi\phi} > 0$ for the three given models. Under the influence of axial fields the sign of the α_{zz} component is opposite to the sign of $\alpha_{\phi\phi}$, as is almost always the case. The right panel of Fig. 124 shows the correlation functions for two values of Pm to be negative for applied axial fields, but they are much smaller than the correlations for applied azimuthal fields.

14. References

[1] G. I. Taylor, Stability of a Viscous Liquid Contained between Two Rotating Cylinders, Philosophical Transactions of the Royal Society of London Series A 223 (1923) 289–343.
[2] S. Chandrasekhar, Hydrodynamic and hydromagnetic stability, Oxford: Clarendon, 1961.
[3] R. J. Donnelly, M. Ozima, Experiments on the Stability of Flow Between Rotating Cylinders in the Presence of a Magnetic Field, Proceedings of the Royal Society of London Series A 266 (1962) 272–286.
[4] D. Michael, The stability of an incompressible electrically conducting fluid rotating about an axis when current flows parallel to the axis, Mathematika 1 (1954) 45–50.
[5] E. Velikhov, Stability of an ideally conducting liquid flowing between cylinders rotating in a magnetic field, Soviet. Phys. JETP 36 (1959) 1389–1404.
[6] Y. V. Vandakurov, Theory for the Stability of a Star with a Toroidal Magnetic Field, Soviet Astronomy 16 (1972) 265.
[7] R. J. Tayler, The adiabatic stability of stars containing magnetic fields-I.Toroidal fields, Month. Not. Roy. Astr. Soc. 161 (1973) 365.
[8] F. N. Edmonds, Jr., Hydromagnetic Stability of a Conducting Fluid in a Circular Magnetic Field, Physics of Fluids 1 (1958) 30–41.
[9] P. H. Roberts, An Introduction to Magnetohydrodynamics, Longmans, 1967.
[10] O. Zikanov, A. Thess, Direct numerical simulation of forced MHD turbulence at low magnetic Reynolds number, Journal of Fluid Mechanics 358 (1998) 299–333.
[11] A. J. Youd, C. F. Barenghi, Hydromagnetic Taylor Couette flow at very small aspect ratio, Journal of Fluid Mechanics 550 (2006) 27–42.
[12] R. J. Tayler, Hydromagnetic Instabilities of an Ideally Conducting Fluid, Proceedings of the Physical Society B 70 (1957) 31–48.
[13] S. Lundquist, On the Stability of Magneto-Hydrostatic Fields, Physical Review 83 (1951) 307–311.
[14] A. Dattner, B. Lehnert, S. Lundquist, Liquid conductor model of instabilities in a pinched discharge, Second UN Geneva Conference (1959) 325–327.
[15] P. H. Roberts, Twisted Magnetic Fields, The Astrophysical Journal 124 (1956) 430.

[16] R. J. Tayler, Stability of Twisted Magnetic Fields in a Fluid of Finite Electrical Conductivity, Reviews of Modern Physics 32 (1960) 907–913.
[17] L. N. Howard, A. S. Gupta, On the hydrodynamic and hydromagnetic stability of swirling flows, Journal of Fluid Mechanics 14 (1962) 463–476.
[18] R. J. Tayler, The adiabatic stability of stars containing magnetic fields. IV - Mixed poloidal and toroidal fields, Month. Not. Roy. Astr. Soc. 191 (1980) 151–163.
[19] S. Chandrasekhar, The Stability of Viscous Flow between Rotating Cylinders in the Presence of a Magnetic Field, Proceedings of the Royal Society of London Series A 216 (1953) 293–309.
[20] J. Priede, I. Grants, G. Gerbeth, Inductionless magnetorotational instability in a Taylor-Couette flow with a helical magnetic field, Physical Review E 75 (4) (2007) 047303.
[21] R. J. Donnelly, M. Ozima, Hydromagnetic Stability of Flow Between Rotating Cylinders, Physical Review Letters 4 (1960) 497–498.
[22] E. R. Niblett, The stability of Couette flow in an axial magnetic field, Canadian Journal of Physics 36 (1958) 1509–1525.
[23] U. H. Kurzweg, The stability of Couette flow in the presence of an axial magnetic field, Journal of Fluid Mechanics 17 (1963) 52–60.
[24] S. Chandrasekhar, The Stability of Non-Dissipative Couette Flow in Hydromagnetics, Proceedings of the National Academy of Science 46 (1960) 253–257.
[25] J. Goodman, H. Ji, Magnetorotational instability of dissipative Couette flow, Journal of Fluid Mechanics 462 (2002) 365–382.
[26] P. H. Roberts, The stability of hydromagnetic Couette flow, Proc. Camb. Phil. Soc. 60 (1964) 635–651.
[27] G. Rüdiger, Y. Zhang, MHD instability in differentially-rotating cylindric flows, Astronomy & Astrophysics 378 (2001) 302–308.
[28] G. Rüdiger, D. A. Shalybkov, MHD Instability in cylindric Taylor-Couette flow, 12th International Couette-Taylor Workshop, Evanston 2001 –arXiv:astro-ph/0108035.
[29] H. Ji, J. Goodman, A. Kageyama, Magnetorotational instability in a rotating liquid metal annulus, Month. Not. Roy. Astr. Soc. 325 (2001) L1–L5.
[30] G. Rüdiger, D. Shalybkov, Stability of axisymmetric Taylor-Couette flow in hydromagnetics, Physical Review E 66 (1) (2002) 016307.
[31] D. A. Shalybkov, G. Rüdiger, M. Schultz, Nonaxisymmetric patterns in the linear theory of MHD Taylor-Couette instability, Astronomy & Astrophysics 395 (2002) 339–343.
[32] G. Rüdiger, M. Schultz, D. Shalybkov, Linear magnetohydrodynamic Taylor-Couette instability for liquid sodium, Physical Review E 67 (4) (2003) 046312.
[33] G. Rüdiger, L. L. Kitchatinov, R. Hollerbach, Magnetic Processes in Astrophysics: theory,simulations, experiments, Wiley-VCH, 2013.
[34] E. L. Koschmieder, Bénard Cells and Taylor Vortices, Cambridge University Press, 1993.
[35] M. Gellert, G. Rüdiger, Axisymmetry vs. nonaxisymmetry of a Taylor-Couette flow with azimuthal magnetic fields, Astronomische Nachrichten 336 (2015) 63.
[36] A. Fournier, H.-P. Bunge, R. Hollerbach, J.-P. Vilotte, Application of the spectral-element method to the axisymmetric Navier-Stokes equation, Geophysical Journal International 156 (2004) 682–700.
[37] M. O. Deville, P. F. Fischer, E. H. Mund, High-Order Methods for Incompressible Fluid Flow, Cambridge University Press, 2002.
[38] M. Gellert, G. Rüdiger, A. Fournier, Energy distribution in nonaxisymmetric magnetic Taylor-Couette flow, Astronomische Nachrichten 328 (2007) 1162.
[39] D. Sisan, N. Mujica, W. Tillotson, Y. Huang, W. Dorland, A. Hassam, T. Antonsen, D. Lathrop, Experimental observation and characterization of the magnetorotational instability, Physical Review Letters 93 (2004) 114502.
[40] M. D. Nornberg, H. Ji, E. Schartman, A. Roach, J. Goodman, Observation of Magnetocoriolis Waves in a Liquid Metal Taylor-Couette Experiment, Physical Review Letters 104 (2010) 074501.
[41] K. Noguchi, V. I. Pariev, S. A. Colgate, H. F. Beckley, J. Nordhaus, Magnetorotational Instability in Liquid Metal Couette Flow, The Astrophysical Journal 575 (2002) 1151–1162.
[42] A. P. Willis, C. F. Barenghi, A Taylor-Couette dynamo, Astronomy & Astrophysics 393 (2002) 339–343.
[43] G. Rüdiger, M. Schultz, Helical magnetorotational instability of Taylor-Couette flows in the Rayleigh limit and for quasi-Kepler rotation, Astronomische Nachrichten 329 (2008) 659.
[44] R. Moreau, On magnetohydrodynamic turbulence, Proc. Symp. on Turbulence of Fluids and Plasmas, Polytechnic Institute of Brooklyn (1968) 359–372.
[45] L. Kit, A. Tsinober, Possibility of creating and investigating two-dimensional turbulence in a strong magnetic field, Magn. Girodin. 7 (1971) 27–34.
[46] H. K. Moffatt, On the suppression of turbulence by a uniform magnetic field, Journal of Fluid Mechanics 28 (1967) 571–592.
[47] G. Ruediger, The influence of a uniform magnetic field of arbitrary strength on turbulence, Astronomische Nachrichten 295 (1974) 275–284.
[48] K.-H. Raedler, On the influence of a large-scale magnetic field on turbulent motions in an electrically conducting medium, Astronomische Nachrichten 295 (1974) 265–273.
[49] U. Schumann, Numerical simulation of the transition from three- to two-dimensional turbulence under a uniform magnetic field, Journal of Fluid Mechanics 74 (1976) 31–58.
[50] J. F. Hawley, S. A. Balbus, A Powerful Local Shear Instability in Weakly Magnetized Disks. II. Nonlinear Evolution, The Astrophysical Journal 376 (1991) 223.
[51] L. L. Kitchatinov, G. Rüdiger, Seed fields for galactic dynamos by the magnetorotational instability, Astronomy & Astrophysics 424 (2004) 565–570.
[52] M. Gellert, G. Rüdiger, M. Schultz, The angular momentum transport by standard MRI in quasi-Kepler cylindrical Taylor-Couette flows, Astronomy & Astrophysics 541 (2012) A124.
[53] A. Guseva, A. P. Willis, R. Hollerbach, M. Avila, Transition to magnetorotational turbulence in Taylor-Couette flow with imposed azimuthal magnetic field, New Journal of Physics 17 (9) (2015) 093018.
[54] S. Fromang, J. Papaloizou, G. Lesur, T. Heinemann, MHD simulations of the magnetorotational instability in a shearing box with zero net flux. II. The effect of transport coefficients, Astronomy & Astrophysics 476 (2007) 1123–1132.
[55] W. J. Duschl, P. A. Strittmatter, P. L. Biermann, A note on hydrodynamic viscosity and selfgravitation in accretion disks, Astronomy &

Astrophysics 357 (2000) 1123–1132.
[56] J.-M. Huré, D. Richard, J.-P. Zahn, Accretion discs models with the β-viscosity prescription derived from laboratory experiments, Astronomy & Astrophysics 367 (2001) 1087–1094.
[57] E. Schartman, H. Ji, M. J. Burin, J. Goodman, Stability of quasi-Keplerian shear flow in a laboratory experiment, Astronomy & Astrophysics 543 (2012) A94.
[58] P. J. Käpylä, M. J. Korpi, Magnetorotational instability driven dynamos at low magnetic Prandtl numbers, Month. Not. Roy. Astr. Soc. 413 (2011) 901–907.
[59] M. Boussinesq, Theorie de lecoulement tourbillonnant et tumultueux des liquides dans les lits rectilignes a grande section , Gauthier-Villars, Paris, 1897.
[60] N. I. Shakura, R. A. Sunyaev, Black holes in binary systems. Observational appearance, Astronomy & Astrophysics 24 (1973) 337–355.
[61] G. Lesur, P.-Y. Longaretti, Impact of dimensionless numbers on the efficiency of magnetorotational instability induced turbulent transport, Month. Not. Roy. Astr. Soc. 378 (2007) 1471–1480.
[62] H. Meheut, S. Fromang, G. Lesur, M. Joos, P.-Y. Longaretti, Angular momentum transport and large eddy simulations in magnetorotational turbulence: the small Pm limit, Astronomy & Astrophysics 579 (2015) A117.
[63] A. Brandenburg, K. Subramanian, Astrophysical magnetic fields and nonlinear dynamo theory, Physics Reports 417 (2005) 1–209.
[64] I. Herron, F. Soliman, The stability of Couette flow in a toroidal magnetic field, Applied Mathematics Letters 19 (2006) 1113–1117.
[65] G. I. Ogilvie, J. E. Pringle, The non-axisymmetric instability of a cylindrical shear flow containing an azimuthal magnetic field, Month. Not. Roy. Astr. Soc. 279 (1996) 152–164.
[66] G. Rüdiger, R. Hollerbach, M. Schultz, D. Elstner, Destabilization of hydrodynamically stable rotation laws by azimuthal magnetic fields, Month. Not. Roy. Astr. Soc. 377 (2007) 1481–1487.
[67] G. Rüdiger, M. Schultz, F. Stefani, M. Mond, Diffusive Magnetohydrodynamic Instabilities beyond the Chandrasekhar Theorem, The Astrophysical Journal 811 (2015) 84.
[68] A. Brandenburg, Magnetic Prandtl Number Dependence of the Kinetic-to-magnetic Dissipation Ratio, The Astrophysical Journal 791 (2014) 12.
[69] R. Hollerbach, V. Teeluck, G. Rüdiger, Nonaxisymmetric Magnetorotational Instabilities in Cylindrical Taylor-Couette Flow, Physical Review Letters 104 (4) (2010) 044502.
[70] G. Rüdiger, M. Gellert, M. Schultz, R. Hollerbach, F. Stefani, Astrophysical and experimental implications from the magnetorotational instability of toroidal fields, Month. Not. Roy. Astr. Soc. 438 (2014) 271–277.
[71] F. Krause, G. Rüdiger, On the Reynolds Stresses in Mean Field Hydrodynamics. I. Incompressible Homogeneous Isotropic Turbulence, Astronomische Nachrichten 295 (1974) 93–99.
[72] S. I. Vainshtein, L. L. Kichatinov, The macroscopic magnetohydrodynamics of inhomogeneously turbulent cosmic plasmas, Geophysical and Astrophysical Fluid Dynamics 24 (1983) 273–298.
[73] J. Szklarski, Reduction of boundary effects in the spiral MRI experiment PROMISE, Astronomische Nachrichten 328 (2007) 499.
[74] J. Szklarski, G. Rüdiger, Ekman-Hartmann layer in a magnetohydrodynamic Taylor-Couette flow, Physical Review E 76 (6) (2007) 066308.
[75] F. Stefani, T. Gundrum, G. Gerbeth, G. Rüdiger, J. Szklarski, R. Hollerbach, Experiments on the magnetorotational instability in helical magnetic fields, New Journal of Physics 9 (2007) 295.
[76] F. Stefani, G. Gerbeth, T. Gundrum, J. Szklarski, G. Rüdiger, R. Hollerbach, Results of a modified PROMISE experiment, Astronomische Nachrichten 329 (2008) 652.
[77] M. Seilmayer, V. Galindo, G. Gerbeth, T. Gundrum, F. Stefani, M. Gellert, G. Rüdiger, M. Schultz, R. Hollerbach, Experimental Evidence for Nonaxisymmetric Magnetorotational Instability in a Rotating Liquid Metal Exposed to an Azimuthal Magnetic Field, Physical Review Letters 113 (2) (2014) 024505.
[78] F. Stefani, T. Gundrum, G. Gerbeth, G. Rüdiger, M. Schultz, J. Szklarski, R. Hollerbach, Experimental Evidence for Magnetorotational Instability in a Taylor-Couette Flow under the Influence of a Helical Magnetic Field, Physical Review Letters 97 (18) (2006) 184502.
[79] G. Rüdiger, R. Hollerbach, F. Stefani, T. Gundrum, G. Gerbeth, R. Rosner, The Traveling-Wave MRI in Cylindrical Taylor-Couette Flow: Comparing Wavelengths and Speeds in Theory and Experiment, The Astrophysical Journal 649 (2006) L145–L147.
[80] M. Seilmayer, T. Gundrum, F. Stefani, Noise reduction of ultrasonic doppler velocimetry in liquid metal experiments with high magnetic fields, Flow Measurement and Instrumentation 48 (2016) 74–80.
[81] G. Rüdiger, M. Gellert, F. Spada, I. Tereshin, The angular momentum transport by unstable toroidal magnetic fields, Astronomy & Astrophysics 573 (2015) A80.
[82] G. I. Taylor, Fluid Friction between Rotating Cylinders. I. Torque Measurements, Proceedings of the Royal Society of London Series A 157 (1936) 546–564.
[83] F. Schultz-Grunow, Zur Stabilität der Couette-Strömung, Zeitschrift für Angewandte Mathematik und Mechanik 39 (1959) 101–110.
[84] F. Wendt, Turbulente Strömungen zwischen zwei rotierenden koaxialen Zylindern, Diss. Göttingen 1934, Ingenieur-Archiv 4 (1933) 557–595.
[85] D. Richard, J.-P. Zahn, Turbulence in differentially rotating flows. What can be learned from the Couette-Taylor experiment, Astronomy & Astrophysics 347 (1999) 734–738.
[86] M. J. Burin, E. Schartman, H. Ji, Local measurements of turbulent angular momentum transport in circular Couette flow, Experiments in Fluids 48 (2010) 763–769.
[87] M. S. Paoletti, D. P. M. van Gils, B. Dubrulle, C. Sun, D. Lohse, D. P. Lathrop, Angular momentum transport and turbulence in laboratory models of Keplerian flows, Astronomy & Astrophysics 547 (2012) A64.
[88] H. Ji, M. Burin, E. Schartman, J. Goodman, Hydrodynamic turbulence cannot transport angular momentum effectively in astrophysical disks, Nature 444 (2006) 343–346.
[89] E. Schartman, H. Ji, M. J. Burin, Development of a Couette-Taylor flow device with active minimization of secondary circulation, Review of Scientific Instruments 80 (2) (2009) 024501–024501.
[90] M. S. Paoletti, D. P. Lathrop, Angular Momentum Transport in Turbulent Flow between Independently Rotating Cylinders, Physical Review

Letters 106 (2) (2011) 024501.
[91] D. P. M. van Gils, S. G. Huisman, G.-W. Bruggert, C. Sun, D. Lohse, Torque Scaling in Turbulent Taylor-Couette Flow with Co- and Counterrotating Cylinders, Physical Review Letters 106 (2) (2011) 024502.
[92] S. G. Huisman, D. P. M. van Gils, S. Grossmann, C. Sun, D. Lohse, Ultimate Turbulent Taylor-Couette Flow, Physical Review Letters 108 (2) (2012) 024501.
[93] S. A. Balbus, Fluid dynamics: A turbulent matter, Nature 470 (2011) 475–476.
[94] S. Merbold, H. J. Brauckmann, C. Egbers, Torque measurements and numerical determination in differentially rotating wide gap Taylor-Couette flow, Physical Review E 87 (2) (2013) 023014.
[95] W. Liu, J. Goodman, I. Herron, H. Ji, Helical magnetorotational instability in magnetized Taylor-Couette flow, Physical Review E 74 (5) (2006) 056302.
[96] O. N. Kirillov, F. Stefani, Y. Fukumoto, A Unifying Picture of Helical and Azimuthal Magnetorotational Instability, and the Universal Significance of the Liu Limit, The Astrophysical Journal 756 (2012) 83.
[97] O. N. Kirillov, F. Stefani, Y. Fukumoto, Local instabilities in magnetized rotational flows: a short-wavelength approach, Journal of Fluid Mechanics 760 (2014) 591–633.
[98] F. Stefani, O. N. Kirillov, Destabilization of rotating flows with positive shear by azimuthal magnetic fields, Physical Review E 92 (5) (2015) 051001.
[99] D. J. Acheson, On the instability of toroidal magnetic fields and differential rotation in stars, Philosophical Transactions of the Royal Society of London Series A 289 (1978) 459–500.
[100] S. Chandrasekhar, On the Stability of the Simplest Solution of the Equations of Hydromagnetics, Proc. Natl. Acad. Sci. USA 42 (1956) 273–276.
[101] J. A. Tataronis, M. Mond, Magnetohydrodynamic stability of plasmas with aligned mass flow, Physics of Fluids 30 (1987) 84–89.
[102] G. Rüdiger, M. Schultz, Tayler instability of toroidal magnetic fields in MHD Taylor-Couette flows, Astronomische Nachrichten 331 (2010) 121.
[103] D. R. Fearn, Boundary conditions for a rapidly rotating hydromagnetic system in a cylindrical container, Geophysical and Astrophysical Fluid Dynamics 25 (1983) 65–75.
[104] E. Pitts, R. J. Tayler, The adiabatic stability of stars containing magnetic fields. IV - The influence of rotation, Month. Not. Roy. Astr. Soc. 216 (1985) 139–154.
[105] M. Gellert, G. Rüdiger, M. Schultz, A. Guseva, R. Hollerbach, Nonaxisymmetric MHD Instabilities of Chandrasekhar States in Taylor-Couette Geometry, The Astrophysical Journal 823 (2016) 99.
[106] D. Biskamp, Magnetohydrodynamic Turbulence, Cambridge University Press, 2003.
[107] A. Kolmogorov, The Local Structure of Turbulence in Incompressible Viscous Fluid for Very Large Reynolds Numbers, Akademiia Nauk SSSR Doklady 30 (1941) 301–305.
[108] V. Dallas, S. M. Tobias, Forcing-dependent dynamics and emergence of helicity in rotating turbulence, Journal of Fluid Mechanics 798 (2016) 682–695.
[109] Y. Zhou, W. H. Matthaeus, P. Dmitruk, Colloquium: Magnetohydrodynamic turbulence and time scales in astrophysical and space plasmas, Reviews of Modern Physics 76 (2004) 1015–1035.
[110] R. Schwenn, E. Marsch, Physics of the Inner Heliosphere II. Particles, Waves and Turbulence, Springer Berlin, 1991.
[111] W.-C. Müller, D. Biskamp, Scaling Properties of Three-Dimensional Magnetohydrodynamic Turbulence, Physical Review Letters 84 (2000) 475–478.
[112] E. Knobloch, On the stability of magnetized accretion discs, Month. Not. Roy. Astr. Soc. 255 (1992) 25P–28P.
[113] E. Knobloch, Symmetry and instability in rotating hydrodynamic and magnetohydrodynamic flows, Physics of Fluids 8 (1996) 1446–1454.
[114] G. Rüdiger, M. Gellert, M. Schultz, R. Hollerbach, Dissipative Taylor-Couette flows under the influence of helical magnetic fields, Physical Review E 82 (1) (2010) 016319.
[115] J. Priede, G. Gerbeth, Absolute versus convective helical magnetorotational instability in a Taylor-Couette flow, Physical Review E 79 (4) (2009) 046310.
[116] J. Priede, Inviscid helical magnetorotational instability in cylindrical Taylor-Couette flow, Physical Review E 84 (6) (2011) 066314.
[117] R. Hollerbach, N. Sibanda, E. Kim, Absolute versus convective helical magnetorotational instability in Taylor-Couette flows, ArXiv e-prints.
[118] G. Rüdiger, R. Hollerbach, M. Schultz, D. A. Shalybkov, The stability of MHD Taylor-Couette flow with current-free spiral magnetic fields between conducting cylinders, Astronomische Nachrichten 326 (2005) 409–413.
[119] J. Szklarski, G. Rüdiger, Nonlinear simulations of magnetic Taylor-Couette flow with current-free helical magnetic fields, Astronomische Nachrichten 327 (2006) 844.
[120] V. P. Lakhin, E. P. Velikhov, Instabilities of highly-resistive rotating liquids in helical magnetic fields, Physics Letters A 369 (2007) 98–106.
[121] R. Hollerbach, G. Rüdiger, New Type of Magnetorotational Instability in Cylindrical Taylor-Couette Flow, Physical Review Letters 95 (12) (2005) 124501.
[122] P. A. Gilman, E. R. Benton, Influence of an Axial Magnetic Field on the Steady Linear Ekman Boundary Layer, Physics of Fluids 11 (1968) 2397–2401.
[123] J. Szklarski, Helical magnetorotational instability in MHD Taylor-Couette flow, Ph.D. thesis, University of Potsdam (2007).
[124] G. Rüdiger, R. Hollerbach, Comment on "Helical magnetorotational instability in magnetized Taylor-Couette flow", Physical Review E 76 (6) (2007) 068301.
[125] R. Hollerbach, A. Fournier, End-effects in rapidly rotating cylindrical Taylor-Couette flow, in: R. Rosner, G. Rüdiger, A. Bonanno (Eds.), MHD Couette Flows: Experiments and Models, Vol. 733 of American Institute of Physics Conference Series, 2004, pp. 114–121.
[126] F. Stefani, G. Gerbeth, T. Gundrum, R. Hollerbach, J. Priede, G. Rüdiger, J. Szklarski, Helical magnetorotational instability in a Taylor-Couette flow with strongly reduced Ekman pumping, Physical Review E 80 (6) (2009) 066303.
[127] D. Shalybkov, Pinch instabilities in Taylor-Couette flow, Physical Review E 73 (1) (2006) 016302.
[128] G. Rüdiger, M. Schultz, D. Shalybkov, R. Hollerbach, Theory of current-driven instability experiments in magnetic Taylor-Couette flows,

Physical Review E 76 (5) (2007) 056309.
[129] M. Gellert, G. Rüdiger, R. Hollerbach, Helicity and α-effect by current-driven instabilities of helical magnetic fields, Month. Not. Roy. Astr. Soc. 414 (2011) 2696–2701.
[130] C. Hoffmann, M. Heise, S. Altmeyer, J. Abshagen, A. Pinter, G. Pfister, M. Lücke, Nonlinear defects separating spiral waves in Taylor-Couette flow, Physical Review E 80 (6) (2009) 066308.
[131] A. Bonanno, A. Brandenburg, F. Del Sordo, D. Mitra, Breakdown of chiral symmetry during saturation of the Tayler instability, Physical Review E 86 (1) (2012) 016313.
[132] N. Weber, V. Galindo, F. Stefani, T. Weier, The Tayler instability at low magnetic Prandtl numbers: between chiral symmetry breaking and helicity oscillations, New Journal of Physics 17 (2015) 113013.
[133] G. Rüdiger, M. Gellert, M. Schultz, K. G. Strassmeier, F. Stefani, T. Gundrum, M. Seilmayer, G. Gerbeth, Critical Fields and Growth Rates of the Tayler Instability as Probed by a Columnar Gallium Experiment, The Astrophysical Journal 755 (2012) 181.
[134] G. Rüdiger, M. Schultz, M. Gellert, The Tayler instability of toroidal magnetic fields in a columnar gallium experiment, Astronomische Nachrichten 332 (2011) 17–23.
[135] H. J. Bräuer, F. Krause, The Mean Energy of a Decaying Magnetic Field in MHD Turbulence, Astronomische Nachrichten 295 (1974) 223–228.
[136] M. Seilmayer, F. Stefani, T. Gundrum, T. Weier, G. Gerbeth, M. Gellert, G. Rüdiger, Experimental Evidence for a Transient Tayler Instability in a Cylindrical Liquid-Metal Column, Physical Review Letters 108 (24) (2012) 244501.
[137] A. Paredes, M. Gellert, G. Rüdiger, Mixing of a passive scalar by the instability of a differentially rotating axial pinch, Astronomy & Astrophysics 588 (2016) A147.
[138] G. Rüdiger, M. Schultz, M. Gellert, F. Stefani, Subcritical excitation of the current-driven Tayler instability by super-rotation, Physics of Fluids 28 (1) (2016) 014105.
[139] A. Bonanno, V. Urpin, The magnetohydrodynamic instability of current-carrying jets, Astronomy & Astrophysics 525 (2011) A100.
[140] A. Bonanno, V. Urpin, Non-axisymmetric instability of axisymmetric magnetic fields, Astronomy & Astrophysics 488 (2008) 1–7.
[141] L. L. Kitchatinov, V. V. Pipin, G. Ruediger, Turbulent viscosity, magnetic diffusivity, and heat conductivity under the influence of rotation and magnetic field, Astronomische Nachrichten 315 (1994) 157–170.
[142] K.-H. Rädler, N. Kleeorin, I. Rogachevskii, The Mean Electromotive Force for MHD Turbulence: The Case of a Weak Mean Magnetic Field and Slow Rotation, Geophysical and Astrophysical Fluid Dynamics 97 (2003) 249–274.
[143] A. Brandenburg, A. Svedin, G. M. Vasil, Turbulent diffusion with rotation or magnetic fields, Month. Not. Roy. Astr. Soc. 395 (2009) 1599–1606.
[144] M. Gellert, G. Rüdiger, Eddy diffusivity from hydromagnetic Taylor-Couette flow experiments, Physical Review E 80 (4) (2009) 046314.
[145] S. A. Denisov, V. I. Noskov, R. A. Stepanov, P. G. Frick, Measurements of turbulent magnetic diffusivity in a liquid-gallium flow, Soviet Journal of Experimental and Theoretical Physics Letters 88 (2008) 167–171.
[146] A. B. Reighard, M. R. Brown, Turbulent Conductivity Measurements in a Spherical Liquid Sodium Flow, Physical Review Letters 86 (2001) 2794–2797.
[147] R. Monchaux, M. Berhanu, M. Bourgoin, M. Moulin, P. Odier, J.-F. Pinton, R. Volk, S. Fauve, N. Mordant, F. Pétrélis, A. Chiffaudel, F. Daviaud, B. Dubrulle, C. Gasquet, L. Marié, F. Ravelet, Generation of a Magnetic Field by Dynamo Action in a Turbulent Flow of Liquid Sodium, Physical Review Letters 98 (4) (2007) 044502.
[148] P. Frick, S. Denisov, V. Noskov, R. Stepanov, Direct measurement of effective electro conductivity of turbulent liquid metal, Astronomische Nachrichten 329 (2008) 706.
[149] P. Frick, V. Noskov, S. Denisov, R. Stepanov, Direct Measurement of Effective Magnetic Diffusivity in Turbulent Flow of Liquid Sodium, Physical Review Letters 105 (18) (2010) 184502.
[150] V. Noskov, S. Denisov, R. Stepanov, P. Frick, Turbulent viscosity and turbulent magnetic diffusivity in a decaying spin-down flow of liquid sodium, Physical Review E 85 (1) (2012) 016303.
[151] M. Gellert, G. Rüdiger, Toroidal field instability and eddy viscosity in Taylor-Couette flows, Astronomische Nachrichten 329 (2008) 709.
[152] A. Brandenburg, P. J. Käpylä, A. Mohammed, Non-Fickian diffusion and tau approximation from numerical turbulence, Physics of Fluids 16 (2004) 1020–1027.
[153] E. Schatzman, Turbulent Transport, Solar Lithium and Solar Neutrinos, The Astrophysical Journal 3 (1969) 139.
[154] E. Schatzman, Turbulent transport and lithium destruction in main sequence stars, Astronomy & Astrophysics 56 (1977) 211–218.
[155] J.-P. Zahn, Circulation and turbulence in rotating stars, Astronomy & Astrophysics 265 (1992) 115–132.
[156] I. Brott, I. Hunter, P. Anders, N. Langer, How Efficient is Rotational Mixing in Massive Stars?, in: B. W. O'Shea, A. Heger (Eds.), First Stars III, Vol. 990 of American Institute of Physics Conference Series, 2008, pp. 273–275.
[157] A. Brandenburg, A. Nordlund, R. F. Stein, U. Torkelsson, Dynamo-generated Turbulence and Large-Scale Magnetic Fields in a Keplerian Shear Flow, The Astrophysical Journal 446 (1995) 741.
[158] J. F. Hawley, C. F. Gammie, S. A. Balbus, Local Three-dimensional Simulations of an Accretion Disk Hydromagnetic Dynamo, The Astrophysical Journal 464 (1996) 690.
[159] S. Fromang, J. Papaloizou, MHD simulations of the magnetorotational instability in a shearing box with zero net flux. I. The issue of convergence, Astronomy & Astrophysics 476 (2007) 1113–1122.
[160] H. C. Spruit, Differential rotation and magnetic fields in stellar interiors, Astronomy & Astrophysics 349 (1999) 189–202.
[161] H. C. Spruit, Dynamo action by differential rotation in a stably stratified stellar interior, Astronomy & Astrophysics 381 (2002) 923–932.
[162] M. Y. Reshetnyak, Hydrodynamic helicity in Boussinesq-type models of the geodynamo, Izvestiya Physics of the Solid Earth 42 (2006) 449–459.
[163] J. Braithwaite, The stability of toroidal fields in stars, Astronomy & Astrophysics 453 (2006) 687–698.
[164] A. Pouquet, U. Frisch, J. Leorat, Strong MHD helical turbulence and the nonlinear dynamo effect, Journal of Fluid Mechanics 77 (1976) 321–354.
[165] G. Rüdiger, R. Hollerbach, The magnetic universe : geophysical and astrophysical dynamo theory, Wiley-VCH, 2004.

[166] J.-P. Zahn, A. S. Brun, S. Mathis, On magnetic instabilities and dynamo action in stellar radiation zones, Astronomy & Astrophysics 474 (2007) 145–154.
[167] M. Gellert, G. Rüdiger, D. Elstner, Helicity generation and α-effect by Tayler instability with z-dependent differential rotation, Astronomy & Astrophysics 479 (2008) L33–L36.
[168] M. Steenbeck, I. M. Kirko, A. Gailitis, A. P. Klawina, F. Krause, I. J. Laumanis, O. A. Lielausis, An Experimental Verification of the α-Effect, Monats. Dt. Akad. Wiss., Berlin 9 (1967) 714–719.
[169] G. Rüdiger, A. Brandenburg, α effect in a turbulent liquid-metal plane Couette flow, Physical Review E 89 (3) (2014) 033009.
[170] M. Wardle, The Balbus-Hawley instability in weakly ionized discs, Month. Not. Roy. Astr. Soc. 307 (1999) 849–856.
[171] S. A. Balbus, C. Terquem, Linear Analysis of the Hall Effect in Protostellar Disks, The Astrophysical Journal 552 (2001) 235–247.
[172] G. Rüdiger, D. Shalybkov, Linear instability of magnetic Taylor-Couette flow with Hall effect, Physical Review E 69 (1) (2004) 016303.
[173] M. L. Dudley, R. W. James, Time-dependent kinematic dynamos with stationary flows, Proceedings of the Royal Society of London Series A 425 (1989) 407–429.
[174] R. Hollerbach, G. Rüdiger, The influence of Hall drift on the magnetic fields of neutron stars, Month. Not. Roy. Astr. Soc. 337 (2002) 216–224.
[175] C. J. Wareing, R. Hollerbach, Hall cascades versus instabilities in neutron star magnetic fields, Astronomy & Astrophysics 508 (2009) L39–L42.
[176] V. Urpin, G. Rüdiger, The stability of magnetized protostellar disks with the Hall effect and buoyancy, Astronomy & Astrophysics 437 (2005) 23–30.
[177] T. Kondić, G. Rüdiger, R. Hollerbach, The shear-Hall instability in newborn neutron stars, Astronomy & Astrophysics 535 (2011) L2.
[178] T. Kondić, G. Rüdiger, R. Arlt, Linear stability analysis of the Hall magnetorotational instability in a spherical domain, Astronomische Nachrichten 333 (2012) 202.
[179] G. Rüdiger, D. A. Shalybkov, M. Schultz, M. Mond, Tayler instability with Hall effect in young neutron stars, Astronomische Nachrichten 330 (2009) 12.
[180] M. J. Molemaker, J. C. McWilliams, I. Yavneh, Instability and Equilibration of Centrifugally Stable Stratified Taylor-Couette Flow, Physical Review Letters 86 (2001) 5270–5273.
[181] I. Yavneh, J. C. McWilliams, M. Jeroen Molemaker, Non-axisymmetric instability of centrifugally stable stratified Taylor Couette flow, Journal of Fluid Mechanics 448 (2001) 1–21.
[182] B. Dubrulle, L. Marié, C. Normand, D. Richard, F. Hersant, J.-P. Zahn, An hydrodynamic shear instability in stratified disks, Astronomy & Astrophysics 429 (2005) 1–13.
[183] D. Shalybkov, G. Rüdiger, Stability of density-stratified viscous Taylor-Couette flows, Astronomy & Astrophysics 438 (2005) 411–417.
[184] O. M. Umurhan, On the stratorotational instability in the quasi-hydrostatic semigeostrophic limit, Month. Not. Roy. Astr. Soc. 365 (2006) 85–100.
[185] E. M. Withjack, C. F. Chen, An experimental study of Couette instability of stratified fluids, Journal of Fluid Mechanics 66 (1974) 725–737.
[186] M. Le Bars, P. Le Gal, Experimental Analysis of the Stratorotational Instability in a Cylindrical Couette Flow, Physical Review Letters 6 (2007) 064502.
[187] R. Ibanez, H. L. Swinney, B. Rodenborn, Observations of the stratorotational instability in rotating concentric cylinders, Physical Review Fluids 1 (5) (2016) 053601.
[188] G. Rüdiger, T. Seelig, M. Schultz, M. Gellert, U. Harlander, C. Egbers, The stratorotational instability of Taylor-Couette flows of moderate Reynolds numbers, ArXiv e-prints.
[189] K. Ooyama, On the Stability of the Baroclinic Circular Vortex: a Sufficient Criterion for Instability, Journal of Atmospheric Sciences 23 (1966) 43–53.
[190] M. Gellert, G. Rüdiger, Stratorotational instability in Taylor-Couette flow heated from above, Journal of Fluid Mechanics 623 (2009) 375.
[191] G. Rüdiger, D. A. Shalybkov, Stratorotational instability in MHD Taylor-Couette flows, Astronomy & Astrophysics 493 (2009) 375–383.
[192] J. Forbriger, V. Galindo, G. Gerbeth, F. Stefani, Measurement of the spatio-temporal distribution of harmonic and transient eddy currents in a liquid metal, Meas. Sci. Techn. 19 (2008) 045704.

15. Acknowledgments

This work was partly supported by the German Leibniz Gemeinschaft within the SAW program, by the Deutsche Forschungsgemeinschaft in frame of the SPP 1488 (PlanetMag), and by the Helmholtz-Gemeinschaft Deutscher Forschungszentren in frame of the Helmholtz alliance LIMTECH.